PAH Processing in Space

PAH Processing in Space

Proefschrift

ter verkrijging van
de graad van Doctor aan de Universiteit Leiden,
op gezag van de Rector Magnificus prof. mr. P.F. van der Heijden,
volgens besluit van het College voor Promoties
te verdedigen op donderdag 12 november 2009
klokke 13.45 uur

door

Elisabetta Rita Micelotta

geboren te Torino, Italië
in 1974

Promotiecommissie

Promotores:	Prof. dr. F. P. Israel Prof. dr. A. G. G. M. Tielens
Co-promotor:	Prof. dr. A. P. Jones (Institut d'Astrophysique Spatiale - Université Paris-Sud XI, Orsay - France)
Overige leden:	Dr. B. R. Brandl Prof. dr. E. F. van Dishoeck Dr. E. Dwek (NASA Goddard Space Flight Center, USA) Prof. dr. H. V. J. Linnartz Dr. T. A. Schlathölter (Rijksuniversiteit Groningen - Atoomfysica Kernfysisch Versneller Institute, KVI)

Alla mia Famiglia

Cover: **Benzene molecule in the Leiden sky**.

Photography of the sky by Elisabetta Micelotta.
Benzene molecule: pencil on paper by Gwenaël Boué.
Design by Guilhem Lavaux & Elisabetta Micelotta.

Benzene (C_6H_6) is an aromatic hydrocarbon (not polycyclic since only one ring is present) and a fundamental unit of the Polycyclic Aromatic Hydrocarbons (PAHs) which are the subject of this thesis.

Table of contents

Was it all worth it, was it all worth it all these years.

Queen, “Was It All Worth It”, The Miracle

Chapter 1

Introduction

The research described in this thesis focuses on the physical processes that Polycyclic Aromatic Hydrocarbons (PAHs) undergo during their journey through space.

On Earth, PAHs are one of the most common chemical compounds. They are naturally present in crude oil and coal deposits, arising from chemical conversion of natural product molecules, and are also formed by incomplete combustion of carbon-containing fuels such as wood, coal, diesel, fat, tobacco, or incense. Hence they are found in car exhaust, cigarette smoke and (too) well-cooked meats. This makes PAHs one of the most widespread organic pollutants, regularly under the attention of the media because some compounds have been identified as carcinogenic, mutagenic, and teratogenic. In particular one PAH compound, benzo[a]pyrene, is notable for being the first chemical carcinogen to be discovered, and is one of many carcinogens found in cigarette smoke.

In space, PAHs have been recognised as an important and ubiquitous component of the Interstellar Medium (ISM). Closely related to dust, they are formed in the outflows of evolved and dying stars. PAHs contribute substantially to the heating of the ISM and play a crucial role in the interstellar chemistry and in the cosmic life cycle. Moreover, they can be used as a diagnostic tracer of the environmental conditions within astrophysical objects.

In §1.1 we describe the various components of the ISM and how they interplay within the cosmic life cycle (Fig. 1.1), with a particular attention to supernova explosions because of their crucial role in PAH processing and evolution. In §1.2 we present an overview on PAHs, describing their structure, how they form and evolve in space, what their excitation mechanisms are and consequently how they can be identified and studied – both in the laboratory and in the ISM – through their infrared (IR) emission. The relevance of interstellar PAHs is discussed in §1.3, while in §1.4 we discuss the relevant processes for dust expected to be responsible for PAH processing as well. Finally, the importance of studying PAH processing in the ISM is highlighted in §1.5 and the content of this thesis is outlined in §1.6.

1.1 The Interstellar Medium

1.1.1 Components of the ISM

As the name already suggests, the term Interstellar Medium (ISM) indicates the material filling the volume between stars in a galaxy. It is mainly composed of tenuous hydrogen and helium gas with a contribution from heavier elements which can be

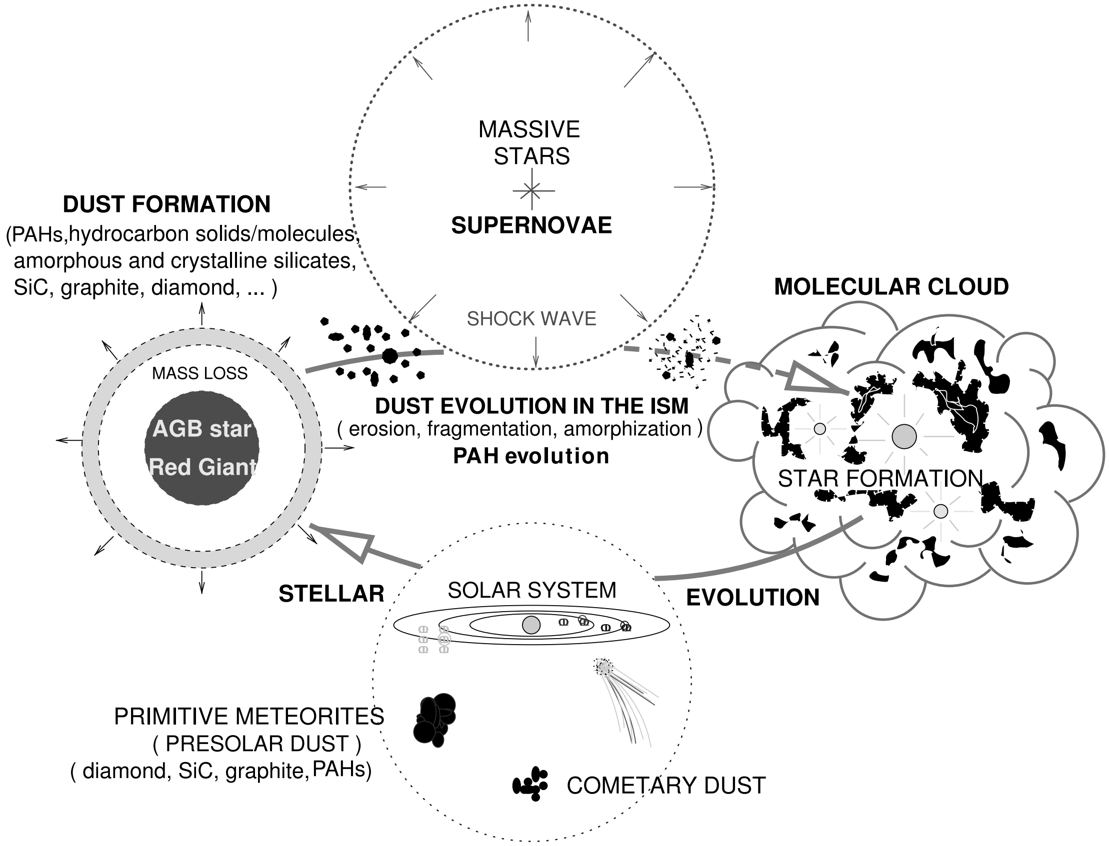

Figure 1.1 — A schematic view of the cosmic life cycle. *Figure adapted from Jones (2004).*

present in the gas phase (in atomic and molecular form) or in the solid state. In the Milky Way the total mass of the ISM gas component is 4.5×10^9 $M_\odot$ (Tielens 2005). For comparison, the mass in stars is 1.8×10^{11} $M_\odot$. The ISM is organized into a variety of phases (Tielens 2005), each characterized by specific physical properties:

- **Molecular gas**. Surveys in the CO J=1-0 transition at 2.6 mm revealed that the molecular gas in the Milky Way is localized in discrete Giant Molecular Clouds with temperatures of 10 – 20 K. This phase has a very small filling factor, only of order of 1%, but accounts for a substantial fraction of the mass, $\sim$ 30 – 60% of the total contents of the Galactic ISM. Molecular clouds are bound by their self-gravity rather than being in pressure equilibrium with other phases of the ISM. The balance of magnetic/turbulent pressure and gravity keeps them stable over timescales of $\simeq 3\times10^{7}$ yr, but at the same time they are nevertheless the sites of active star formation. The typical cloud size and density are $\simeq$ 40 pc and 200 cm^{-3}, with masses of 4×10^5 $M_\odot$, but they contain cores with sizes of $\simeq$ 1 pc, densities exceeding 10^4 cm^{-3} and masses in the range 10 – 10^3 $M_\odot$. The gravitational collapse of these cores leads to the formation of new stars. CO is a widely used tracer of interstellar molecular gas, but the dominant molecular species is thought to be H_2, which cannot be directly detected because of the lack of dipole transitions (the molecule is symmetric). The quantity of H_2 can be estimated from the CO using an empirical conversion factor.

- **Cold Neutral Medium (CNM)** and **Warm Neutral Medium (WNM)**. The neutral gas is traced by the 21 cm line of atomic hydrogen, and is organized into cold ($\simeq$ 100 K) diffuse H I clouds (CNM) and warm ($\simeq$ 8000 K) intercloud gas (WNM). The CNM occupies 1 – 4% of the total volume and a standard cloud has a typical density of 50 cm^{-3} and size of 10 pc. The WNM has a much lower density ($\simeq$ 0.5 cm^{-3}) but occupies a substantial fraction of the total volume ($\sim$ 30 – 60%). The mass distribution varies with the galactic latitude. Between 4 and 8 kpc from the galactic center, 80% of the H I mass in the plane of the galaxy is located in diffuse clouds, while at higher latitudes much of the H I gas is in the intercloud medium.
- **Warm Ionized Medium (WIM)**. This phase is most clearly associated with H II regions, where the gas is photoionized by hot young stars and emits in the Hα recombination line. Although most of the Hα luminosity of the Milky Way arises from distinct H II regions, almost all the mass of ionized gas (10^9 $\mathrm{M}_\odot$) resides in a diffuse component having a low density ($\simeq$ 0.1 cm^{-3}), a temperature of $\sim$ 8000 K and a filling factor of $\simeq$ 0.25. The source of ionization remains uncertain: while photoionization from young stars seems to be the dominant mechanism near the midplane of disk galaxies, outside the galactic plane shock heating or suprathermal particle heating become probably more important.
- **Hot Ionized/Intercloud Medium (HIM)**. This hot and tenuous phase of the ISM ($T \sim 3 - 10 \times 10^5$ K and density around 10^{-3} cm^{-3}) occupies a large fraction of the volume of the halo (while the filling factor in the disk is more controversial) but has a very small mass content. The hot gas can be detected in absorption against bright background sources in highly ionized species (e.g. C IV, S VI, N V, O III, O VI), or through continuum and line emission in the far ultraviolet and X-ray wavelength range. The HIM is heated by strong shocks driven by violent stellar winds from early-type stars and supernova explosions. The hot gas detected at high latitude may have been vented by superbubbles and flown out above and below the plane through galactic chimneys.
- **Interstellar dust**. The presence of this solid state component of the ISM has been deduced from various phenomena, see e.g. Draine (2003) and references therein. Photon absorption and scattering by small dust grains results in a general reddening and extinction of the light coming from distant stars. Non-spherical dust grains may be aligned by magnetic fields or other agents such as radiation pressure or mechanical effects, resulting in the polarization of the star light when transmitted or scattered. In the proximity of bright stars, the light scattered by dust grains produces a reflection nebula. In the diffuse interstellar medium the cold dust (10 – 100 K) is heated by visible and UV radiation, and re-emits the absorbed energy as a continuum spectrum at far-infrared wavelengths. The grain size distribution as a function of the grain radius a, $n(a) \sim a^{-3.5}$ in the range a = 50 – 2500 Å (MRN distribution, Mathis et al. 1977), has been inferred from measurements of the extinction curve over a large wavelength range. Large grains dominate the total dust volume, while small grains dominate the number density and surface area. Dust grain emission is strictly related to grain size

(Draine 2003). Big grains ($a \gtrsim 1000$ Å) are in radiative equilibrium with the interstellar radiation field at temperatures of $\simeq 15-20$ K and re-emit the absorbed interstellar photons at infrared and sub-millimeter wavelengths. Rotating grains ('spinning dust') also give rise to radio emission (Ferrara & Dettmar 1994; Draine & Lazarian 1998). Very small grains ($a \lesssim 100$ Å) are instead quantum heated by the absorption of single UV photons, which may cause large temperature fluctuations (Draine & Li 2001), and emit at mid-IR wavelengths ($25-60$ μm).
Dust grains lock up the majority of the refractory elements (e.g. C, Si, Mg, Fe, Al, Ti, Ca etc), containing about 1% by mass of the gas. The composition of the interstellar dust is still under debate, but there is a general agreement to consider silicates and graphitic/carbonaceous materials as the most important dust components. It is widely accepted that dust is mainly formed at high densities and temperatures in the ejecta of evolved stars such as those populating the Red Giant Branch and the Asymptotic Giant Branch (RGB and AGB stars, Tielens 1997). Carbon-rich stars produce carbonaceus dust ("soot"), while oxygen-rich stars produce silicate dust ("sand") rich in magnesium, with a fraction of 15% at most in crystalline form (e.g. Waters 2004). During the formation of carbonaceous dust, in a process probably comparable to the formation of terrestrial soot in flames (Frenklach & Feigelson 1989a), Polycyclic Aromatic Hydrocarbons (PAHs – see §1.3) may be formed, presumably as an intermediate product when converting gas-phase C (in the form of C_2H_2) to soot. Dust grains can be also formed in the diffuse ISM itself (Draine 2009) and in the ejecta of type II supernovae (Dwek 1998), which at the same time represent the major agent responsible for dust destruction (Dwek et al. 2008).

- **Large interstellar molecules**. Besides dust grains, the interstellar medium also contains a population of large molecules which are generally identified as Polycyclic Aromatic Hydrocarbons (PAHs). Because the *processing* of these molecules in space (we will explain later on what this means) is in fact the subject of this thesis, the properties of PAHs and their importance in the interstellar environment are discussed in a dedicated section (1.3). We emphasize here that PAHs are probably the most visible representative of the molecular universe, but may be not the only one. Interstellar grains are known to contain several populations of nano-particles, whose properties differ from those of bulk materials and are much closer to those of classical large molecules. Moreover, the so-called Diffuse Interstellar Bands (DIBs), prominent absorption features observed in the visible spectra of stars, are too broad to arise from atomic transitions. Their detection implicates the presence of a large number of different molecular species, such as unsaturated carbon chains. Interstellar PAHs have often been suggested as possible carriers of the DIBs and several groups have been working on the comparison between DIBs and PAH spectra (Romanini et al. 1999; Bréchignac & Pino 1999; Salama et al. 1999; Ruiterkamp et al. 2002; Bouwman et al. 2009). Note that generally only PAH cations are considered as potential DIB carriers as neutral PAHs - at least the smaller ones - absorb more to the UV than to the visible. Nevertheless, a recent study by Kokkin et al. (2008) opens up the possibility to test neutral PAHs as carriers of the DIBs.

- **Cosmic rays**. Cosmic rays (CRs) are energetic particles consisting mainly of relativistic protons, helium (10 %), and heavier elements and electrons (1 %). The heavier elements are thought to originate from ions sputtered from dust grains in supernova shocks and subsequently accelerated through the Fermi mechanism. They seem to take about 10 % of the kinetic energy of the supernova ejecta, and their pressure provides support against gravity for the gas in the ISM. High energy ($\gtrsim$ 100 MeV/nucleon) particles contribute considerably to the energy density of the ISM ($\simeq$ 2 eV cm^{-3}). The flux of low-energy (5 – 100 MeV) cosmic rays is difficult to measure because of the *solar modulation*, i.e. the action of the solar wind which prevents low-energy CRs from entering the heliosphere or severely slows them down, with a subsequent variation (modulation) of the observed spectrum. Low-energy cosmic rays are very efficient at ionizing and heating the gas, and in fact cosmic ray ionization is the cornerstone of gas phase chemistry. Conversely, molecular observations can be used to determine the cosmic ray ionization rate, which allows us to constrain the cosmic ray spectrum at low energies. Finally, cosmic rays can induce important structural changes when impinging on dust grains and molecules.
- **Interstellar shocks**. A shock wave is defined as a pressure gradient propagating through a fluid at supersonic speed. Because of the supersonic velocity the upstream material cannot dynamically respond to the upcoming material before it arrives. The shock will then compress, heat and accelerate the medium. The heated material cools through photon emission lines, further compressing the medium. A detailed description of the physics of shock waves can be found in Zel'dovitch & Raizer (1966). Shock waves are very common phenomena in the interstellar (and intergalactic) medium, originating from supernova explosions, AGN jets, strong stellar winds from massive stars or collisions between clouds or galaxies, whenever material moves at velocities exceeding the sound speed in the surrounding medium. Two types of shocks are of interest in the interstellar medium. J-type (J for Jump) shocks, i.e. where the physical conditions (density, temperature and velocity) change abruptly between the pre-shock and post-shock regions. In this case, the gas is suddenly stopped and heated to a high temperature and insignificant radiative and non-radiative relaxation can take place. The second type of shocks occur in a magnetized medium with a low degree of ionization. These are called C-type (C for Continuous) shocks, because the physical parameters vary smoothly across the shock front. In this thesis we will consider only J-shocks in the low density interstellar/intercloud medium.

  Interstellar shocks play a crucial role in the ISM. They are the major agent responsible for the fragmentation and destruction of dust grains, with a consequent modification of the grain size distribution, which in turn may reflect on variations of the extinction curve. The fragmentation (shattering) of bigger grains will produce smaller species, possibly including PAHs which are expected to be processed as well. Interstellar shocks are also thought to be the acceleration mechanism for cosmic rays with energies below 10^{15} eV. The compression of the ISM induced by a shock can trigger star-formation, like usually observed in the spiral arms of disk galaxies. Moreover the energy injected by shock waves into the interstellar – or intergalactic – medium is responsible for the heating of the gas to X-ray emitting temperatures ($> 10^6$ K).

The various phases and components of the ISM are not static and isolated from each other. At the contrary, they interact continuously through the cosmic life cycle described below.

1.1.2 The cosmic life cycle

The cosmic life cycle is summarized in Fig. 1.1. The story of a new star begins in the dark and cold cores of dense molecular clouds. As far as the pressure force is able to compensate the effect of gravity, the cloud is stable. However, if the mass of the core exceeds a critical value, gravitation will overcome the magnetic/turbulent pressure and the core will start to collapse. If the temperature and density are sufficiently high to initiate the nuclear burning of hydrogen into helium, a new star is born. In the case of low and intermediate mass stars, the energy released by the nuclear fusion will prevent the star from further collapsing during the long (10^7 – 10^{10} yr) and stable main-sequence phase of its life. Nuclear reactions in these stars can form elements up to C, O and N. After leaving the main sequence, the star will eventually move into the Asymptotic Giant Branch (AGB). In this phase, the outer layes are loosely bound to the stellar core, while thermal instabilities cause the core material (C and O) to be mixed and brought up to the stellar surface. In the end, the outer envelope will be completely stripped away, exposing the extended nebula around the star to the hot ionizing core. The result is a planetary nebula. Without further nuclear burning, the core will eventually cool down and end its life as a white dwarf.

The evolution of a high-mass star ($M_* > 8\ M_\odot$) is quite different. Massive stars burn their nuclear fuel much faster than low-mass stars. Moreover, they are able to burn C and O into heavier elements up to iron. No further burning is possible because the reaction will be endothermic, so the core will finally collapse while the outer shells will explode: the star has become a type II Supernova. The explosion may totally destroy the star or leave a relic neutron star or pulsar. Explosive nucleosynthesis can occur during the final phases of the star, producing elements heavier than Fe which will be ejected into the ISM.

During their life, stars strongly affect their surroundings, and their life cycle is intimately linked with the physical and chemical evolution of the material of the ISM. Ionizing photons from O and B stars (hot, massive and luminous) create HII regions and are able to destroy interstellar molecules. The majority of the heavy elements synthetized by stars are injected into the ISM in the form of small solid dust particles, which are mainly formed in the expanding cooling outflows of evolved or dying stars (AGB and RGB), possibly in supernova ejecta (but the amount of dust formed in SNe is not well established) and in supergiants, Wolf-Rayet stars and novae (minor production sites). Besides dust particles, the ejecta of evolved stars and supernovae also contain various molecules, from the simplest ones such as CO to much larger ones such as acetylenic chain derivatives (e.g. C_7H) and PAHs.

After injection into the ISM through stellar winds or explosions, the newly-formed stardust and molecules can cycle many times between the intercloud and cloud phases.

UV irradiation in the diffuse ISM and reactions with ions continuously break and reform molecular bonds, allowing only the most stable species to survive. In the WIM dust is mainly processed by strong shocks driven by supernova explosions. Collisions with energetic ions in the hot shocked gas can sputter atoms from the grains, while high velocity grain-grain collisions can lead to vaporization, melting, phase transformation and shattering of the colliding partners (Jones et al. 1994, 1996). In the denser media - diffuse and dense clouds - the physical conditions allow the accretion of gas phase species onto the grains, forming a mantle. In diffuse clouds, accretion seems to proceed preferentially through chemisorption[1] - partly because the high flux of FUV photons will rapidly photodesorb the physisorbed species. In molecular clouds, the mantles consist of simple molecules such as H_2O, CO, CO_2 and CH_3OH in the form of ices, which can be processed by UV photons and high energy cosmic rays into larger and more complex species more tightly bound to the cores. While these processes are experimentally well established, their role in the interstellar scenario is more controversial and not supported by strong observational evidence.

The molecular clouds hosting dust and molecules may become gravitationally unstable and then collapse, giving birth to a new generation of stars, whose elemental composition is determined by the previous stellar population. Protoplanetary disks may form around low-mass stars and likely all intersteller grains are completely vaporized and recondensed as solar system condensates. The circle is closed and the cycle starts again.

1.1.3 Supernova explosions

Supernova explosions play a crucial role in the cosmic life cycle described in the previous section. As already mentioned, they release into the ISM the heavy elements produced by the massive supernova precursor star or during explosive nucleosynthesis. Supernova driven shock waves are the major agent responsible for dust processing in the warm intercloud ISM. In addition, supernova explosions are at the origin of the coronal phase of the ISM (Hot Ionized Medium – HIM, cf. §1.1.1), where dust and molecules are processed by collisions with high velocity thermal ions and electrons in the hot gas, while the expansion of the supernova remnants into the surrounding material strongly contributes to shaping the ISM itself.

At the end of its life, a high mass star ($M_* > 8M_\odot$) ejects a significant fraction of its mass (1 – 5 $M_\odot$) in an explosive event. The ejecta have velocities of some 10^4 km s^{-1} and the typical kinetic energy associated with the explosion is some 10^{51} erg (Ostriker & McKee 1988). The ejecta will expand into the surrounding material following

---

[1] *Adsorption* is the accumulation of atoms or molecules on the surface of a material. This process creates a film of the adsorbate (the molecules or atoms being accumulated) on the adsorbent's surface. *Chemisorption* (or *chemical adsorption*) is adsorption in which the forces involved are valence forces of the same kind as those operating in the formation of chemical compounds.
Physisorption (or *physical adsorption*) is adsorption in which the forces involved are intermolecular forces (van der Waals forces) of the same kind as those responsible for the imperfection of real gases and the condensation of vapours, and which do not involve a significant change in the electronic orbital patterns of the species involved. *Photodesorption* is an increase in the desorption (depletion) of a substance from a surface in the presence of light.

a three-stage process. The first stage starts with the mass of the ejecta totally overcoming the mass of the swept-up interstellar medium and ends when these two masses becomes equal. During this phase the velocity of the ejecta does not change and at the end the kinetic energy has been thermalized and created a bubble of hot shocked gas. In the second phase, called the Sedov – Taylor phase, the bubble of hot gas will expand following a self-similar motion (e.g. McCray & Snow 1979a, and references therein). As long as the shock velocity is above ~ 250 km s^{-1} (corresponding to a temperature of the post-shock gas of 10^6 K) gas cooling is inefficient, because the most abundant atoms are fully ionized, and the expansion is then adiabatic. The accumulating mass of swept-up material will slow down the expansion but the total energy is conserved. The phase ends when the gas temperature drops below $\sim 10^6$ K because of adiabatic expansion. At this point radiative cooling becomes important, the shock becomes isothermal (for practical purposes) and the supernova remnant enters the radiative expansion phase, also called pressure-driven snowplow phase. The overpressure of the remnant with respect to the interstellar medium drives further expansion. Because of the rapid radiative cooling, the density contrast across the shock is very large, almost a factor of 100 even when limited by magnetic fields, and a dense, thin shell of shocked material will develop, which will move into the ISM as the snow in front of the snowplow. This last phase ends when the shock wave velocity approaches the ambient sound speed, $C_0 = 12$ km s^{-1}.

Supernova explosions inject energy into turbulent motions of the ISM and during their evolution will create regions of very hot but tenuous gas which cool only very slowly. When supernovae are abundant, the disks of galaxies puff up because of the turbulent motions, and part of the volume becomes filled with the hot gas, which represents a separate phase of the ISM, the HIM in which the other phases are embedded. If the supernova rate per unit volume is high, the lifetime of the remnant is long and its final volume is large, the expanding supernova remnants will then start to overlap and form a connected tunnel network filled with hot gas. Supernovae will sweep up the warm WNM/WIM phases into thin but dense walls surrounding the tenuous hot phase (HIM). Thermal instability within these walls could lead to the dense CNM phase. The effect of this SN dominated regime shows up in a carved and very filamentary interstellar medium.

Supernova remnants are not randomly distributed. Actually, many of them occur in OB associations. The effect of the many SNe exploding in OB associations, combined with the strong stellar winds of their OB progenitors, may lead to the formation of superbubbles in the ISM. The superbubbles expand and may blow out into the halo, setting up a galactic fountain (Bregman 1980). The expansion and the following explosion of the superbubble creates "chimneys" in the galactic disks through which intermediate/high velocity clouds and hot gas are vented into the halo. The clouds will fall back to the disk following ballistic trajectories, while the gas will eventually cool and condense into clouds which will rain down onto the disk again. The chimneys also provide a natural pathway for both ionizing photons (from OB associations) and heavy elements (produced by the SNe) to flow into the halo. Galactic chimneys represent a strategic mechanism to mantain the disk-halo circulation. Another example of venting into the halo is the supernova-driven galactic-scale "superwind" associated with the starburst galaxy M82 (Fig. 1.2, Griffiths et al. 2000; Strickland & Heckman 2007). In this case there is a huge single outflow from the starburst nucleus, instead of a series of chimneys distributed over the galactic disk. In both chimneys and superwinds, material can be entrained by the outgoing flow, i.e. incorporated into the flow and transported outside the plane but retaining much of its original character (albeit with some modification). We will show in this thesis how important this mechanism is in term of PAH processing.

1.2 Polycyclic Aromatic Hydrocarbons

As already mentioned in §1.1, besides dust grains, the interstellar medium also contains a population of large molecules which are generally identified as Polycyclic Aromatic Hydrocarbons (PAHs). This identification has been carried out through the analysis of the IR emission from a variety of sources. The IR spectrum of most objects, ranging from single HII regions and reflection nebulae to galactic nuclei and entire galaxies (see Tielens 2008 for a recent review) is dominated by broad infrared emission features which show striking similarities with the features characteristic of PAH materials. These bands result from the vibrational relaxation process of FUV-pumped PAH species containing some 50-100 C-atoms. With a very high abundance of $\sim 10^{-7}$ by number relative to hydrogen, PAHs lock up about 10% of the elemental carbon and represent an important component of the ISM.

Interstellar PAHs are often "associated" with dust grains because, on the one hand, they are formed as a by-product of the formation of carbonaceous dust, and on the other hand, they seem indeed to represent, together with the other large interstellar molecules, an extension of the interstellar grain size distribution into the molecular domain. Some properties of grains can reasonably be extrapolated to PAHs taking into account a few details due to their small size, e.g. the calculation of PAH charge, see Tielens (2005). Nevertheless it is important to remember that PAHs are molecules, thus the solid state physics approach used for dust grains, for instance to treat the collisional processing in shocks, is not valid for molecules, whose physics (and chemistry) are different from that of dust in many ways.

1.2.1 Definition, characteristics and structure

PAHs belong to the family of hydrocarbons and are characterized by the arrangement of carbon atoms in a honeycombed lattice structure of fused six-membered aromatic rings with H-atoms located at the edges. Three of four valence electrons of carbon atoms are used to form covalent, σ bonds[2] with neighboring C- or H-atoms, resulting in a planar structure. The remaining electron is located in a p-orbital perpendicular to the plane. The superposition of the p-orbitals of adjacent C-atoms forms π bonds[3]

---

[2] The σ bond is the strongest type of covalent chemical bond. A covalent bond is characterized by the sharing of pairs of electrons between atoms and the overlap of the electron orbitals. The distinguishing feature of a σ bond is that the orbital overlap occurs directly between the nuclei of the atoms.

[3] The π bond is a covalent chemical bond where two lobes of one involved electron orbital overlap two lobes of the other involved electron orbital. While the σ bond has orbital overlap directly between the two nuclei, the π bond has orbital overlap off to the sides of the line joining the two nuclei.

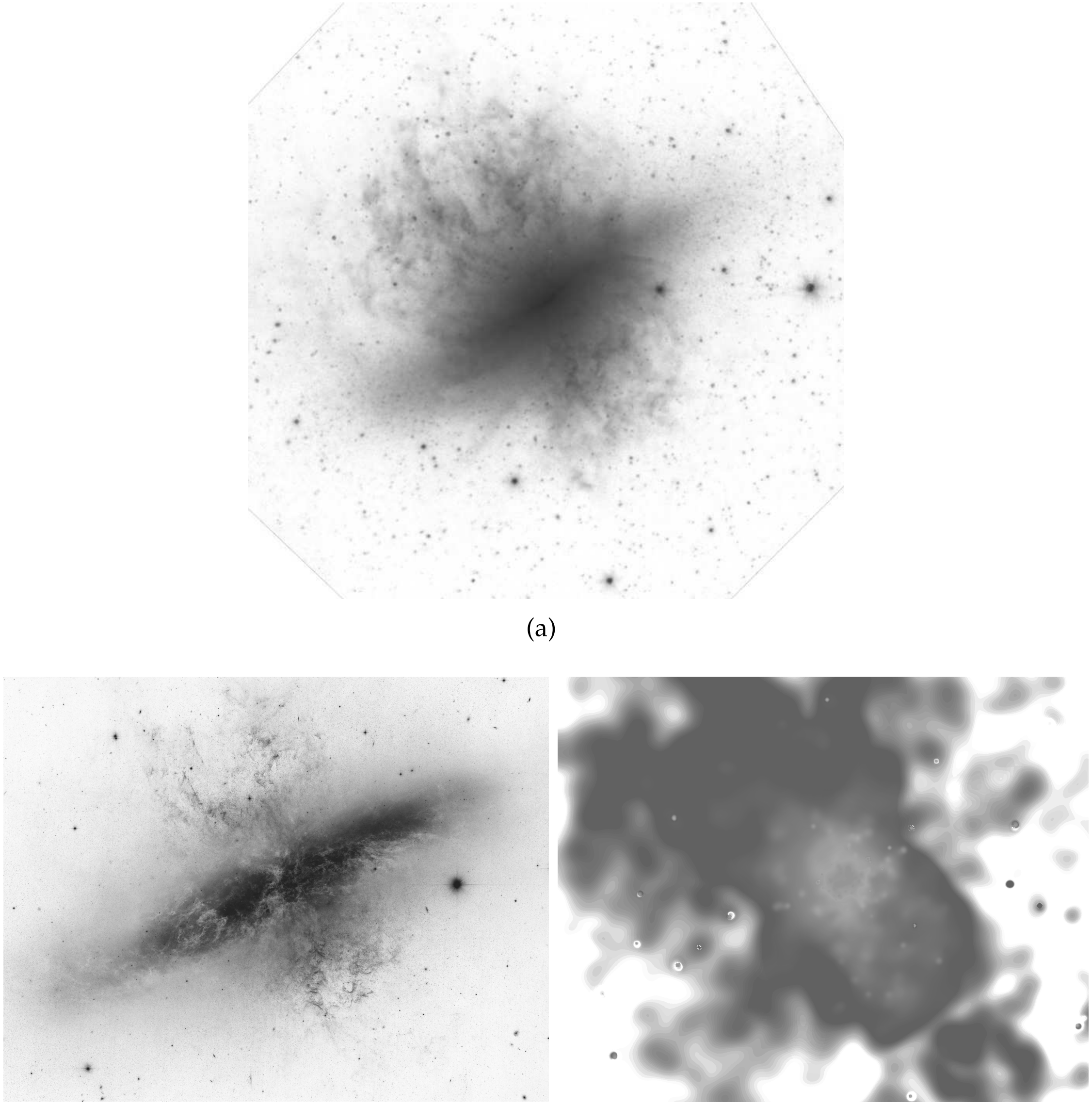

(a)

(b) (c)

Figure 1.2 — The starburst galaxy M82 at different wavelengths. (a): infrared 3.6 μm emission from stars in the disk surrounded by infrared 8 μm PAH-dominated emission from a huge dusty halo (Spitzer IRAC). (b): optical light from stars in the galactic disk and Hα emission from filaments of glowing hydrogen blasting out of the central regions (Hubble Space Telescope). (c): X-ray emission (Chandra ACIS). The disk emission is dominated by visible light while the spectacular bipolar outflow driven by the galactic superwind is traced by the million degrees X-ray emitting gas with interwoven PAH emission. The vertical extent of the infrared emission is at least 6 kpc. *Credit – X-ray: NASA/CXC/JHU/D.Strickland; Optical: NASA/ESA/STScI/AURA/The Hubble Heritage Team; IR: NASA/JPL-Caltech/Univ. of AZ/C. Engelbracht*.

and a delocalized electron cloud above and below the plane of the molecule. The existence of such a cloud of delocalized electrons is responsible for the high stability of these species, for which reactions are possible only if the σ bonding is broken and the aromatic π ensemble is disrupted.

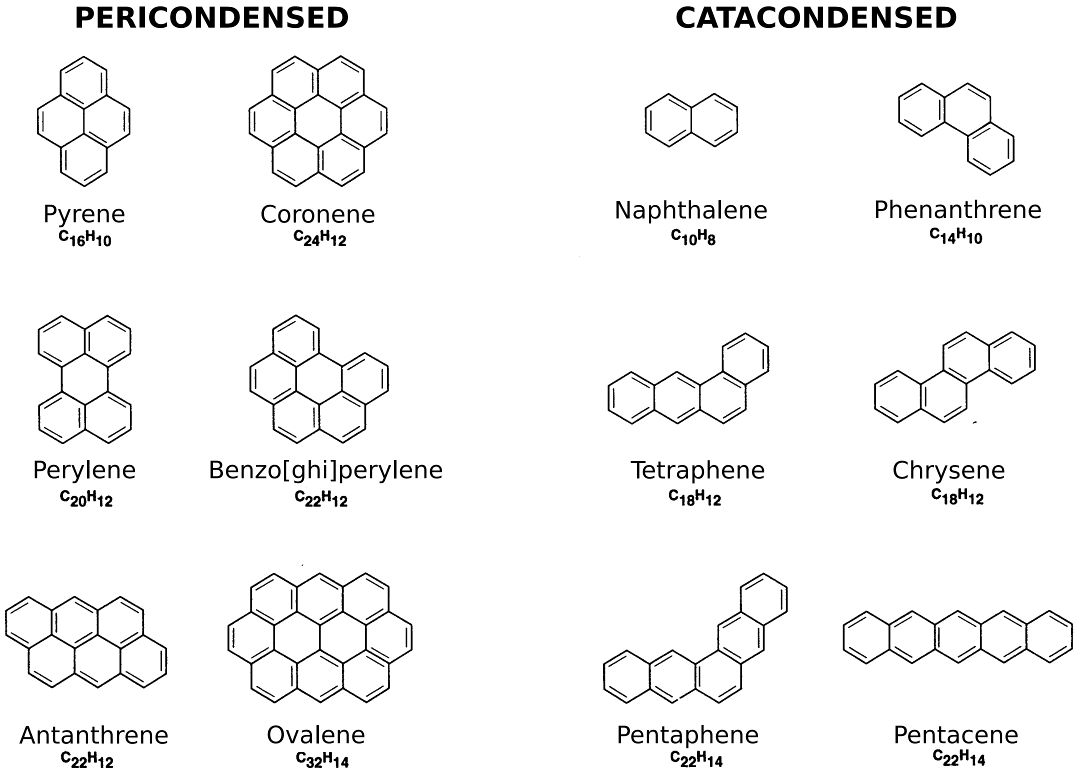

Figure 1.3 — The molecular structure of some representative PAHs. *Figure adapted from Salama et al. (1996).*

PAHs are classified into two main groups showed in Fig. 1.3. Pericondensed PAHs (left panel) have a compact structure where C-atoms are members of three or two separate rings (in the latter case only on the periphery). Within this class we find the centrally condensed, quasi-circular PAHs such as coronene and circum-coronene, where the central cycle is surrounded by a series of rings. These compact centrally condensed PAHs are among the most stable, because their structure allows complete electron delocalization and truly aromatic bonding between all adjacent carbon atoms. The radius of the pallet of a centrally condensed compact PAH is given by $a \simeq 0.9\times \sqrt{N_C}$ Å, where N_C is the number of carbon atoms in the molecule. A typical interstellar PAH with $N_C = 50$ therefore has a radius of $\sim$ 6.4 Å, while dust grains typically contain many hundreds or thousands of atoms, as derived from extinction measurements. Thus, albeit that the small end of the grain size distribution is not well constrained by these studies, typical PAH sizes in the ISM are definitely smaller with respect to the 'classical' dust grains. Catacondensed PAHs (right panel) are characterized by open structures where no C-atom belongs to more than two rings. The aromatic rings are arranged in linear chains (naphthalene, anthracene, tetracene, ...) or bend rows (phenanthrene, tetraphene, ...).

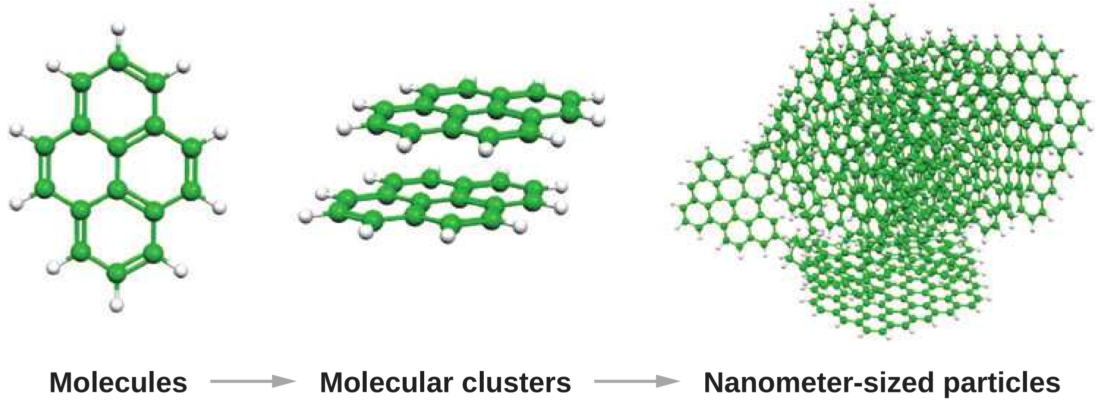

Figure 1.4 — From individual PAH molecules to amorphous carbon nanoparticles which are the constituent of carbon soot. PAH clusters form the bridge between these two aggregation states. *Figure reproduced from Tielens (2008).*

1.2.2 Formation and evolution

Interstellar PAHs are thought to originate in the envelopes of carbon-rich AGB stars, as a byproduct of the processes leading to the formation of carbonaceous dust grains (‘soot’). Because of their high stability and structure, PAHs are indeed the building blocks of carbon soot. In the outflows of C-rich AGB stars, most of the carbon is locked in CO and C_2H_2 molecules. Because CO is very stable, the dominant precursors for PAHs and soot are likely acetylene (C_2H_2) and its radical derivatives. The formation of PAH molecules occurs through a two-step process: the first aromatic ring has to be built out from C_2H_2 (probably the most difficult step), afterwards the molecule grows through repeated radical formation by abstraction of a H-atom and addition of hydrocarbons. When PAH molecules are formed, they can grow and coagulate to form clusters, platelets and eventually amorphous carbon particles the solid-state branches of soot are made of (Fig. 1.4). In H-poor environments PAH formation has to occur through a different chemical pathway, which can also lead to the formation of non-planar molecules such as fullerene (Curl & Smalley 1988).

Because PAHs are closely related to dust grains, likely they will follow a similar evolution pattern. After being released into the ISM, PAHs will undergo dramatic changes. They can grow and accrete, may become part of a dust grain itself, and incorporate heavier heteroatoms such as nitrogen. In cold and dense molecular clouds, PAHs get frozen into the ice mantles covering the surface of dust grains. UV irradiation and cosmic ray bombardment trigger a rich surface chemistry with possible formation of more complex species, e.g. the substitution of a peripheal H-atom of the PAH with a methyl group (Bernstein et al. 1999). As dust grains, PAHs are also subjected to destructive processes. High energy photons, cosmic rays and strong shocks in the diffuse ISM can partially or totally destroy them, although photodestruction seems to be effective only on small PAHs ($\sim 20 - 30$ C-atoms, Jochims et al. 1994a; Allain et al. 1996). After a protostar is born from a molecular cloud, the new complex PAHs mentioned above are easily photodestroyed by UV photons because of their minor stability with respect to the classical ones. The extremely energetic radiation field in proximity of the newly born star will cause the complete destruction of all PAHs, including the most stable species.

1.2.3 Excitation mechanisms and IR spectroscopy

Let us now consider a small, neutral PAH molecule in the singlet electronic ground state, S_0. The absorption of UV photons with energies corresponding to the discrete electronic energy levels of the molecule will induce a transition to the upper electronic states S_1, S_2 or higher. The PAH molecule is now in an excited state which can be followed by a variety of de-excitation processes, including ionization and photodissociation. The predominant de-excitation channel depends on the environments where the molecule finds itself. On Earth, the high ambient density generally leads to collisional de-excitation. In the collision-free environment of space, instead infrared fluorescence will be dominant. The excited molecule will move to a lower-lying electronic state through internal conversion, leaving most of the initial excitation energy in the form of vibrational energy. Subsequently, the highly vibrationally excited molecule cools down, mainly by IR emission in specific vibrational modes. In order to calculate the IR emission spectrum of PAHs, we need to relate the energy of the absorbed UV photon with the temperature of the emitter. Because of their small size and small specific heat capacity, the classical approach used to determine the temperature of e.g. dust grains absorbing photons cannot be applied to PAH molecules. While dust grains reach an equilibrium temperature resulting from the balance between UV photon absorption and IR photon emission, a PAH may reach temperatures as high as 1000 K immediately after the photon absorption, but after a few seconds it may have cooled down to 10 K and remain that cold until it absorbs another UV photon after a day of so, depending on the local FUV flux (the higher the flux, the shorter the interval between two absorption). This behaviour is illustrated in Fig. 1.5, which shows the temporal evolution of the temperature of four carbonaceous grains with decreasing size. The grains are heated by the average starlight background and cooled by emission of infrared photons, over a time span of about a day. Grains with radii $a \gtrsim 200$ Å can be approximated as having a steady temperature. Grains with $a \lesssim 50$ Å , however, undergo very large temperature excursions, and the notion of "average temperature" cannot be applied (Draine 2003). Interstellar PAHs are smaller than carbonaceous grains, and they can reach peak temperatures as high as 1000 K. A PAH molecule has to be treated as a microcanonical ensemble using the methods appropriate for statistical mechanics (Tielens 2005).

We already mentioned that the IR spectrum of almost every object and region where gas and dust are exposed to UV radiation is dominated by relatively broad emission features at 3.3, 6.2, 7.7, 8.6, 11.3 and 12.7 μm (Fig. 1.6), plus various other weaker features. For almost a decade the carriers of these features remained mysterious, so they became collectively known as Unidentified InfraRed bands (UIR). Later on (Leger & Puget 1984), the comparison of astronomical spectra with laboratory spectroscopy and quantum chemical calculations of the transitions of well charactarized materials allowed the identification of PAH materials as carriers of the UIR bands. The observed features are characteristic for the stretching and bending vibrational modes of aromatic hydrocarbon materials. The 3 μm region is characteristic for C-H stretching modes: the

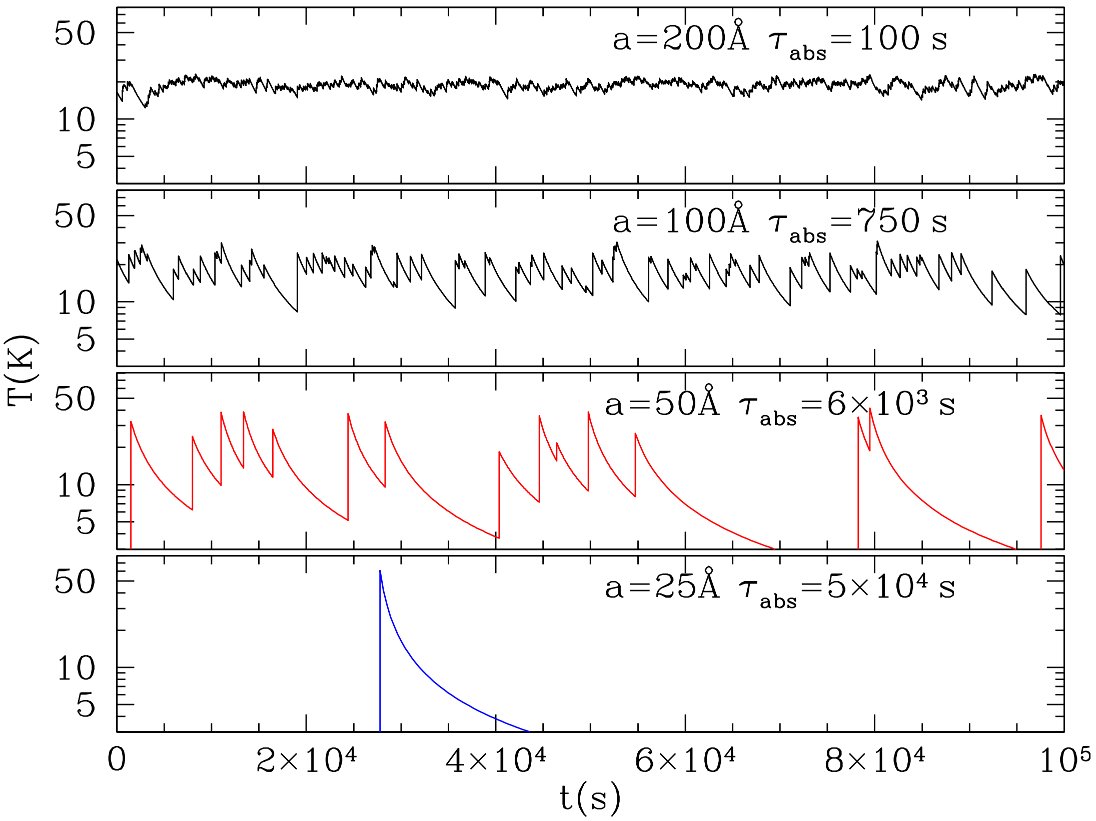

Figure 1.5 — Temporal evolution of the dust temperature for decreasing grain sizes. The dust is heated by the local interstellar radiation field, $\tau_{\rm abs}$ is the mean time between photon absorptions. *Figure reproduced from Draine (2003).*

3.3 μm band is due to the C-H stretching mode in aromatic species, while the 3.4 μm band may arise from aliphatic groups attached as functional groups to the PAHs or to PAHs with extra H bonded to some carbons. The range 6.1 – 6.5 μm is typical for pure C-C stretching modes, while slightly longwards (6.5 – 8.5 μm) lie combined vibrations involving C-C stretching and C-H in-plane bending modes, and C-H in-plane wagging modes give rise to bands in the 8.3 – 8.9 μm range. Longward of $\sim$ 11 – 13 μm, emission bands reflect in-plane and out-of-plane ring bending motions of the carbon skeleton; hence these modes are more molecule specific, particularly at the longer wavelengths. A more detailed overview of the PAH vibrational modes, including the description of the experimental techniques and theoretical approaches involved in their study, can be found in Tielens (2008).

The charge state also has a remarkable effect on the intrinsic IR spectra of PAHs, as is illustrated in Fig. 1.7 where the absorption spectrum of a mixture of neutral PAHs is compared to the spectrum of the same species in their cationic states. It clearly emerges that ionization strongly affects the strength of the features, particularly in the 3 and 11 – 15 μm regions, while the peak frequencies are almost unchanged. Using this property it has been possible to demonstrate that the variations in the UIR spectra from a variety of astrophysical environments may arise from the presence of both neutral and charged PAHs distributed over different charge states.

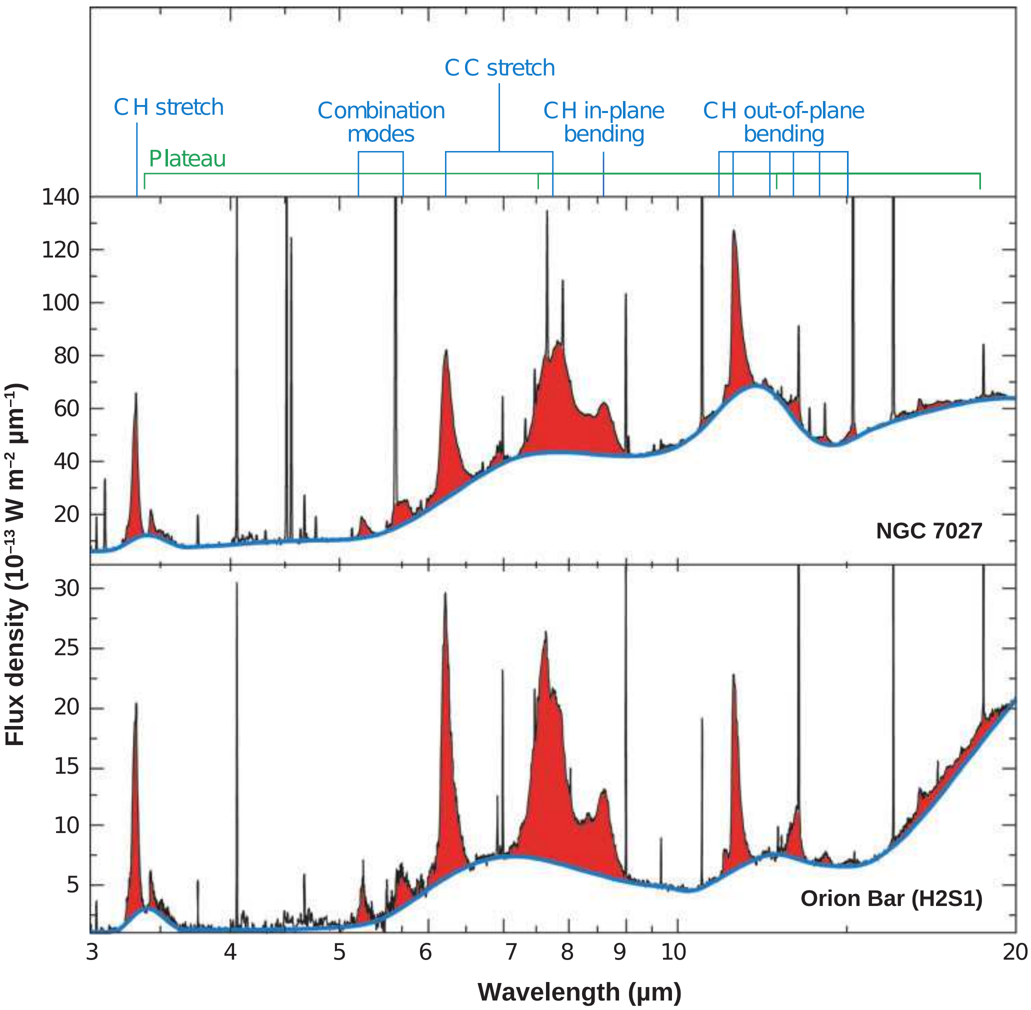

Figure 1.6 — The mid-infrared spectra of the photodissociation region in the Orion Bar and in the planetary nebulae NGC 7027. The spectra are dominated by a rich set of emission features, (almost) universally attributed to vibrational modes of polycyclic aromatic hydrocarbon molecules (top panel). The narrow features are atomic or ionic lines originating in the HII region or photodissociation region. *Figure reproduced from Tielens (2008), adapted from Peeters et al. (2002a).*

In fact, while the aromatic nature of the carriers of the UIR band is undisputed, the identification of the precise species has been the subject of a long debate. Carbonaceous solids with an abundant aromatic component – such as coal, amorphous carbon soots and chars – also show infrared emission with a general resemblance to the observed interstellar spectra. However, these are disordered materials and their features are often much broader than the observed ones. The detection of the UIR bands in photodissociation regions (PDRs, Tielens 2005) far from the illuminating star puts a strong constraint on the size of the carrier. Emission at the observed wavelengths requires temperatures that carbonaceous solids cannot apparently reach under these conditions, while small species can be heated to very high temperatures upon absorption of a single UV photon. The observed ratio of the 3.3 to the 11.3 μm band indicates a size of 50 – 80 C-atoms, while the plateau emission underneath the 6.2 and 7.7 μm bands coupled with the absence of comparable emission in the C-H stretching mode region, suggests a size for the carrier of some 350 – 600 C-atoms. The size requirement combined with the aromatic nature of the carrier strongly favor the choice of PAHs, as molecules and/or small clusters, although no specific molecules have yet been identified. One difficulty arises from the fact that the PAHs studied in laboratory are much smaller (< 50 C-atoms) than the supposed interstellar ones. In addition, the situation is complicated for instance by the lack of a permanent dipole moment in neutral PAHs, which hence have no allowed pure rotational spectrum, by a bad partition function, by the overlapping of the fundamental vibrational modes and by the difficulty to estimate relative abundances. Nevertheless it seems more likely the presence of a family of PAHs rather than a single specific PAH molecule.

1.3 The importance of interstellar PAHs

The first striking characteristic of interstellar PAHs is that they are everywhere. The UIR bands, for which PAHs are the most accredited carriers, have been found in the mid-IR spectrum of almost every astrophysical environment where dust and gas are illuminated by UV photons, which of course does not exclude their presence in regions where they do not get the chance of being excited. Considering only the 'visible' sources, PAH features have been detected in PDRs, reflection nebulae, young stellar objects, planetary nebulae, post-AGB objects, galactic nuclei, starburst galaxies and ultraluminous infrared galaxies (ULIRGs), as well as in the IR cirrus at high galactic latitudes, on the surfaces of dark clouds, and in the general interstellar medium of galaxies - see Tielens (2008) and references therein.

In consideration of this impressive ubiquity, it is not surprising that PAHs are thought to play a crucial role in many astrophysical processes. Because of the high stability of PAHs, the high tendency of aromatic fuels to soot, and the structural similarity between their carbon backbone and that of soot, PAHs are considered the building blocks in the carbon condensation route. Through the photoelectric effect, infrared emission and gas-grain collisional cooling, PAHs (and small grains) dominate the heating and cooling of the ISM, which ultimately controls the physical conditions and the phase structure of the ISM and therefore its evolution in galaxies (Hollenbach & Tielens 1999). PAHs influence the charge balance, which reflects in the equilibrium state of chemical reactions and the gas-phase abundances in molecular clouds. They offer a large area for surface chemical reactions and so play a significant role in the interstellar chemistry. PAHs have been proposed as one possible carrier of the Diffuse Interstellar Bands (DIBs - see §1.1.1), and may also be involved in the 2175 Å feature which dominates the interstellar UV extinction curve.

Because of their characteristics, PAHs also have a promising role as a tracer for various astrophysical phenomena. The ubiquity of their emission features and their predominance in the mid-IR spectra of massive star-forming regions make PAHs a potentially powerful tool for the study of star formation throughout the universe. Essentially, the PAHs act as a dye for the presence of pumping FUV photons and hence trace the presence of massive stars (Peeters et al. 2004). The presence of PAH features has also been used to distinguish between shocked gas and PDRs (van den Ancker et al.

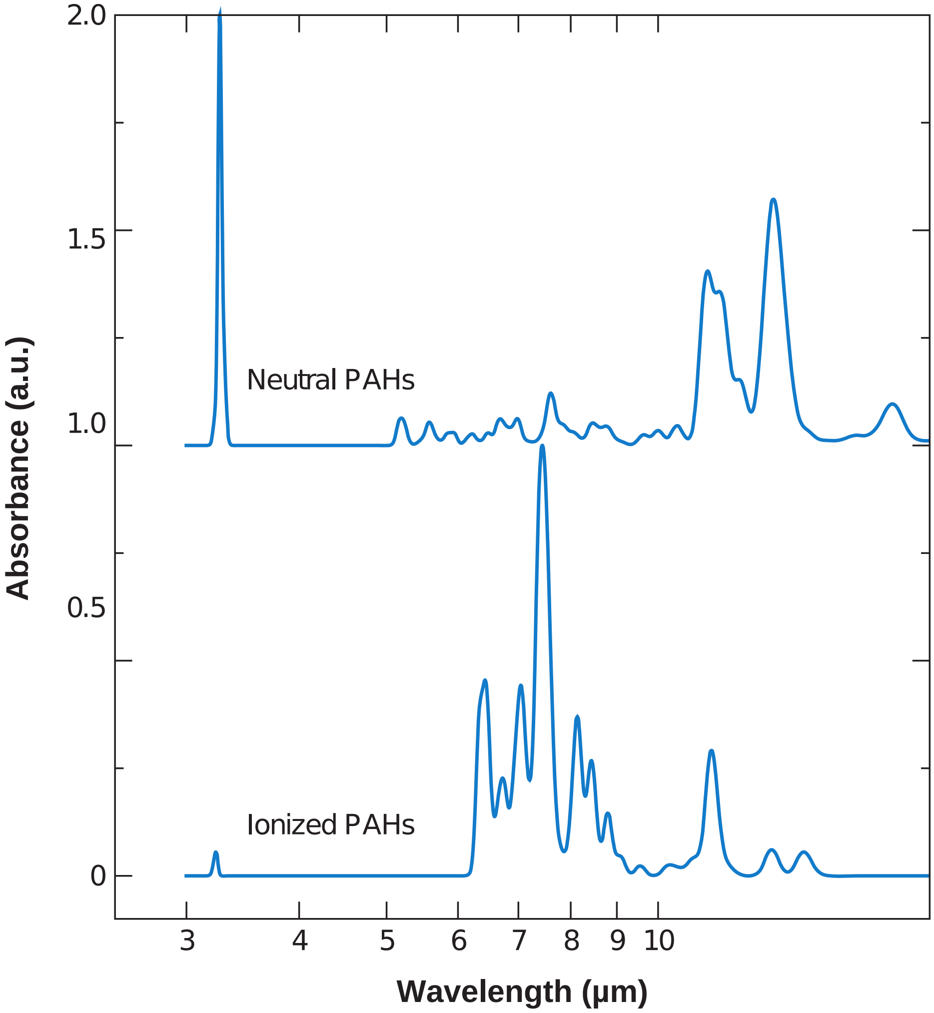

Figure 1.7 — The absorption spectrum of a mixture of neutral PAHs (top) compared with the spectrum of the same species in their cationic states (bottom). The ionization state has an extreme effect on the strength of the features, in particular the C-C modes has increased considerably relative to the C-H modes in the 3-μm and 1115-μm region, while the influence on the peak frequencies is negligible. *Figure reproduced from Allamandola et al. (1999).*

2000). In combination with the emission lines, PAHs have been employed in extragalactic studies as diagnostics for the ultimate physical processes powering galactic nuclei (e.g. Genzel et al. 1998; Tran et al. 2001). These studies show that ULIRGs are largely powered by star formation rather than active galactic nucleus activity. Consequently, the strengths of the PAH bands can also be used to probe evolutionary effects and to trace the elemental evolution in external galaxies. PAH features have also been detected in regions spatially correlated with X-ray emission from the hot gas in the star-forming region M17 and in the outflow of the starburst galaxy M82 (Engelbracht et al. 2006). Likely this emission arises from entrained gas ablated from molecular clouds and transported by superwinds or galactic fountains. PAHs could then be used as a dye for the entrained material to trace these transportation mechanisms.

1.4 Dust processing in the ISM

PAHs and dust grains are generally tightly correlated (cf. §1.2.2), thus the processes dust particles undergo during their cycling between the different phases of the ISM will also affect PAHs. In the following sections we summarize the mechanisms, able to induce structural changes, disrupt or even completely destroy dust grains. Apart from photo-processing, all the processes are *collisional* processes, i.e. based on the interaction with ions, molecules or other dust grains. Fig. 1.8 shows the results of dust processing in a typical interstellar shock with velocity of 100 km s^{-1} (Jones et al. 1996) due to the mechanisms listed below.

1.4.1 Processes affecting the dust-to-gas mass ratio

- **Sputtering** This process consists of the ejection of atoms from the grain surface, with return to the gas phase, and consequent erosion of the dust particle. The erosion is due to grain collisions with high velocity atoms and ions in energetic environments (Jones et al. 1994). Depending on the velocity distribution of the colliding partners, sputtering is defined *non-thermal* or *inertial* when collisions are determined by the relative motion between the grains and the gas, and is defined *thermal* when collisions arise from the thermal motion of the gas (Barlow 1978; Cowie 1978). Thermal sputtering is effective only for gas temperatures above 10^5 K and is dominated by collisions with H and He atoms and ions, which are the lightest and most abundant elements in the gas phase (Draine & Salpeter 1979a,c). Since thermal sputtering acts in the opposite way as accretion, a layer of equal thickness is removed from grains of any radius, resulting in the preferential destruction of the smaller grains and a less dramatic erosion of the larger ones. In grain collisions with hydrogen/protons, inertial sputtering is effective for relative velocities greater than $\simeq$ 30- 40 km s^{-1} (Tielens et al. 1994) and at lower velocities is likely dominated by collisions with the heavier projectiles (atoms and ions) in the gas (Field et al. 1997). Because the dynamics of the grains varies with their size, the effect of inertial sputtering will be size-dependent as well.
- **Vaporization** Grain-grain collisions with impact velocities above $\simeq$ 20 km s^{-1} (Tielens et al. 1994) can lead to the partial or complete vaporization of the colliding partners, followed by release of the elemental dust components into the gas phase.
- **Accretion** The adsorption and sticking onto grain surfaces of atoms, ions, radicals and molecules (possibly with the exception of the lightest species H, H_2 and He) progressively increases both the grain radius and the dust-to-gas ratio. For refractory elements such as Mg, Si and Fe, accretion can occur at temperatures as high as 1000 K, while temperatures below $\approx$ 100 K are required for species leading to icy mantles formation. Photodesorption, cosmic ray induced desorption and photoevaporation counterbalance the adsorption process. Since the adsorption rate onto a grain is proportional to the grain cross section, to a first approximation the thickness of the accreted mantle is independent of the grain radius, leading to the disappearance of the smallest grains (Guillet et al. 2008).

1.4.2 Processes conserving the dust-to-gas mass ratio

- **Shattering** This process occurs in grain-grain collisions with velocities above a threshold value of few km s^{-1}, and consists of the fragmentation of the dust particles into smaller fragments, with a consequent redistribution of the mass toward smaller grain sizes. The effects of shattering strongly depend on the relative velocity between the two grains, their relative sizes and physical properties, ranging from the pulverization of one or both colliding grains, to partial fragmentation or craterization of the surface of the bigger of the two (Borkowski & Dwek 1995a; Jones et al. 1996).
- **Coagulation** Grains colliding with velocities below a critical value can stick together producing conglomerates, with a consequent redistribution of the dust mass towards larger grains (Chokshi et al. 1993; Poppe & Blum 1997). The critical velocity depends on the grain composition and radius, varying from $\sim$ 1 m s^{-1} for μm sized grains to 1 km s^{-1} for $\simeq$ 100 Å -sized grains, and is enhanced by the presence of icy mantles which increase the contact surface and the interaction time during the collision.

1.5 Why study collisional PAH processing in the ISM

The photophysics and photochemistry of PAHs in space have been extensively investigated. PAH photoexcitation with subsequent IR emission and photodestruction have been well studied theoretically and experimentally, and observational consequences have been evaluated. Quantum chemical calculations verified the possible vibrational modes of different PAH molecules and identified the modes measured in the laboratory. Theoretical modeling has attested to the central role of PAHs in gas chemistry and a number of theoretical studies based on unimolecular dissociation theories have assessed the importance of fragmentation of highly vibrationally excited PAHs in space (Leach 1987; Geballe et al. 1989; Allain et al. 1996; Le Page et al. 2001, 2003; Tielens 2005). Laboratory studies of molecules in conditions similar to those expected in the interstellar medium have improved the knowledge on the nature of the emitting interstellar species and on the processes involved. The ISO and Spitzer satellites have reinforced the ubiquitous nature of the UIR bands and revealed the incredible richness of the UIR spectrum and the widespread variations in the relative strength and profiles of these features, from source to source and within sources.

Concerning dust grains, their processing in the ISM has been extensively studied not only in terms of interaction with photons (e.g. scattering, extinction, photoelectric heating), but also in terms of collisional processing (§1.3), mainly by supernova shocks. Jones et al. (1996) have modelled dust shattering due to grain-grain collisions in interstellar (supernova-driven) shocks. Their calculation predicts the complete disruption of large dust grains in fast shocks propagating through the warm phase of the interstellar medium (WIM). Shocks with velocities greater than 50 km s^{-1} are able to shatter the largest grains in the MRN distribution (1000 Å $\leq a \leq$ 2500 Å) into fragments with radius smaller than $\approx$ 500 Å . The fragmentation products could also include PAH molecules which are expected to be processed as well by the shock. Unfortunately these models do not account for the destruction of PAHs by sputtering in the post-

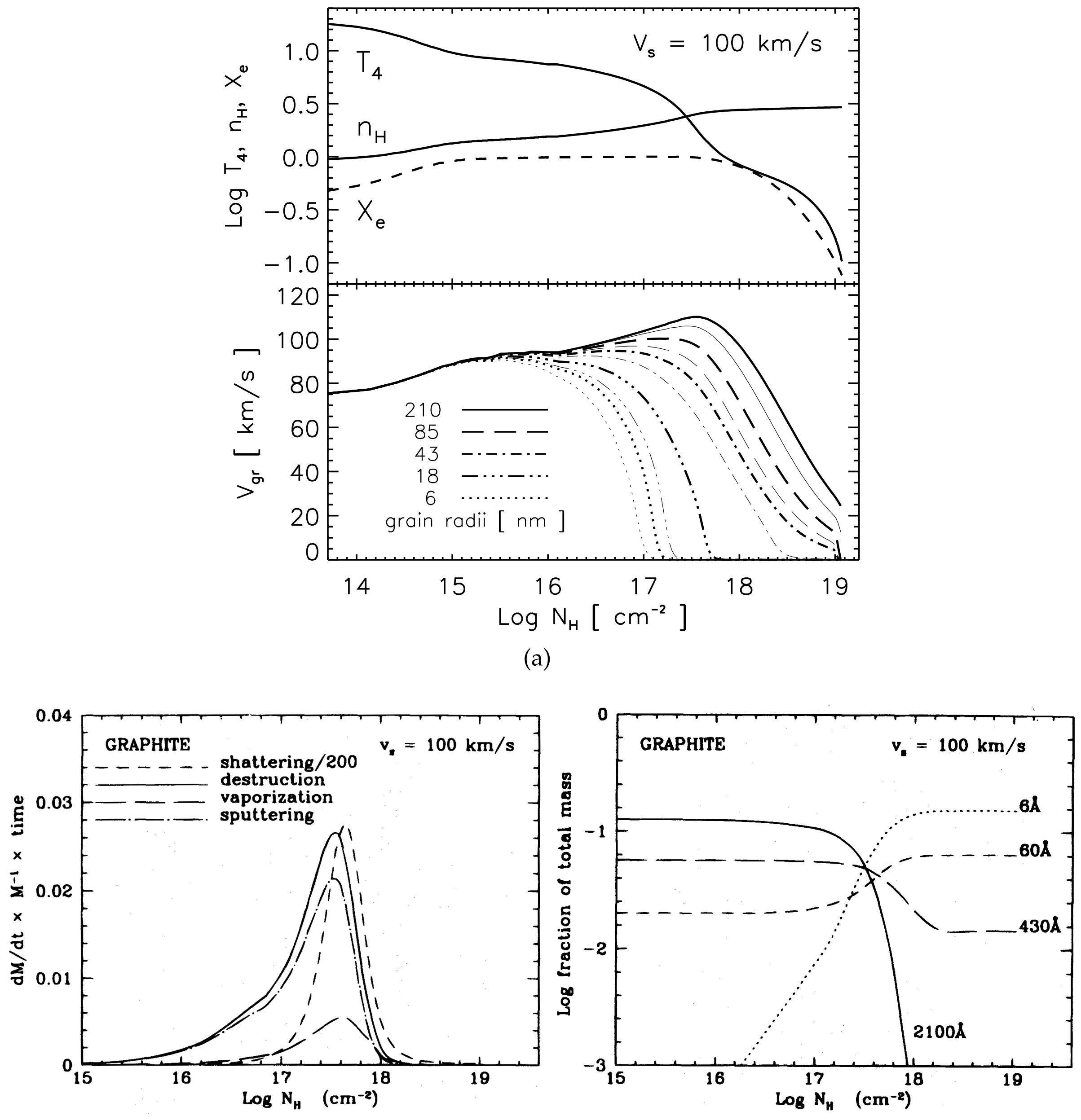

(a)

(b) (c)

Figure 1.8 — (*a*): Profile of a shock with velocity v_s = 100 km s^{-1} (*top panel*). The temperature, T_4 = T(K)/10^4, the density, n_H and the electron relative abundance, X_e are represented as a function of the shocked column density, N_H, for the preshock density, n_0 = 0.25 cm^{-3} and the magnetic field, B_0 = 3 μG. Also shown are the graphite grain velocities (*bottom panel*) as a function of N_H for three grain radii. The column density $N_H = n_0 \, v_s \, t$ is related to time through the following relation: log t (yr) = log N_H (cm^{-2}) - 13.9. (*b*): Total graphite destruction (vaporization + sputtering) and disruption (shattering) rates multiplied by time and divided by the total initial grain mass, plotted as a function of the shocked column density for the 100 km s^{-1} shock. Equal areas show equal destruction. Shattering so dominates that the shattering rate for the grains in the largest mass bin (radii = 2100 Å) is divided by 200 to fit on the figure. (*c*): Graphite grain bin masses for four grain radii plotted as a function of the shocked column density, for the shock with velocity v_s = 100 km s^{-1}. The 6 Å bin is empty at the start of the calculation. The plot clearly shows the rapid disruption of the largest grains, and the formation of small grains by shattering. *Figure reproduced from Jones et al. (1996).*

shock gas, which nevertheless may be relevant for the evolution of the interstellar PAH population.

Looking at this picture then, one can see that one important link in the chain is missing: the treatment of the collisional processing of PAHs in the ISM. PAHs and dust grains are intimately linked and they are reasonably expected to undergo the same kind of collisional processes during their lifecycle. While for dust grains the physics of these processes has been investigated and the astrophysical implications evaluated, this is not the case for PAHs. Theoretical models concerning collisional processes are missing, especially in terms of PAH damage and destruction, and this lack of information makes the interpretation of PAH observations difficult in regions subjected to such processes. From the observational point of view in fact, there is presently little evidence for the presence of PAHs in regions processed by supernova shocks. Largely, this reflects the difficulty of discerning the emission of supernova remnants against that of galactic background material. Reach et al. (2006) have identified four SNRs out of a sample of 95 whose IR colors suggest excess emission from PAHs, but most sources were too confused by the background. On the other hand, a study of the SNR N132D in the Large Magellanic Cloud revealed the presence of a steeply rising mid-IR continuum and weak emission features at 16.4 and 17.4 μm (Tappe et al. 2006). These features are attributed to relatively large carbon PAH species ($N_C \sim 4000$ C atoms). PAH emission has been detected in association with the shock-heated, X-ray emitting gas in the star-forming region M17, and the superwind driven by the nuclear starburst in M82, some 8 kpc above the plane (Engelbracht et al. 2006).

The aim of our study is to fill this key gap in our understanding of the physics behind collisional processing of PAHs and to clarify how this affects the PAH evolution in the astrophysical context. This knowledge could help to better understand the effective role of PAHs in the cosmic life cycle described in §1.1.2, particularly in terms of their relationship to dust grains. These results could also give new insights to interpret the detection – or non-detection of PAHs in specific regions and eventually provide additional arguments in favor of PAHs as a molecular dye, e.g. to trace regions of denser entrained material.

1.6 Thesis outline

The research described in this thesis aims to establish *how* the different conditions in the ISM affect PAHs, focusing on the *collisional* processing due to high velocity ions and electrons. These high velocities arise from the thermal and relative (inertial) motion induced in the gas by moderate velocity shocks, from the energy injected into the gas by very fast shocks (thermal motion), and from cosmic ray acceleration. In fact, a detailed study of the physics of the interaction between PAHs and high energy particles (ions and electrons) was still lacking, although PAHs are a key component of the ISM and these processes play a crucial role in the evolution of PAHs. In this perspective, the first key question we address in this thesis is:

What happens to PAH molecules when bombarded by high energy ions and electrons? Will they be able to survive, maintaining their character, or will they be severely damaged or even completely destroyed?

This is a general question, which is important to answer for a better understanding of the physics of PAHs.

From this it follows the second key question:

What are the astrophysical implications of PAH processing?
i.e.
What is the connection between the microscopic processes (ion/electron – PAH interaction) and the macroscopic effects on the interstellar PAH population?

This is crucial for drawing conclusions from observations: for example, to interpret the possible detection of PAHs in a (shocked) hot gas, we need to know which physical processes PAHs undergo (collisions with ions and electrons – microscopic processes) and how these processes affect the PAH population under the specific conditions of the gas (macroscopic effect). Moreover, this knowledge will contribute to a better understanding of the role of PAHs in the global ecology of the ISM.

In **Chapter 2** we present a multiwavelength study of the environment of the supernova remnant N157B in the Large Magellanic Cloud. This complex region, which besides the SNR includes a molecular cloud, dust filaments, bubbles of hot shocked gas, an OB association and a HII region, provides a very good example of the interaction between the various components of the ISM and of the variety of conditions under which PAHs can find themselves. We investigate the relative importance of shock excitation by the SNR and photo-ionization by the OB stars and the interaction between the supernova remnant and its environment, with particular attention to the dust/PAH component.

In **Chapter 3** and **Chapter 4** we present the models that we developed to describe the collisions of PAH molecules with ions and electrons and the subsequent transfer of energy, which can lead to carbon atom loss with consequent disruption and destruction of the molecules. These are the microscopic processes mentioned above. We need to develop specific models because PAHs are molecules and not small solid fragments, thus the classical approach from solid state physics cannot be applied. The results in terms of PAH destruction cannot be extrapolated from the behaviour of dust grains and strongly depend on the kind of projectile and on the energies involved. We then use our models to estimate the lifetime of PAHs (macroscopic effect) in interstellar shocks with velocities between 50 and 200 km s^{-1} (**Chapter 3**) and to evaluate the PAH survival time in a shock-heated X-ray emitting gas (**Chapter 4**), using our results to interpret existing observations. This study provides for the first time a quantitative evaluation of PAH processing in such harsh environments and gives new insights about the connection with the *dust* processing.

In **Chapter 5** we develop analogous models to evaluate the destructive effects of primary cosmic ray collisions (ions and electrons) on PAHs and estimate for how long they can survive this ubiquitous bombardment in various environments (galactic disks, galactic halos, starburst galaxy outflows and cooling flow galaxy clusters). We need specific models because the energy of cosmic rays is much higher than those of the corresponding particles in shocks and hot gas and the treatment of the interactions thus requires a different formalism. The resulting survival time has been compared with the previously calculated PAH lifetimes against other destruction mechanisms. This provides a map of the expected presence of PAHs as a function of the environmental conditions which can be compared with observations. Furthermore, this study allows us to check the capability of PAHs to act as molecular dye for entrained material and improves our understanding of their relationship with the other components of the ISM under a variety of conditions.

In **Chapter 6** we finally summarize our conclusions and illustrate the perspective of future research.

Chapter 2

Spitzer observations of the N157B supernova remnant and its surroundings

Abstract. We study the LMC interstellar medium in the field of the nebula N157B, which contains a supernova remnant, an OB association, ionized gas, and high-density dusty filaments in close proximity. We investigate the relative importance of shock excitation by the SNR and photo-ionization by the OB stars, as well as possible interactions between the supernova remnant and its environment. We apply multiwavelength mapping and photometry, along with spatially resolved infrared spectroscopy, to identifying the nature of the ISM using new infrared data from the *Spitzer* space observatory and X-ray, optical, and radio data from the literature. The N157B SNR has no infrared counterpart. Infrared emission from the region is dominated by the compact blister-type HII region associated with 2MASS J05375027-6911071 and excited by an O8-O9 star. This object is part of an extended infrared emission region that is associated with a molecular cloud. We find only weak emission from the shock-indicator [FeII], and both the excitation and the heating of the extended cloud are dominated by photo-ionization by the early O stars of LH 99. Any possible impact by the expanding SNR does not now affect the extended cloud of molecules and dust, despite the apparent overlap of SNR X-ray emission with infrared and Hα emission from the cloud. This implies that the supernova progenitor cannot have been more massive than about 25 $M_{\odot}$.

E. R. Micelotta, B. R. Brandl, F. P. Israel,
Astronomy & Astrophysics, **500**, 807 (2009)

2.1 Introduction

The Hα-emitting region N157 B (Henize 1956) in the Large Magellanic Cloud is on the southwestern fringe (projected linear distance 90 pc from the center) of the major star-forming complex 30 Doradus. In a limited area of (projected) diameter 65 pc, the field contains a supernova remnant, an OB association, HII emission regions, bubbles of low-density hot gas, as well as the neutral material in dense clouds (Lazendic et al. (2000) and references therein). The structure, dynamics, and energy balance of this region are poorly understood. There is even uncertainty about the nature of the emission observed at different wavelengths.

The OB association LH 99 (Lucke & Hodge 1970) is seen on the sky in the same direction as N157B, and is often considered to be associated with it because it has the same foreground extinction (Wang & Gotthelf 1998). LH 99 contains a large number of (early) O stars (Schild & Testor 1992), powerful ionizing sources whose strong stellar winds are expected to produce bubbles of low-density hot gas (Townsley et al. 2006) and to illuminate the dusty filaments and clouds such as the nearby molecular cloud 30Dor-22 (Johansson et al. 1998).

Much of the nebula N157 B can be identified with the Crab-like supernova remnant (SNR) B0538-691. Its embedded X-ray pulsar PSR J0537-6910 suggests an age of about 5000 yr (Marshall et al. 1998; Wang & Gotthelf 1998). The N157B radio counterpart MC 69 (Le Marne 1968; McGee et al. 1972) has a spectral index $\alpha = -0.19$, $S_\nu \propto \nu^\alpha$ (Mills et al. 1978; Lazendic et al. 2000). Such a flat spectrum is characteristic of thermal HII region emission, as well as of nonthermal Crab-type SNR emission. However, various observations strongly support the latter interpretation: bright X-ray emission coincides with the radio source (Long & Helfand 1979), the ratio of radio-to-optical intensity is quite high (Dickel et al. 1994), spectral line images (Danziger et al. 1981) reveal filamentary structures with a high line ratio[SII]/H$\alpha \geq 0.7$, the lines of [OI], [FeII], and [FeIII] are strong, whereas the HeI λ4686 Å line is weak. The SNR has a peculiar one-sided morphology, does not have a well-determined outer boundary, and exhibits bright radio/X-ray core surrounded by an extended envelope of linear size of 30×20 pc (Chu et al. 1992; Dickel et al. 1994; Lazendic et al. 2000), or even larger (Townsley et al. 2006) making the remnant unusually large in both radio and X-ray emission (Lazendic et al. 2000; Wang & Gotthelf 1998).

In such a complex environment, shocks from SNRs and photons from luminous stars compete as heating agents for the ISM. The conditions in and around N157B have therefore been a frequent subject of study. Several authors, e.g. Chu et al. (1992); Townsley et al. (2006); Chen et al. (2006) have concluded that the expanding SNR is presently colliding with the molecular cloud to its south. The impact of a shock front on dense cloud material should leave a signature detectable at mid-infrared (MIR) wavelengths (Oliva et al. 1999; Reach & Rho 2000). Confirmation of the proposed collision is of great interest, as it would identify an excellent source for studying the physics of ongoing dense ISM processing by shocks.

The use of infrared observations is particularly well-suited to trace physical conditions in dusty environments because of their insensitivity to extinction. In the following, we combine our *Spitzer* observations with literature data at a variety of wave-

Table 2.1 — IRS observational setup. The IRS modules are SL: Short-Low, LL2: Long-Low 2, SH: Short-High, LH: Long-High.

Cycles number	Duration^a (sec)	IRS module	$\Delta\lambda$ (μm)	Resolving Power
2	14	SL	5.2 − 14.5	64 − 128
2	14	LL2	14.0 − 21.3	64 − 128
3	30	SH	9.9 − 19.6	600
3	60	LH	18.7 − 37.2	600

(*a*): Total integration time: SL + LL2 = 112 sec, SH + LH = 540 sec.

lengths to study the role of the different physical components (SNR, HII region, OB association, dust clouds) and heating processes (shock-excitation, photo-ionization) in shaping the N157B region. Throughout, we adopt a distance of 50 kpc for the LMC (Westerlund 1997), so that 10 ″ correspond to 2.4 pc.

2.2 Observations and data processing

We have observed N157B with the Infrared Array Camera (IRAC) (Fazio et al. 2004) and with the Infrared Spectrograph (IRS) (Houck et al. 2004) on board the Spitzer Space Telescope (Werner et al. 2004), as part of the IRS guaranteed-time program (PID 63, PI J. R. Houck). The images from the Multiband Imaging Photometer for Spitzer (MIPS) have been retrieved from the archive (MIPS 24 μm: program 3680, PI K.J. Borkowski, MIPS 70 μm: program 20203, PI M. Meixner).

The IRAC data (Fig. 2.1) were taken on 7 December 2003 and consist of mosaic images in four channels at 3.6, 4.5, 5.8 and 8.0 μm. The Basic Calibrated Data (BCD) products from the Spitzer Science Center (SSC) pipeline were used to construct the mosaic images.

The IRS spectra were taken on 26 May 2005 using the standard IRS “Staring Mode” Astronomical Observing Template (AOT). The observational setup is reported in Table 2.1. The IRS slit coverage is shown in Fig. 2.2 - left panel, outlined with rectangles: SL goes from East to West, LL2 from North to South and SH and LH are the two small rectangles in the center of the field.

Each cycle yielded two exposures at different nod positions along the slit. The data have been pre-processed by the SSC data reduction pipeline version 12.0.2 (Spitzer Observer's Manual, chapter 7[1]). The two-dimensional BCD constituted the basis for further processing. First we corrected the BCD frames for bad and rogue pixels with the IRSCLEAN[2] tool. IRSCLEAN identifies bad and rogue pixels and replaces them with the average of good nearest neighbors. Rogue pixels are single-detector pixels that show time-variable and abnormally high flux values. Next, we combined the frames from the same nod position using the mean where two frames were available,

---

[1] http://ssc.spitzer.caltech.edu/documents/SOM

[2] available at http://ssc.spitzer.caltech.edu/archanaly/contributed/

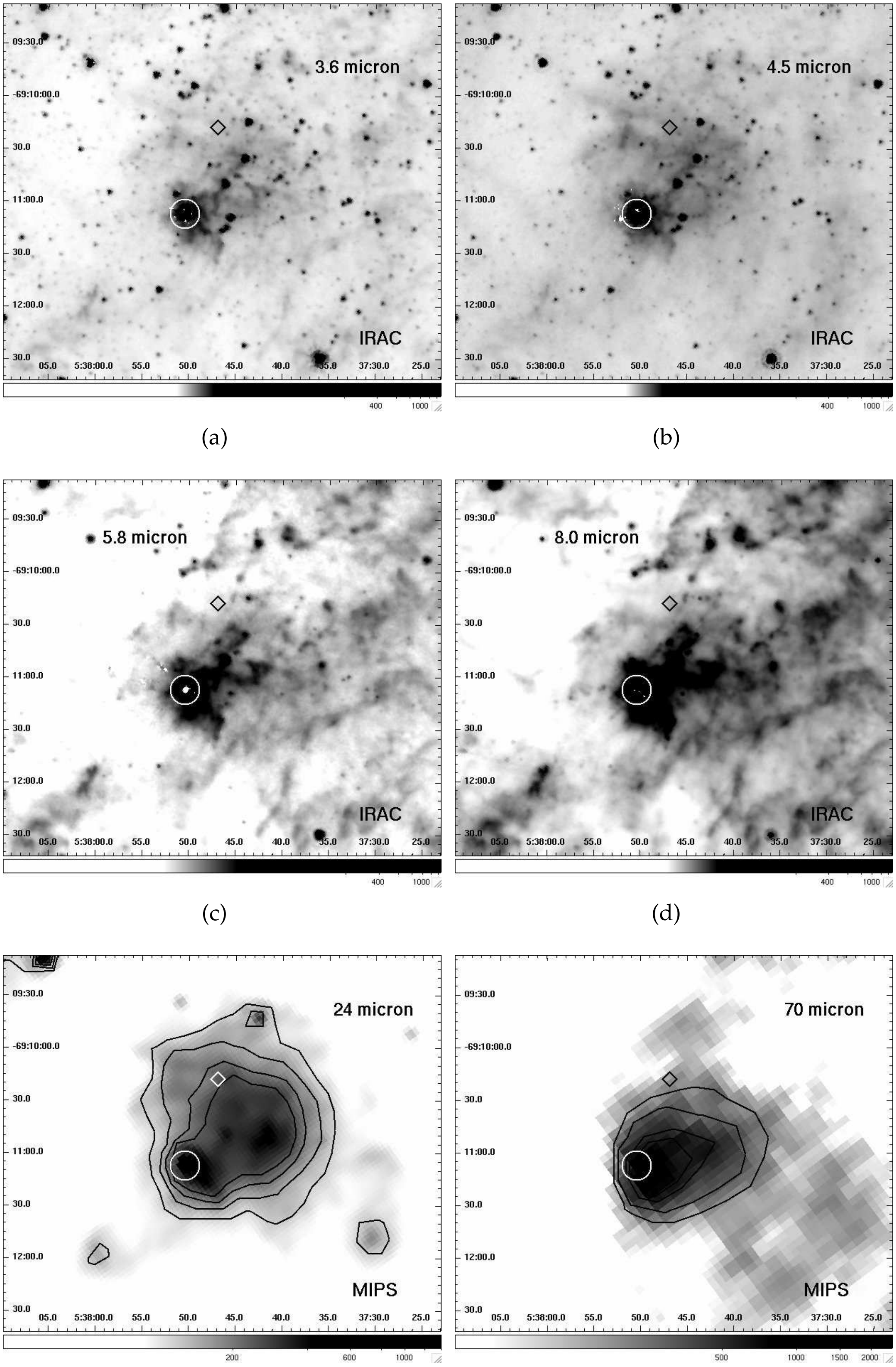

(a) (b)

(c) (d)

(e) (f)

Figure 2.1 — IRAC and MIPS images of the N157B region, calibrated in MJy/sr. The diamond marks the peak of the supernova remnant X-ray emission (Sasaki et al. 2000) and the circle marks the 2MASS compact source J05375027-6911071. The coordinates are (RA, dec) J2000.

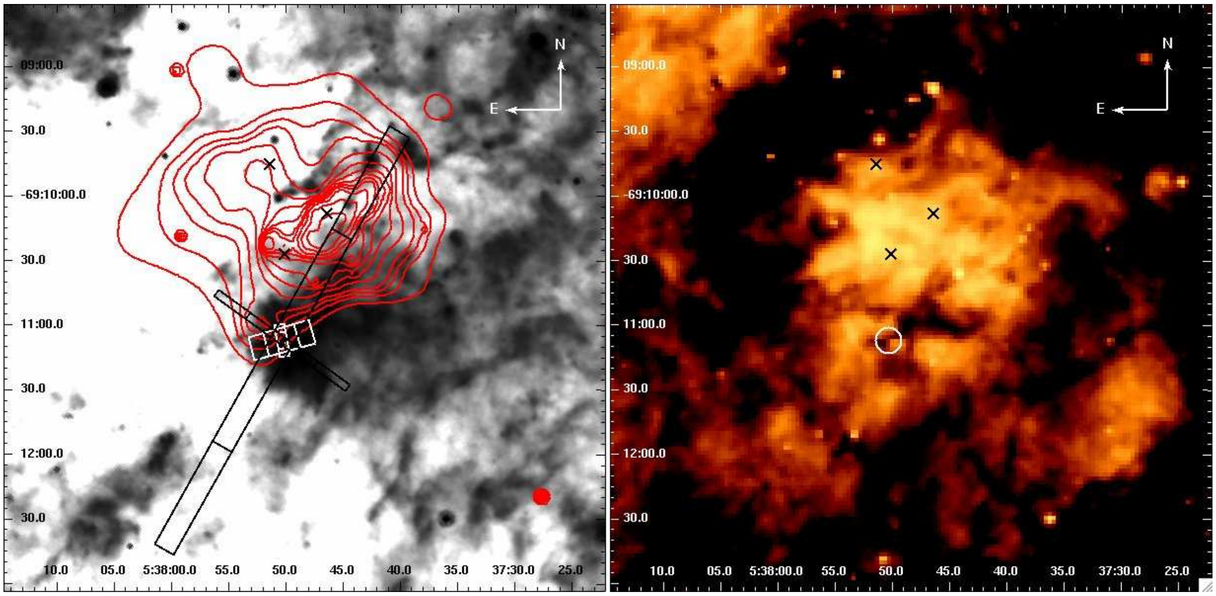

Figure 2.2 — *Left panel*: IRAC 8.0 μm map overlaid with Chandra ACIS-S X-ray intensity contours of N157B at 4, 5, 7, 8, 12, 16, 20, 25, 30, 35, 50, 100, 500, 30000 $\times 10^{-2}$ counts sec^{-1} arcsec^{-2} (courtesy D. Wang). The rectangles mark the IRS slit locations: SL = east-west black, LL2 = north-south black, SH and LH are the two small white boxes in the center of the field. The O3 stars ST 1-62, 1-71, 1-78 in LH 99 ((Schild & Testor 1992)) with projected positions inside the N157B X-ray contours are marked with an "X" (Schild & Testor 1992). *Right panel*: MCELS Hα image of N157B (Smith & MCELS Team 1998), again with the O3 stars marked. Note the correspondence between the 8 μm IR emission and Hα extinction. The compact object J05375027-6911071 is marked by a circle which also identifies the area over which we determined the Hα/[S II] ratio (see Sect. 4.1). In both panels the coordinates are (RA, dec) J2000.

and using the median in case of three available frames. For each integration at the same position on the target, an off-source sky exposure is provided, so we computed the mean/median sky (depending again on the number of available frames) and subtracted it from the corresponding nod position frame.

Further processing was done using the SMART package version 5.5 (Higdon et al. 2004) - a suite of IDL software tools developed for spectral extraction and spectral analysis of IRS data. The high-resolution spectra were extracted using full slit extraction. The low-resolution spectra were instead extracted using SMART's interactive column extraction. The calibration is based on observations of standard stars (Decin et al. 2004). The ends of each orders, where the noise increases significantly, were manually clipped. To obtain a good match between the low and high resolution modules, the SL + LL2 spectra were scaled up by 10%. Finally the resulting spectra from the two nod positions were averaged to obtain the final spectrum shown in Fig. 2.4.

2.3 Results and analysis

2.3.1 IRAC and MIPS images

The IRAC and MIPS images (Fig. 2.1) of the N157B region are dominated by emission from the dust associated with the molecular cloud south of the X-ray emission region (peak marked by a diamond). Relatively faint in the 3.6 μm and 4.5 μm images,

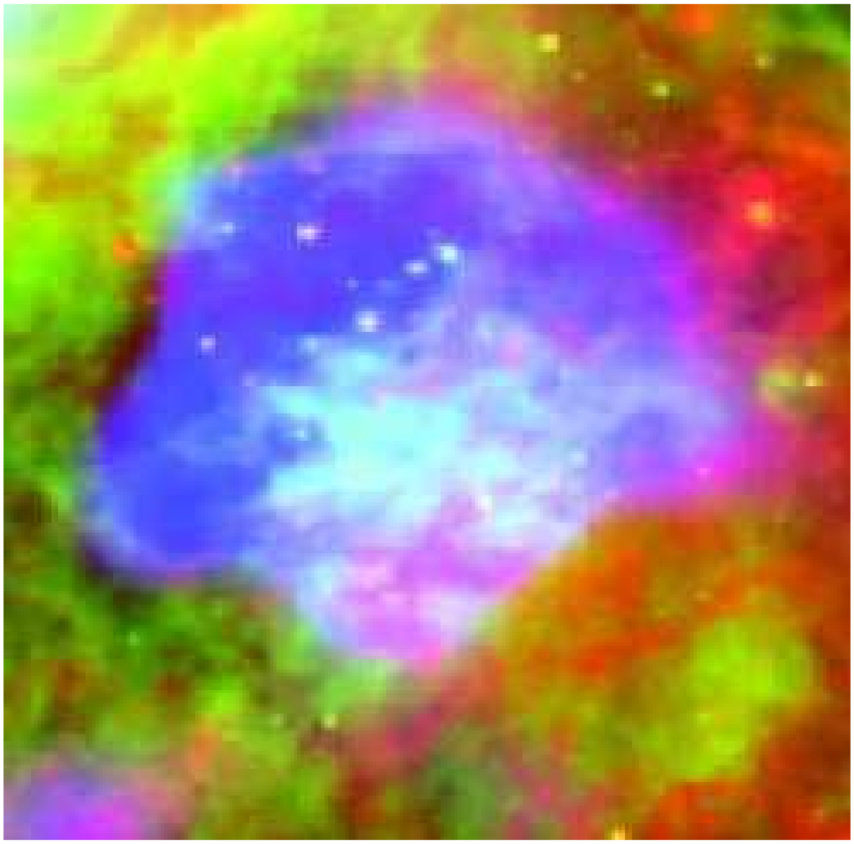

Figure 2.3 — Composite image of the N157B region: red = Spitzer IRAC 8.0 μm, green = MCELS Hα, blue = Chandra *ACIS* 0.9 - 2.3 keV. The blue area in the center shows X-rays from the northend parts of the remnant filling a prominent hole in the 8.0 μm. The contours of the optical and infrared emission (see Fig. 2.2) are recognisable in the cyan and magenta areas respectively . This picture is part of a large image of 30 Dor from Townsley et al. (2006). (*Reproduced by permission of the AAS.*)

the irregularly shaped diffuse emission is quite bright at 5.8 μm, 8.0 μm, and 24 μm where it appears more extended with a quasi-circular shape. In the 70 μm image, it no longer stands out clearly as it suffers from confusion with the very extended low-surface brightness emission characteristic of the whole 30 Doradus region. The cloud is listed as object no. 1448 in the IRAS catalogue of LMC sources by Schwering (1989) and shows up in the relatively low-resolution IRAS maps as an extension of the main 30 Doradus IR source. Fig. 2.2 (left) and Fig. 2.3 show that the contour of the 8 μm *emission* (sensitive to PAHs) from the cloud follows reasonably well the outline of *extinction* in the Hα image (Fig. 2.2 - right). Much of the infrared-emitting dust must therefore be either in front of the ionized gas, or embedded within it. From the MIPS 24 μm, the size of the cloud is roughly 2$'$ (28.8 pc). Its dimensions are thus similar to those of the SNR but the two are offset from one another, as shown by the superposition of the X-ray and 8 μm maps in Fig. 2.2, left-hand panel. Although there is considerable overlap between the X-ray and Hα emission regions (Fig. 2.2, right-hand panel), there is no trace of an IR counterpart to the X-ray SNR emission: the two occur almost side-by-side.

The bright and compact object at RA = 5h37m50.28s, DEC = -69°11$'$07.1$''$ (J2000) is located within the confines of the infrared cloud. In the IRAC images, it has a diameter

Table 2.2 — Infrared flux densities.

Origin	λ (μm)	Bandwidth (μm)	Flux Density (Jy) Compact Object	Flux Density (Jy) Extended Cloud
2MASS	1.24	0.16	0.0013 ± 0.0001	—
	1.66	0.25	0.0022 ± 0.0002	—
	2.16	0.26	0.017 ± 0.006	—
IRAC	3.6	0.75	0.13 ± 0.02	1.7 ± 0.3
	4.5	1.01	0.33 ± 0.05	3.2 ± 0.5
	5.8	1.42	0.66 ± 0.1	7.2 ± 1.1
	8.0	2.93	0.98 ± 0.2	19 ± 3.0
MIPS	24	4.7	1.7 ± 0.3	38 ± 6.0
	70	19	3.6 ± 0.5	139 ± 21.
	160	35	2 ± 0.3	105 ± 16.
IRAS	12	7.0	—	3 ± 0.5
	25	11.2	—	22 ± 3.0
	60	32.5	—	124 ± 19.
	100	31.5	—	312 ± 47.

of ∼3 pc and it is the brightest source in the field in all IRAC bands. Centimeter-wavelength radio maps by Dickel et al. (1994) and Lazendic et al. (2000) reveal weak radio emission at its position. Although there is ISO SWS and LWS spectroscopy of the extended cloud just described (Vermeij & van der Hulst 2002), the ISO apertures did not include this bright object. We have chosen this object, which is identical to the 2MASS near-IR source J05375027-6911071, as the reference position for the IRS slits (Fig. 2.2 - left panel).

We have collected infrared flux densities for both the compact object and the whole dust cloud shown in Fig. 2.1 by integrating the emission over circles with radii 6″ and 57″ centered on RA(5h37m50.3s), DEC(-69°11′07″) and RA(5h37m45.3s), DEC(-69°10′47″), respectively. The results are listed in Table 2.2, which for convenience also yields the relevant flux densities taken from the 2MASS on-line data archive, and the IRAS database published by Schwering (1989). Although all flux-densities in Table 2.2 have very small formal errors, a major uncertainty (easily a factor of two) arises in the separation of the source from its surroundings. As noted by Schwering, this is clearly true for the IRAS flux densities, which are very hard to separate from the overwhelming emission of the 30 Doradus complex, but a glance at Fig. 2.1 shows that this problem is not limited to the IRAS data, but also extends to the Spitzer mapping of this complex region.

2.3.2 IRS Spectroscopy of J05375027-6911071

The combined high- and low-resolution spectrum of the 2MASS source J05375027-6911071 covers the wavelength range from 5 μm to 38 μm, and is shown in Fig. 2.4.

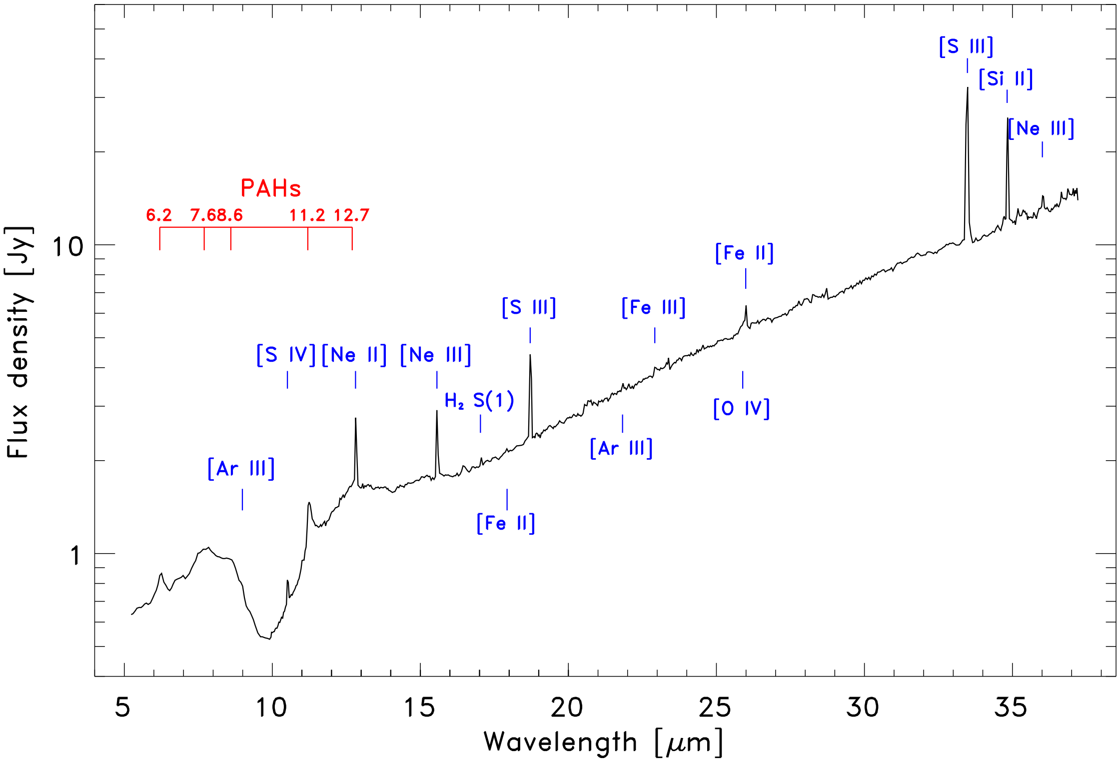

Figure 2.4 — Combined low- and high-resolution IRS spectrum of the 2MASS source J05375027-6911071.

The (short-wavelength) low-resolution part has been extracted from the *single slit segment* centered on 2MASS-J05375027-6911071 (see below), while the high resolution part results from integration over the *full length* covered by the SH and LH slits (see Fig. 2.2 - left-hand panel). This area includes J05375027-6911071 but also some of its fainter surroundings. As a result, the spectrum in Fig. 2.4 accurately reflects the emission from J05375027-6911071 shortwards of $\sim$20 μm. However, at wavelengths beyond 20 μm the spectrum includes a non-negligible contribution from the surrounding diffuse emission.

Different ISM processes have left their mark on the spectrum: emission from PAHs, absorption by silicates around 10 μm and in a broad band between 15 μm and 22 μm, various fine-structure emission lines and steeply increasing continuum emission from hot dust. The dust PAH features have been modelled with the program PAHFIT[3] (Smith et al. 2007) and the results are presented in Table 2.4. PAHFIT is an IDL tool for decomposing Spitzer IRS spectra, with special attention to PAH emission features, and it is primarily designed for use with Spitzer low-resolution IRS spectra. The program is based on a model consisting of starlight, thermal dust continuum with temperature from 35 to 300 K, resolved dust features and feature blends, prominent emission lines and dust extinction dominated by the silicate absorption bands at 9.7 μm and 15-22 μm. PAHFIT uses Gaussian profiles to recover the full strength of emission lines and Drude profiles for dust emission features and blends. The fine-structure lines have been measured by single Gaussian fits within SMART, and the results are listed in

---

[3] Available at http://turtle.as.arizona.edu/jdsmith/pahfit.php

Table 2.3 — Spitzer fine-structure lines observed in J05375027-6911071.

Line ID	λ_{rest} [μm]	EP^a [eV]	Flux^b [10^{-20} Wcm^{-2}]	EW^a [nm]
Clear detections				
[S IV]	10.51	34.8	2.35 ± 0.26	10
[Ne II]	12.81	21.6	17.2 ± 4.0	80
[Ne III]	15.56	41.0	8.4 ± 0.26	40
[S III]	18.71	23.3	13.3 ± 0.3	60
[Fe II]	25.99	7.9	3.32 ± 0.93	20
[S III]	33.48	23.3	55.6 ± 1.4	210
[Si II]	34.82	8.15	20.7 ± 0.8	70
[Ne III]	36.01	41.0	1.64 ± 0.52	5
Marginal detections				
[Ar III]	8.99	27.6	1.20 ± 0.27	4.27
H_2 S(1)	17.03	–	0.8 ± 0.37	6.54
[Fe II]	17.93	7.9	0.17 ± 0.19	1.70
[Ar III]	21.83	27.6	0.74 ± 0.20	4.00
[Fe III]	22.92	16.2	1.47 ± 0.40	6.53

Note. - Emission line properties obtained from single Gaussian fits in the IRS spectrum (Fig. 2.4).

(*a*): EP = Excitation Potential, EW = Equivalent Width (observed).

(*b*): Quoted uncertainties are the errors from the line fit and do not include calibration uncertainties.

Table 2.3. All these lines, except the iron lines, are typically associated with ionized gas in photon-dominated regions (PDRs - e.g. Martín-Hernández et al. 2002; Tielens 2005).

2.3.3 IRS spectroscopy of the extended dust cloud

As shown in Fig. 2.2, the SH and LH slits cover only a very limited part of the cloud, mainly the compact 2MASS object. The two much longer low-resolution slits LL2 and SL sample a much larger part of cloud, even extending into the cloud surroundings. The slits are almost perpendicular to one another and overlap at the position of the compact object 2MASS J05375027-6911071.

In order to study the spatial variation of the spectral features along the two slits, we sub-divided the region covered by each slit into 33 segments and extracted a spectrum from each segment. We have chosen overlapping extraction windows of three pixels width, moving them along the slit in single-pixel steps. Thus, adjacent extractions are not independent of one another as they overlap by two pixels. The corresponding spectrum is therefore effectively a boxcar-smoothed spectrum. These particular choices

Table 2.4 — PAH dust emission features measured in J05375027-6911071.

λ^{a}_{cent} [μm]	Flux^{b} [10^{-20} Wcm^{-2}]	EW^{c} [nm]	Relative^{d} strength
6.2	36.06 ± 0.58	34.1	1.00
7.7	53.00 ± 0.36	51.5	1.47
8.6	41.42 ± 0.54	40.3	1.15
11.2	32.77 ± 0.64	36.7	0.90
12.7	27.45 ± 0.36	26.7	0.76

(*a*): Central wavelength.
(*b*): The quoted uncertainties are the errors from the line fit and do not include the calibration uncertainties.
(*c*): EW = Equivalent Width (observed).
(*d*): Strength relative to 6.2 μm feature.

resulted from tests performed on the data to find the minimum extraction requirements needed to obtain spectra free of sampling artifacts. For the same reason, the region containing the bright object J05375027-6911071 was treated slightly differently. Here, we applied an extraction window five pixels wide, not overlapping with the adjacent pixels. As a consequence, the size of the extraction window for J05375027-6911071 exceeds the dimensions of the intersection region common to both the SL and LL2 slits; it corresponds to a 7 pc × 2.7 pc rectangle. We used PAHFIT with its default set of lines and continuum features to determine the intensities of the spectral features at every slit position. We have plotted the intensities of fine-structure emission lines and dust features thus extracted as a function of the position along the slit, expressed in terms of the distance (positive and negative) from J05375027-6911071 in Figs. 2.5, 2.6 and 2.7.

The SL spectra show PAH emission in the 6.2, 7.7, 8.6, 11.2 and 12.7 μm bands. In determining the intensity of the latter, we first removed the contribution from the [NeII] 12.8 μm line. We note that the PAH emission from the N157B region is remarkably weak compared to that of other sources in 30 Doradus (Brandl 2008).

2.4 Discussion

2.4.1 The nature of the compact object J05375027-6911071

The flux densities in Table 2.2 are not accurate enough to warrant detailed SED fitting of J05375027-6911071. However, by comparing various modified blackbody fits with straightforward integration we find an integrated flux of $5 - 11 \times 10^{-13}$ W m^{-2} which implies a luminosity $L = 3.8 - 8.6 \times 10^{4}$ L$_{\odot}$. This luminosity corresponds to that of a B1-O9 star if all stellar photons are converted to IR emission; it thus places a lower limit on the spectral type of the exciting star(s). Much of the emission must arise from hot dust, with temperatures between 180 and 350 K. The exciting star must therefore be close to the dense neutral material, and we would expect the interface between star

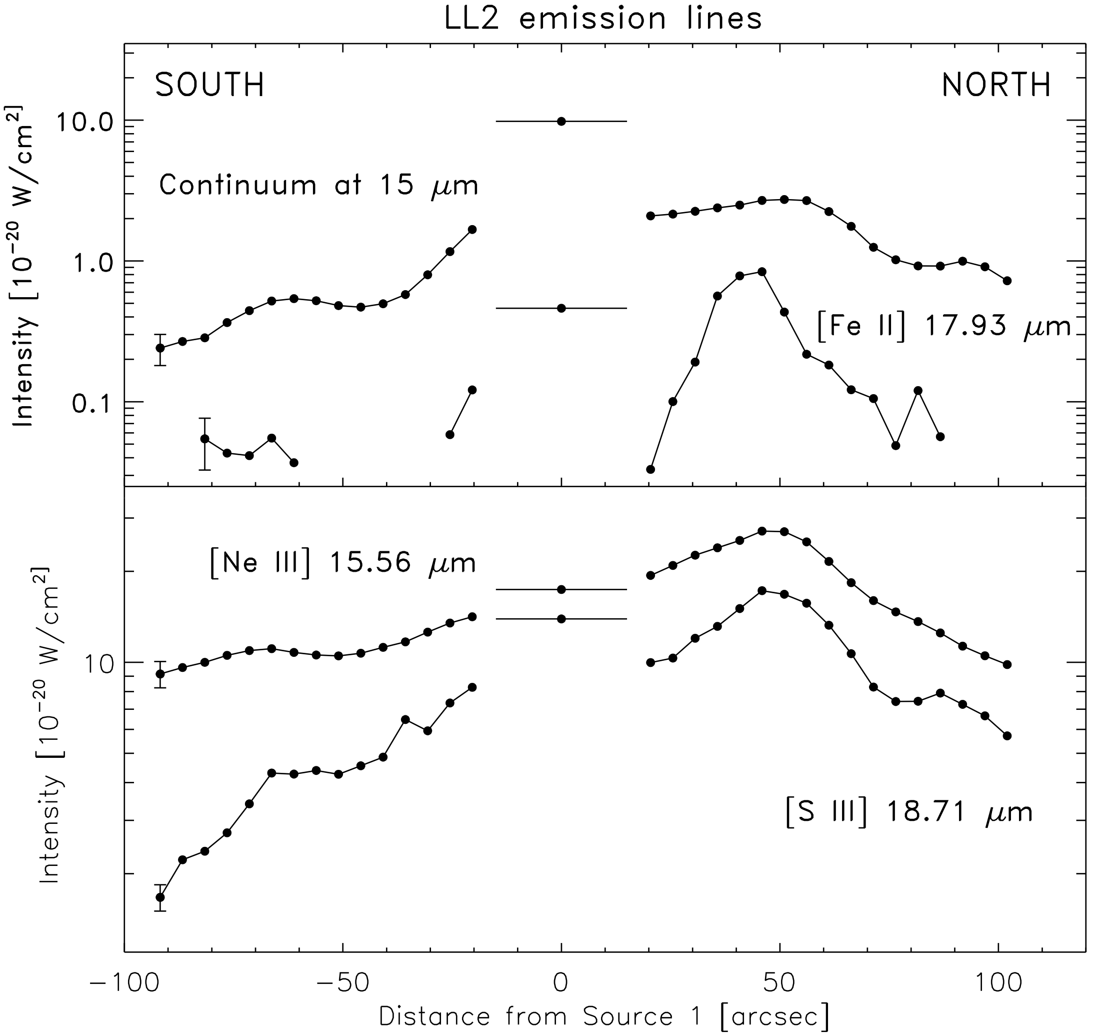

Figure 2.5 — Spatial variation of continuum and emission line intensities along the low-resolution slit LL2, calculated with the program PAHFIT. The vertical bar on the left mark indicates the representative error on fitted intensities. Spatial distances along the slit are measured from the position of J05375027-6911071 (0 arcsec). The horizontal bar indicates the size of the five-pixel wide extraction window for J05375027-6911071; all other data points refer to three-pixel wide extraction windows.

and neutral material to consist of very dense ionized gas.

The *Spitzer* spectrum of J05375027-6911071 (Fig. 2.4) contains several diagnostic fine-structure lines. The [SIII] lines at 18.7 μm and 33.5 μm arise from different levels with the same excitation energy and their ratio provides a measure of the electron density (e.g. Tielens 2005). We find a [SIII] 18.7 μm/ [SIII] 33. 5μm ratio of 0.24. Collisional excitation models (Alexander et al. 1999) place this ratio in the low-density limit, and indicate the presence of an ionized gas with $n_e \approx 100$ cm^{-3}. Such a density is not uncommon for a parsec-sized HII region (cf. Fig. 2 in Habing & Israel 1979). It is also quite consistent with the weak radio emission (about 40 mJy at $\lambda\lambda$3.5–13cm) in the maps published by Lazendic et al. (2000) and Dickel et al. (1994). Assuming all radio emission in this direction to be thermal and optically thin free-free emission, we calculate an r.m.s. electron density $< n_e^2 >^{0.5} = 100 - 250$ cm^{-3}. It is unlikely that the ionized

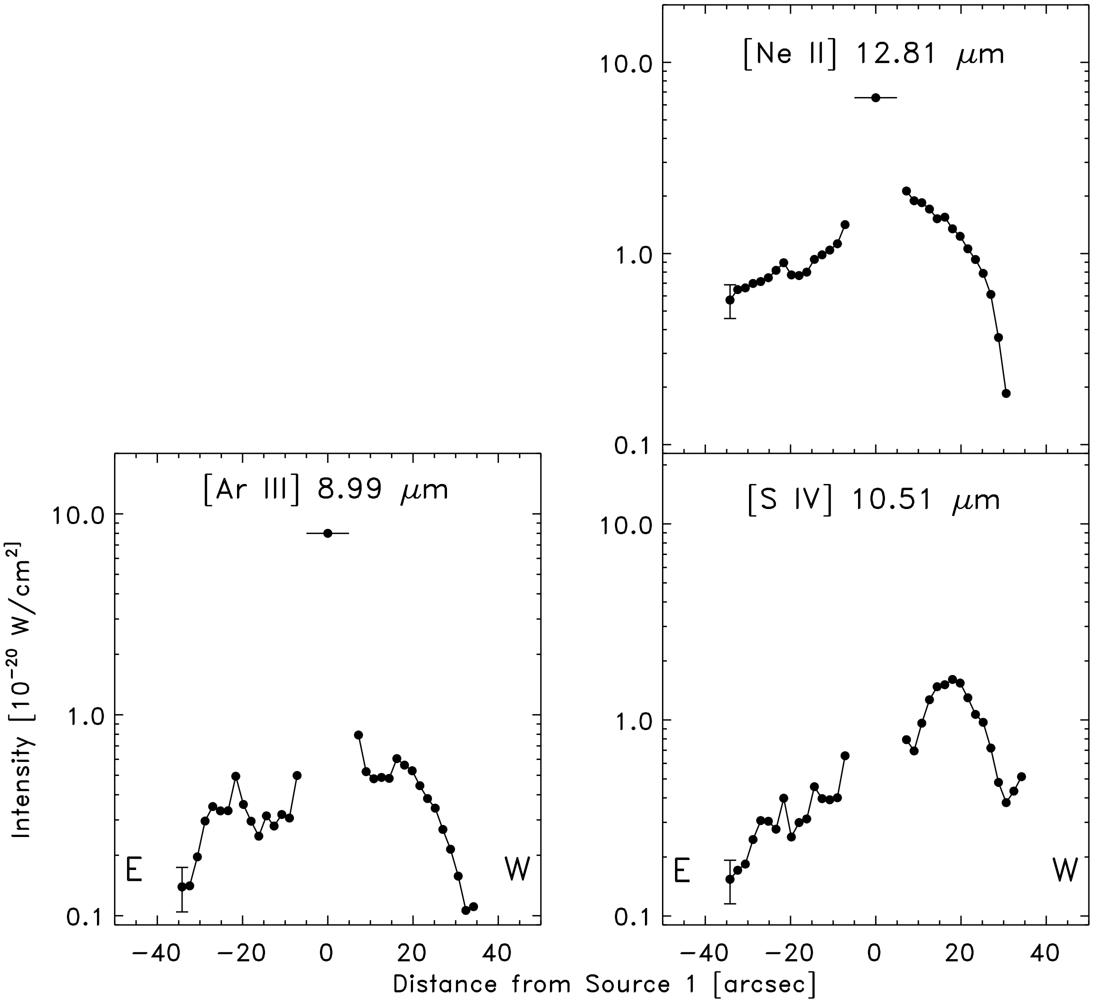

Figure 2.6 — Spatial variation of emission line intensities along the low-resolution slit SL. Otherwise as Fig. 2.5. Towards J05375027-6911071 the [S IV] line is undetectable because of strong silicate absorption.

gas and the hot dust have different sources of excitation. We must conclude that the bulk of the infrared line and radio continuum emission arises from gas extended over a volume much larger than occupied by the dense ionized gas surmised in the previous paragraph. As we have not resolved structure on scales less than a few parsecs, this is quite feasible.

The ratios of lines of the same species but arising from different ionization states reflect the degree of ionization and the hardness of the stellar radiation field. We have measured such pairs of neon and sulphur lines and find ratios [SIV]/[SIII] = 0.18 and [NeIII]/[NeII] = 0.49. In a sample of HII regions with different metallicities in the Milky Way, the LMC, and the SMC these two ratios are tightly correlated (cf. Fig. 1 by Martín-Hernández et al. 2002). Our result fits this correlation very well but the individual ratios are lower than those in the (very) bright LMC HII regions which have [SIV]/[SIII] = 0.6–1.0, and [NeIII]/[NeII] = 1.4–6.3. Not surprisingly, the gas in J05375027-6911071 thus has a lower degree of ionization as is expected from excitation by stars less hot than the ionizing stars in the bright LMC HII regions. The photoionization models by

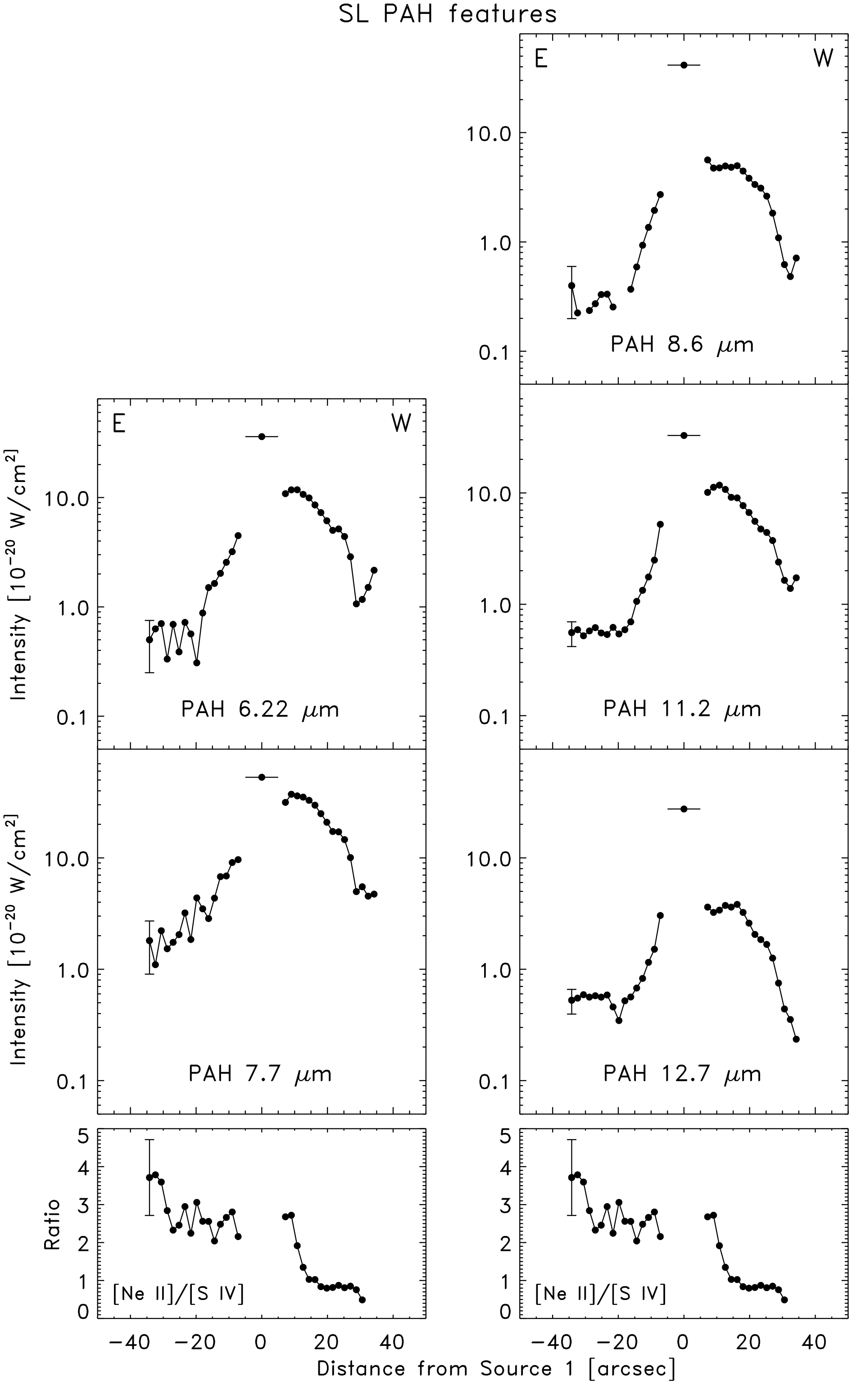

Figure 2.7 — Spatial variation of PAH feature intensities (top panels) compared to the [Ne II]/[S IV] ratio (same plot reproduced in both bottom panels for clarity) along the low-resolution slit SL. The vertical bar on the left mark indicates the representative error on fitted intensities in the region between -35 and -5 arcsec. The oscillations are due to instabilities in the fit caused by weak signals. Otherwise as Fig. 2.5.

Schaerer & de Koter (1997) (CoStar) and by Pauldrach et al. (2001) show our line ratios to result from stellar radiation fields with $T_{\rm eff} = 33000 - 40000$ K corresponding to spectral type O5–O9 (cf. Martins et al. 2002). Under the same assumption of optically thin free-free radio emission, we calculate from the maps by Dickel et al. (1994) and Lazendic et al. (2000) a minimum required Lyman-continuum photon flux $N_{\rm L} = 48.96$ s^{-1}. This corresponds to the output of an O7.5–O9 star (Vacca et al. 1996).

Bright [FeII] 17.9 μm, [FeII] 26.0 μm and [SiII] 34.8 μm lines trace the return of iron and silicon to the gas phase following the destruction of dust grains by shocks (Oliva et al. 1999; Reach & Rho 2000), but a strong [SiII] line is also frequently detected in PDRs (Peeters et al. 2002b). In J05375027-6911071 [SiII] is one of the strongest detected lines, whereas the [FeII] lines are weak with respect to the others. The [SI] 25 μm line, also expected in shocked gas (**?**), is missing but sulphur is detected as [SIII] and [SIV], a situation characteristic for photo-ionized gas.

The intensity of the optical lines [SII] $\lambda\lambda$6717, 6731 Å and Hα λ6563 Å provides a reliable tool to discriminate between shock-excited and photo-ionized plasma (Long et al. 1990)) and were, in fact, used to establish the nature of N157B (Danziger et al. 1981). In SNRs, [SII] emission is usually stronger than in photoionized HII regions, where sulphur is mostly doubly ionized. The value of the [S II]/Hα ratio separating SNRs and HII regions is about 0.4 (D'Odorico et al. 1980; Fesen et al. 1985; Long et al. 1990). No optical spectra are available for J05375027-6911071, but we may estimate the [SII]/Hα ratio from the MCELS line emission maps. The lines are close enough to assume that they suffer approximately the same extinction. We find a ratio [SII]/Hα = 0.2, which is typical for H II regions (Long et al. 1990). Note that in most of N157B, this ratio exceeds $\sim$ 0.7 (Danziger et al. 1981).

Finally, we note that the 9.7 μm silicate absorption feature is very strong towards J05375027-6911071, with an optical depth $\tau_{9.7} \approx 1.1$. This implies the presence of a large column of neutral material in front of the ionized line emission region.

Thus, the 2MASS source J05375027-6911071 contains a purely photo-ionized gas of moderate density. The high column-density and elevated temperature of the dust suggests a blister-type geometry (Israel 1978) seen from the back, and a source of excitation located close to the interface of the HII region with the obscuring dense neutral material. In that case, no more than about half of the ionizing photons may escape, and we conclude from this and the local radiation field hardness that the excitation of J05375027-6911071 is caused by an obscured but no longer embedded O8 or O9 star.

2.4.2 The northeast edge of the dust cloud

The intensity variation of the spectral features along the rather short SL slit is shown in Fig. 2.6 and 2.7. The SL slit runs from northeast to southwest. It is potentially of interest as it cuts across the X-ray SNR/IR dust cloud boundary (Fig. 2.2 left-hand panel). Apart from J05375027-6911071, most of the emission in all lines comes from the dust cloud, outside the X-ray contours. The [S IV] intensities peak around +15 arcsec (3.5 pc) southwest from J05375027-6911071. Towards the object itself, because of the low resolution of the SL slit we could not separate the [SIV] emission from the silicate absorption at 9.7 μm, contrary to the high resolution spectrum where the [SIV] is well detected. Both [Ar III] and [Ne II] have intensity distributions strongly peaking on

J05375027-6911071, and that of [ArIII] is almost symmetrical. The [NeII] distribution has an asymmetry similar to but less outspoken than that of [SIV]. The ion with the highest ionization potential (S[IV]) appears to trace the dust continuum best, but the lack of more extensive spectral coverage makes it very hard to draw any solid conclusions.

The various (weak) PAH features have symmetrical intensity distributions, very similar to each other (Fig. 2.7) and consistent with the 8.0 μm image which shows the stronger emission in southwest of the X-ray contours. Fig. 2.7 also shows the [NeII]/[SIV] ratio. The excitation potentials of NeII and SIV are 21.6 and 34.8 eV respectively. The ratio of the corresponding ionic lines [NeII]/[SIV] can be used as a tracer of the hardness of the interstellar radiation field (ISRF) in a similar way as the ratio [NeII]/[NIII] (see for exemple Giveon et al. 2002): a lower ratio corresponds to a harder ISRF. If PAHs were destroyed by FUV photons (e.g. Madden et al. 2006), PAH intensities should be correlated with the [NeII]/[SIV] ratio.

Inspection of Fig. 2.7 reveals a clear trend: the PAH profiles peak where the [NeII] over [SIV] ratio dives (+20″ W) probably indicating the edge of an ionized region where PAHs are destroyed. We refer for a more extensive and detailed discussion of PAHs in the whole 30 Doradus region to Bernard-Salas (2008).

2.4.3 Conditions in the extended dust cloud

Fig. 2.5 depicts the spatial intensity variation of spectral features along the significantly longer SE-NW LL2 slit. The slit extends from a region with weak IR emission and no X-rays to the northwest, fully crossing the Hα and X-ray emitting SNR (Fig. 2.2 left-hand panel). The compact source J05375027-6911071 is brighter than its surroundings in the continuum, and in the [SIII] and [FeII] lines, but not in the [NeIII] line. Beyond this source, the distributions of [SIII], [NeII] and the continuum are similar and peak about 50 arcsec (12 pc projected distance) to its northwest. The [FeII] from the diffuse cloud is relatively sharply peaked. Although uncertain, this peak may indicate the presence of shocked gas at an SNR/dust cloud interface. As the Ne[III] and [SIII] intensity distributions peak closest to the early O stars in LH 99 (see Fig. 2.2 and Sec. 4.3), they seem to reflect the radiative effects of these.

The ISO SWS and LWS instruments have provided spectroscopy from differently-sized regions (Vermeij et al. 2002) roughly covering the O3 stars marked in Fig. 2.2. The LL2 slit misses the SWS aperture completely, but does overlap with part of the LWS aperture. The [NeIII] 15.6/36.0 μm, [SIII] 18.7/33.5 μm, and [OIII] 51.8/88.4 μm ratios (6.73, 0.40, 0.56 resp.) are all in the low-density limit, indicating $n_e \leq 100\,\mathrm{cm}^{-3}$. The ISO spectra also show [FeII] 26.0 μm and [SiII] 34.8 μm line emission but not sufficiently dominant to be ascribed unequivocally to shock excitation. More importantly, the ISO data by Vermeij et al. (2002) imply ratios [SIV]/[SIII] = 0.25 and [NeIII]/[NeII] = 1.74. These values are also in excellent agreement with the relation established by Martín-Hernández et al. (2002), and place the cloud somewhat closer to the bright LMC nebulae. Although there are complications briefly discussed by Martín-Hernández et al. (2002), the ratios, taken at face value, suggest excitation by O5-O6 stars rather than by O3 stars.

The spectral energy distribution of the extended infrared cloud is shown in Fig. 2.8.

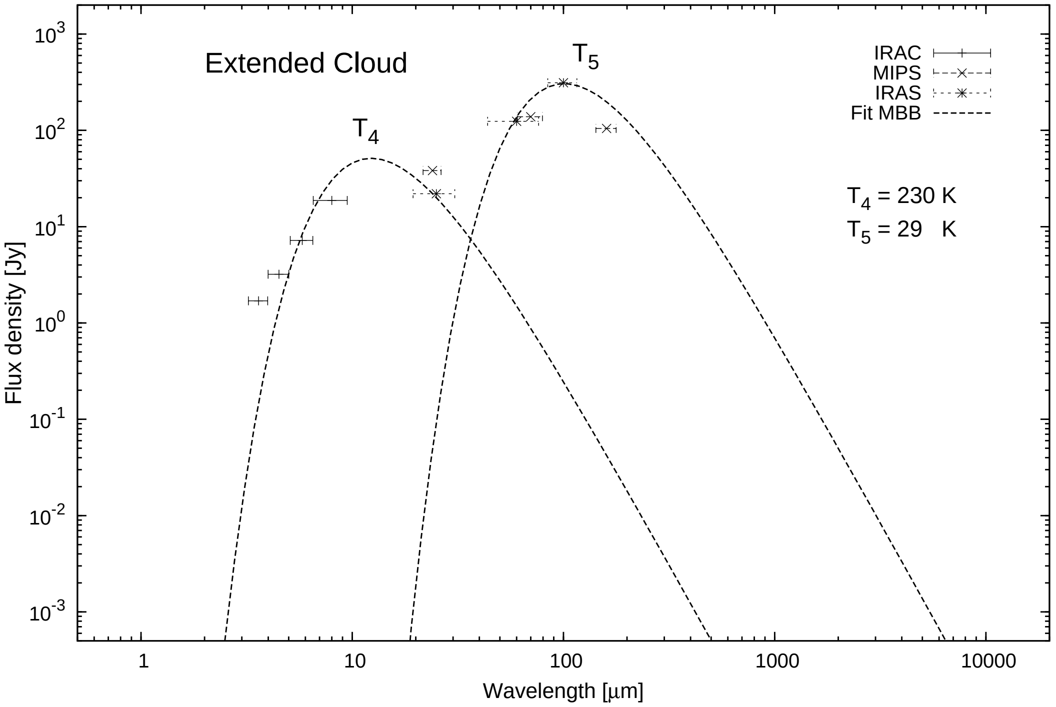

Figure 2.8 — Spectral energy distribution of infrared emission from the extended dust cloud. The data points are fitted with two modified black-body with $T = 230$ and $T = 29$ K. The horizontal bars indicate the width of the IRAC (Fazio et al. 2004), MIPS (Rieke et al. 2004) and IRAS bands (Schwering 1989). The 12 μm IRAS point has been removed because of the strong 10 μm silicate absorption of the compact source, which makes it impossible to separate out the extended cloud contribution.

The emission peak is consistent with a modified black-body of temperature $T = 29$ K ($B(\nu, T) \times \nu^{\beta}$, with $\beta = 2$). Integration of the emission yields a flux of $1.1 - 1.5 \times 10^{-11}$ W m^{-2} implying a luminosity $L = 0.8 - 1.1 \times 10^{6}$ L$_{\odot}$. There is a second hot dust component, with a temperature $T \approx 230$ K, and a luminosity (excluding emission from J05375027-6911071) $L = 4 - 5 \times 10^{5}$ L$_{\odot}$. In the 12 μm IRAS band the compact source has a strong silicate absorption at 10 μm, which makes not possible the separation of the compact source and extended cloud contributions. Before fitting the hot dust component we thus removed the 12 μm IRAS point, for which the flux density is in fact 30 times lower than for the neighboring bands. Because of the very strong temperature dependence of dust emissivity, the mass in the hot dust component represents only a minute fraction of the total mass. The three O3 stars dominating the LH 99 population are projected onto the northeastern edge of the infrared cloud as depicted at 24 μm in Fig. 2.1. To their southwest, i.e. closer to the brightest part of the nebula, there are at least 2 O5 stars, 5 O6 stars, and 5 O7 stars (cf. Schild & Testor 1992). Using the luminosity scale by Vacca et al. (1996), we find that these stars add another L(O5-O7) = 4.1×10^{6} L$_{\odot}$ to the luminosity L(O3) = 3.6×10^{6} L$_{\odot}$ already provided by the brightest stars. The hardness of the resulting mean radiation field should therefore not be very different from the one estimated above.

Emission from the radio source appears to avoid the dark cloud (see Fig. 4 in Dickel et al. 1994). This is not expected if the dust cloud is only a foreground object, and it therefore indicates physical contact between the radio (SNR) and infrared (molecular cloud) sources respectively. However, the infrared cloud reradiates at most 15% of the total photon output of the association members, requiring it to cover only about a steradian as seen from the average O star. LH 99 should thus be deemed to be quite capable of providing the energy to power the infrared cloud, and there seems to be no need to invoke energy inputs provided by an SNR impact.

Chu et al. (1992) have suggested that no more than about 20% of the radio emission from MC 69 is thermal in origin, so that $S_{5\mathrm{GHz}}(th) \leq 0.45$ Jy (cf. Lazendic et al. 2000). This requires a maximum Lyman continuum photon flux $N_{\mathrm{L}} \leq 1.0 \times 10^{50}\ \mathrm{s}^{-1}$. The three somewhat excentric O3 stars provide a combined flux $N_{\mathrm{L}} = 2.5 \times 10^{50}\ \mathrm{s}^{-1}$, and the more embedded later-type O stars an almost equal $N_{\mathrm{L}} = 2.4 \times 10^{50}\ \mathrm{s}^{-1}$. Thus, the UV photon flux likewise should be sufficient to provide for the ionization of the HII nebula associated with the SNR and dust cloud.

2.4.4 The SNR revisited

The actual location of the cloud with respect to the remnant is still poorly determined. The data presented here have revealed no evidence for shocked material, although the dense cloud of dust and molecules does appear to be quite close to the SNR. Is the absence of such impact (shock) signatures consistent with the dynamical evolution of the remnant? We assume that the remnant expansion is in the Sedov phase (Wang & Gotthelf 1998), so that the temporal evolution of the spherical blast wave with radius R_S, produced by the supernova explosion into a medium of uniform density ρ_0, is described by (Sedov 1959; McCray & Snow 1979b):

$$R_{\mathrm{S}} = 1.15\,(E_0/\rho_0)^{1/5}\,t^{2/5} \approx 13\,(E_{51}/n_0)^{1/5}\,t_4^{2/5}\quad \mathrm{pc}. \tag{2.1}$$

We assume an initial energy $E_{51} = E_0/(10^{51}\ \mathrm{erg\ s}^{-1}) = 1$, a remnant age $t_4 = t/(10^4\ \mathrm{yr}) = 0.5$ (Marshall et al. 1998), and a remnant radius $R_{\mathrm{S}} \simeq 15$ pc (Chu et al. 1992; Dickel et al. 1994; Lazendic et al. 2000; Chen et al. 2006). Thus, the present size of the supernova remnant requires an initial density of no more than $n_0 = 0.12\ \mathrm{cm}^{-3}$. This rules out the possibility of N157B having expanded into an interstellar gas cloud of any significant density, and confirms the notion that expansion occurred inside a windblown cavity cleared out by the supernova progenitor (Chu et al. 1992). In their X-ray study of 30 Doradus and N157B, Townsley et al. (2006) present a composite X-ray/Hα/mid-IR image (their Fig. 14) that indeed shows a shell of ionized gas and warm dust surrounding the SNR. To verify whether a suitable low-density cavity could have been generated by the supernova progenitor, we calculate its expected size by (McCray & Snow 1979b,and references therein):

$$R_{\mathrm{S}} \approx 27\,L_{36}^{1/5}\,n_0^{-1/5}\,t_6^{3/5}\quad \mathrm{pc} \tag{2.2}$$

where R_{S} is the cavity radius, L_{36} the constant wind luminosity in units of $10^{36}\ \mathrm{erg\ s}^{-1}$, n_0 the ambient gas particle density in cm^{-3}, and t_6 the time that the wind has been blowing in millions of years. The wind luminosity L_{36} is given by:

$$L_{36} \approx 0.3(M_*/20M_\odot)^{2.3}\quad \mathrm{ergs}^{-1}. \tag{2.3}$$

We adopt a $M_* = 25$ M$_\odot$ (corresponding to an O8–O9 star), intermediate between the values predicted by the Thielemann et al. (1996), Heger et al. (2003) and Woosley & Weaver (1995) models so that $L_{36} = 0.5$. The relevant time $t_6 = 3.2$ is the entire lifetime of the progenitor, derived from e.g. Karttunen (1995): $t \sim (M_*/M_\odot)^{-2.5} \times 10^{10}$ yr. The observed radius R_S of about 15 pc implies an average density of $n_0 = 310$ cm^{-3} for the ambient medium into which the windblown shell has expanded. Such a value is compatible with the densities of a few hundred per cc that we estimated in the previous section for the clouds in the region. Even the larger radius $R_S \approx 22$ pc gleaned from Townsley et al. (2006) can be accommodated as it still yields $n_0 = 50$ cm^{-3}. This situation changes rapidly, however, if we consider a more massive supernova progenitor. For instance, for $M_* = 50$ M$_\odot$ and $R_S = 15$ pc we have $L_{36} = 2.5$ and $t_6 = 0.6$, and find an average ambient density of only $n_0 = 9$ cm^{-3}.

Thus, we conclude that the lack of clear indications for an SNR impact on the dust cloud seen in the IRAC and MIPS images is consistent with the supernova explosion of a moderately massive star. Only now would the SNR expanding in the cavity begin to overtake the windblown shell produced by the star over its lifetime. The apparent lack of shocks is not easily reconcilable with a supernova progenitor as massive as the presently most luminous members of the LH 99 association. This confirms an independent conclusion by Chen et al. (2006) that the progenitor should have been in the narrow mass range $M = 20 - 25$ M$_\odot$.

2.5 Conclusions

From an analysis of Spitzer photometric mapping and spectroscopy of the SNR – dominated region N157B in the LMC, we find that there is no evidence of an infrared counterpart to the supernova remnant in the IRAC and MIPS images. The infrared emission is dominated by a cloud of dust and molecular gas adjacent to the remnant, containing the compact 2MASS source J05375027-6911071.

The object J05375027-6911071 has a diameter of about 3 pc, an electron-density of 100-250 cm^{-3}, and is photo-ionized by an O8–O9 star. It is probably an open HII blister structure, seen from the back. In spite of the projected overlap between the SNR X-ray emission and the infrared cloud, there is at best very marginal evidence of shocked gas, while almost all data suggest photo-ionization and photon-heating to be the mechanisms dominating the infrared cloud.

The extended dust cloud is associated with ionized emission of a density of typically 100 cm^{-3}, presumably at the edges of a denser molecular cloud. As the extended dust reradiates only about 10 per cent of the luminosity of the 15 brightest and nearby O stars in the LH 99 OB association, these stars are sufficient to explain the heating of the dust cloud.

The absence of clear evidence of shocks implies that at present the molecular/dust cloud is not significantly impacted by the remnant. This suggests that the supernova progenitor was a moderately massive star of mass $M \approx 25$ M$_\odot$.

Acknowledgements

We gratefully acknowledge D. Wang, J. Dickel, and R. Gruendl for providing Chandra data, radio continuum observations, and information on the N157B stellar population, and we would like to thank the referee for careful reading and useful comments. E.R.M. thanks A. Jones and A. Tielens for support and useful discussions and acknowledges financial support by the EARA Training Network (EU grant MEST-CT-2004-504604). This work is based in part on observations made with the *Spitzer Space Telescope*, which is operated by the Jet Propulsion Laboratory, California Institute of Technology, under NASA contract 1047.

Chapter 3

PAH processing in interstellar shocks

Abstract. PAHs appear to be an ubiquitous interstellar dust component but the effects of shocks waves upon them have never been fully investigated. The aim of this work is to study the effects of energetic ($\approx 0.01 - 1$ keV) ion (H, He and C) and electron collisions on PAHs in interstellar shock waves. We calculate the ion-PAH and electron-PAH nuclear and electronic interactions, above the threshold for carbon atom loss from a PAH, in $50 - 200$ km s^{-1} shock waves in the warm intercloud medium. We find that interstellar PAHs ($N_{\mathrm{C}} = 50$) do not survive in shocks with velocities greater than 100 km s^{-1} and larger PAHs ($N_{\mathrm{C}} = 200$) are destroyed for shocks with velocities ≥ 125 km s^{-1}. For shocks in the $\approx 75 - 100$ km s^{-1} range, where destruction is not complete, the PAH structure is likely to be severely denatured by the loss of an important fraction ($20 - 40\%$) of the carbon atoms. We derive typical PAH lifetimes of the order of a few $\times 10^8$ yr for the Galaxy. These results are robust and independent of the uncertainties in some key parameters that have yet to be well-determined experimentally. The observation of PAH emission in shock regions implies that that emission either arises outside the shocked region or that those regions entrain denser clumps that, unless they are completely ablated and eroded in the shocked gas, allow dust and PAHs to survive in extreme environments.

E. R. Micelotta, A. P. Jones, A. G. G. M. Tielens

accepted for publication in Astronomy & Astrophysics

3.1 Introduction

Interstellar Polycyclic Aromatic Hydrocarbon molecules (PAHs) are an ubiquitous and important component of the interstellar medium. The mid-infrared spectrum of the general diffuse interstellar medium as well as energetic environments near massive stars such as HII regions and reflection nebulae are dominated by broad emission features at 3.3, 6.2, 7.7, and 11.2 μm. These emission features are now generally attributed to infrared fluorescence by large PAH molecules containing 50-100 C-atoms, pumped by single FUV photons (see Tielens 2008, for a recent review). The observed spectra also show evidence for PAH clusters containing a few hundred C-atoms (Bregman et al. 1989; Rapacioli et al. 2005; Berné et al. 2007) as well as very small dust grains ($\sim$30 Å; Desert et al. 1990). It seems that the interstellar grain size distribution extends all the way into the molecular domain (Allamandola et al. 1989; Desert et al. 1990; Draine & Li 2001). The origin and evolution of interstellar PAHs are somewhat controversial. On the one hand, based upon extensive laboratory studies of soot formation in terrestrial environments, detailed models have been made for the formation of PAHs in the ejecta of C-rich giants (Frenklach & Feigelson 1989b; Cherchneff et al. 1992) – as intermediaries or as side-products of the soot-formation process – and studies have suggested that such objects might produce enough PAHs to seed the ISM (Latter 1991). On the other hand, models have been developed where PAHs (as well as very small grains) are the byproduct of the grinding-down process of large carbonaceous grains in strong supernova shock waves which permeate the interstellar medium (Borkowski & Dwek 1995b; Jones et al. 1996). Grain-grain collisions shatter fast moving dust grains into small fragments and, for graphitic progenitor grains, these fragments might be more properly considered PAH molecules. The destruction of interstellar PAHs is equally clouded. Laboratory studies have shown that small (less than 16 C-atoms), (catacondensed) PAHs are rapidly photodissociated by $\sim$ 10eV photons (Jochims et al. 1994a). However, this process is strongly size-dependent as larger PAHs have many more modes over which the internal energy can be divided and PAHs as large as 50 C-atoms might actually be stable against photodissociation in the ISM (Le Page et al. 2001; Allamandola et al. 1989). While strong shock waves have been considered as formation sites for interstellar PAHs, the destruction of these PAHs in the hot postshock gas has not been evaluated. Yet, high energy ($\sim$ 1 keV) collisions of PAHs with ions and electrons are highly destructive.

The observational evidence for PAHs in shocked regions is quite ambiguous. The majority of supernova remnants does not show PAH features (e.g. Cas A, Smith et al. 2008), but observations of N132D (Tappe et al. 2006) suggest the possibility of PAH survival in shocks. Recent work by Andersen et al. (2007) investigates the presence of PAHs in a subset of galactic supernova remnants detected in the GLIMPSE survey. Unfortunately the interpretation of such observations is not straightforward, because of the difficulty in disentangling the PAH features intrinsic to the shocked region with those arising from the surrounding material. Another interesting case is the starburst galaxy M82, which shows above and below the galactic plane a huge bipolar outflow of shock-heated gas interwoven with PAH emission[1] (Armus et al. 2007). PAHs have

---

[1] http://chandra.harvard.edu/photo/2006/m82/

also been observed at high galactic latitudes in the edge-on galaxies NGC 5907 and NGC 5529 (Irwin & Madden 2006; Irwin et al. 2007). Shock driven winds and supernovae can create a so-called "galactic fountain" (Bregman 1980) transporting material into the halo and these detections of PAHs suggests the possibility of survival or formation of the molecules under those conditions. On the other hand O'Halloran et al. (2006, 2008) have found a strong anti-correlation between the ratio [FeII]/[NeII] and PAH strenght in a sample of low-metallicity starburst galaxies. Since [FeII] has been linked primarly to supernova shocks, the authors attributed the observed trend to an enhanced supernova activity which led to PAH destruction.

In our previous study (Jones et al. 1996), we considered the dynamics and processing of small carbon grains with $N_{\mathrm{C}} \geq 100$. The processing of these grains by sputtering (inertial and thermal) in ion-grain collisions and by vaporisation and shattering in grain-grain collisions was taken into account for all the considered grain sizes. In that work, the smallest fragments ($a_{\mathrm{f}} < 5$ Å) were collected in the smallest size bin and not processed. In this work we now consider what happens to these smallest carbon grain fragments that we will here consider as PAHs. In this paper, we will consider relatively low velocity (≤ 200 km s^{-1}) shocks where the gas cools rapidly behind the shock front but, because of their inertia, PAHs (and grains) will have high velocity collisions even at large postshock column densities. Collisions between PAHs and the gas ions occur then at the PAH velocity which will slowly decrease behind the shock front due to the gas drag. This relative velocity is thus independent of the ion mass and, for dust grains, destruction is commonly called inertial sputtering. Destruction of PAHs in high velocity (≥ 200 km s^{-1}) shocks – which cool slowly through adiabatic expansion – is dominated by thermal sputtering and these shocks are considered in Chapter 4 (paper Micelotta et al. 2009b, hereafter MJT09b).

This chapter is organized as follows: § 3.2 describes the theory of ion interaction with solids, § 3.3 illustrates the application of this theory to PAH processing by shocks and § 3.4 presents our results on PAH destruction. The PAH lifetime in shocks and the astrophysical implications are discussed in § 3.5 and our conclusions summarized in § 3.6.

3.2 Ion interaction with solids

3.2.1 Nuclear interaction

The approach used in our earlier work is not valid for planar PAH molecules with of the order of tens of carbon atoms. Here, we assume that collisions are binary in nature, as is assumed in work on solids (Lindhard et al. 1963, 1968; Sigmund 1981). If the energy transfer is above the appropriate threshold value, we assume that the carbon target is ejected from the molecule. Below that threshold, there will be an internal vibrational redistribution of the transferred energy, eventually followed by radiation emission.

In this description the "bulk" nature of the target enters only after the first interaction, when the projectile propagates into the material. We therefore consider only the first interaction, which is described in the binary collision approximation in a way that then conveniently allows us to take into account the "molecular" nature of the target.

In addition to the energy directly transferred to the target nucleus through elastic scattering (*nuclear stopping* or *elastic energy loss*), the energy loss to the atomic electrons (*electronic stopping* or *inelastic energy loss*) should also be considered (Lindhard et al. 1963, 1968). In a solid the energy transferred via electronic excitation is distributed around the impact region. For a PAH, which has a finite size, the energy will be spread out over the entire molecule. At this stage a fragment can be ejected or the electronically excited molecule will move to a lower-lying electronic state through internal conversion, leaving most of the initial excitation energy in the form of vibrational energy which will eventually decrease by IR emission.

Nuclear and electronic stopping are simultaneous processes which can be treated separately (Lindhard et al. 1963). Fig. 3.11 illustrates these effects and shows the PAH evolution following the loss of carbon atoms, $N_{\rm C}$(lost), for the two limiting cases: 1) where there is an instantaneous and random removal of the lost carbon atoms and 2) where the carbon atoms are removed only from the periphery in order to preserve aromatic domain as much as possible. The reality of PAH erosion in shocks probably lies somewhere between these two extremes and will involve isomerisation and the formation of five-fold carbon rings that distort the structure from a perfectly two-dimensional form. This then begs the question as to the exact form and structure of small carbon species once growth resumes by atom insertion and addition. The full treatment of the nuclear stopping is given here, for the electronic stopping only the results of the calculations are shown, for the complete description of the phenomenon we refer the reader to Chapter 4 - paper MJT09b.

The treatment of PAH processing by shocks should also include the effects of fast electrons present in the gas. Because of their low mass, electrons can reach high velocities and hence high collision rates even at relatively low temperatures ($T \sim 10^5$ K), leading to potentially destructive collisions. Again for a detailed description of the electron-PAH interaction see Chapter 4 - paper MJT09b.

The theory of ion penetration into solids described here considers collisions where the transferred energy T goes from 0 to the maximum transferable energy. For this study, we are interested in only those collisions that are able to remove carbon atoms from the PAH, i.e. for which the energy transferred is greater than the minimum energy T_0 required for C ejection. In §3.2 we present the modifications we introduce into the theory in order to treat the case of collisions above this threshold.

To describe the binary collision between a moving atom (or ion) and a stationary target atom (e.g. Sigmund 1981), a pure classical two-particle model using the Coulomb repulsion between the nuclei (Rutherford scattering) is adequate only at high energies, i.e. when $\varepsilon \gg 1$, where ε is the dimensionless *Lindhard's reduced energy*

$$\varepsilon = \frac{M_2}{M_1 + M_2} \, \frac{a}{Z_1 \, Z_2 \, e^2} \, E \tag{3.1}$$

where M_1 and Z_1 are the mass and atomic number of incident particle respectively, M_2 and Z_2 the mass and atomic number of target particle, E is kinetic energy of incident particle and e is the electron charge, with e^2=14.39 eVÅ. The quantity a is the *screening length*, a parameter that defines the radial spread of the electronic charge about the

Table 3.1 — Kinetic energy E and reduced energy ε for H, He and C ions with velocity $v_{\rm p1}$ = 37.5 km s^{-1} and $v_{\rm p2}$ = 150 km s^{-1} impacting on a carbon atom. The projectile velocity is defined by the shock velocity $v_{\rm S}$ via the equation $v_{\rm p} = \frac{3}{4}\, v_{\rm S}$, with $v_{\rm S}$ = 50 and 200 km s^{-1} respectively. The reduced energy is calculated from Eq. 3.1 and Eq. 3.2.

Projectile	$E^a(v_{\rm p1})$	$\varepsilon^b(v_{\rm p1})$	$E^a(v_{\rm p2})$	$\varepsilon^b(v_{\rm p2})$
H	7.30	0.031	117.4	0.50
He	29.4	0.048	469.7	0.76
C	88.1	0.028	1409.	0.45

(a): Kinetic energy in eV.
(b): Dimensionless.

nucleus. For the screening length we adopt the Universal Ziegler - Biersack - Littmark (ZBL) screening length $a_{\rm U}$ (Ziegler et al. 1985)

$$a_{\rm U} \cong 0.885\, a_0\, (Z_1^{0.23} + Z_2^{0.23})^{-1} \qquad (3.2)$$

where a_0 = 0.529 Åis the Bohr radius. The condition $\varepsilon \gg 1$ implies that the energies are large enough that the nuclei approach closer to each other than the screening length a. At lower energies, $\varepsilon \lesssim 1$, it is essential to consider the *screening* of the Coulomb interaction. In this case the Rutherford approximation is not adequate and the scattering problem must be treated using a different approach.

To choose the appropriate formalism to describe our interaction, we need to calculate the reduced energy for our projectiles. For our study of the behaviour of PAHs in shocks, we consider the binary collision between H, He and C ions (projectiles) and a carbon atom (target) in the PAH molecule. The velocity $v_{\rm p}$ of the projectile is determined by the shock velocity $v_{\rm S}$ through the relation $v_{\rm p} = \frac{3}{4}\, v_{\rm S}$. We consider here shock velocities between 50 and 200 km s^{-1}. The corresponding projectile kinetic energies E and reduced energies ε are reported in Table 3.1 for the two limiting cases $v_{\rm p1} = \frac{3}{4}(50)$ = 37.5 km s^{-1} and $v_{\rm p2} = \frac{3}{4}(200)$ = 150 km s^{-1}.

The calculation clearly shows that for the shocks we are considering $\varepsilon \lesssim 1$, implying that our problem cannot be treated in terms of Rutherford scattering but requires a different formalism, described by Sigmund (1981) and summarized below. The scattering geometry for an elastic collision of the projectile particle 1 on target particle 2 is illustrated in Fig. 3.1. Particle 1 has mass M_1, initial velocity v_0 and impact parameter p, where the impact parameter is the distance of closest approach of the centers of the two atoms/ions that would result if the projectile trajectory was undeflected. Particle 2 has mass M_2 and is initially at rest. After the impact, the projectile is deflected by the angle ϑ and continues its trajectory with velocity v_1. A certain amount of energy T is transferred to the target particle which recoils at an angle ϕ with velocity v_2. The maximum transferable energy corresponds to a head-on collision (impact parameter p = 0) and is given by

$$T_{\rm m} = \gamma\, E = \frac{4\, M_1\, M_2}{(M_1 + M_2)^2}\, E \qquad (3.3)$$

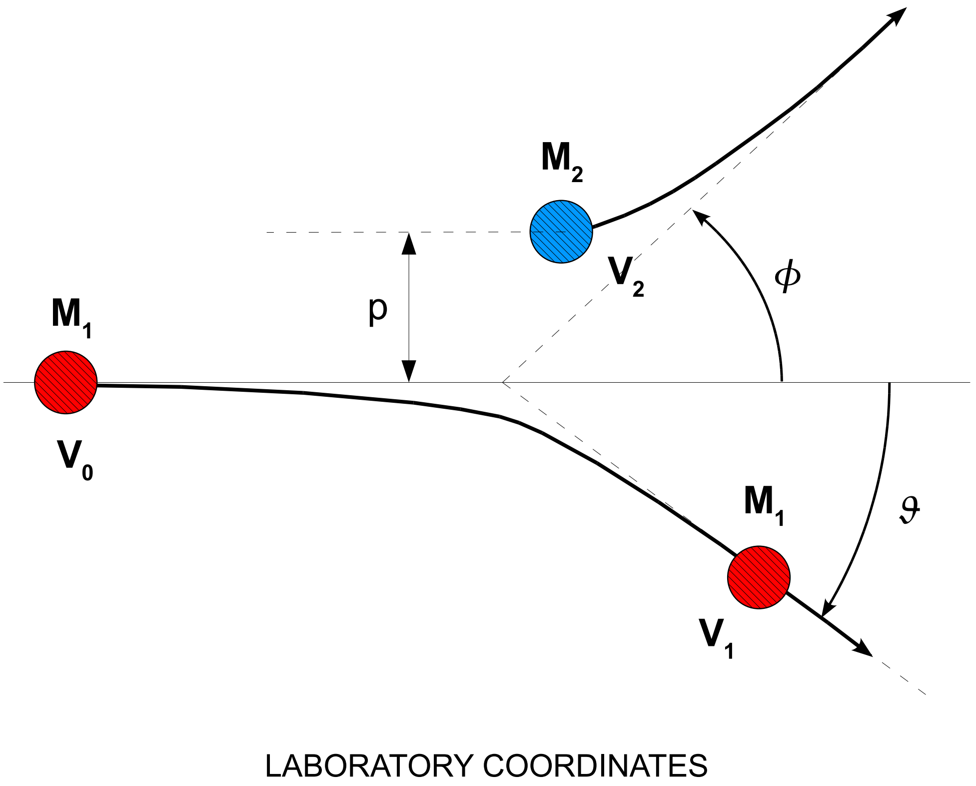

Figure 3.1 — Scattering geometry for an elastic collision of particle 1 (mass M_1, initial velocity v_0, impact parameter p), on particle 2 (mass M_2, initial velocity zero). After the impact, the projectile particle 1 is deflected by the angle ϑ and continues its trajectory with velocity v_1. The target particle 2 recoils at an angle ϕ with velocity v_2.

An important quantity to consider is the *nuclear stopping cross section* $S_\mathrm{n}(E)$, which is related to the average energy loss per unit path length of a particle travelling through a material of atomic number density N (Lindhard et al. 1963)

$$\frac{\mathrm{d}E}{\mathrm{d}R} = N\, S_\mathrm{n}(E) = N \int \mathrm{d}\sigma(E,T) \cdot T \tag{3.4}$$

where $\sigma(E,T)$ is the energy transfer cross section (see Appendix A for details). $S_\mathrm{n}(E)$ has the dimensions of (energy $\times$ area $\times$ atom^{-1}) and in fact represents the average energy transferred per atom in elastic collisions when summed over all impact parameters.

The nuclear stopping cross section can be expressed in terms of the Lindhard's reduced energy ε and the dimensionless *reduced* nuclear stopping cross section $s_\mathrm{n}(\varepsilon)$ (Lindhard et al. 1968, see Eq. 3.34 and 3.35). For this latter we adopt the Universal reduced Ziegler - Biersack - Littmark (ZBL) nuclear stopping cross section s_n^U (Ziegler et al. 1985), which is an analytical approximation to a numerical solution that reproduces well the experimental data. The ZBL reduced nuclear stopping cross section has the form

$$s_{\mathrm{n}}^{\mathrm{U}}(\varepsilon) = \begin{cases} \dfrac{0.5 \ln(1+1.1383\,\varepsilon)}{\varepsilon + 0.01321\,\varepsilon^{0.21226} + 0.19593\,\varepsilon^{0.5}} & \varepsilon \leq 30 \\ \dfrac{\ln \varepsilon}{2\varepsilon} & \varepsilon > 30 \end{cases} \tag{3.5}$$

and the nuclear stopping cross section $S_{\mathrm{n}}(E)$ can be written as

$$S_{\mathrm{n}}(E) = 4\,\pi\,a_{\mathrm{U}}\,Z_1\,Z_2\,e^2\,\frac{M_1}{M_1+M_2}\,s_{\mathrm{n}}^{\mathrm{U}}(\varepsilon) \tag{3.6}$$

with the screening length a_{U} from Eq. 3.2.

3.2.2 Nuclear interaction above threshold

For this study we are interested in *destructive* collisions, i.e., collisions for which the average transferred energy T exceeds the minimum energy T_0 required to remove a carbon atom from the PAH. The theory discussed in §3.1 does not treat this situation and considers the specific case where $T_0 = 0$ (no threshold). To include the treatment of collisions *above* threshold ($T_0 > 0$) we developped the appropriate expressions for the relevant quantities described in the previous sections.

The definition of the nuclear stopping cross section S_{n}(E) can be written in a more general way as

$$S_{\mathrm{n}}(E) = \int_{T_0}^{T_{\mathrm{m}}} \mathrm{d}\sigma(E,T)\cdot T \tag{3.7}$$

where $T_0 \geq 0$. The *total* energy transfer cross section per carbon atom σ(E) is defined by

$$\sigma(E) = \int_{T_0}^{T_{\mathrm{m}}} \mathrm{d}\sigma(E,T) \tag{3.8}$$

In this case the threshold T_0 must be strictly positive, otherwise σ would diverge (this can be verified by substituting the expression for dσ from Eq. 3.31 and evaluating the integral). Finally, the *average* energy transferred in a binary collision is given by the ratio between S_{n} and σ

$$< T(E) >= \frac{S_{\mathrm{n}}(E)}{\sigma(E)} \tag{3.9}$$

The condition $\gamma E = T_{\mathrm{m}} > T_0 = \gamma\,E_{0\mathrm{n}}$ then imposes, for the kinetic energy of the incoming ion, the condition that $E > E_{0\mathrm{n}} = T_0/\gamma$. In Table 3.2 we report the critical energies $E_{0\mathrm{n}}$ for H, He and C ions corresponding to different values of the threshold energy T_0.

Table 3.2 — Threshold transferred energy T_0 and corresponding critical kinetic energy $E_{0\mathrm{n}}$ for H, He and C ions impacting on a carbon atom. Both T_0 and $E_{0\mathrm{n}}$ are in eV.

T_0	$E_{0\mathrm{n}}$(H)	$E_{0\mathrm{n}}$(He)	$E_{0\mathrm{n}}$(C)
4.5	15.8	6.0	4.5
7.5	26.4	10.	7.5
10.	35.2	13.	10.
12.	42.3	16.	12.
15.	52.8	20.	15.

Using dσ from Eq. 3.31 and evaluating the above integrals we obtain

$$S_\mathrm{n}(E) = \frac{C_m\,E^{-m}}{1-m}\,[T_\mathrm{m}^{1-m} - T_0^{1-m}] \tag{3.10}$$

$$\sigma(E) = \frac{C_m\,E^{-m}}{m}\,[T_0^{-m} - T_\mathrm{m}^{-m}] \tag{3.11}$$

$$< T(E) >= \frac{m}{1-m}\,\frac{T_\mathrm{m}^{1-m} - T_0^{1-m}}{T_0^{-m} - T_\mathrm{m}^{-m}} \tag{3.12}$$

To calculate the quantity $m = m(E)$ we use the following expression from Ziegler et al. (1985)

$$m(E) = 1 - \exp\left[-\exp\sum_{i=0}^{5} a_i\left(0.1\ln\left(\frac{\varepsilon(E)}{\varepsilon_1}\right)^i\right)\right] \tag{3.13}$$

with $\varepsilon_1 = 10^{-9}$ and $a_i = $ -2.432, -0.1509, 2.648, -2.742, 1.215, -0.1665.

Combining Eq. 3.33 and Eq. 3.34, after some algebraic manipulation, we can rewrite the above expressions for S_n, σ and $< T >$ in the more convenient form shown below. The full calculation is reported in Appendix A. As explained in §3.1, we adopt for the reduced stopping cross section the ZBL function $s_\mathrm{n}^\mathrm{U}(\varepsilon)$ (Eq. 3.5) with the appropriate screening length a_U.

$$S_\mathrm{n}(E) = 4\pi a Z_1 Z_2\, e^2 \frac{M_1}{M_1+M_2} s_\mathrm{n}^\mathrm{U}(\varepsilon)\left[1 - \left(\frac{E_{0\mathrm{n}}}{E}\right)^{1-m}\right] \tag{3.14}$$

$$\sigma(E) = 4\pi a Z_1 Z_2 e^2 \frac{M_1}{M_1+M_2} s_\mathrm{n}^\mathrm{U}(\varepsilon)\frac{1-m}{m}\frac{1}{\gamma E}\left[\left(\frac{E_{0\mathrm{n}}}{E}\right)^{-m} - 1\right] \tag{3.15}$$

$$< T(E) >= \frac{m}{1-m} \gamma \frac{E^{1-m} - E_{0\mathrm{n}}^{1-m}}{E_{0\mathrm{n}}^{-m} - E_m^{-m}} \tag{3.16}$$

Note that the term outside of the square brackets in Eq. 3.14 and 3.15 is the stopping cross section $S_\mathrm{n}(E)$ when $T_0 = 0$ (no threshold).

The nuclear stopping cross section $S_\mathrm{n}(E)$ (eV Å^2 atom^{-1}), the total energy transfer cross section $\sigma(E)$ (Å^2 atom^{-1}) and the average energy transferred $< T(E) >$ (eV), for H, He and C ions (charge +1) impacting on a carbon atom, calculated from the above expressions assuming a threshold $T_0 = 7.5$ eV, are shown in Fig. 3.2.

The sharp cut on the left-hand side of the curves arises from the fact that we are treating collisions above threshold, and these quantities are defined only for energies of the incident ion greater than the critical value $E_{0\mathrm{n}}$. It can be seen that all quantities increase in absolute value with increasing atomic number and mass of the projectile (Z_1 and M_1). The two vertical lines indicate the minimum and maximum kinetic energy of the projectile considered in our study, corresponding to the PAH velocity in the 50 and 200 km s^{-1} shocks respectively. The values are those calculated in §3.1 and reported in Table 3.1. The figure cleary shows that for hydrogen the critical value $E_{0\mathrm{n}}$ is greater than the lower limit of energy range. This implies that in the lower velocity shocks hydrogen is not energetic enough to cause carbon ejection. The curves for S_n presents a characteristic convex shape with a maximum, illustrating that nuclear energy transfer is important only for projectiles with energy falling in a specific range. In particular, the nuclear stopping goes asymptotically to zero at high energies, with a limiting value depending on projectile and target: in our case, going from H to C impacting on carbon, the curves extend further to the right, in the direction of higher energies. In the high energy regime, the energy transfer is dominated by electronic stopping (Chapter 4 - paper MJT09b).

For a given incident ion energy, the difference between the values of S_n in the threshold and no-threshold cases results from the definition of the nuclear stopping and from the properties of $\mathrm{d}\sigma$. The differential cross section (cf. Eq. 3.31) strongly prefers collisions with low energy transfers ($T \ll T_\mathrm{m}$) and, moreover, decreases in absolute magnitute with increasing E. For each E, S_n is defined as the integral over the transferred energy T, of the product between T and the corresponding cross section $\mathrm{d}\sigma$. Choosing $T_0 > 0$ means excluding from the integral all energy transfers $T < T_0$, for which the cross section has the highest values. The remaining terms have higher values of T but lower values of $\mathrm{d}\sigma$, then the integral gives a result smaller than the no-threshold case, which includes all small energy transfers with their higher cross sections.

The total cross section σ(E) clearly shows that the projectiles can efficiently transfer energy to the target atom only when their kinetic energy lies in the appropriate window. In particular, it can be seen that the average energy transferred $< T >$ increases with E, nevertheless at high energies σ is close to zero (and the collision rate will be small). For a fixed target atom (in our case, carbon), the width of the σ curve, and consequently the width of the energy window, increases with Z and M of the projectile. Heavier ions transfer more energy and in a more efficient way.

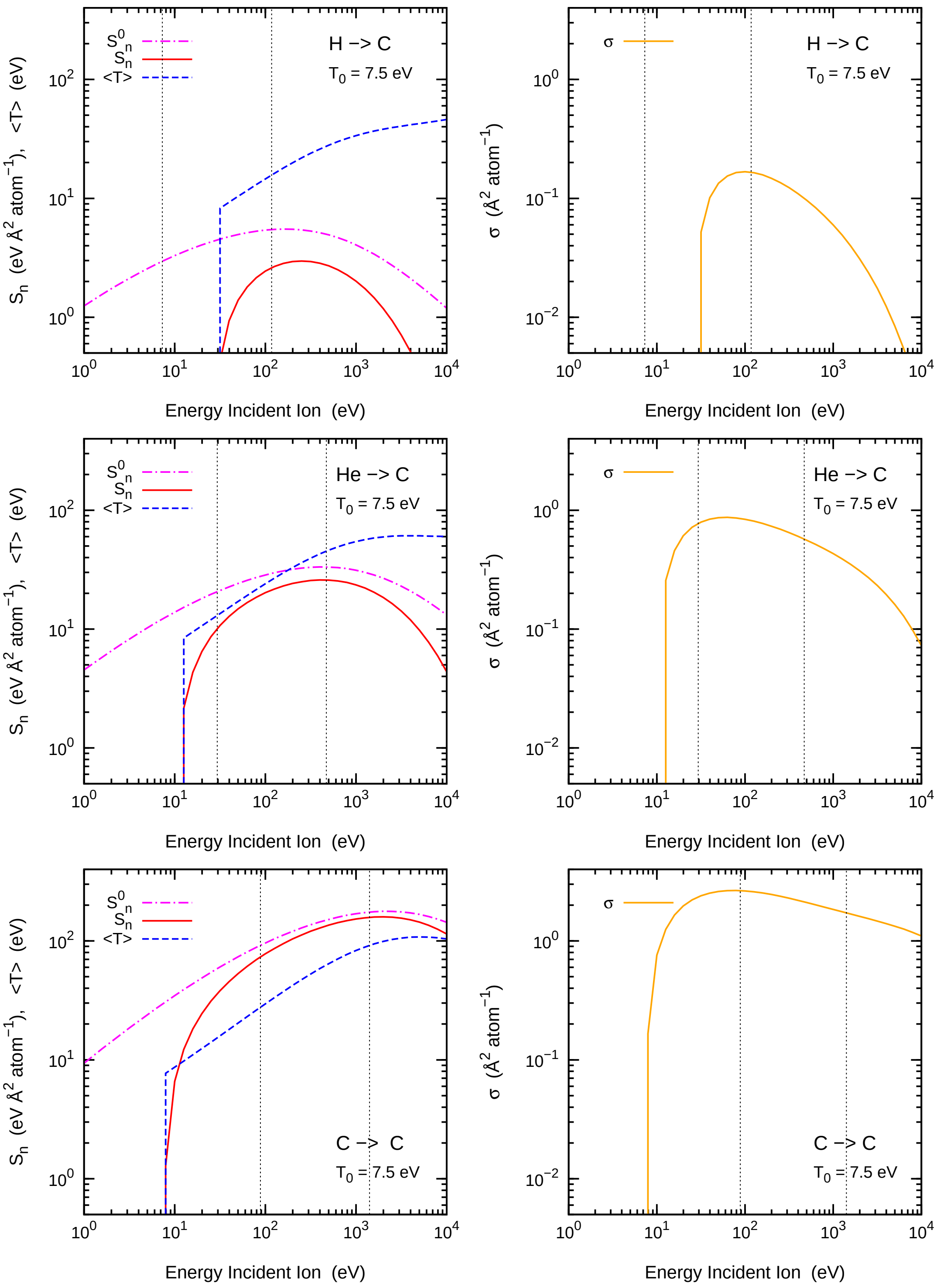

Figure 3.2 — The nuclear stopping cross section $S_n(E)$, the total cross section $\sigma(E)$ and the average energy transferred $< T(E) >$ calculated for H, He and C ions impacting on a carbon atom. The curves are calculated for the threshold energy $T_0 = 7.5$ eV. The nuclear stopping cross section S^0_n corresponding to $T_0 = 0$ (no threshold) is shown for comparison. The two vertical lines indicate the limiting energies for the incident ion. These are defined as the kinetic energies of the projectile when its velocity v_p equals $\frac{3}{4}$ $(v_{S1,S2})$, where $v_{S1} = 50$ km s^{-1} and $v_{S2} = 200$ km s^{-1} are the lowest and highest shock velocities considered in this study.

3.2.2.1 The threshold energy T_0

The threshold energy, T_0, is the minimum energy that must be transferred via nuclear excitation to a carbon atom, in order to eject that same atom from the PAH molecule. The choice for T_0 for a PAH is unfortunately not well-constrained. There are no experimental determinations, and the theoretical evaluation is uncertain. The analog of T_0 in a solid is the displacement energy T_d, defined as the minimum energy that one atom in the lattice must receive in order to be moved more than one atomic spacing away from its initial position, to avoid the immediate hop back into the original site. For graphite, the data on the threshold energy for atomic displacement differ significantly, varying from $\sim$30 eV (Montet 1967; Montet & Myers 1971) to 12 eV (Nakai et al. 1991) largely depending on direction (eg., within or perpendicular to the basal plane). For a PAH, the lower value (corresponding to the perpendicular direction) seems then more appropriate. For amorphous carbon, Cosslett (1978) has found a low value of 5 eV. Electron microscopy studies by Banhart (1997) on graphitic nanostructures irradiated with electrons of different energies, indicate that a value of $T_d \sim$ 15-20 eV seems appropriate for the perpendicular direction. The in-plane value, however, could be much higher, presumably above 30 eV.

Instead of graphite, fullerenes and carbon nanotubes may be a better analog for PAH molecules. For fullerene, T_d has been found between 7.6 and 15.7 eV (Füller & Banhart 1996). Single walled nanotubes consist of a cylindrically curved graphene layer. Unfortunately, also in this case the threshold for atomic displacement is not precisely determined. However it is expected to be lower than in a multi-layered tube, for which a value of $T_\mathrm{d} \sim$ 15-20 eV has been found (Banhart 1997) close to the value of graphite. We note that 4.5 and 7.5 eV are close to the energies of the single and double C-bond respectively.

Because we cannot provide a well-defined T_0, we decided to explore a range of values, to study the impact of the threshold energy on the PAH processing. For our standard case, we adopt 7.5 eV that we consider a reasonable value consistent with all the experimental data. However, we have varied T_0 from 4.5 to 15 eV (cf. Table 3.2).

Fig. 3.3 shows the comparison between S_n, σ and $< T >$ calculated for He on C assuming T_0 = 4.5, 7.5 and 15 eV. Coherently with their definition, S_n and σ increase with decreasing threshold, because more collisions are effective and the cross section increases with decreasing energy. Of course, the average energy transferred will decrease when the threshold energy is decreased.

In § 3.4.1 we discuss the effect of the choice of different values for T_0 on the PAH survival in shocks.

3.3 PAHs in shocks

When grains and PAHs enter a shock they become charged and then gyrate around the compressed magnetic field lines. This leads to relative gas-particle velocities and hence to collisions with the gas (and other grains/PAHs). Collisions with the gas result in drag forces and therefore a decrease in the relative gas-particle velocity. However, these same collisions with the gas can also lead to the removal of atoms from the particle if the relative velocites are larger than the given threshold for an erosional process.

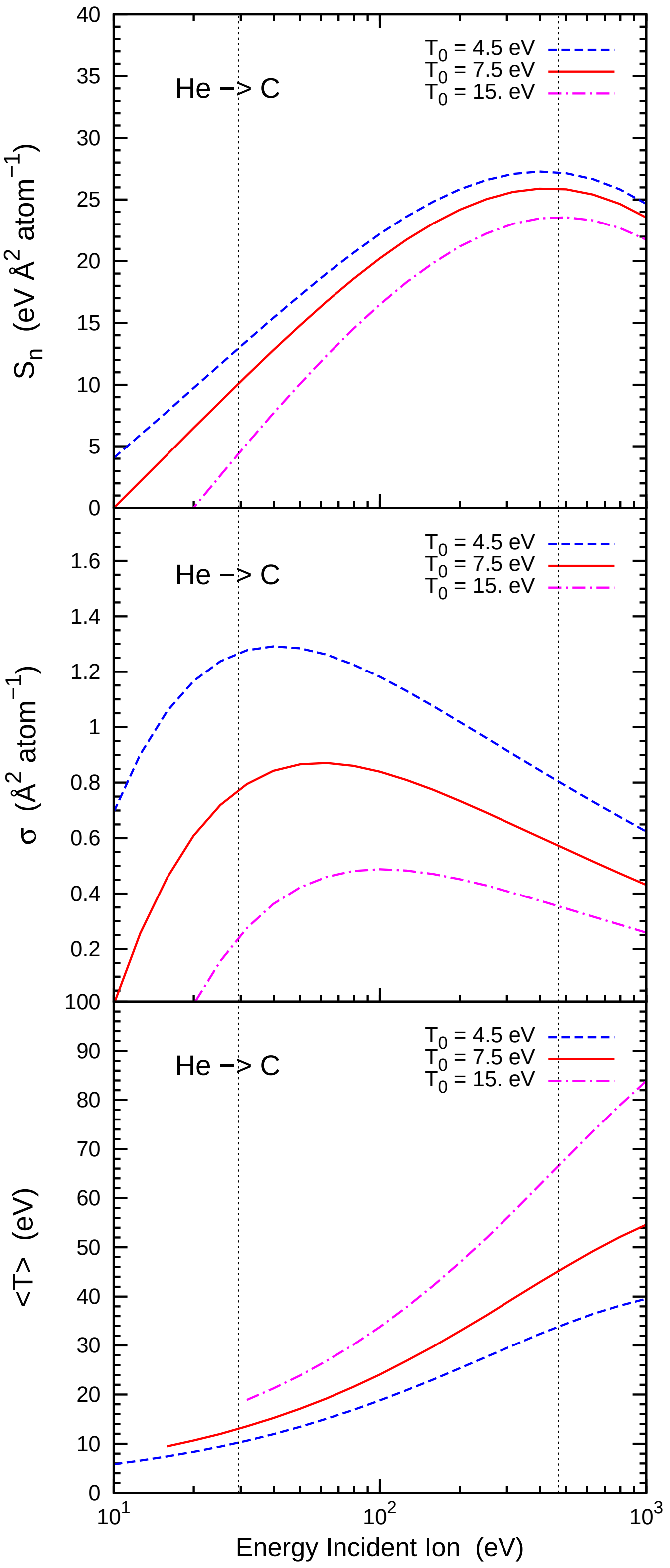

Figure 3.3 — The nuclear stopping cross section $S_n(E)$, the cross section $\sigma(E)$ and the average energy transferred $< T(E) >$ calculated for He ions impacting on a carbon atom, calculated for three values of the threshold energy T_0: 4.5, 7.5 and 15 eV. The two vertical lines delimit the energy range of interest (cf. Fig. 3.2).

The removal of carbon atoms from the PAH due to ion collisions, where the impact velocity is determined by the relative motion between the two partners, is the analog of the inertial sputtering of dust particles due to ion-grain collisions. In the following we will then refer to it using the term *inertial*, and the same will apply for all the related quantities.

In determining the processing of PAHs in shock waves, as with all grain processing, it is the relative gas-grain velocity profile through the shock that determines the level of processing. In calculating the relative ion-PAH velocity through the shock we use the same approach as in our previous work (Jones et al. 1994, 1996), which is based on the methods described in McKee et al. (1987). The PAH velocity is calculated using a 3D particle of the same mass as the 50 carbon atom PAH under consideration. The PAH velocity depends then on the PAH mass and average geometric cross section. For a PAH with N_C carbon atoms, these are given by $N_C m_C$ and $0.5\pi a_{\rm PAH}^2$ with $a_{\rm PAH}$ given by $0.9 N_C$ Å, appropriate for a compact PAH (Omont 1986) and the factor 1/2 in the cross section takes the averaging over impact angle into account. The PAH and grain cross sections are very close (to within 11% for $N_C = 50$), thus we are justified in using the same numerical approach even though we are using a 3D grain to calculate the velocity profile of a 2D PAH through the shock.

The PAHs are injected into the shock with 3/4 of the shock speed, as are all grains, and their trajectories are then calculated self-consistently with their coupling to the gas, until the relative gas-PAH veocity becomes zero. The velocity calculation includes the effects of the direct drag with the gas due to atom and ion collisions and the drag due to the ion-charged PAH interaction in the post-shock plasma. We find that for some shock velocities, in our case for $v_S = 75$ and $100\,{\rm km\,s^{-1}}$, the PAHs (and grains) experience betatron acceleration in the post-shock gas. All the relevant expressions and assumptions for the calculation of the grain velocity, betatron acceleration and grain charge are fully described in McKee et al. (1987). Thus, in calculating the post-shock PAH velocity profiles, we follow exactly the same methods as used in our previous work. The structure of the $125\,{\rm km\,s^{-1}}$ shock is shown in Fig. 3.4 as a function of the column density N_H. Fig. 3.5 shows the velocity profile for a 50 carbon atom PAH in the same shock, together with the effective charge of the molecule, used to calculate the velocity profile itself. The 50 C-atoms PAH is positively charged (charge between +2 and +3) during the whole slowing process, and approaches neutrality at the end of the shock. We do not consider the destructive effect of charge exchange (charge accumulation on the PAH due to ion impacts with consequent destabilization of the molecule and possible breaking apart) because the PAH charge is an average value resulting from a balancing process, thus there is no charging up of the molecule.

3.3.1 Ion collisions: nuclear interaction

Knowing the velocity profile of the PAH, we can then calculate the inertial collision rate PAH-ions $R_{\rm n,I}$ ($\rm s^{-1}$) through the shock. This is given by the following equation

$$R_{\rm n,I}(N_H) = 0.5\ \chi_i\ n_H\ v_{\rm PAH}\ \sigma\ N_C\ F_C \tag{3.17}$$

where $n_H(N_H)$ is the hydrogen particle density along the shock, $\rm v_{PAH}(N_H)$ the PAH-ion relative velocity along the shock and χ_i is the relative abundance of the projectile

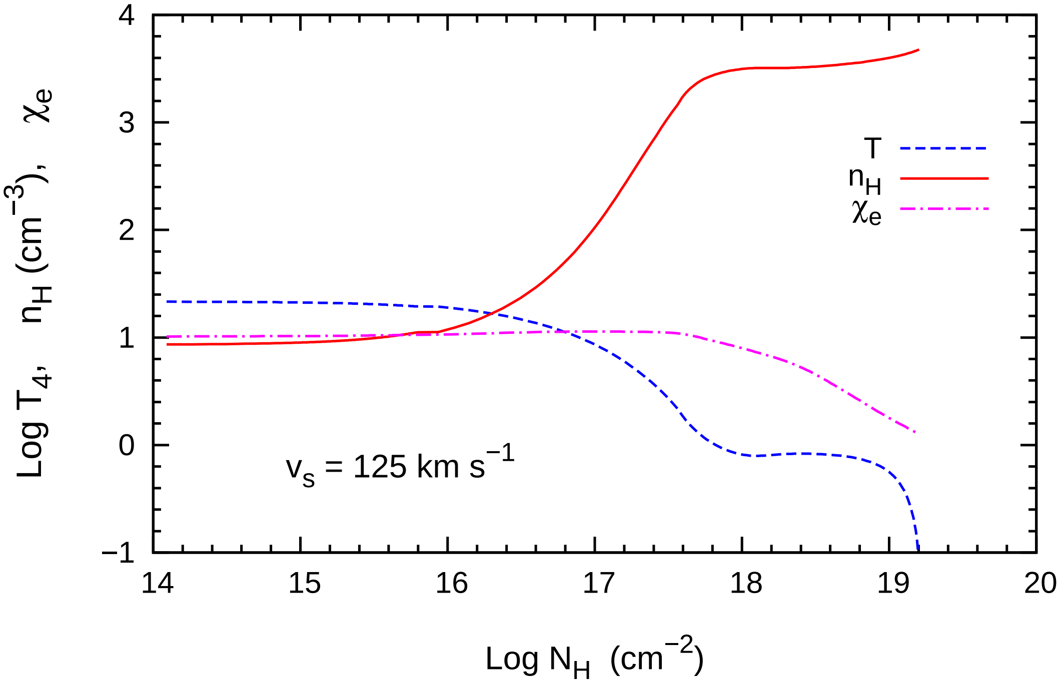

Figure 3.4 — The structure of the 125 km s^{-1} shock: temperature $T_4 = T/10^4$ K, hydrogen density n_H and electron relative abundance χ_e. All quantities are plotted as a function of the shocked column density $N_H = n_0 \, v_S \, t$, where the preshock density n_0 = 0.25 cm^{-3}. To convert column density to time, use the following relation: log t(yr) = log N_H(cm^{-2}) - 13.9 (Jones et al. 1996).

ion with respect to hydrogen. We adopt the gas phase abundances $\chi_H : \chi_{He} : \chi_C$ = 1 : 10^{-1} : 10^{-4}, where the carbon abundance is between the values (0.5 - 1)$\times 10^{-4}$ and 1.4$\times 10^{-4}$ from Sofia (2009) and Cardelli et al. (1996) respectively.

The term $\sigma(N_H)$ is the cross section averaged over those collisions that transfer an energy larger than the threshold energy T_0 per C-atom and this cross section should therefore be multiplied by the number of carbon atoms in the PAH, N_C. The factor 0.5 takes the angle averaged orientation into account (see appendix C).

Because both collision partners are charged, the effect of the Coulombian potential must be included as well. Depending on whether the interaction is attractive or repulsive, the energy transfer cross section will be increased or reduced by the coulombian factor F_C given by

$$F_C = 1 \, - \, \frac{2 \, Z_{\rm ion} \, Z_{\rm PAH} \, e^2}{4 \, \pi \, \varepsilon_0 \, a_{\rm PAH} \, M_1 \, m_H \, v_{\rm PAH}^2}. \tag{3.18}$$

where Z_{ion} = +1 and M_1 are the charge and the atomic mass (in amu) of the incident ion, Z_{PAH} is the charge of the PAHs along the shock, a_{PAH} is the PAH radius and v_{PAH} the PAH-ion relative velocity. The constant e is the electron charge, ε_0 is the permittivity of the free space and m_H the mass of the proton. The total number of destructive collisions is then given by the integral of the collision rate (Eq. 3.17) behind the shock,

$$N_t \; = \int R_{n,I} \, (N_H) \; dt \tag{3.19}$$

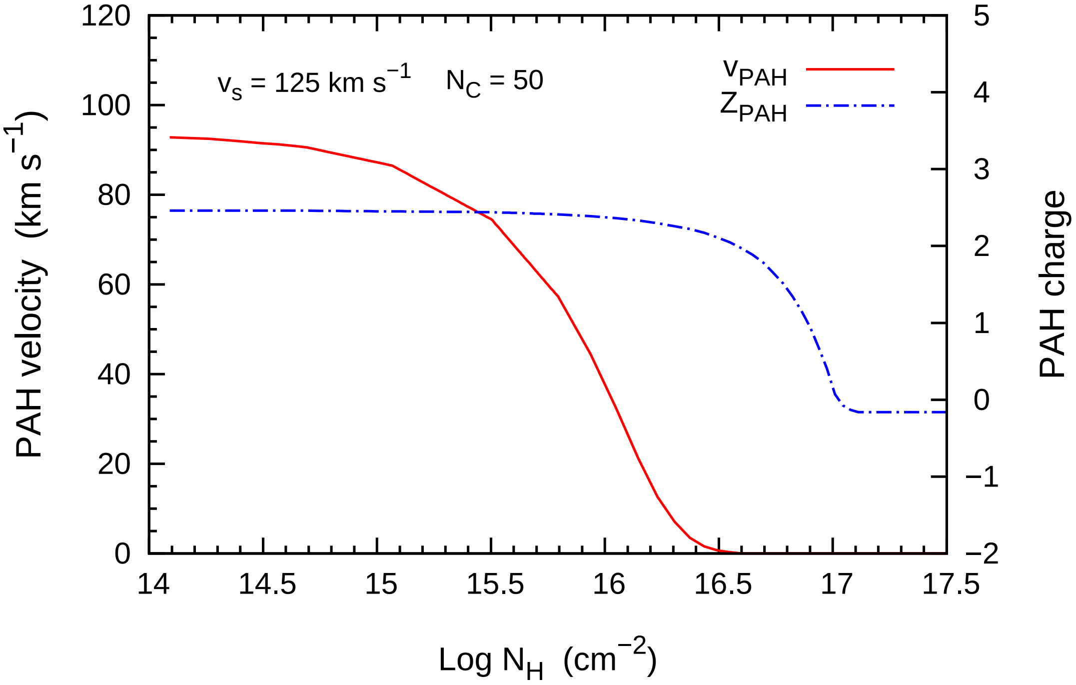

Figure 3.5 — The velocity profile of a 50 C-atom PAH in a shock with velocity v_S = 125 km s^{-1}. The PAH velocity v_{PAH}, plotted as a function of the shocked column density N_H, represents the relative velocity between the molecule and the ions present in the shock. Overlaid is the PAH charge Z_{PAH} along the shock, calculated using the theory described in McKee et al. (1987).

where it should be understood that the postshock column density N_H and the time, t, are related through $N_H = n_0 v_S t$. With the proper cross section, this number N_t, is then equal to the number of carbon atoms lost by a PAH in collisions with H, He, or C.

Figure 3.6 illustrates the destructive collisions for a 50 C-atom PAH behind a 125 km s^{-1} shock assuming $T_0 = 7.5$eV. These results are plotted in such a way that equal areas under the curve indicate equal contributions to the total number of destructive collisions. $R_{n,I}$ drops precipitously because of the drop in relative PAH-gas velocity. Because heavier projectiles are more energetic in inertial collisions, this drop off shifts to higher column densities for heavier species. The results show that He is much more effective in destroying PAHs than H because of the increased energy transferred for heavier collision partners (cf. Figure 3.2). The low abundance of C depresses its importance in inertial sputtering.

The number of carbon atoms in a PAH is now given by

$$N_C(t) = N_C(0) \exp\left[-N_t/N_C\right] \tag{3.20}$$

and the fraction of carbon atoms ejected from this PAH is

$$F_L = \left(1 - \exp\left[-N_t/N_C\right]\right) \tag{3.21}$$

where N_t is now evaluated throughout the shock.

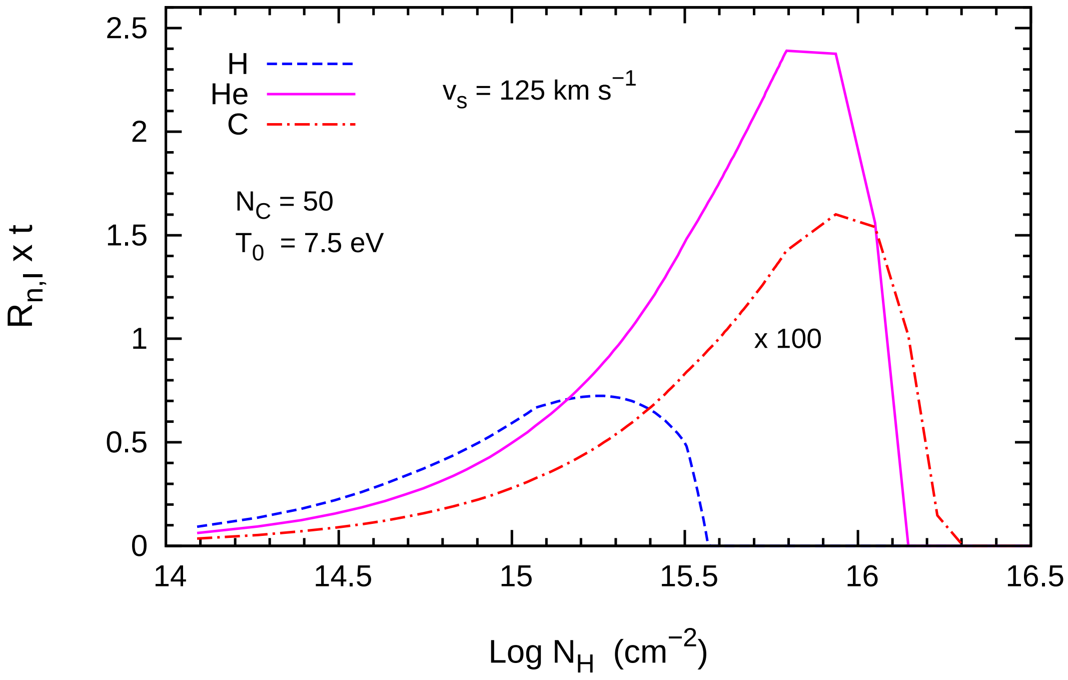

Figure 3.6 — The number of collisions $N_t = R_{n,I} \times t$ of a 50 C-atom PAH with H, He and C ions in a 125 km s^{-1} shock, as a function of the shocked column density, N_H. The cross section has been evaluated for a threshold energy, T_0, of 7.5 eV. The carbon curve has been multiplyied by a factor 100 for comparison.

In the shocked gas, the velocity of the ions is not only determined by the relative motion with respect to the PAH (inertial case), but also by the temperature of the shocked gas. In principle, the inertial and thermal velocity should be added vectorally and averaged over the angle between the inertial motion and the (random) thermal motion as well as over the thermal velocity distribution. However, that becomes a quite cumbersome calculation and, hence, we will follow calculations for sputtering of dust grains in interstellar shocks (cf. Jones et al. 1994) and evaluate these two processes (inertial and thermal sputtering) independently. Studies have shown that this reproduces more extensive calculations satisfactorily (Guillet et al. 2007). The thermal destruction rate is given by

$$R_{n,T}(N_H) = N_C \, 0.5 \, \chi_i \, n_H \int_{v_0}^{\infty} F_C(v) \, v \, \sigma(v) \, f(v,T) \, dv \tag{3.22}$$

with $f\,(v,T)$ the Maxwellian velocity distribution. The temperature has to be evaluated along the shock profile (cf. Figure 3.4) and care should be taken to only include velocities corresponding to energies larger than the threshold energy, T_0 (e.g., with $E > E_{0n}$; cf., Table 3.2). The fraction of C-atoms ejected by this process can be evaluated analogously to Eq. 3.21.

3.3.2 Ion collisions: electronic interaction

As reported in the introduction of the paper, the collision between PAH and ions triggers two simultaneous process, which can be treated separately: the nuclear stopping (*elastic energy loss*) and the electronic stopping (*inelastic energy loss*). The first has been extensively discussed in the previous sections, while for the full treatment of the electronic interaction we refer the reader to Chapter 4 - paper MJT09b. For the sake of clarity, we report here the essential concepts and the principal equations which will be used in the following.

The energy transferred to the electrons is spread out over the entire molecule, leaving the PAH in an excited state. De-excitation occurs through two pricipal decay channels: emission of infrared photons and dissociation and loss of a C_2 fragment. This latter is the process we are interested in, because it leads to the PAH fragmentation. The dissociation probability p (see §4.1 in Chapter 4 - paper MJT09b) depends on the binding energy of the fragment E_0, on the PAH size, N_C, and on the energy transferred, which in turns depends on the initial energy (velocity) of the projectile.

For a fixed value of the transferred energy, the dissociation probability decreases for increasing E_0 and N_C because either more energy is required in the bond that has to be broken or because the energy is spread over more vibrational modes and hence the internal excitation temperature is lower. On the other hand, the more energy that is deposited in the PAH, the higher is the dissociation probability. The energy transferred via electronic excitation increases with the energy of the projectile up to a maximum value, corresponding to an incident energy of 100 keV for H (and higher for more massive particles), and decreases for higher energies. The deposited energy also increases with the path-length through the molecule and will be higher for larger PAHs impacted at grazing collision angles. For the shocks considered in this study, the energy transferred increases with incident energy (velocity) and hence the dissociation probability increases as well.

As for the nuclear stopping, also for the electronic interaction we have to consider the effect of both inertial and thermal velocities. The *inertial* collision rate is given by

$$R_{\mathrm{e,I}}(N_\mathrm{H}) = v_\mathrm{PAH}\, \chi_i\, n_\mathrm{H}\, F_\mathrm{C} \int_{\vartheta=0}^{\pi/2} \sigma_\mathrm{g}(\vartheta)\, p(v_\mathrm{PAH}, \vartheta)\, \sin\vartheta\, \mathrm{d}\vartheta \tag{3.23}$$

where ϑ is the angle between the axis normal to the PAH plane and the direction of the incoming ion. The term σ_g is the geometrical cross section seen by an incident particle with direction defined by ϑ. The PAH is modelled as a thick disk with radius a_PAH and thickness d, then the cross section is given by

$$\sigma_\mathrm{g} = \pi\, a_\mathrm{PAH}^2 \cos\vartheta \,+\, 2\, a_\mathrm{PAH}\, d\, \sin\vartheta \tag{3.24}$$

which reduces to $\sigma_\mathrm{g} = \pi a_\mathrm{PAH}^2$ for $\vartheta = 0$ (face-on impact) and to $\sigma_\mathrm{g} = 2 a_\mathrm{PAH} d$ for $\vartheta = \pi/2$ (edge-on impact). The term $p(v_\mathrm{PAH}, \vartheta)$ represents the total probability for dissociation upon collision via electronic excitation, for a particle with relative velocity v_PAH and incoming direction ϑ (see §4.1 in Chapter 4 - paper MJT09b).

For the *thermal* collision rate we have

$$R_{\mathrm{e,T}}(N_\mathrm{H}) = \int_{v_0}^{\infty} R_{\mathrm{e,I}}(v)\, f(v, T)\, \mathrm{d}v \tag{3.25}$$

where the temperature $T = T(N_H)$ is evaluated along the shock. The lower integration limit v_0 is the ion velocity corresponding to E_0. The number of carbon atoms lost can be evaluated analogously to the nuclear interaction but care should be taken to include the loss of 2 C-atoms per collision.

There is a clear distinction between the nuclear and electronic interactions. In nuclear interactions, a C-atom is ejected because a direct collision with the impacting ion transfers enough energy and momentum to kick out the impactee instantaneously. In electronic interaction, the impacting ion excites the electrons of the PAH. Internal conversion transfers this energy to the vibrational motions of the atoms of the PAH. Rapid intramolecular vibrational relaxation leads then to a thermalization of this excess energy among all the vibrational modes and this can ultimately lead to dissociation (or relaxation through IR emission). The threshold energy in the nuclear process, T_0, differs therefore from the electronic dissociation energy, E_0. The latter really is a parameter describing the dissociation rate of a highly excited PAH molecules using an Arrhenius law and this does not necessarily reflect the actual binding energy of the fragment to the PAH species (cf. Tielens 2005). Following Chapter 4 - paper MJT09b, we will adopt the canonical value of 4.6 eV for E_0. However, this energy is very uncertain and we will evaluate the effects of reducing and increasing this parameter to a value of 3.65 and 5.6 eV respectively (Chapter 4 - paper MJT09b).

3.3.3 Electron collisions

For the full treatment of the PAH collisions with *electrons*, we refer again to Chapter 4 - paper MJT09b, providing here a short summary of the basic concepts and equations.

Because of their small mass, the thermal velocity of the electrons always exceeds the inertial velocity of the PAH. Hence, only the thermal destruction needs to be evaluated. We follow the same formalism used for the electronic interaction in ion-PAH collisions. The energy dumped into the molecule during collisions with electrons is spread over and determines (with E_0 and N_C) the value of the dissociation probability. The electron energy loss rises sharply with the electron energy, reaching its maximum for incident energy around 100 eV. This energy range falls exactly in the interval relevant for our shocks, implying that the electrons optimally transfer their energy.

The thermal *electron* collision rate can be written as

$$R_{\mathrm{elec,T}}(N_H) = \int_{v_{0,\mathrm{elec}}}^{\infty} \Sigma(v)\, f(v,T)\, \mathrm{d}v \tag{3.26}$$

$$\Sigma(v) = v\, \chi_e\, n_H\, F_{Ce} \int_{\vartheta=0}^{\pi/2} \sigma_g(\vartheta)\, p(v,\vartheta)\, sin\vartheta\, \mathrm{d}\vartheta \tag{3.27}$$

where $v_{0,\mathrm{elec}}$ is the electron velocity corresponding to E_0 and χ_e is the electron relative abundance along the shock. The electron coulombian factor F_{Ce} is always equal to 1 (within less than 1%) because electrons have low mass and high velocities with respect to ions. The temperature T evaluated along the shock is the same as for the ions, but electrons will reach much larger velocities. From Eq. 3.26 and 3.27 we expect then to find a significantly higher collision rate with respect to the ion case. The fraction of C-atoms lost by electron collisions can be evaluated analogously to that for ions (cf. Eq. 3.21).

3.4 Results

Fig. 3.7 and 3.8 show the fraction of carbon atoms ejected from a 50 and 200 C-atoms PAH due to collisions with electrons and H, He and C, assuming the nuclear threshold energy T_0 = 7.5 eV and the fragment binding energy E_0 = 4.58 eV. The results concerning nuclear, electronic and electron interaction are discussed in the following sections.

3.4.1 PAH destruction via nuclear interactions

For the *inertial* nuclear interactions, the fraction of ejected carbon atoms F_L depends on both σ and χ. Hydrogen has the highest abundance (χ_H = 1) but the lowest absolute value for the cross section (see Fig. 3.2). In addition, σ is significantly different from zero only for the highest shock velocities. This results in contribution to atom ejection which is only relevant for v_S above 150 km s^{-1}. Helium is ten times less abundant than hydrogen (χ_{He} = 0.1), but this is compensated for by a higher cross section for all shock velocities. In particular, the C-atom ejection curve shows a peak between 50 and 125 km/s due to betatron acceleration: because of the higher velocity, the collision rate increases (cf. Eq. 3.17) and then the PAHs experience more destructive collisions. After the peak, as expected the curve increases with the shock velocity. In the case of carbon, the increased cross section is not sufficient to compensate for the low abundance (χ_C = 10^{-4}), resulting in a totally negligible contribution to PAH destruction. For all shock velocities, the fraction of C-atoms removed because of inertial nuclear interaction does not exceed the value of 20%.

Concerning the *thermal* nuclear interaction, carbon does not contribute to PAH destruction because of its very low abundance compared to H and He, as for the inertial case. For hydrogen and helium, as expected for low velocity shocks, the temperature is generally not sufficiently high to provide the ions with the energy required to remove C-atoms. Nevertheless, the ions in the high velocity tail of the Maxwellian distribution can be energetic enough to cause C-atom ejection, as can be seen for He at 100 km s^{-1}. This is less evident for hydrogen. In this case the critical energy E_{0n} is higher than for helium and carbon. The corresponding critical velocity v_0 will be higher as well. For the lower velocity shocks, the peak of the hydrogen maxwellian function $f(v,T)$ is well below v_0, as a consequence the integrand of Eq. 3.22 is close to zero over the integration range, and the same will be true for the collision rate. At the highest shock velocities the curves show a similar trend, with a steep rise beyond 125 km s^{-1} leading to complete PAH destruction, i.e. removal of ALL carbon atoms, for shock velocities above 150 km s^{-1}. At around 135 km s^{-1} the hydrogen contribution becomes larger than that for helium. At these high velocities the He and H cross sections reach approximately their maximum values (cf. Fig. 3.2) and the abundance of H is a factor of 10 higher than for He.

As discussed in §3.2.1, the threshold energy for carbon ejection via nuclear excitation is not well-constrained. We consider T_0 = 7.5 eV to be a reasonable value, but experimental determinations are necessary. Fig. 3.9 illustrates how the fraction of ejected C-atoms changes as a function of the adopted value for the threshold energy. The curves show the cumulative effect of H, He and C, calculated for T_0 = 4.5, 7.5 and 15 eV in the inertial and thermal case. Both in the inertial and thermal case, the curves corresponding to the various thresholds follow the same trend, and for each value considered of T_0 the inertial destruction dominates at low velocity and the thermal destruction at high velocities. As expected the fraction of ejected C-atoms increases for decreasing T_0 in the inertial case, while the curves shift to the left in the thermal case, implying that the PAHs will start to experience significant damage at lower shock velocities. Our results also show that, even assuming a high threshold energy, PAHs experience a substantial loss of carbon atoms, which is complete for velocities above 175 km s^{-1} is all cases.

Finally, we investigated how the nuclear destruction process depends on the size of the PAH. Fig. 3.8 shows the fraction of ejected carbon atoms from a big PAH with N_C = 200. The destruction of a 200 C-atom PAH follows the same trends with shock velocity as for the 50 C-atom case and the curves are almost identical. This is due to the fact that the velocity and temperature profiles for the 50 and 200 C-atoms molecules are quite similar, and the collision rate and F_L scale linearly with N_C in both the inertial and thermal case (see Eq. 3.17, 3.21 and 3.22).

3.4.2 PAH destruction via electronic interaction by ion collisions

Inspection of Fig. 3.7 and 3.8 reveals that electronic excitation by impacting ions plays only a marginal role in the destruction process. For both PAH sizes, carbon is unimportant because of its very low abundance. In the inertial case H does not contribute and He contributes marginally at the highest shock velocities, while in the thermal case they lead to a substantial atomic loss only for N_C = 50 in the highest velocity shock (200 km s^{-1}). For a 50 C-atom PAH, the low destruction rate due to electronic excitation reflects the small cross section for this process for these low velocity shocks. The inertial velocities of the PAH lead to electronic excitation only being important for the highest shock velocities where the impacting ions have a high enough temperature to excite the PAHs sufficiently (cf. Chapter 4 - paper MJT09b). The larger number of modes available in 200 C-atom PAHs, makes the electronic excitation of such PAHs completely negligible over the full velocity range of the shocks considered here.

3.4.3 PAH destruction due to electron collisions

The fractional carbon atom loss F_L due to collisions with thermal electrons is also shown in Fig. 3.7 and 3.8. For N_C = 50, the number of ejected carbon atoms rises sharply above 75 km s^{-1}, leading to total destruction above 100 km s^{-1}. For N_C = 200, the damage is negligible up to 100 km s^{-1}, increases significantly beyond that and leads to complete destruction above 150 km s^{-1}.

The energy transferred by impacting electrons rises sharply for velocities in excess of 2×10^3 km s^{-1}. This results in a dissociation probability p shaped as a step function: for $v \gtrsim 2\times10^3$ km s^{-1} p jumps from values close to zero up to 1. This limiting velocity applies to a 50 C-atoms PAH; for N_C = 200 the value is higher (4×10^3 km s^{-1}), due to the fact that for a bigger PAH more energy has to be transferred for dissociation. These velocities correspond to electron temperatures of 10^5 K and 3×10^5 K, which are reached for shock velocities of approximately 100 and 150 km s^{-1}, respectively.

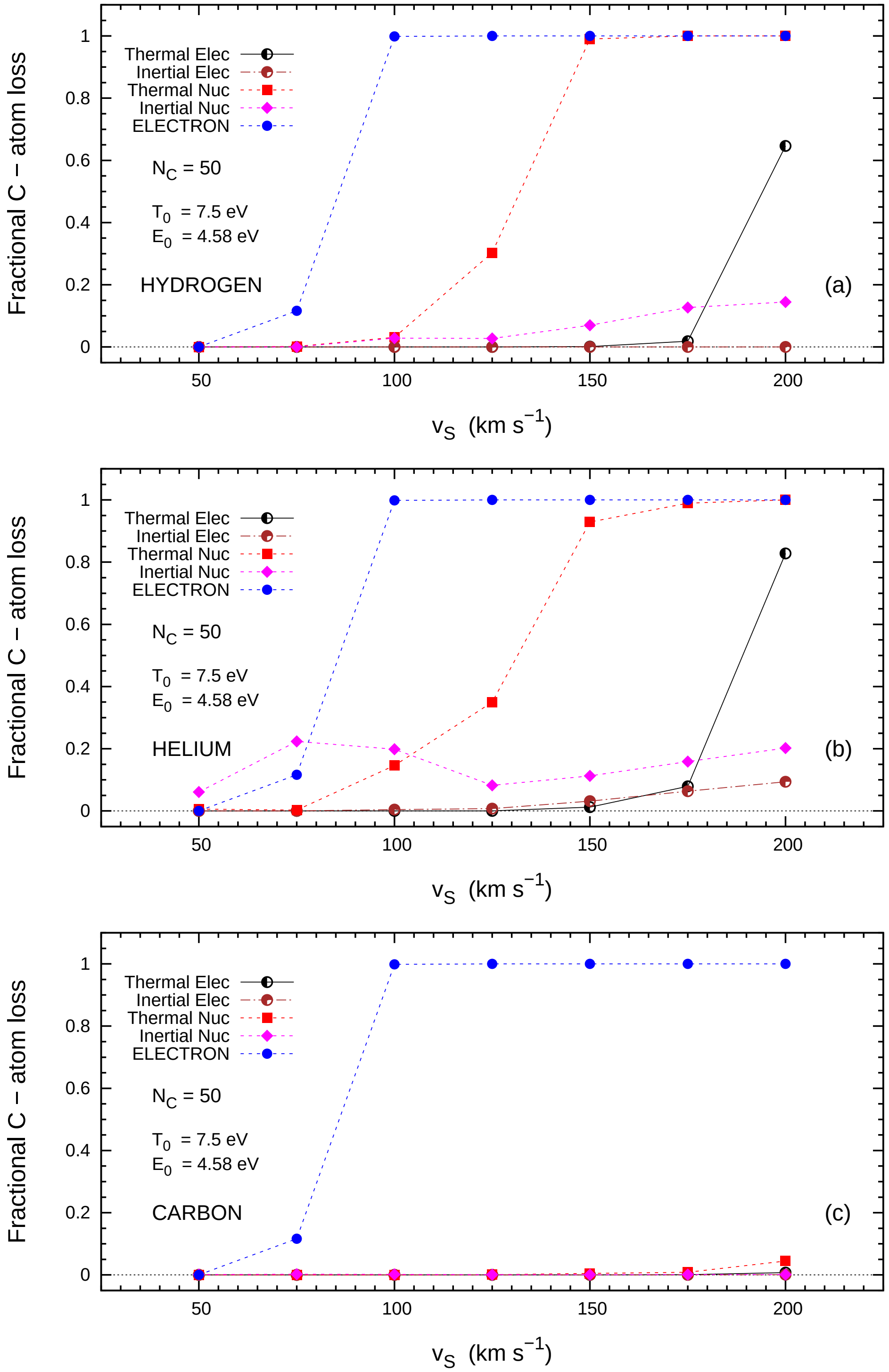

Figure 3.7 — The fractional C-atom loss F_L, due to collisions with H, He and C ions and electrons, as a function of the shock velocity. F_L is defined as the total number of ejected carbon atoms divided by the initial number N_C of C-atoms in the PAH molecule. The destructive effect of thermal and inertial 'sputtering' induced by collisions with the projectiles are shown. In the nuclear case, each lost atom is the result of a single collision with a given projectile, in other words, every collision removes a C-atom from the molecule so, the number of destructive collisions equals the number of ejected carbon atoms. For electrons as projectiles and for electronic interaction, each collision leads to the ejection of two carbon atoms. The points are calculated for a 50 C-atoms PAH assuming the nuclear threshold energy T_0 = 7.5 eV and the electronic dissociation energy E_0 = 4.58 eV.

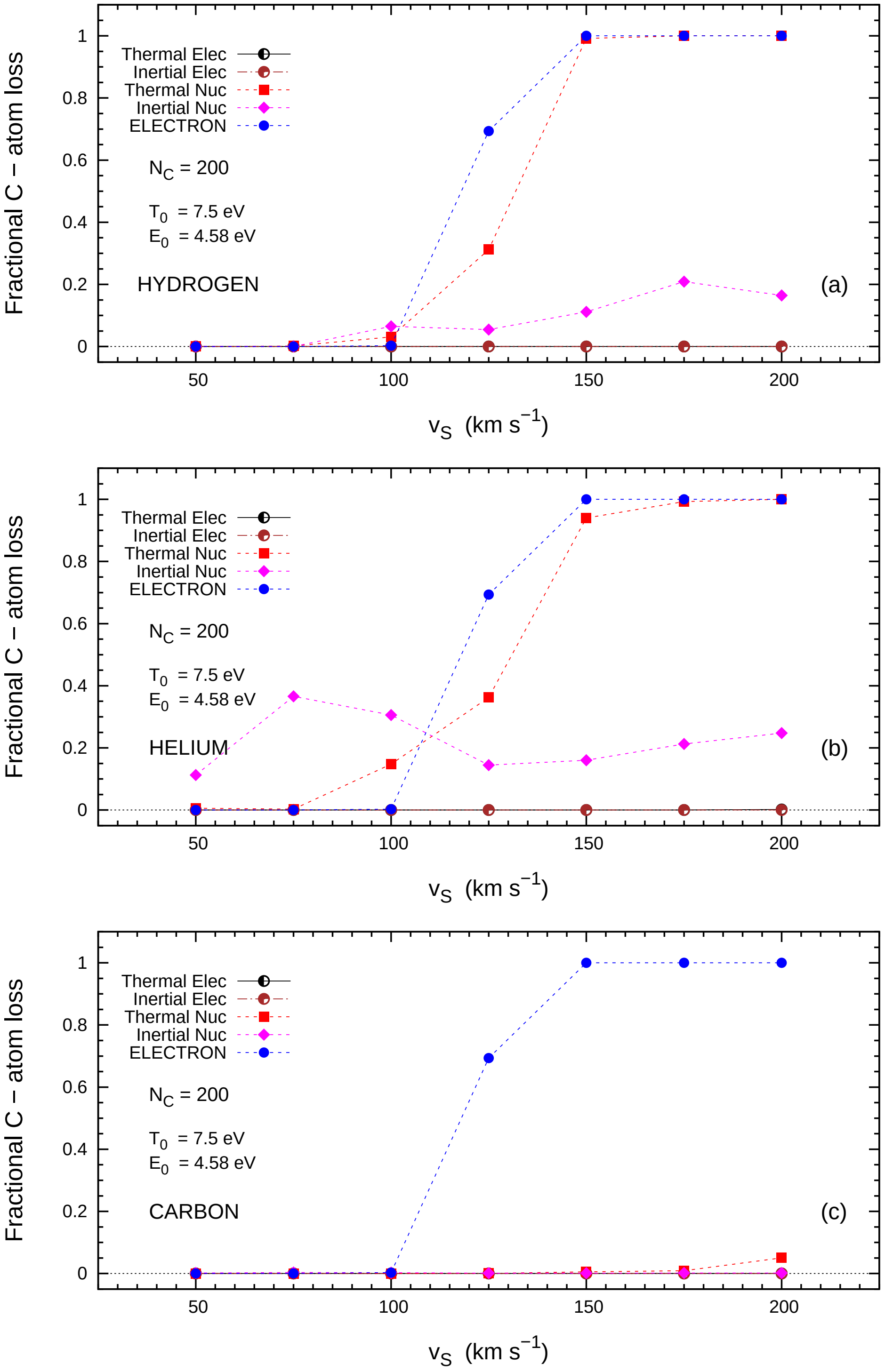

Figure 3.8 — Same as Fig. 3.7 calculated for a 200 carbon atoms PAH.

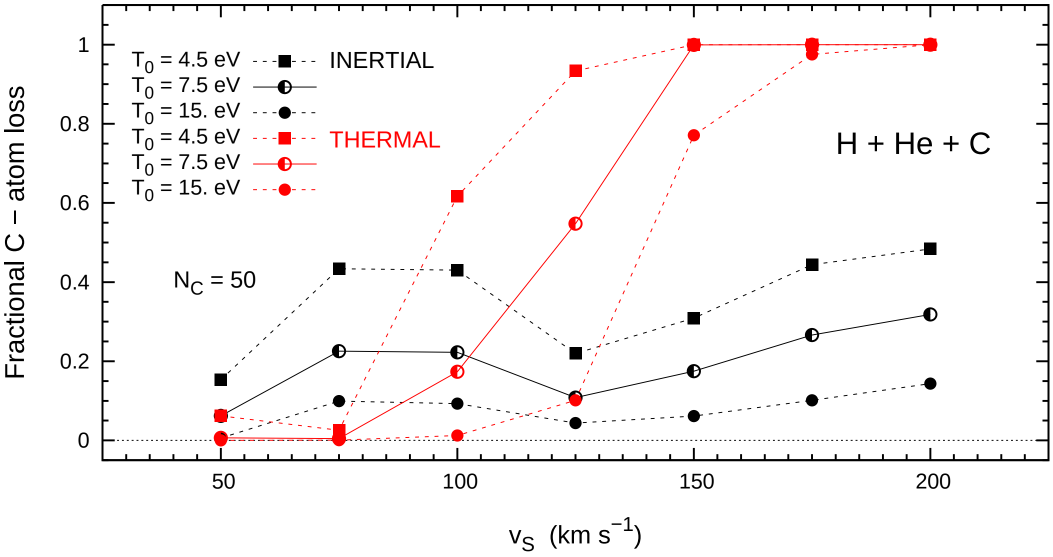

Figure 3.9 — Carbon atom loss due to collisions with thermal and inertial ions (H + He + C) via nuclear interaction. The figure shows the comparison betwen the three threshold values T_0 = 4.5, 7.5 and 15 eV for a 50 carbon atom PAH.

3.4.4 Summary

A summary of our findings from Fig. 3.7 and 3.8 is presented in Fig. 3.10. This shows the fractional atomic loss, F_L, due to electron and ion collisions, calculated for the two PAH sizes N_C = 50 and 200. To show how the fractional loss changes as a function of the adopted value for E_0, we added the results obtained assuming for the electronic dissociation energy the values 3.65 and 5.60 eV, lower and higher respectively than our standard value 4.58 eV,

For ionic collisions, F_L is determined by nuclear interaction: inertial for low v_S and thermal for high v_S. For the 50 C-atoms PAH, the electronic contribution emerges for the lowest value of E_0, 3.65 eV. As already mentioned, the dissociation probability increases for decreasing E_0, so we are not surprised to find F_L enhanced by electronic excitation (both inertial and thermal). The electronic contribution disappears for higher dissociation energies, as demonstrated by the coincidence between the curves for E_0 = 4.58 and 5.60 eV. For N_C = 200, all three ionic curves are coincident, indicating that electronic excitation by impacting ions does not contribute to PAH destruction below 150 km s^{-1}. Above this value, the carbon loss due to electronic interaction is covered by the other processes.

The shift between the ionic curves for the two PAH sizes is due to the small differences in the velocity profiles – due to betatron acceleration –, which imply in the inertial case a slightly higher damage for the bigger PAH. In the thermal case F_L is instead independent on the PAH size because the number of ejected C-atoms scales linearly with N_C (see §4.1). The resulting effect is an almost linear rise for both PAH sizes up to 150 km s^{-1}, beyond which the destruction is complete.

The 'Electron' curves reproduce the behaviour observed in Fig. 3.7 and 3.8. The comparison with the ionic F_L clearly indicates that a 50 carbon atoms PAH is already damaged in a non-negligible way in low velocity shocks (50 - 75 km s^{-1}, ion collisions) and is totally destroyed above 100 km s^{-1} (electron collisions). When E_0 = 3.65 eV, the fraction of ejected C-atom for v_S = 75 km s^{-1} increases from 0.1 to ∼0.35 but the minimum shock velocity for complete destruction is unchanged (100 km s^{-1}). For $v_S \geq$ 75 km s^{-1}, the 5.6 eV curve is almost parallel to the 3.65 eV curve and shifted by 25 km s^{-1} toward higher shock velocities. For the 200 C-atom PAH, the carbon atom loss is dominated by ionic collisions for shocks with velocity below 100 km s^{-1}. Above this value, the combined effect of ions and electrons leads to a complete destruction. A lower electronic dissociation energy shifts back by 25 km s^{-1} the minimum shock velocity required for total carbon ejection. When E_0 = 5.60 eV, destruction starts to be important only above 125 km s^{-1}, and becomes almost complete at 150 km s^{-1}.

We adopt the quantity F_L as destruction efficiency to calculate the PAH lifetime in shocks.

3.4.5 Uncertainties discussion

The main sources of uncertainties which have to be considered for this study are related to the adopted shock profiles, to the accuracy of the fitting function for the ZBL nuclear stopping cross section, and to the choice of an appropriate value for the nuclear threshold energy T_0 and for the electronic dissociation energy E_0.

The uncertainties related to the adopted shock profiles here are principally due to our assumption that we can equivalently treat a small, two-dimensional PAH molecule as a small three-dimensional grain. In the calculation of the PAH velocity profiles through the shocks we use the same formalism as for the grains (Jones et al. 1996), i.e., we assume that the PAH behaves as a three-dimensional grain of the same mass. Any uncertainties are then due to the inherent differences in the cross section to mass ratios for PAHs and grains. As mentioned in §3, once the PAH cross section is averaged over all possible orientations, the differences in the PAH and grain cross sections turn out to be only of the order of 11%, for a 50 carbon atom PAH, and are therefore rather small compared to the other uncertainties that we discuss here.

The accuracy of the ZBL nuclear stopping cross section depends on the accuracy of the single analytical function used by Ziegler et al. (1985) to calculate the interatomic potentials between atoms. This universal function has been compared with experimentally determined potentials, with a resulting standard deviation between theory and experiment of 5% (O'Connor & Biersack 1986). An additional test has been made comparing the results from the ZBL function with much more complex theoretical calculations including more effects. In this case as well the results agree within few percent (see Ziegler et al. 1985, and references therein).

The main source of uncertainty in the nuclear stopping calculation is the choice of the threshold energy T_0. This quantity is not well constrained (see §3.2.1) so we explored a set of plausible values. In Fig. 3.9 we plotted together the values for F_L resulting from the total effect of H, He and C, calculated in both inertial and thermal case for three different threshold energies T_0 = 4.5, 7.5 and 15 eV. The curves corresponding to the highest and lowest threshold T_0^{max} and T_0^{min} identify a region which can be interpreted as the variation in the amount of destruction due to the uncertainty in the threshold energy. For the inertial case, this uncertainty introduces a variation in

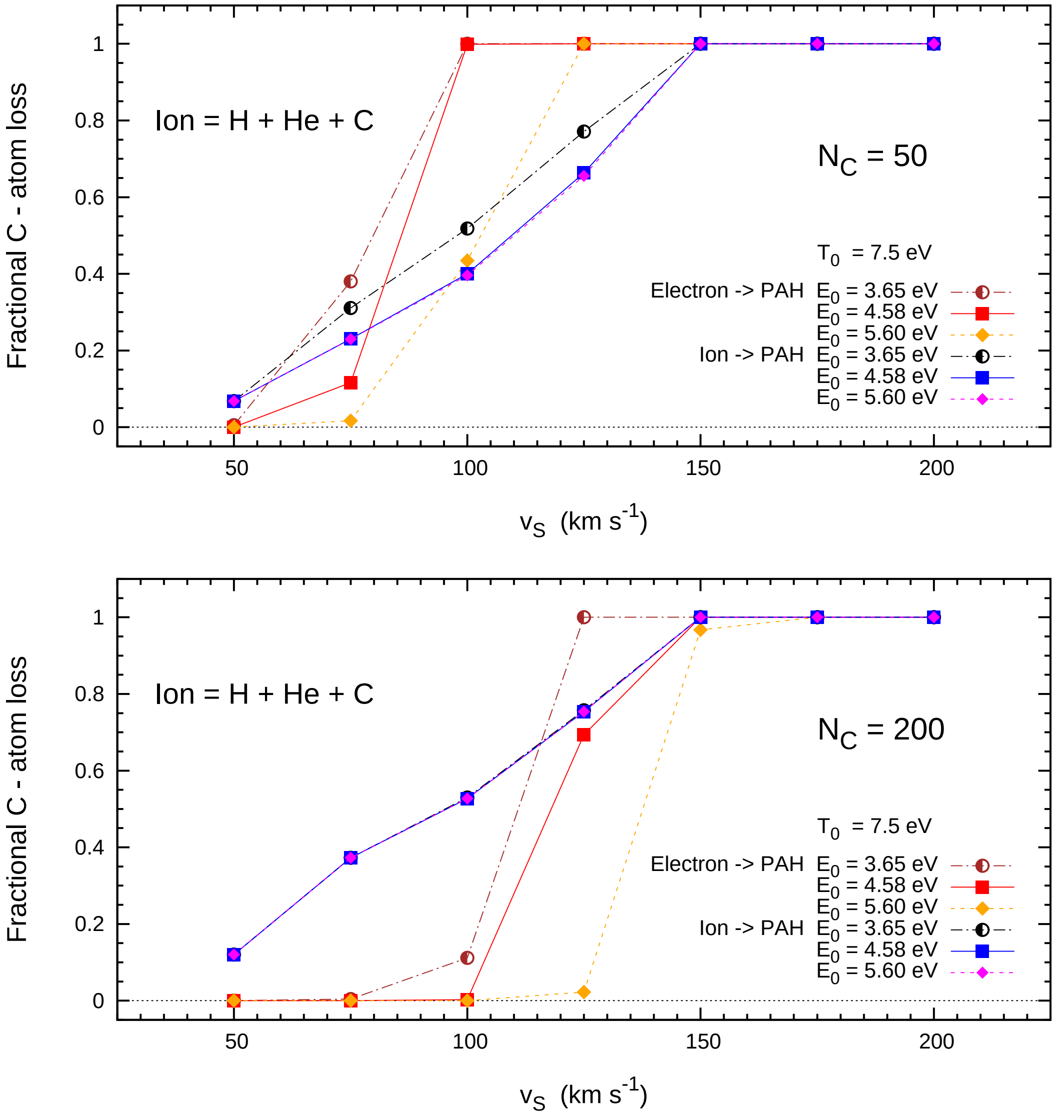

Figure 3.10 — The fractional C-atom loss F_L as a function of the shock velocity, calculated for three values of the parameter E_0: 3.65, 4.58 and 5.60 eV. F_L is defined as the total number of ejected carbon atoms divided by the initial number N_C of C-atoms in the PAH molecule. For the two PAH sizes N_C =50 (top panel) and N_C = 200 (bottom panel), the curves labelled ‘Ion’ illustrate the cumulative effect of all destructive processes for the ions considered in this study: inertial and thermal ‘sputtering’ due to nuclear and electronic excitation during PAH collisions with H, He and C in the shocks. The curves labelled ‘Electron’ show the destructive effect of thermal electrons. We assume T_0 = 7.5 eV.

the destruction efficiency of a factor less than about 2. For the thermal case, the uncertainty introduces a shift of the critical shock velocity above which thermal destruction is dominant from about 100 to 150 km s^{-1} for T_0 ranging from 4.5 to 15 eV.

An important issue for the electronic and electron stopping calculation is the choice of the value for the parameter E_0. We adopt the value 4.58 eV, which has been extrapolated for interstellar conditions from experimental data. Unfortunately the extrapolation procedure is very model–dependent, so the same set of experimental data can lead to significantly different values for the interstellar E_0. The problematic fragment binding energy is extensively discussed in Chapter 4 - paper MJT09b, the result of a different choice for E_0 (3.65, 4.58 and 5.6 eV) on PAH processing by shocks is shown in Fig. 3.10. The differences are quite significant, indicating the importance of experimental studies on the critical energy E_0 describing the dissociation probability of highly excited PAHs. To summarize, the errors related to the shock profiles and ZBL fitting function are quite small, for T_0 we identified a range of plausible values, but experimental determinations would be desirable, while the choice of the parameter E_0 is very uncertain and urgently requires a better determination.

3.5 Discussion

3.5.1 PAH lifetime in shocks

To calculate the timescale for supernova shock waves to destroy the interstellar PAHs in the Galaxy, t_{SNR}, we adopt the same approach used in our previous works (Jones et al. 1994, 1996), which is based on the method of McKee (1989):

$$t_{\mathrm{SNR}} = \frac{M_{\mathrm{ISM}}}{\left(1/\tau'_{\mathrm{SN}}\right) \int \varepsilon(v_{\mathrm{S}})\, \mathrm{d}M_{\mathrm{S}}(v_{\mathrm{S}})} \tag{3.28}$$

where $M_{\mathrm{ISM}} = 4.5\times10^9\, M_\odot$ is the mass of the Galactic interstellar medium (gas and dust including PAHs), τ'_{SN} = 125 yr is the effective interval between supernovae (McKee 1989), $\varepsilon(v_{\mathrm{S}})$ is in this case the efficiency of PAH destruction by a shock of velocity v_{S} and M_{S} is the mas of gas shocked to at least v_{S} by a supernova remnant in the Sedov-Taylor stage (in this stage the energy is conserved, so that $M_{\mathrm{S}}\, v_{\mathrm{S}}^2 \propto E$). In a three-phase model of the interstellar medium (McKee & Ostriker 1977), with a ratio between warm and hot intercloud filling factor of $f_{\mathrm{w}}/f_{\mathrm{h}} = 0.3/0.7 = 0.43$, the mass M_{S} and the timescale t_{SNR} become

$$M_{\mathrm{S}}(v_{\mathrm{S}}) = 2914\, M_\odot / v_{\mathrm{S7}}^2 \tag{3.29}$$

$$t_{\mathrm{SNR}} = \frac{9.7 \times 10^7}{\int \varepsilon(v_{\mathrm{S7}})/v_{\mathrm{S7}}^3\, \mathrm{d}v_{\mathrm{S7}}}\ \mathrm{yr} \tag{3.30}$$

were v_{S7} is shock velocity in units of 100 km s^{-1} and the assumed mean supernova energy is 10^{51} erg.

Using our calculated fractional destruction data, we derived analytical expressions for the destruction efficiency $\varepsilon(v_{\mathrm{S7}})$ for electrons and ions. The ionic term represents the total contribution of all considered ions (H, He and C) and processes (nuclear and electronic stopping, inertial and thermal). Below 150 km s^{-1}, we adopt a power law fit for $N_{\mathrm{C}} = 50$ and a linear fit for $N_{\mathrm{C}} = 200$, while for the remaining velocities the efficiency is 1. For electrons, for $F_{\mathrm{L}} < 1$, the destruction efficiencies are well fit by two linear functions ($N_{\mathrm{C}} = 50$) and a logarithmic function ($N_{\mathrm{C}} = 200$). The analytical fits reproduce the calculated data within few percent. The functional form, fitting parameters and corresponding timescales calculated from Eq. 3.30 are reported in Table 3.3.

Table 3.3 — PAH destruction analytical fit parameters and survival timescales for electron and ion collisions, calculated assuming T_0 = 7.5 eV and E_0 = 4.6 eV.

	Electron		Fit parameters	
	$N_C = 50$	$N_C = 200$		
$\varepsilon(v_{S7}) = m_1 x + q_1$	$0.50 \leq v_{S7} \leq 0.75$	—	$m_1 = 0.464$	$q_1 = - 0.232$
$\varepsilon(v_{S7}) = m_2 x + q_2$	$0.75 \leq v_{S7} \leq 1.00$	—	$m_2 = 3.536$	$q_2 = - 2.536$
$\varepsilon(v_{S7}) = c\, ln\, (x^d)\, /x$	—	$0.50 \leq v_{S7} \leq 1.50$	$c = 5.366$	$d = 0.7$
$\varepsilon(v_{S7}) = k$	$1.00 \leq v_{S7} \leq 2.00$	$1.50 \leq v_{S7} \leq 2.00$	$k = 1$	
t_{SNR} (yr)	1.6×10^8	4.0×10^8		

	Ion		Fit parameters	
	$N_C = 50$	$N_C = 200$		
$\varepsilon(v_{S7}) = m_3 x + q_3$	—	$0.50 \leq v_{S7} \leq 1.50$	$m_3 = 0.879$	$q_3 = - 0.319$
$\varepsilon(v_{S7}) = a x^b$	$0.50 \leq v_{S7} \leq 1.50$	—	$a = 0.405$	$b = 2.232$
$\varepsilon(v_{S7}) = k$	$1.50 \leq v_{S7} \leq 2.00$	$1.50 \leq v_{S7} \leq 2.00$	$k = 1$	
t_{SNR} (yr)	1.8×10^8	1.4×10^8		

For electron collisions we find t_{SNR} = 1.6 $\times 10^8$ yr for $N_C = 50$ and 4.0 $\times 10^8$ yr for $N_C = 200$. In case of ion collisions the lifetimes are 1.8 $\times 10^8$ yr and 1.4 $\times 10^8$ yr for the small and big molecule respectively. The largest uncertainty in these lifetimes result from the uncertainty in the values adopted for T_0 and E_0 (cf. §4.5). If we assume the lowest values considered (4.5 and 3.65 eV), these lifetimes decrease to 9.2×10^7 yr and 8×10^7 yr (for $N_C = 50$ and 200 respectively), while the maximum values considered for these energies result in lifetimes of 2.5×10^8 yr and 3.3×10^8 yr. for the small and big PAH. Thus, while these parameters are quite uncertain, the derived values for the lifetimes are quite robust. Essentially, PAHs are destroyed by shocks larger than about 100 km/s and, typically, interstellar gas encounters such shocks once every 100 million years (McKee 1989).

From the results obtained assuming our standard values (T_0 = 7.5 eV and E_0 = 4.6 eV), we argue then that small PAHs are preferentially destroyed by electrons whereas big PAHs are more affected by ions.

Our derived values for t_{SNR} for PAHs are significantly shorter than the 6 $\times 10^8$ yr calculated by Jones et al. (1996) for graphite/amorphous carbon grains in the warm intercloud medium. Ignoring betatron acceleration, the total number of collisions per C-atom required for stopping the inertial motion is independent of grain size. The difference in lifetimes reflects then a difference in sputtering efficiency. This is not surprising because of the different approaches adopted for the ion-particle interactions for PAHs and grains. In both cases, and for the shocks that we consider here, it is the sputtering processes that completely dominate dust destruction. In the case of grains not every atom that is 'knocked on' by an incident ion is lost, i.e. sputtered, from the grain. The displaced atom is often embedded deeper into the grain and therefore not sputtered from the grain even when the displacement energy significantly exceeds the threshold energy for target atom displacement. This is reflected in the fact that, for grains, the sputtering yield is usually much less that unity. The shorter lifetime for the PAHs is then be ascribed to the fact that in any incident ion interaction the target atom is always lost from the PAH when the energy to displace it is greater that the required threshold energy. In this case the equivalent PAH sputtering yield is then unity.

Our derived PAH lifetime is much closer to the value of $\sim 2\times\ 10^8$ yr found for a size distribution of hydrogenated amorphous carbon (a-C:H) grains, typical of the diffuse interstellar medium, by Serra Díaz-Cano & Jones (2008). This is perhaps just coincidental; it has its origin in lower average binding energy of C-atoms in amorphous carbon than in graphite. a-C:H grains are found, as we find for PAHs, to be more susceptible to sputtering erosion than graphite/amorphous carbon grains (Jones et al. 1996). However PAHs are much more susceptible to erosion than a-C:H in fast shocks (≥ 150 km s^{-1}) and this is simply due to their small sizes. Thermal sputtering in the hot post-shock gas of fast shocks is proportional to the surface area and, small particles having a larger surface area per unit mass than large particles, are more rapidly eroded.

3.5.2 Astrophysical implications

As shown in § 3.5.1, the PAH lifetime against shock destruction is much shorter than the stardust injection timescale into the interstellar medium $t_{\rm inj}$ = 2.5 $\times 10^9$ yr. Gas shocked to velocities of the order of 50 - 150 km s^{-1} is observed in many regions of the interstellar medium: e.g. toward the star ζ Ori (Welty et al. 2002), in Herbig-Haro jets in the Orion and Vela star forming regions (Podio et al. 2006), and in the local interstellar cloud (Slavin 2008). Hence, according to our calculations, PAH destruction should be widespread in the ISM.

If we assume globally that the same $t_{\rm inj}$ holds for PAHs as for 'standard' interstellar dust, i.e., that dust and PAH formation are coeval in and around evolved stars, our calculated survival times for PAHs, i.e., $t_{\rm SNR}$, indicate that they need to be re-formed in the ISM even more rapidly than the larger interstellar grains. If PAHs are formed by the fragmentation of larger carbonaceous grains then their 'effective' survival time must just be the same as that of the larger grains from which they originate. However, this can only be true for low velocity shocks, or turbulent regions of the ISM, where grain-grain collisions at relatively low velocities (of the order of a few km s^{-1}) can form PAHs via fragmentation and where there is no associated destructive process in operation.

On a region by region basis our results indicate that PAHs should not exist in environments shocked to high velocities (> 100 km s^{-1}). We conclude that PAHs that exist in unshocked regions do not survive the passage of shocks with velocities above $100 - 150$ km s^{-1} (depending on their size). They are in fact destroyed rather early in in the shock at shocked column densities of the order of $10^{16} - 10^{17}$ cm^{-2}. Any 'daughter' PAHs produced in the post-shock region, by grain fragmentation in grain-grain collisions at shocked column densities of the order of $10^{17} - 10^{18}$ cm^{-2}, will be destroyed by erosion due to their high injection velocities into the gas following the fragmentation of their larger, 'parent' grains that undergo betatron-acceleration (Jones et al. 1996). Thus, high velocity shocks destroy all the PAHs that they both interact with and produce by fragmentation in high velocity grain-grain collisions.

In contrast observations show that PAHs lock up about 3% of the elemental carbon in the ISM (cf. Tielens 2008). Disentangling these two scenarios is not easy observationally. Here we now consider the case where the PAH emission is assumed to come from within the shocked region. This scenario requires an efficient (re)formation route for PAHs in the diffuse ISM (see above). However, this is difficult to understand since PAHs are a product of high temperature chemistry involving abundant carbon bearing precursors such as CH_4 and C_2H_2. In the low temperature diffuse ISM, an O-rich environment, these precursor species are never really very abundant. This conundrum is very reminiscent of the general problem of rapid dust destruction in the ISM and the long injection time scale for freshly formed dust (Dwek & Scalo 1980; Draine & Salpeter 1979b; Jones et al. 1994, 1996). We note that, while dust grains may be rapidly covered by (thin)protective coatings between successive shock passages (cf. Tielens 1998), this is not a way out of this conundrum for PAHs. Perhaps, PAHs can be formed through prolonged photolysis of ice mantles accreted inside dense molecular clouds, although, presently, there is no experimental support for this suggestion. Lastly, observations have revealed the presence of PAHs associated with hot shocked gas in stellar (eg., M17) and galactic (e.g., M82) wind regions (cf. § 3.1). As will be discussed more extensively in Chapter 4 - paper MJT09b, these PAHs likely trace entrained cold gas which has not been fully exposed to the destructive effects of high velocity shocks.

For $v_S < 75$ km s^{-1}, PAH are disrupted only by inertial 'sputtering' due to nuclear interactions. Serra Díaz-Cano & Jones (2008) have studied the erosion of hydrogenated amorphous carbon (a-C:H) arising from ion irradiation in shocks in the warm intercloud medium, using exactly the same shock profiles that we use for our PAH study, and it is interesting to note that, for a 50 carbon atom PAH molecule, the percentage of destruction is the same as for a-C:H, indicating that the lower density, more easily sputtered a-C:H and PAHs exhibit similar erosion characteristics in lower velocity shocks ($\simeq 125$ km s^{-1}), as discussed in the previous section.

We now consider what happens to a PAH as a result of the ejection of aromatic carbon atoms, by the impacting ions, as a function of the fraction of carbon atoms removed from the structure. Our results show that ionic collisions severely modify PAH in shocks with velocities between 75 - 150 km s^{-1}. Nuclear and electronic interaction lead to distinctly different molecular destruction routes. Specifically, electronic excitation (either by impacting ions or electrons) lead to a high vibrational excitation of the PAH and this PAH will relax by 'losing' the weakest link in its skeleton. Initially, this will be the peripheral H-atoms or other functional groups. For large PAHs (50-100 C-atoms), the resulting 'pure-C' may quickly isomerize to very stable carbon cluster such as fullerenes. Fullerenes are very stable against C_2 loss. Measured dissociation energies of fullerenes are in the range of 7 to 9.5 eV, with C_{60} itself at $E_0 = 9.8 \pm 0.1$ eV (Tomita et al. 2001).

In contrast, nuclear interaction will act on the C-atom hit by the projectile ion. This will randomly remove C-atoms from the C-skeleton of the PAH. Some isomerization may occur if internal excitation energy is left behind. However, unless the C-atom loss in the shock is very large, likely this is insufficient to affect the overall PAH structure. In a simple 'geometrical' analysis, if one randomly removes C atoms from a PAH with $N_C = 50$, in the absence of any annealing of the PAH chemical structure, we find that

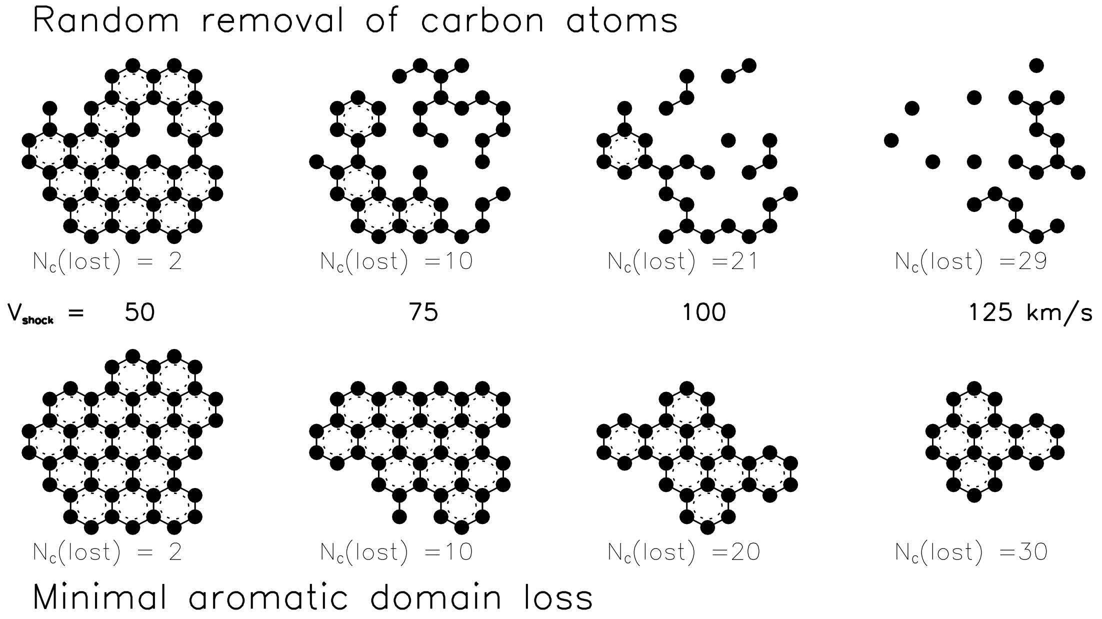

Figure 3.11 — The evolution of a 50 carbon atom PAH following the loss of N_C(lost) carbon atoms, as a function of the shock velocity, for the two limiting cases: instantaneous and random removal of the lost carbon atoms (top row), and carbon atom removal only from the periphery of the molecule (bottom row).

the loss of 10% of the C atoms leads to a loss of of the order of $\approx 50\,\%$ of the aromatic character. However, the loss of $\approx 20\,\%$ of the C atoms leads to the almost complete loss of aromatic character and to the onset of the fragmentation of the molecule. Fig. 3.11 illustrates these effects and shows the PAH evolution following the loss of carbon atoms, N_C(lost), for the two limiting cases: 1) where there is an instantaneous and random removal of the lost carbon atoms (appropriate for nuclear interaction) and 2) where the carbon atoms are removed only from the periphery in order to preserve aromatic domain as much as possible (likely appropriate for electronic excitation through either impact ions or electrons). The reality of PAH erosion in shocks may well lie somewhere between these two extremes and may also involve isomerisation and the formation of five-fold carbon rings that distort the structure from a perfectly two-dimensional form. This then begs the question as to the exact form and structure of small carbon species once growth resumes by atom insertion and addition.

After the shock wave has passed, the resulting PAH can react chemically with impacting H, C, O, and N atoms. A distinction can be made between H and O in the one hand and C and N on the other hand. The latter can restore the stable aromatic character of the PAH skeleton while the former lead only to very unstable structures. Likely, then, H and O atom addition can be reversed by UV photon absorption without loss of C (Allamandola et al. 1989). Hence, the PAH carbon skeleton may be able to 'repair' itself to an aromatic structure, possibly incorporating N-atoms. The possible presence of N-atoms deeply in the C-skeleton of PAHs in the diffuse medium (but not in C-dust birth sites such as C-rich planetary nebulae) has been inferred from the peak position of the 6.2 μm band (Peeters et al. 2002a). It has also been suggested that the 6.2 μm band position variations can be explained by a varying aliphatic to aromatic carbon content in carbonaceous particles (Pino et al. 2008). The difference in molecular structure between circumstellar PAHs and the general ISM implies an active chemistry in the ISM that is able to insert N atoms deeply in the carbon skeleton. This is very puzzling given the very stable character of the aromatic backbone and the low temperature of the ISM. Here, we surmise that, unlike UV photolysis or chemical attack, nuclear interactions in interstellar shocks may be a viable pathway to promote N-incorporations deep inside PAHs. However, given that the nitrogen abundance is a factor of a few lower than that for carbon – depending on the fraction of carbon remaining in dust and PAHs – carbon atom insertion ought to be favoured over that for nitrogen, in the absence of any chemically-selective route for nitrogen insertion.

3.6 Conclusions

We have extensively studied the effects of PAH processing by shocks with velocities between 50 and 200 km s^{-1}, in terms of collisions with ions and electrons which can lead to carbon atom loss, with a consequent disruption and destruction of the molecule.

An ionic collision consists of two simultaneous processes which can be treated separately: a binary collisions between the projectile and one single atom in the target (nuclear interaction) and the energy loss to the atomic electrons (electronic interaction). For the nuclear interaction, we modified the existing theory in order to treat collisions able to transfer energy *above* a specific threshold. This is the case we are interested in, which has not been treated in previous studies. For electronic interaction and collisions with electrons we developed specific models for PAH, described in Chapter 4 - paper MJT09b.

The PAH dynamics in the shocks is evaluated using the same approach as in our previous work (Jones et al. 1994, 1996). For nuclear interaction, the level of carbon atom loss increases for decreasing values of the threshold energy T_0. We adopt T_0 = 7.5 eV as a reasonable value, but experimental determinations are necessary. In ionic collisions, the carbon contribution to PAH destruction is totally negligible because of its very low abundance with respect to H and He. The fractional destruction induced by nuclear excitation increases with the PAH size, while in case of electronic excitation and electron collisions is lower for higher N_C values, i.e. bigger PAHs are more resistant than the smaller ones against electron and electronic processing.

The parameter E_0 required for the evaluation of PAH destruction due to electron and electronic interaction is unfortunately not well constrained. We adopt a value of 4.58 eV consistent with extrapolations to interstellar conditions, but better determinations would be desirable.

Electronic interaction, both inertial and thermal, plays a marginal role in PAH processing by shocks. We find that 50 carbon atoms PAHs are significantly disrupted in ionic collisions for shock velocities below 75 km s^{-1}, mainly by inertial 'sputtering' by helium during nuclear interaction. Our results indicate $5 - 15\,\%$ C atom loss, sufficient to cause a severe de-naturation of the PAH aromatic structure. Above 100 km s^{-1} such PAHs are instead totally destroyed by collisions with thermal electrons. For

$N_C = 200$, PAHs experience increasing damaging caused by nuclear ionic collisions up to 100 km s^{-1}, which turns into complete atomic loss for higher velocities. In this case the destruction is due to the combined effect of electrons and nuclear interaction with thermal ions.

The calculation of PAH lifetime against destruction $t_{\rm SNR}$ is $\approx 1.6 \times 10^8$ yr and $\approx 1.4 \times 10^8$ yr for N_C = 50 and 200 respectively. Small PAHs are preferentially destroyed by electrons, big PAHs by ions. The calculated lifetimes are smaller than the values found for carbonaceous grains (6×10^8 yr) but close to that for hydrogenated amorphous carbon (2×10^8 yr), and far from the stardust injection timescale of 2.5×10^9 yr. The presence of PAHs in shocked regions therefore requires an efficient reformation mechanism and/or a protective environment.

We surmise that the molecular structure of PAHs is strongly affected by shock processing in the interstellar medium. Electronic excitation by impacting ions or electrons may lead to isomerization into stable pure-C species such as fullerenes. In contrast, nuclear interaction may lead to the formation of N-containing PAHs. Further laboratory studies are required to demonstrate the viability of these chemical routes.

3.7 Appendix A: S_n, σ and $< T >$

A fundamental quantity to describe the nuclear scattering is the *energy transfer cross section* $\sigma(E, T)$, which is function of the kinetic energy E of the projectile and of the energy T transferred to the target by the projectile in a single collision. At low energies ($\varepsilon \lesssim 1$), an approximated expression for the cross section can be calculated using the power approximation to the Thomas-Fermi model of interatomic interaction, i.e. with a potential of the form $V(r) \propto r^{-1/m}$, where r is the distance between colliding nuclei and m is a parameter related to the steepness of the interatomic potential. The quantity m can also be interpreted as an indicator of the energy of the projectile, varying slowly from m = 1 at high energies to $m \approx 0$ at low energies (Lindhard et al. 1968; Winterbon et al. 1970). We have that

$$d\sigma(E,T) \cong C_m\, E^{-m}\, T^{-1-m}\, dT \qquad 0 \lesssim T \lesssim T_{\rm m} \tag{3.31}$$

with

$$C_m = \frac{\pi}{2}\, \lambda_m\, a^2 \left(\frac{M_1}{M_2}\right)^m \left(\frac{2\, Z_1\, Z_2\, e^2}{a}\right)^{2m} \tag{3.32}$$

where $T_{\rm m}$ is the maximum transferable energy, corresponding to a head-on collision (impact parameter p = 0). The dimensionless quantity $\lambda_m = \lambda_m(m)$ varies slowly from 0.5 for m = 1 (high energy, i.e. pure Rutherford scattering, Simmons 1965a), to 24 for m = 0 (very low energy).

The power approximation of the Thomas-Fermi cross section (Eq. 3.31) gives the following expression for the nuclear stopping cross section, obtained evaluating the integral in Eq. 3.4 between 0 and $T_{\rm m}$:

$$S_{\rm n}(E) = \frac{1}{1-m}\, C_m\, \gamma^{1-m}\, E^{1-2m} \tag{3.33}$$

For Thomas-Fermi interaction, using Eq. 3.1, 3.32, 3.3 and 3.33, this leads to

$$S_{\rm n}(E) = 4\,\pi\, a\, Z_1\, Z_2\, e^2\, \frac{M_1}{M_1 + M_2}\, s_{\rm n}(\varepsilon) \tag{3.34}$$

with

$$s_{\rm n}(\varepsilon) = \frac{\lambda_m}{2\,(1-m)}\, \varepsilon^{1-2m} \tag{3.35}$$

For heavy screening ($\varepsilon \ll 1, m \cong 0$) the accuracy of the Thomas-Fermi reduced stopping cross section $s_{\rm n}(\varepsilon)$ to reproduce the experimental data is at best a factor of two. For this reason we adopt instead the Universal reduced stopping cross section $s_{\rm n}^{\rm U}$ (Eq. 3.5) from Ziegler et al. (1985) with the appropriate screening length $a_{\rm U}$ (Eq. 3.2), which provides a good fit to the experimental data at low energies as well.

The nuclear stopping cross section above threshold is given by Eq. 3.10. Remembering that $T_{\rm m} = \gamma E$ and $T_0 = \gamma E_{0\rm n}$, this can be rewritten as follows

$$\begin{aligned} S_{\rm n}(E) &= \frac{C_m\, E^{-m}}{1-m}\, [T_{\rm m}^{1-m} - T_0^{1-m}] & (3.36)\\ &= \frac{C_m\, E^{-m}}{1-m}\, T_{\rm m}^{1-m} - \frac{C_m\, E^{-m}}{1-m}\, T_0^{1-m} & (3.37)\\ &= \frac{C_m\, \gamma^{1-m}}{1-m}\, E^{1-2m} - \frac{C_m\, \gamma^{1-m}}{1-m}\, E^{-m}\, E_{0\rm n}^{1-m} & (3.38) \end{aligned}$$

The first term in the right side of the equation is equal to the nuclear stopping cross section in the no-threshold case (T_0 = 0)

$$\frac{C_m\, \gamma^{1-m}}{1-m}\, E^{1-2m} \;=\; 4\,\pi\, a\, Z_1\, Z_2\, e^2\, \frac{M_1}{M_1+M_2}\, s_{\rm n}(\varepsilon) \;\equiv\; S_{\rm n}^0(E). \tag{3.39}$$

In the second term we use the equality $E^{-m} = (E^{1-2m}/E^{1-m})$ to obtain

$$\begin{aligned} \frac{C_m\, \gamma^{1-m}}{1-m}\, E^{-m}\, E_{0\rm n}^{1-m} &= \frac{C_m\, \gamma^{1-m}}{1-m}\, E^{1-2m} \left(\frac{E_{0\rm n}}{E}\right)^{1-m} & (3.40)\\ &= 4\,\pi\, a\, Z_1\, Z_2\, e^2\, \frac{M_1}{M_1+M_2}\, s_{\rm n}(\varepsilon) \times \left(\frac{E_{0\rm n}}{E}\right)^{1-m} & (3.41) \end{aligned}$$

Combining the two we obtain the following expression for $S_{\rm n}$

$$S_{\rm n}(E) \;=\; 4\pi a Z_1 Z_2\, e^2 \frac{M_1}{M_1+M_2} s_{\rm n}(\varepsilon) \left[1 - \left(\frac{E_{0\rm n}}{E}\right)^{1-m}\right] \tag{3.42}$$

The total cross section is given by Eq. 3.11

$$\sigma(E) = \frac{C_m\, E^{-m}}{m}\,[T_0^{-m} - T_{\rm m}^{-m}] \tag{3.43}$$

$$= C_m\, E^{-m}\,\frac{T_0^{-m}}{m} - C_m\, E^{-m}\,\frac{T_{\rm m}^{-m}}{m}. \tag{3.44}$$

The term (T_0^{-m}/m) can be rewritten as follows

$$\frac{T_0^{-m}}{m} = \frac{T_{\rm m}^{1-m}}{1-m} \times \frac{1-m}{m} \times \frac{T_0^{-m}}{T_{\rm m}^{1-m}} \tag{3.45}$$

$$= \frac{\gamma^{1-m}\, E^{1-m}}{1-m} \times \frac{1-m}{m} \times \frac{\gamma^{-m}\, E_{0\rm n}^{-m}}{\gamma^{1-m}\, E^{1-m}} \tag{3.46}$$

$$= \frac{\gamma^{1-m}\, E^{1-m}}{1-m} \times \frac{1-m}{m} \times \frac{1}{\gamma\, E}\left(\frac{E_{0\rm n}}{E}\right)^{-m}. \tag{3.47}$$

Then we have

$$C_m\, E^{-m}\,\frac{T_0^{-m}}{m} = \frac{C_m\, \gamma^{1-m}}{1-m}\, E^{1-2m} \times \frac{1-m}{m} \times \frac{1}{\gamma\, E}\left(\frac{E_{0\rm n}}{E}\right)^{-m} \tag{3.48}$$

$$= S_{\rm n}^0(E) \times \frac{1-m}{m} \times \frac{1}{\gamma\, E}\left(\frac{E_{0\rm n}}{E}\right)^{-m}. \tag{3.49}$$

Using a similar approach we can write the term $(T_{\rm m}^{-m}/m)$ as

$$\frac{T_{\rm m}^{-m}}{m} = \frac{T_{\rm m}^{-m}}{m} \times \frac{1-m}{1-m} \times \frac{T_{\rm m}}{T_{\rm m}} \tag{3.50}$$

$$= \frac{T_{\rm m}^{1-m}}{1-m} \times \frac{1-m}{m} \times \frac{1}{T_{\rm m}} \tag{3.51}$$

$$= \frac{\gamma^{1-m}\, E^{1-m}}{1-m} \times \frac{1-m}{m} \times \frac{1}{\gamma\, E}. \tag{3.52}$$

Then second term in the right side of the equation then becomes

$$C_m\, E^{-m}\,\frac{T_{\rm m}^{-m}}{m} = \frac{C_m\, \gamma^{1-m}}{1-m}\, E^{1-2m} \times \frac{1-m}{m} \times \frac{1}{\gamma\, E} \tag{3.53}$$

$$= S_{\rm n}^0(E) \times \frac{1-m}{m} \times \frac{1}{\gamma\, E}. \tag{3.54}$$

Combining the two terms we obtain for $\sigma(E)$ the final expression

$$\sigma(E) = 4\pi a Z_1 Z_2 e^2 \frac{M_1}{M_1 + M_2} s_{\rm n}(\varepsilon)\,\frac{1-m}{m}\,\frac{1}{\gamma\, E}\left[\left(\frac{E_{0\rm n}}{E}\right)^{-m} - 1\right] \tag{3.55}$$

The expression for the average transferred energy $< T(E) >$ derives directly from Eq. 3.12 when applying the relations $T_{\mathrm{m}} = \gamma E$ and $T_0 = \gamma E_{0\mathrm{n}}$

$$< T(E) > = \frac{m}{1-m} \frac{T_{\mathrm{m}}^{1-m} - T_0^{1-m}}{T_0^{-m} - T_{\mathrm{m}}^{-m}} \tag{3.56}$$

$$= \frac{m}{1-m} \frac{\gamma^{1-m} \left(E^{1-m} - E_{0\mathrm{n}}^{1-m}\right)}{\gamma^{-m} \left(E_{0\mathrm{n}}^{-m} - E^{-m}\right)} \tag{3.57}$$

$$= \frac{m}{1-m} \gamma \frac{E^{1-m} - E_{0\mathrm{n}}^{1-m}}{E_{0\mathrm{n}}^{-m} - E^{-m}}. \tag{3.58}$$

3.8 Appendix B: Low and high energy regime above threshold

In the low energy regime m can be taken equal to 0, so the differential cross section $\mathrm{d}\sigma$ becomes

$$\mathrm{d}\sigma(E,T) = \cong \frac{\pi}{2} \lambda_0 a^2 T^{-1} \mathrm{d}T. \tag{3.59}$$

The corresponding expressions for $S_{\mathrm{n}}(E)$, $\sigma(E)$ and $< T(E) >$ above threshold are calculated from Eq. 3.7, Eq. 3.8 and Eq. 3.9 respectively

$$S_{\mathrm{n}}(E) = \frac{\pi}{2} \lambda_0 a^2 \gamma (E - E_{0\mathrm{n}}) \tag{3.60}$$

$$\sigma(E) = \frac{\pi}{2} \lambda_0 a^2 \ln \frac{E}{E_{0\mathrm{n}}} \tag{3.61}$$

$$< T(E) > = \gamma (E - E_{0\mathrm{n}}) \left(\ln \frac{E}{E_{0\mathrm{n}}} \right)^{-1} \tag{3.62}$$

In the high enery regime $m = 1$, then we have

$$\mathrm{d}\sigma(E,T) \cong \frac{M_1}{M_2} Z_1^2 Z_2^2 e^4 \pi \frac{1}{E} T^{-2} \mathrm{d}T \tag{3.63}$$

and consequently

$$S_{\mathrm{n}}(E) = \frac{M_1}{M_2} Z_1^2 Z_2^2 e^4 \pi \frac{1}{E} \ln \frac{E}{E_{0\mathrm{n}}} \tag{3.64}$$

$$\sigma(E) = \frac{M_1}{M_2} Z_1^2 Z_2^2 e^4 \pi \frac{1}{E} \frac{1}{\gamma E_{0\mathrm{n}}} \tag{3.65}$$

$$< T(E) > = \gamma E_{0\mathrm{n}} \ln \frac{E}{E_{0\mathrm{n}}} \tag{3.66}$$

3.9 Appendix C: Orientation correction

To calculate the orientation correction factor $< S >$, let us consider the two versors $\vec{u}$ and $\vec{n}$, perpendicular to the PAH surface and forming between each other the angle ϑ. This configuration defines two possible orientations for the molecule. The average orientation is then given by the following integral:

$$< S >= \frac{1}{2\pi} \int \vec{u} \cdot \vec{n} \, \mathrm{d}\Omega \tag{3.67}$$

where $\mathrm{d}\Omega = \sin\vartheta \, \mathrm{d}\vartheta \, \mathrm{d}\varphi$ is the solid angle element and $\vec{u} \cdot \vec{n} = \cos\vartheta$ is the scalar product between the two versors. With these substitutions we obtain

$$< S >= \frac{1}{2\pi} \int_{\varphi=0}^{2\pi} \mathrm{d}\varphi \int_{\vartheta=0}^{\pi/2} \cos\vartheta \, \sin\vartheta \, \mathrm{d}\vartheta \; = \; \frac{1}{2} \tag{3.68}$$

Acknowledgements

We are grateful to L. Allamandola and L. Verstraete for useful discussions, and we acknowledge the referee for careful reading and helpful comments. E.R.M. thanks G. Lavaux for support and technical assistance and acknowledges financial support by the EARA Training Network (EU grant MEST-CT-2004-504604).

Chapter 4

PAH processing in a hot gas

Abstract. PAHs are thought to be a ubiquitous and important dust component of the interstellar medium. However, the effects of their immersion in a hot (post-shock) gas have never before been fully investigated. The aim of this work is to study the effects of energetic ion and electron collisions on PAHs in the hot post-shock gas behind interstellar shock waves. We calculate the ion-PAH and electron-PAH nuclear and electronic interactions, above the carbon atom loss threshold, in HII regions and in the hot post-shock gas for temperatures ranging from $10^3 - 10^8$ K. PAH destruction is dominated by He collisions at low temperatures ($T < 3{\times}10^4$ K), and by electron collisions at higher temperatures. Small PAHs are destroyed faster for $T < 10^6$ K, but the destruction rates are roughly the same for all PAHs at higher temperatures. The PAH lifetime in a tenuous hot gas ($n_{\rm H} \approx 0.01$ cm^{-3}, $T \approx 10^7$ K), typical of the coronal gas in galactic outflows, is found to be about thousand years, orders of magnitude shorter than the typical lifetime of such objects. In a hot gas, PAHs are principally destroyed by electron collisions and not by the absorption of X-ray photons from the hot gas. The resulting erosion of PAHs occurs via C_2 loss from the periphery of the molecule, thus preserving the aromatic structure. The observation of PAH emission from a million degree, or more, gas is only possible if the emitting PAHs are ablated from dense, entrained clumps that have not yet been exposed to the full effect of the hot gas.

E. R. Micelotta, A. P. Jones, A. G. G. M. Tielens
accepted for publication in Astronomy & Astrophysics

4.1 Introduction

The mid-infrared spectral energy distribution of the general interstellar medium of galaxies is dominated by strong and broad emission features at 3.3, 6.2, 7.7 and 11.3 μm. These features are now univocally attributed to vibrational fluorescence of UV pumped, large ($\simeq$ 50 C-atoms) Polycyclic Aromatic Hydrocarbon (PAHs) molecules. These large molecules are very abundant (3×10^{-7} relative to H-nuclei) and ubiquitous in the ISM (for a recent review see Tielens 2008). Besides large PAH molecules, the spectra also reveal evidence for clusters of PAHs – containing some hundreds of carbon atoms – and very small grains ($\simeq$ 30 Å). Indeed, PAHs seem to represent the extension of the interstellar dust size distribution into the molecular domain (e.g. Desert et al. 1990; Draine & Li 2001).

PAH molecules are an important component of the ISM, for example, dominating the photoelectric heating of neutral atomic gas and the ionization balance of molecular clouds. Small dust grains and PAHs can also be important agents in cooling a hot gas, at temperatures above $\sim 10^6$ K (e.g. Dwek 1987), through their interactions with thermal electrons and ions. The energy transferred in electron and ion collisions with the dust is radiated as infrared photons. The evolution of dust in such hot gas ($T \gtrsim 10^6$ K), e.g., within supernova remnants and galactic outflows, is critical in determining the dust emission from these regions and therefore the cooling of the hot gas. The destruction of PAHs and small dust grains in a hot gas may also be an important process in the lifecycle of such species (Dwek et al. 1996; Jones et al. 1996).

Observationally, there is little direct evidence for PAH emission unequivocally connected to the hot gas in supernova remnants. Reach et al. (2006) have identified four supernova remnants with IR colors that may indicate PAH emission. Tappe et al. (2006) have detected spectral structure in the emission characteristics of the supernova remnant N132D in the Large Magellanic Cloud that they attribute to spectral features of PAHs with sizes of $\simeq$ 4000 C-atoms. Bright 8μm emission has been observed by IRAC/Spitzer associated with the X-ray emission from the stellar winds of the ionizing stars in the M17 HII region (Povich et al. 2007). Likely, this emission is due to PAHs – probably, in entrained gas ablated from the molecular clouds to the North and West of the stellar cluster. Finally, bright PAH emission has been detected associated with the hot gas of the galactic wind driven by the starburst in the nucleus of the nearby irregular galaxy, M82 (Engelbracht et al. 2006; Beirão et al. 2008; Galliano et al. 2008b).

Electron and ion interactions with dust and the implications of those interactions for the dust evolution and emission have already been discussed in the literature (e.g. Draine & Salpeter 1979b; Dwek 1987; Jones et al. 1994; Dwek et al. 1996; Jones et al. 1996). In this work we extend this earlier work to the case for PAHs, using our study of PAH evolution due to ion and electron interactions in shock waves in the ISM (Chapter 3 - paper Micelotta et al. 2009a, hereafter MJT09a). Here we consider the fate of PAHs in the hot gas behind fast non-radiative shocks and in a hot gas in general.

The aim of this chapter is to study the PAH stability against electron and ion collisions (H, He and C) in a thermal gas with temperature T in the range 10^3 – 10^8 K.

The chapter is organized as follows: § 4.2 and § 4.3 describe the treatment of ion and electron interactions with PAHs, § 4.4 illustrates the application to PAH processing in a hot gas and § 4.5 presents our results on PAH destruction and lifetime. The astrophysical implications are discussed in § 4.6 and our conclusions summarized in § 4.7.

4.2 Ion interaction with PAHs

4.2.1 Electronic interaction

The ion – PAH collision can be described in terms of two simultaneous processes which can be treated separately (Lindhard et al. 1963): *nuclear stopping* or *elastic energy loss* and *electronic stopping* or *inelastic energy loss*.

The nuclear stopping consists of a binary collision between the incoming ion (projectile) and a single atom in the target material. We do not consider a series of binary collisions because the timescale for the ion – atom interaction is very short, so we can reasonably assume that the interaction is completed before the next ion arrives. A certain amount of energy will be transferred directly to the target atom, which will be ejected if the energy transferred is sufficient to overcome the threshold for atom removal. The physics of the nuclear interaction for a PAH target was presented in Chapter 3 (paper MJT09a). A summary of the theory is provided in §2.2 and we here present the results of our calculation.

In this chapter we focuse on the electronic stopping, which consists of the interaction between the projectile and the electrons of the target PAH, with a subsequent energy transfer to the whole molecule. The resulting electronic excitation energy will be transferred to the molecular vibrations of the PAH through radiationless processes (eg., interconversion & intramolecular vibrational redistribution). The vibrationally excited molecule will decay through either (IR) photon emission or through fragmentation (i.e., H-atom or C_2H_n loss, where $n = 0, 1, 2$).

We do not treat plasmon[1] excitations because we are not considering the quantum nature of the molecule. Ling & Lifshitz (1996) studied plasmon excitation in PAHs by photoionization. They observed a giant collective plasmon resonance in several gas phase PAHs, which is a similar phenomenon to the one observed for C_{60}. However, the dominant decays modes of the plasmon excitation may be electron emission and light emission, while autoionization via the plasmon excitation seems to have a negligible contribution to fragmentation processes.

No specific theory describes the energy transfer to a PAH via electronic excitation, so we adopt the same approach developed by e.g. Schlathölter et al. (1999) and Hadjar et al. (2001) who modelled electronic interactions in fullerene, C_{60}. To calculate the energy transferred to a PAH, we treat the large number of delocalized valence electrons in the molecule as an electron gas, where the inelastic energy loss of traveling ions is due to long range coupling to electron-hole pairs (Ferrell 1979).

In the energy range we consider for this study, the energy transferred scales linearly with the velocity v of the incident ion and can be described in term of the stopping power S, which is widely used in the treatment of ion-solid collisions. The stopping

---

[1] A plasmon is a collective excitation involving the simultaneous coherent motions of the less tightly bound electrons in an absorber.

power is defined as the energy loss per unit length and has the form of a friction force:

$$S = \frac{\mathrm{d}T}{\mathrm{d}s} = -\,\gamma(r_s)\,v \tag{4.1}$$

where $\mathrm{d}T$ is the energy loss over the pathlength $\mathrm{d}s$ (Sigmund 1981). The total energy loss can then be obtained integrating Eq. 4.1

$$T_e = \int \gamma(r_s)\,v\,\mathrm{d}s \tag{4.2}$$

The friction coefficient γ (Puska & Nieminen 1983) depends on the density parameter $r_s = \left(\frac{4}{3}\pi n_0\right)^{-1/3}$ which is a function of the valence electron density n_0. The choice of the valence electron density is a delicate issue for PAHs. In the case of fullerene, this is assumed to be the spherically symmetric jellium shell calculated by Puska & Nieminen (1993), which can be approximated by the following expression (Hadjar et al. 2001):

$$n_0 = 0.15\,\exp\left[-(r-6.6)^2\,/\,2.7\right] \tag{4.3}$$

where r (in atomic units, a.u.[2]) is the distance from the fullerene center. The electron density decays outside the shell and toward the center in such a way that the major contribution comes from the region with $4 < r < 9$.

The similarity in π electronic structure and bonding allows us to apply this jellium model also to PAHs. However, the spherical geometry is clearly not appropriate for PAHs, which we model instead as a thick disk analogously to the distribution from Eq. 4.3

$$n_0 = 0.15\,\exp\left[-(x)^2\,/\,2.7\right] \tag{4.4}$$

where x is the coordinate along the thickness of the disk. This electron density peaks at the center of the molecule and vanishes outside, leading to a thickness $d\ \sim 4.31$ Å. The radius R of the disk is given by the usual expression for the radius of a PAH: $a_{\mathrm{PAH}} = R = 0.9\,\sqrt{(}N_{\mathrm{C}})$ Å, where N_{C} is the number of carbon atoms in the molecule (Omont 1986). For a 50 C-atoms PAH, $R = 6.36$ Å.

To calculate the energy transferred from Eq. 4.2, we adopt the coordinate system shown in Fig. 4.1, where the pathlength through the PAH s is expressed as a function of the coordinate x and of the angle ϑ between the axes of the molecule and the direction of the incoming ion. In this way for each trajectory given by ϑ the corresponding energy transferred can be computed. We have $\mathrm{d}x = \mathrm{d}s\,\cos\,\vartheta$ and the electron density is then given by

$$n_0(s,\vartheta) = 0.15\,\exp\left[-(s\,\cos\,\vartheta)^2\,/\,2.7\,\right] \tag{4.5}$$

The density parameter can be rewritten as $r_{\mathrm{s}}(s,\vartheta) = \left(\frac{4}{3}\pi n_0(s,\vartheta)\right)^{-1/3}$ The friction coefficient γ has been calculated by Puska & Nieminen (1983) for various projectile ions and r_{s} values. It can be interpolated by the exponential function

$$\gamma(r_{\mathrm{s}}) = \Gamma_0\,\exp\left[\frac{-(r_{\mathrm{s}}(s,\vartheta)-1.5)}{R_2}\right] \tag{4.6}$$

---

[2] Length (a.u.) = a_0 = 0.529 Å, Velocity (a.u.) = 0.2 $\sqrt{E(\mathrm{keV/amu})}$, Energy (a.u.) = 27.2116 eV

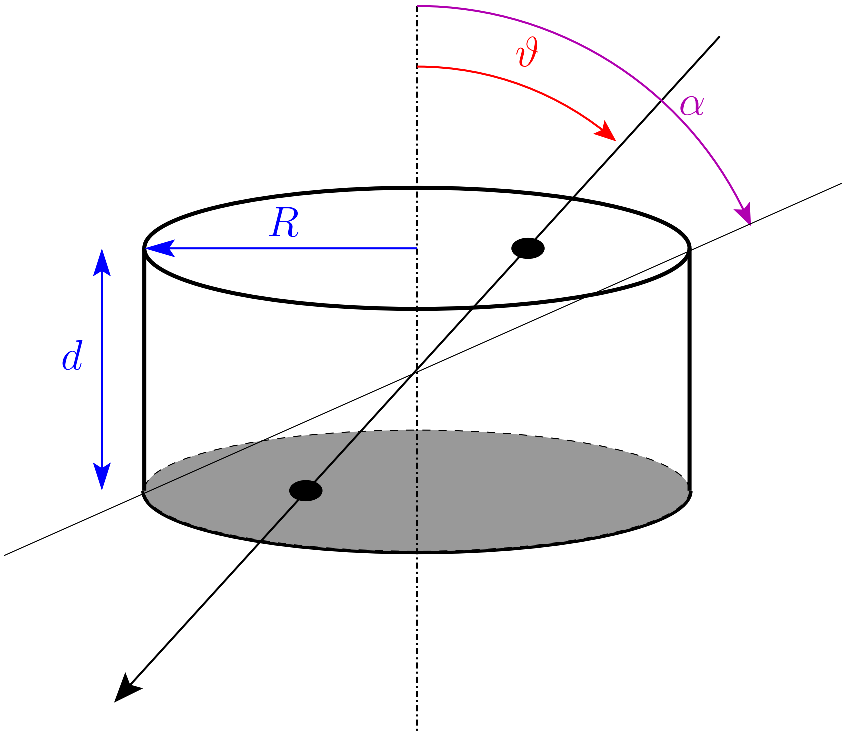

Figure 4.1 — The coordinate system adopted to calculate the energy transferred to a PAH via electronic excitation by ion collisions and by impacting electrons. The molecule is modeled as a disk with radius R and thickness d. The trajectory of the incoming particle is identified by the angle ϑ, while the angle α corresponds to the diagonal of the disk.

where Γ_0 is the value of γ when $r_s = 1.5$. For hydrogen, helium and carbon the fit parameter R_2 equals 2.28, 0.88 and 0.90, respectively.

The energy transferred is then given by the following equation

$$T_e(\vartheta) = 27.2116 \int_{-R/\sin\vartheta}^{R/\sin\vartheta} v\,\gamma(r_s)\,\mathrm{d}s \tag{4.7}$$

with $\gamma(r_s)$ from Eq. 4.6. The constant 27.2116 converts the dimensions of T_e from atomic units to eV. For a given velocity of the incident particle, the value of T_e will be maximum for $\vartheta = \pi/2$ ($s = 2R$, the longest pathlength) and minimum for $\vartheta = 0, \pi$ ($s = d$, the shortest pathlength). The deposited energy also increases with the pathlength across the molecule, and then will be higher for larger PAHs impacted under a glancing collision.

The energy transferred determines the PAH dissociation probability upon electronic excitation, which is required to quantify the destruction induced by inelastic energy loss in the hot gas (see §4.4).

4.2.2 Nuclear interaction above threshold

In the present study we have to consider not only the electronic interaction described above, but the nuclear part of the ionic collision as well. The theory of nuclear interaction above threshold has been described in detail in Chapter 3. We summarize here for clarity the essential concepts and the equations which will be used in the following.

For the nuclear interaction we consider only collisions above threshold, i.e. collisions able to transfer more than the minimum energy T_0 required to remove a C-atom from the PAH. The energy transferred by collisions below threshold goes into molecular vibrations of the PAH, but is not sufficient to induce any fragmentation.

To calculate the PAH destruction due to nuclear interaction, we use the rate of collisions above threshold between PAHs and ions in a thermal gas, as given by Eq. 22 in Chapter 3:

$$R_{\mathrm{n,T}} = N_{\mathrm{C}}\, 0.5\, \chi_i\, n_{\mathrm{H}} \int_{v_0}^{\infty} F_{\mathrm{C}} v\, \sigma(v)\, f(v,T)\, \mathrm{d}v \tag{4.8}$$

where $f(v,T)$ is the Maxwellian velocity distribution function for ion, i, in the gas, F_{C} is the Coulombian correction factor, $\sigma(v)$ is the nuclear interaction cross section per atom above threshold (Eq. 15 in Chapter 3 where E is the kinetic energy corresponding to v), and the factor 1/2 takes the averaging over the orientation of the disk into account.

For T_0 we adopt a value of 7.5 eV (see discussion in Chapter 3, § 3.2.2.1). The kinetic energy required for the incoming ion to transfer T_0 is the critical energy E_0. The lower integration limit v_0 in Eq. 4.8 is the critical velocity corresponding to $E_{0\mathrm{n}}$, which is the minimum kinetic energy for the projectile to have the nuclear interaction cross section different from zero (cf. § 3.2.2 in Chapter 3).

4.3 Electron collisions with PAHs

Fast electrons are abundant in a hot gas. Because of their low mass, they can reach very high velocities with respect to the ions, and hence high rates of potentially destructive collisions. We consider gas temperatures up to 10^8 K, corresponding to a thermal electron energy of $\sim$10 keV, well below the relativistic limit of $\sim$500 keV. Under these low-energy conditions, with respect to the relativistic regime, elastic collisions between electrons and target nuclei are not effective. The energy transfer occurs through inelastic interactions with target electrons (as for electronic excitation by impacting ions), which lead to a collective excitation of the molecule, followed eventually by dissociation or relaxation through IR emission.

The calculation of the energy transferred by such 'slow' electrons is in fact a delicate matter. The theory developed under the first Born approximation (Bethe 1930) can be applied only to the most energetic electrons (around few keV) but is unsuitable for the rest of our range. At low energies ($<$10 keV), where the first Born approximation is no longer valid, the Mott elastic cross section must be used instead of the conventional Rutherford cross section (Mott & Massey 1949; Czyzewski et al. 1990). The Monte Carlo program CASINO (Hovington et al. 1997) computes the Mott cross sections in the simulation of electron interactions with various materials. Unfortunately the stopping power $\mathrm{d}E/\mathrm{d}x$ is not included in the program output. An empirical expression for $\mathrm{d}E/\mathrm{d}x$ has been proposed by Joy & Luo (1989), which nevertheless is reliable only down to 50 eV, while we are interested in the region between 10 and 50 eV as well.

We decided thus to derive the electron stopping power from experimental results. Measurements of the electron energy loss in PAHs are not available in our energy range

Table 4.1 — Analytical fit to the electron stopping power in solid carbon.

$S(E) = h\,\log(1 + a\,E)\,/\,f\,E^g + b\,E^d + c\,E^e$			
a	b	c	d
-0.000423375	-3.57429×10^{-11}	-3.37861×10^{-7}	-3.18688
e	f	g	h
-0.587928	-0.000232675	1.53851	1.41476

of interest, so we use the measurement of $\mathrm{d}E/\mathrm{d}x$ in solid carbon for electrons with energy between 10 eV and 2 keV (Joy 1995). The data points are well fitted (to within few %) by the following function:

$$S(E) = \frac{h\,\log(1 + a\,E)}{f\,E^g + b\,E^d + c\,E^e} \tag{4.9}$$

where E is the electron energy (in keV). The values of the fitting parameters are reported in Table 4.1. $S(E)$ has the same functional form as the ZBL reduced stopping cross section for nuclear interaction (cf. § 3.2.1 in Chapter 3). The datapoints and the fitting function are shown in the top panel of Fig. 4.2.

The stopping power increases sharply at low electron energies, reaches its maximum at ∼0.1 keV, and decreases smoothly afterwards. Between 0.01 and 0.1 keV a small variation of the energy of the incident electron will translate into a large change in the transferred energy per unit length. The shape of $S(E)$ implies that only those electrons with energies that fall in a well defined window will efficiently transfer energy, while electrons below ∼0.02 keV and above ∼2 keV are not expected to contribute significantly to PAH excitation.

Once the stopping power $\mathrm{d}E/\mathrm{d}x$ is known, we can calculate the energy transferred by an electron of given energy when travelling through the PAH. We adopt the same configuration used for electronic interaction, shown in Fig. 4.1. The trajectory of the incoming electron is defined by its impact angle ϑ and by the geometry of the molecule.

Because the thickness of the PAH is non-negligible with respect to its radius, the stopping power is not constant along the electron path. To calculate the energy loss we thus follow the procedure described below. We have $\mathrm{d}E/\mathrm{d}x = -S(E)$, then

$$\int \mathrm{d}x = -\int \frac{\mathrm{d}E}{S(E)} = F(E) \tag{4.10}$$

Thus, $x_1 - x_0 = -[F(E_1) - F(E_0)]$ where $x_1 - x_o = l(\vartheta)$ is the maximum pathlength through the PAH. From inspection of Fig. 4.1, one can see that, if $|\tan(\vartheta)| < \tan(\alpha)$, $l(\vartheta) = d/|\cos\vartheta|$, otherwise $l(\vartheta) = 2R/|\sin\vartheta|$. E_0 is the initial energy of the impacting electron, E_1 is the electron energy after having travelled the distance $l(\vartheta)$, which needs to be calculated so we can then determine the energy transferred to the PAH

$$T_{\mathrm{elec}}(\vartheta) = E_0 - E_1 \tag{4.11}$$

The integral F, calculated numerically as a function of E, is shown in the bottom panel of Fig. 4.2. We recognize that for low energies, F rises sharply, reflecting the small energy stopping power in this energy range (cf., top panel in Fig. 4.2). For higher energies, $F(E)$ rises slowly (and linearly) with increasing energy over the relevant energy range. We note that the initial rise depends strongly on the (uncertain) details of the stopping power at low energies. However, it is of no consequence in our determination of the amount of energy deposited since we are only concerned with those collisions for which the energy deposition is in excess of the threshold energy ($\gtrsim$10 eV) over a pathlength of $\simeq 10-20$ Å. Or to phrase it differently, at low energies a much larger pathlength has to be traversed (than is relevant for PAHs) in order to transfer sufficient energy to cause fragmentation. Then, since we know E_0, we can calculate $F(E_0)$, and $F(E_1)$ is then given by $F(E_0) - l(\vartheta)$. We also calculated E as a function of $F(E)$. We can then determine E_1 from $F(E_1)$ and, finally, $T_{\rm elec}$ from Eq. 4.11.

4.4 PAH destruction

4.4.1 Dissociation probability

Ion or electronic collisions (or UV photon absorption) can leave the molecule internally (electronically) excited with an energy $T_{\rm E}$. Internal conversion transfers this energy to vibrational modes, and the molecule can then relax through dissociation or IR emission. These two processes[3] are in competition with each other. To quantify the PAH destruction due to ion and electron collisions we need to determine the probability of dissociation rather than IR emission.

In the microcanonical description of a PAH, the internal energy, $T_{\rm E}$, is (approximately) related to the effective temperature of the system, $T_{\rm eff}$, by the following equation

$$T_{\rm eff} \simeq 2000 \left(\frac{T_{\rm E}({\rm eV})}{N_{\rm C}}\right)^{0.4} \left(1 - 0.2\,\frac{E_0({\rm eV})}{T_{\rm E}({\rm eV})}\right) \tag{4.12}$$

where E_0 is the binding energy of the fragment (Tielens 2005). This effective temperature includes a correction for the finite size of the heat bath in the PAH. The temperature $T_{\rm eff}$ is defined through the unimolecular dissociation rate, $k_{\rm diss}$, written in Arrhenius form

$$k_{\rm diss} = k_0\,(T_{\rm eff})\,\exp\left[-\,E_0/k\,T_{\rm eff}\right] \tag{4.13}$$

where $k = 8.617\times10^{-5}$ eV/K is the Boltzmann's constant (cf. Tielens 2005).

Consider the competition between photon emission at a rate $k_{\rm IR}$ (photons s^{-1}) and dissociation at a rate of $k_{\rm diss}$ (fragments s^{-1}). For simplicity, we will assume that all photons have the same energy, $\Delta\varepsilon$. The probability that the PAH will fragment between the nth and $(n+1)$th photon emission is given by

$$\varphi_n = p_{n+1} \prod_{i=0}^{n} (1 - p_i) \tag{4.14}$$

---

[3] Relaxation through thermionic electron emission is negligible.

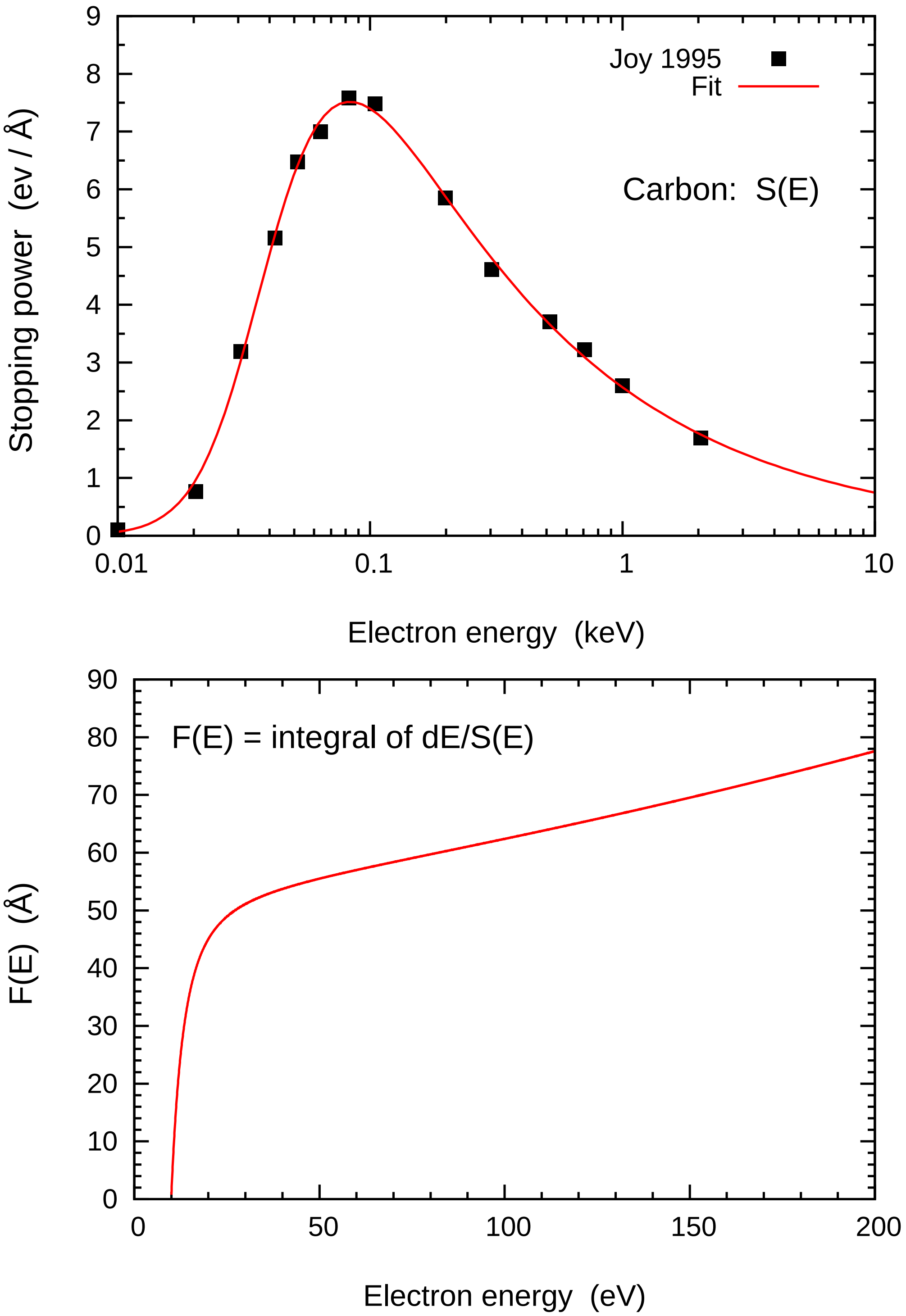

Figure 4.2 — Top panel - Experimental measurement of dE/dx in solid carbon for electrons with energy between 10 eV and 2 keV, from Joy (1995), overlaid with the fitting function $S(E)$ (solid line). Bottom panel - Integral F calculated numerically as a function of the energy of the incident electron, E.

The (un-normalized) probability per step p_i is given by $p_i = k_{\rm diss}(E_i)/k_{\rm IR}(E_i)$ and $E_i = (T_{\rm E} - i \times \Delta\varepsilon)$, with $T_{\rm E}$ the initial internal energy, coincident with the energy transferred into the PAH. The total dissociation probability is then given by

$$P(n_{\rm max}) = \sum_{n=0}^{n_{\rm max}} \varphi_n \tag{4.15}$$

If we ignore the dependence of $k_{\rm IR}$ on E_i, the temperatures (Eq. 5.14) drop approximately by $T_i/T_{i-1} = (1 - 0.4\Delta\varepsilon/T_{\rm E})$. The probability ratio is approximately:

$$\frac{p_i}{p_{i-1}} = \exp\left[\left(\frac{E_0}{kT_{i-1}}\right) 0.4\,\frac{\Delta\varepsilon}{\varepsilon}\right] \tag{4.16}$$

These equations become very difficult to solve in closed form. However, let us just assume that p_i does not vary and is given by $p_{\rm av}$. Then we have the total un-normalized dissociation probability

$$P(n_{\rm max}) = (n_{\rm max} + 1)\, p_{\rm av} = \frac{k_0 \exp\left[-E_0/k\,T_{\rm av}\right]}{k_{\rm IR}/(n_{\rm max} + 1)} \tag{4.17}$$

where we adopt $k_{\rm IR}$ = 100 photons s^{-1} (Jochims et al. 1994b), and the average temperature is chosen as the geometric mean

$$T_{\rm av} = \sqrt{T_0 \times T_{n_{\rm max}}} \tag{4.18}$$

where T_0 and $T_{n_{\rm max}}$ are the effective temperatures corresponding to $T_{\rm E}$ (initial internal energy equal to the energy transferred) and $(T_{\rm E} - n_{\rm max} \times \Delta\varepsilon)$ (internal energy after the emission of $n_{\rm max}$ photons). For the energy of the emitted IR photon we adopt the value $\Delta\varepsilon$ = 0.16 eV, corresponding to a typical CC mode.

If the p_i's were truly constant, then $n_{\rm max}$ would be $n_{\rm max}$ = $(T_{\rm E} - E_0)/\Delta\varepsilon$. However, they do decrease. So, rather we take it to be when the probability per step has dropped by a factor 10. A direct comparison between the full evaluation and this simple approximation yields $n_{\rm max}$ = 10, 20 and 40 for $N_{\rm C}$ = 50, 100 and 200 respectively. The quantity $n_{\rm max}$ scales with $N_{\rm C}$ because for a constant temperature (eg., required to get the dissociation to occur), the internal energy has to scale with $N_{\rm C}$. As a result, the number of photons to be emitted also has to scale with $N_{\rm C}$.

The choice of the values to adopt for k_0 and E_0 is a delicate matter. In the laboratory the dissociation of highly vibrationally excited PAHs is typically measured on timescales of 1-100 μs because either the molecules are collisionally de-excited by ambient gas or the molecules have left the measurement zone of the apparatus. In contrast, in the ISM, the competing relaxation channel is through IR emission and occurs typically on a timescale of 1 s. As is always the case for reactions characterized by an Arrhenius law, a longer timescale implies that the internal excitation energy can be lower. This kinetic shift is well established experimentally and can amount to many eV. Moreover, only small PAHs (up to 24 C-atoms) have been measured in the laboratory and the derived rates have to be extrapolated to much larger ($\sim$ 50 C-atoms) PAHs that are astrophysically relevant. In an astrophysical context, the unimolecular dissociation of highly vibrationally excited PAHs – pumped by FUV photons – has been studied experimentally by Jochims et al. (1994b) and further analyzed by Le Page et al. (2001). Here, we will modify the analysis of Tielens (2005) for H-loss by UV pumped PAHs to determine the parameters for carbon loss. The dissociation rate – given by Eq. 4.13 – is governed by two factors, the pre-exponential factor k_0 and the energy E_0. The pre-exponential factor is given by

$$k_0 = \frac{kT_{\rm eff}}{h} \exp\left[1 + \frac{\Delta S}{R}\right] \tag{4.19}$$

where ΔS is the entropy change which we set equal to 10 cal mole^{-1} (Ling & Lifshitz 1998). We will ignore the weak temperature dependence of k_0 in the following and adopt 1.4×10^{16} s^{-1}. The parameter E_0 can now be determined from a fit to the experiments by Jochims et al. (1994b) on small PAHs. These experiments measured the appearance energy $E_{\rm ap}$ – the internal energy at which noticable dissociation of the PAH first occurred. The rate at which this happened was assumed to be 10^4 s^{-1}. Adopting this value, the appearance energy can be estimated from Eq. 4.13. The results of our analysis are shown in Fig. 4.3. The internal energy required to dissociate a PAH depends strongly on the PAH size. Likewise the kinetic shift associated with the relevant timescale at which the experiment was performed is quite apparent. Indeed, this kinetic shift can amount to tens of eV for relevant PAHs.

The derived Arrhenius energy of 3.65 eV is small compared to the binding energy of a C_2H_2 group in a PAH (4.2 eV, Ling & Lifshitz 1998). This is a well known problem in statistical unimolecular dissociation theories (cf. Tielens 2008). We emphasize that these results show that a typical interstellar PAH with a size of 50 C-atoms would have a dissociation probability of $\sim 1/2$ after absorption of an FUV photon of $\sim$12 eV (cf. Fig. 4.3). Hence, PAHs would be rapidly lost in the ISM through photolysis. It seems that the experiments on small PAHs cannot be readily extrapolated to larger, astrophysically relevant PAHs. Possibly, this is because experimentally C_2H_2 loss has only been observed for very small catacondensed PAHs with a very open carbon skeleton (e.g., naphthalene, anthracene, and phenanthrene) which are likely much more prone to dissociation than the astrophysically more relevant pericondensed PAHs. Indeed, the small pericondensed PAHs, pyrene and coronene did not show any dissociation on the experimental timescales (Jochims et al. 1994b; Ling & Lifshitz 1998).

Turning the problem around, we can determine the Arrhenius energy, E_0, as a function of the dissociation probability by adopting an IR relaxation rate of 1 s^{-1} and an internal excitation energy equal to a typical FUV photon energy (12 eV). The results for a 50 C-atom PAH are shown in Fig 4.4. If we adopt a lifetime, $\tau_{\rm PAH}$, of 100 million years, a PAH in the diffuse ISM will have typically survived some $\sigma_{\rm uv}\, N_{\rm uv}\, \tau_{\rm PAH} = 2 \times 10^6\, N_{\rm C}$ UV photon absorptions (with $\sigma_{\rm uv} = 7 \times 10^{-18}$ cm^2, $N_{\rm uv} = 10^8$ photons cm^{-2} s^{-1} in a Habing field). Hence, if the lifetime of the smallest PAHs in the ISM (eg., with $N_{\rm C} \simeq 50$ C-atom) is set by photodissociation of the C-skeleton, the probability for dissociation has to be 5×10^{-7} corresponding to an Arrhenius energy of 4.6 eV (Fig. 4.4). We note that in a PDR the photon flux is higher ($G_0 \sim 10^5$) while the lifetime (of the PDR) is smaller ($\tau_{\rm PDR} \simeq 3 \times 10^4$ yr), resulting in 6×10^7 UV photons absorbed over the PDR lifetime. Survival of PAHs in a PDR environment would therefore require a somewhat

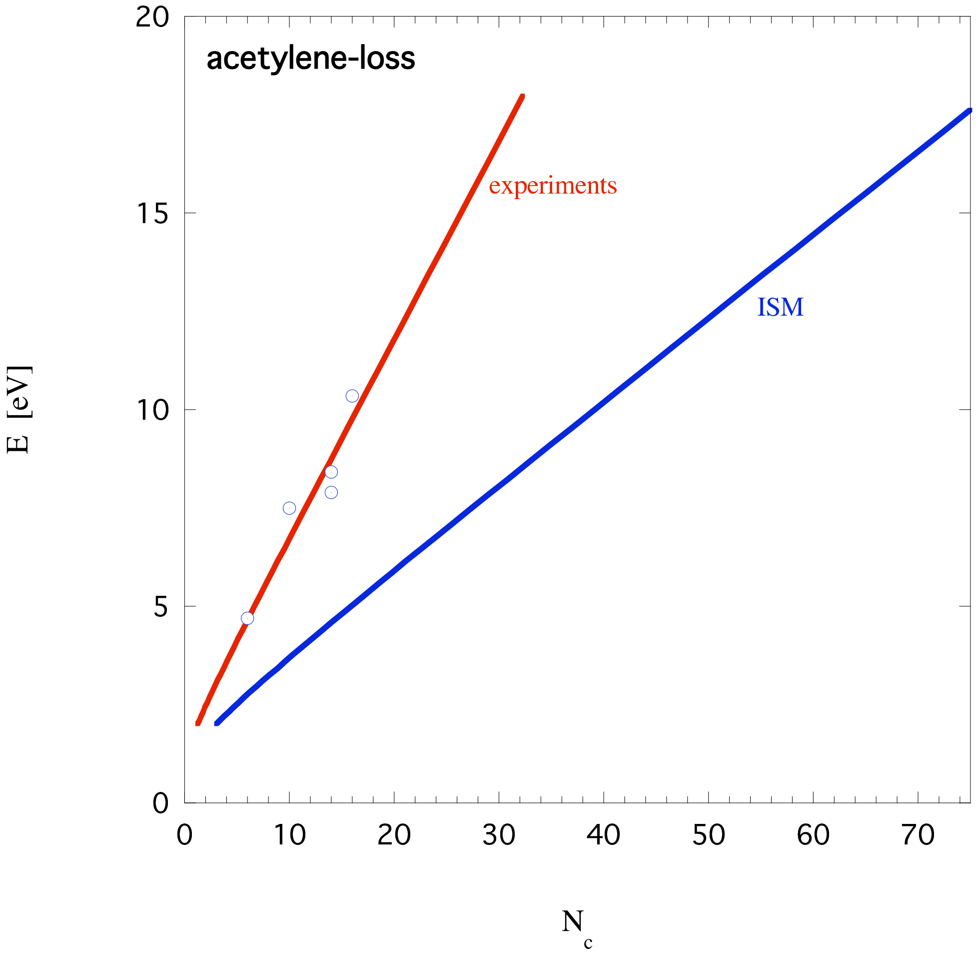

Figure 4.3 — The appearance energy as a function of the number of C-atoms in the PAH. The red line provides a fit to the experimental data using Eq. 4.13 for an assumed pre-exponential factor $k_0 = 1.4 \times 10^{16}$ and a (fitted) Arrhenius energy, $E_0 = 3.65$ eV. The data points are the experimental results of Jochims et al. (1994b). The blue line is the appearance energy for ISM conditions (eg., at a rate of 1 s^{-1}).

larger E_0 (or alternatively, only slightly larger PAHs could survive in such an environment).

We note that the binding energy of a C_2H_2 group to small PAHs is estimated to be 4.2 eV and is probably somewhat larger for a 50 C-atom condensed PAH. Loss of pure carbon, on the other hand, requires an energy of 7.5 eV, close to the binding energy of C to graphite. Loss of C_2 from fullerenes has a measured E_0 of 9.5 ± 0.1 eV (Tomita et al. 2001). These latter two unimolecular dissociation channels are for all practical purposes closed under interstellar conditions. Finally, likely, H-loss will be the dominant destruction loss channel for large PAHs ($E_0 = 3.3$ eV), leading to rapid loss of all H's (Le Page et al. 2001; Tielens 2005). The resulting pure C-skeleton may then isomerize to much more stable carbon clusters, in particular fullerenes, and this may be the dominant 'loss' channel for interstellar PAHs (cf. Tielens 2008, and references therein). It is clear that there are many uncertainties in the chemical destruction routes of interstellar PAHs and that these can only be addressed by dedicated experimental studies. For now, in our analysis of the unimolecular dissociation of PAHs – excited by electron

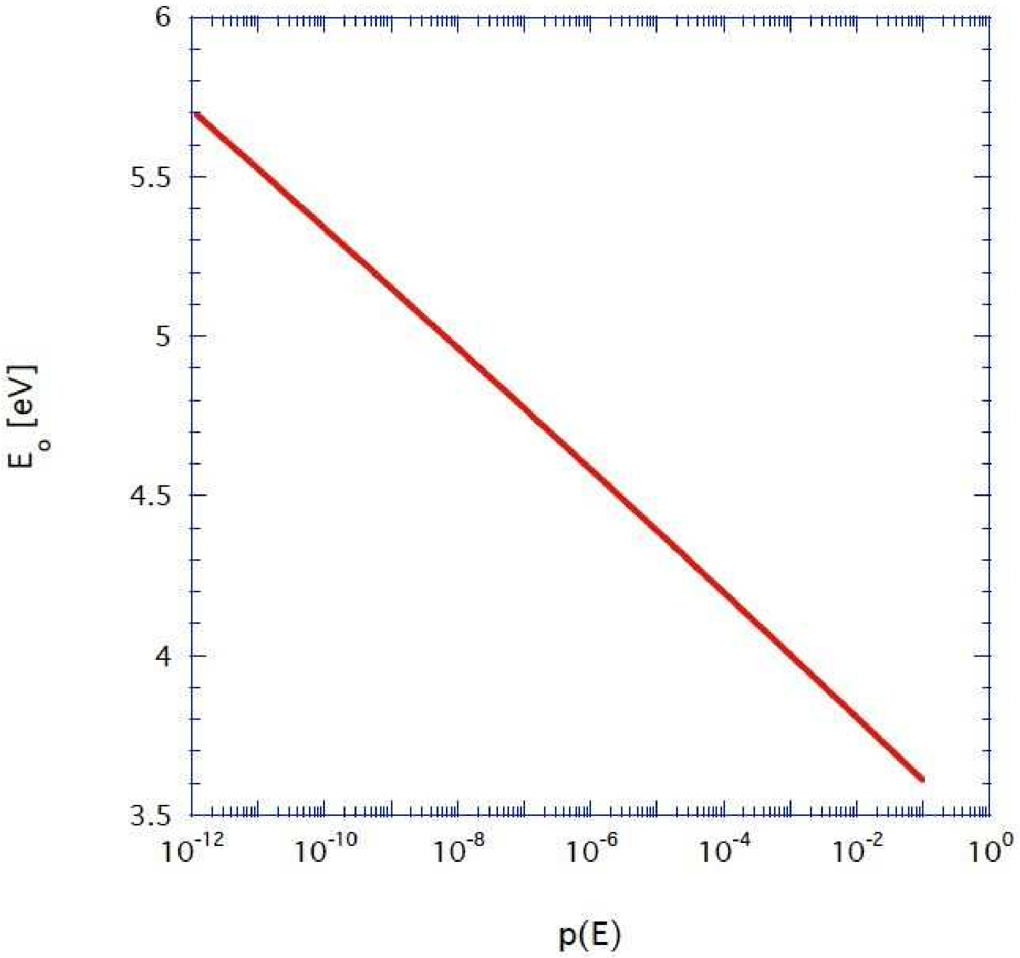

Figure 4.4 — The probability for dissociation of a 50 C-atom PAH excited by 10 eV as a function of the Arrhenius energy, E_0.

or ion collisions – we will adopt $E_0 = 4.6$ eV as a standard value. We will however also examine the effects of adopting $E_0 = 3.65$ eV (eg., $p = 1/2$) and $E_0 = 5.6$ eV (eg., $p = 3 \times 10^{-12}$).

4.4.2 Collision rate

Once the dissociation probability is determined, we can calculate the the destruction rate through electronic excitation following electron or ion collision. Adopting the configuration shown in Fig. 4.1, the destruction rate is given by

$$R_{\rm e} = v\,\chi\,n_{\rm H}\,F_{\rm C}\,\frac{1}{2\pi}\int {\rm d}\Omega\,\sigma_{\rm g}(\vartheta)\,P(v,\vartheta) \tag{4.20}$$

with $\Omega = \sin\vartheta {\rm d}\vartheta {\rm d}\varphi$, φ running from 0 to 2π and ϑ from 0 to $\pi/2$. Eq. 4.20 can be re-written as

$$R_{\rm e} = v\,\chi\,n_{\rm H}\,F_{\rm C}\int_{\vartheta=0}^{\pi/2} \sigma_{\rm g}(\vartheta)\,P(v,\vartheta)\,\sin\vartheta\,{\rm d}\vartheta \tag{4.21}$$

The term v is the velocity of the incident particle, χ is the ion/electron relative abundance in the gas, and F_C is the Coulombian correction factor, taking into account the fact that both target and projectiles are charged, and thus the collision cross section could be enhanced or diminished depending on the charge sign. The electron coulombian factor is always equal to 1 (to within 1%) because electrons have low mass. For a fixed temperature they reach higher velocities, with respect to the ions, and are thus less sensitive to the effects of the Coulombian field. The quantity ϑ is the angle between the vertical axes of the PAH and the direction of the projectile. The term σ_g is the geometrical cross section seen by an incident particle with direction defined by ϑ. The PAH is modelled as a thick disk with radius R and thickness d. The cross section is then given by

$$\sigma_g = \pi R^2 \cos\vartheta + 2Rd\sin\vartheta \tag{4.22}$$

which reduces to $\sigma_g = \pi R^2$ for $\vartheta = 0$ (face-on impact) and to $\sigma_g = 2Rd$ for $\vartheta = \pi/2$ (edge-on impact). The term $P(v, \vartheta)$ represents the total probability for dissociation upon electron collisions and electronic excitation, for a particle with velocity v_{PAH} and incoming direction ϑ. It was calculated from Eq. 5.12 using the appropriated value of the energy transferred: T_{elec} for electrons (Eq. 4.11) and T_{e} for electronic excitation (Eq. 4.7)

We are considering a hot gas and therefore we are interested in the thermal collision rate, given by

$$R_{\mathrm{e,T}} = \int_{\mathrm{v_{0,e}}}^{\infty} R_{\mathrm{e}}(v)\, f(v, T)\,\mathrm{d}v \tag{4.23}$$

where $v_{0,\mathrm{e}}$ is the electron/ion velocity corresponding to the electronic dissociation energy E_0. The temperature T is the same for both ions and electrons, but these latter will reach much larger velocities. From Eq. 4.21 we then expect to find a significantly higher collision rate with respect to the ion case.

4.5 Results

4.5.1 PAH destruction in a hot gas

To describe the destructive effects on PAHs of collisions with ions i (i = H, He, C) and electrons in a thermal gas we have to evaluate the rate constant for carbon atom loss.

For all processes the rate constant J is defined by the ratio $J = R_{\mathrm{T}}/n_{\mathrm{H}}$, where R_{T} is the thermal collision rate appropriate for nuclear and electronic excitation and electron collisions (cf. Eq. 4.8 and 4.23), and n_{H} is the density of hydrogen nuclei. For electronic and electron interactions the rate must be multiplyied by a factor of 2, to take into account the fact that each collision leads to the loss of two carbon atoms.

The electron, nuclear and electronic rate constants for three PAH sizes (Nc = 50, 100 and 200 C-atom) are shown in Fig. 4.5 as a function of the gas temperature. We assume for the nuclear threshold energy T_0 the value of 7.5 eV (Chapter 3), and for the electronic dissociation energy the value 4.58 eV (§ 4.4.1).

For the nuclear interaction, the threshold energy T_0 is independent from the PAH size, so the three curves start at the same temperature (not shown in the plot). The small separation between the curves is due to the fact that the PAH 'surface area' – and hence the rate constant – scales linearly with N_C, therefore J is higher for bigger PAHs.

For nuclear (and electronic) interactions, the rate constants decrease from hydrogen to carbon because of the lower abundance of the heavier projectiles with respect to hydrogen (H : He : C = 1 : 0.1 : 10^{-4}). On the other hand, the nuclear curves shift toward lower temperatures from lighter to heavier projectiles. This is the reflection of the fact that the critical energy of the particle, required to transfer the threshold energy T_0, decreases with increasing mass of the projectile itself. Then, a carbon atom with a temperature of $\sim 4{\times}10^3$ K is hot enough to transfer the energy required for atom removal via nuclear interaction, whereas for hydrogen a temperature of at least 10^4 K is necessary. The almost-constant behaviour after the initial rise reflects the large maximum observed in the nuclear cross section (cf. Fig. 3.2 in Chapter 3).

The dissociation probability $P(n_{\rm max})$ (Eq. 5.12) depends on the binding energy of the fragment E_0, on the PAH size N_C and on the energy transferred (through $T_{\rm av}$), which in turns depends on the initial energy (velocity) of the projectile. For a thermal distribution, this latter will be determined by the gas temperature T.

The electronic rate constant curves for the different PAH sizes are well separated at the lowest temperatures. This reflects the fact that, for a fixed value of the transferred energy and of the electronic dissociation energy E_0, the dissociation probability decreases for increasing N_C because either more energy is required in the bond that has to be broken or because the energy is spread over more vibrational modes and hence the internal excitation temperature is lower. On the other hand, the more energy that is deposited into the PAH, the higher is the dissociation probability. The energy transferred via electronic excitation (and then $T_{\rm av}$) increases with the energy of the projectile up to a maximum value, corresponding to an incident energy of 10 keV for H (and higher for more massive particles), and decreases beyond that for higher energies. The energy content of a thermal gas at $T = 10^8$ K is $\sim$ 9 keV, thus, in the temperature range considered in this study, the energy transferred increases with temperature (energy) and hence the dissociation probability increases as well. This is the basis for the monotonic rise of the electronic rate constant. After the initial separation, the three curves converge, because the rise in the transferred energy compensates the effect of increasing N_C.

As discussed in § 4.3, the energy transferred by impacting electrons rises sharply for energies in excess of 10 eV, peaks at $\sim$ 100 eV and decreases more slowly down to 10 keV. This results in a dissociation probability shaped as a step function: for 10 eV $\lesssim v \lesssim$ 4 keV, $P(n_{\rm max})$ jumps from values close to zero up to 1. These limiting energies apply to a 50 C-atom PAH; for N_C = 200 the width of the step is smaller (100 eV $\lesssim v \lesssim$ 1 keV), due to the fact that for a bigger PAH more energy has to be transferred for dissociation. This behaviour is reflected in the shape of the electron rate constant, where a steep rise is followed by a maximum, which is emphasised by the logarithmic scale used for the plot. As expected, the electron rate constant overcomes the electronic one, except for the highest gas temperatures. This results from the fact that, for a given temperature, electrons can reach higher velocities with respect to the ions (cf. Eq. 4.21 and 4.23).

To summarize, from Fig. 4.5 we can infer that, according to our model, the destruction process is dominated by nuclear interaction with helium at low temperatures

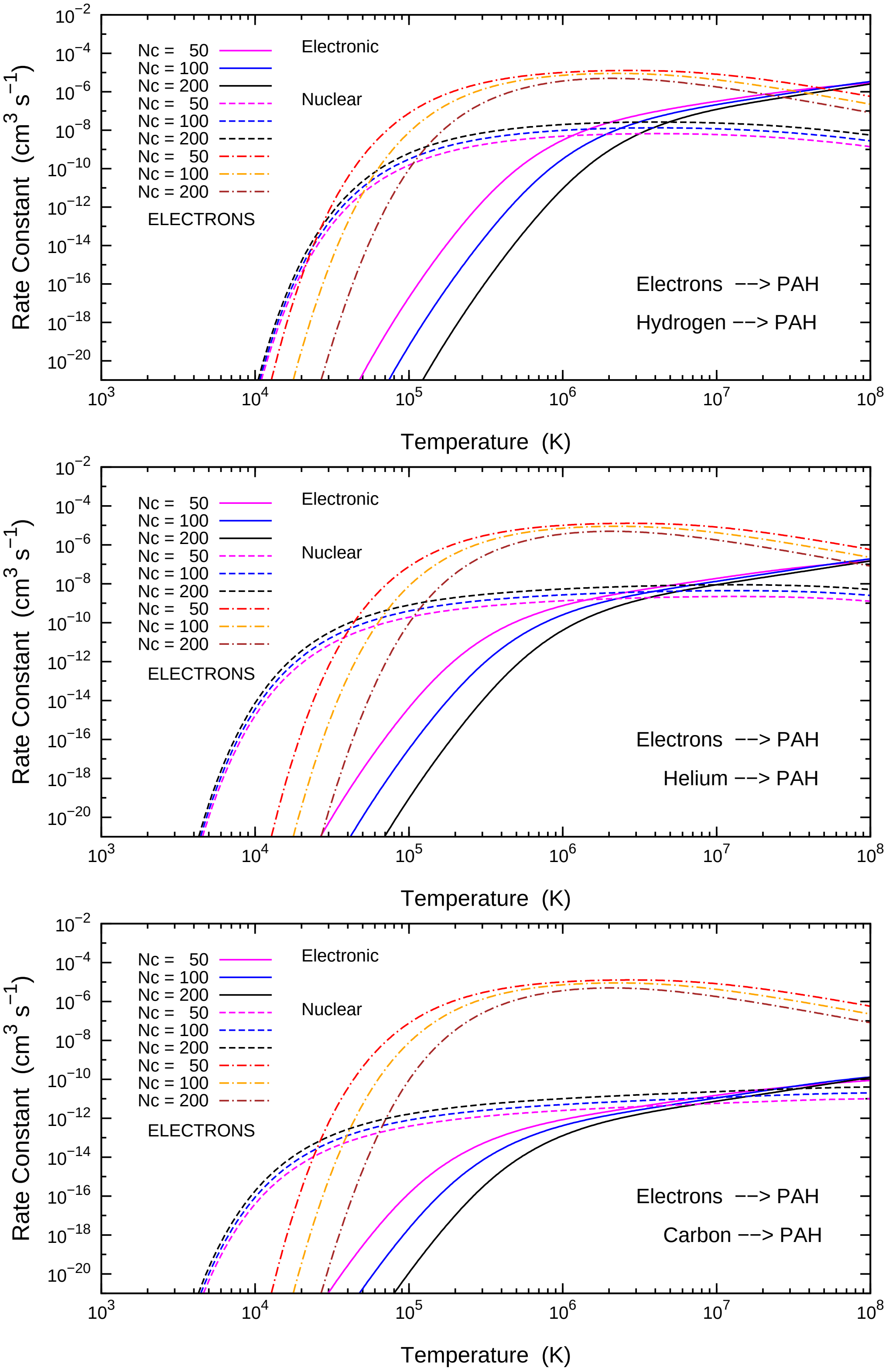

Figure 4.5 — Nuclear (dashed lines), electronic (solid lines) and electron (dashed-dotted lines) rate constant for PAH carbon atom loss due to collisions with H, He, C and electrons in a thermal gas. The rate constants are calculated as a function of the gas temperature for three PAH sizes N_C = 50, 100, 200 C-atoms, assuming the nuclear threshold energy T_0 = 7.5 eV and the electronic dissociation energy E_0 = 4.58 eV.

(below $\sim 3\times10^4$ K), and by electron collisions above this value. Small PAHs are easier destroyed than big ones for temperatures below $\sim 10^6$ K, while the difference in the destruction level reduces significantly for hotter gas.

The calculated rate constants, shown in Fig. 4.5, are well fitted by the function $g(T) = 10^{f(\log(T))}$, where $f(T)$ is a polynomial of order 5

$$f(T) = a + b\,T + c\,T^2 + d\,T^3 + e\,T^4 + f\,T^5 \tag{4.24}$$

For each PAH size we provide the fit to the electron rate constant; for the ions, the fit is over the sum of the nuclear and electronic rate constants, in order to provide an estimate of the global contribution from ionic collisions. The fits are shown in Fig. 4.6, and the fitting parameters are reported in Table 4.2. To provide an example of the accuracy of our fitting procedure, Fig. 4.7 shows the comparison between the calculated rate constant and the corresponding analytical fit, for electrons and helium impacting on a 50 C-atom PAH. The He fit is over the sum of the nuclear and electronic rate constants. The average fitting discrepancy is ~15 % and the fits are therefore well within any uncertainties in the method.

Fig. 4.8 shows the comparison between the carbon loss rate constants for a very big PAH, N_C = 1000, and a 50 C-atom molecule. We assume T_0 = 7.5 eV and E_0 = 4.6 eV. Because of the decrease of the dissociation probability when the PAH size increases, as expected, the electron and electronic rate constants are strongly suppressed, and both curves shift toward higher temperatures. Indeed, for such a big PAH, a much higher internal energy is required to reach the internal temperature where dissociation sets in. On the other hand, the nuclear rate constant increases linearly with the PAH size. As a result, for a 1000 carbon atoms PAH, the nuclear interaction is the dominant (and efficient) destruction mechanism up to $T \sim 2\times10^7$ K. In conclusion, electrons are responsible for the destruction of small/medium size PAH, while for big molecules this role is taken by ions.

As mentioned at the end of §4.1, we examined the effects of adopting different values for the Arrhenius energy, E_0 = 3.65 and 5.6 eV, lower and higher, respectively, than our canonical value 4.6 eV. The results are shown in Fig. 4.9. The dissociation probability decreases for increasing E_0, because more energy is required in the bond that has to be broken. Hence, as expected, both the electron and electronic rate constants decrease in absolute value and shift toward highest temperatures. In particular the electronic thermal shift is very pronounced, indicating how sensitive this process is with respect to the assumed E_0. A variation in the adopted electronic excitation energy translates into a significant variation of the rate constant, reemphasizing the importance of experimental studies of this critical energy.

4.5.2 PAH lifetime

Under the effect of electron and ion collisions in a hot gas, the number of carbon atoms in a PAH molecule varies with time. After a time t, this number is

$$N_C(t) = N_C(0)\exp\left[-t\,/\,\tau_0\right] \tag{4.25}$$

and the number of carbon atoms ejected from this PAH is

$$F_L(t) = \left(1 - \exp\left[-t\,/\,\tau_0\right]\right) \tag{4.26}$$

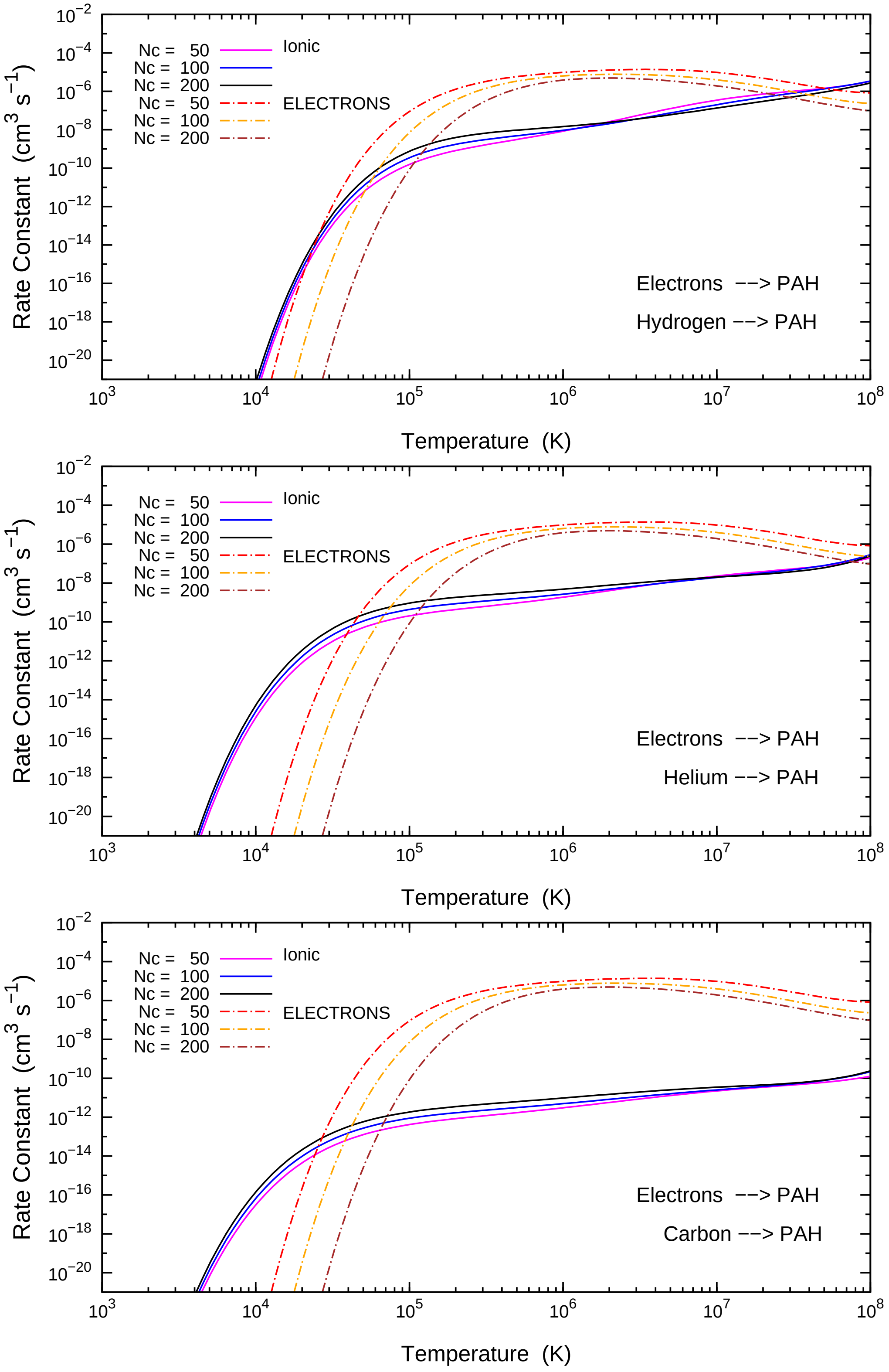

Figure 4.6 — Analytical fits to the calculated rate constants shown in Fig. 4.5. The 'Ionic' curve is the fit to the sum of the nuclear and electronic rate constants, thus represents the total contribution from ion collisions to PAH destruction.

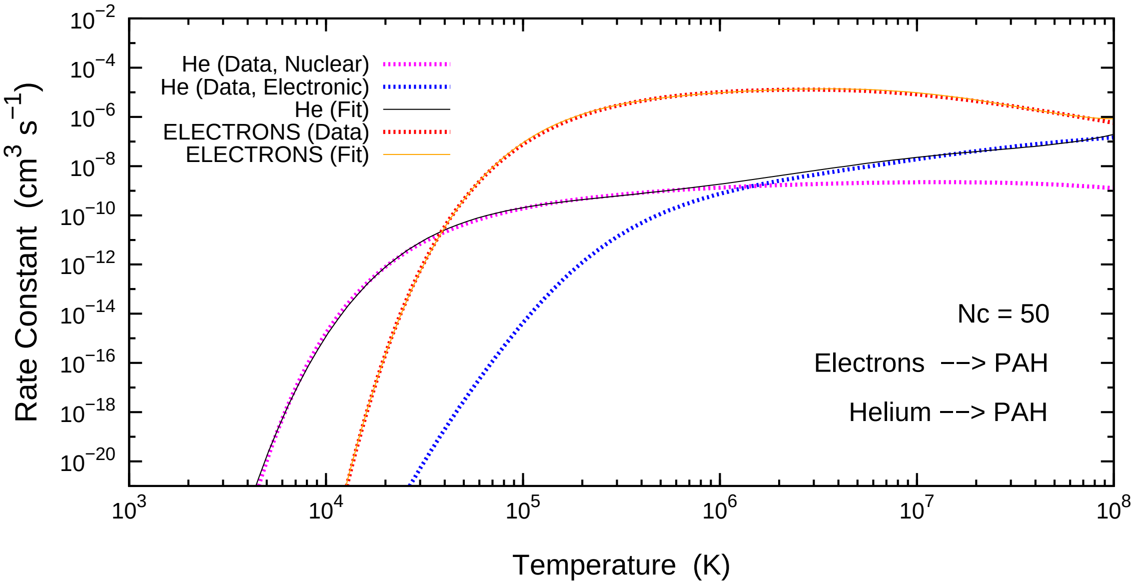

Figure 4.7 — Calculated rate constants for electrons and helium impacting on a 50 C-atom PAH, overlaid are the corresponding analytical fits. The He fit is for the sum of the nuclear and electronic rate constants. The average discrepancy is ∼15 %.

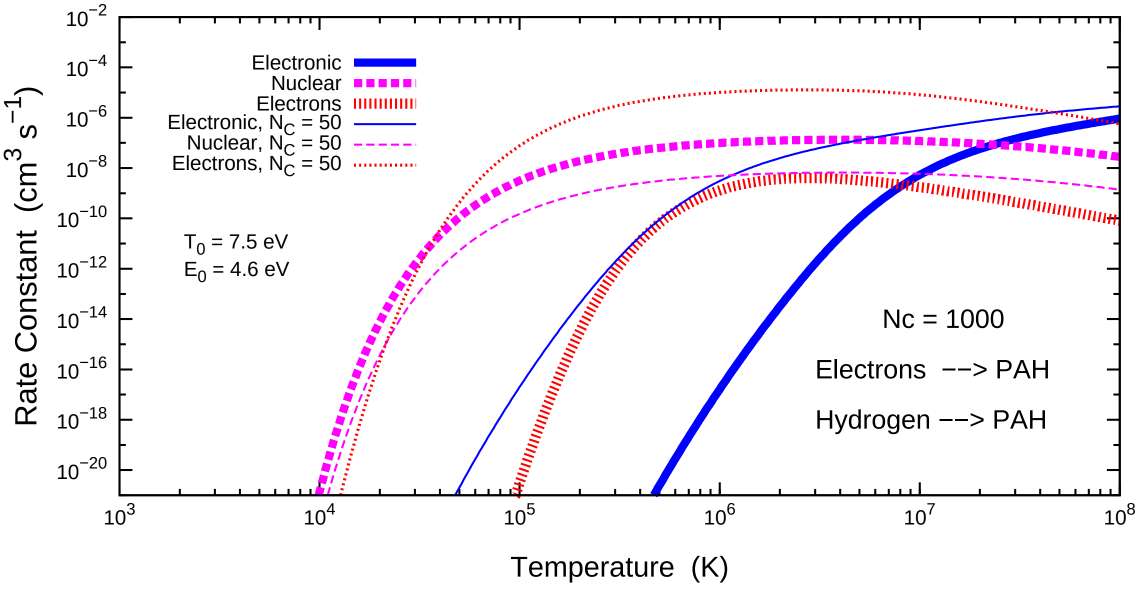

Figure 4.8 — Carbon atom loss rate constant for electrons and hydrogen impacting against a 1000 C-atom PAH. The rate constants for N_C = 50 are shown for comparison.

Table 4.2 — Analytical fit parameters for the PAH carbon atom loss rate constant, calculated for electron and ion collisions.

Fitting function		$f(T) = a + b\,T + c\,T^2 + d\,T^3 + e\,T^4 + f\,T^5$					
		a	b	c	d	e	f
$N_C = 50$	Electrons	2136.83	1632.17	-499.822	76.4347	-5.82964	0.177174
	H	-1896.69	1480.8	-462.733	71.8957	-5.54719	0.169996
	He	-971.448	770.259	-245.561	38.8995	-3.05787	0.0954303
	C	-704.392	551.313	-175.063	27.6506	-2.16871	0.0675643
$N_C = 100$	Electrons	-2255.38	1681.45	-503.451	75.4339	-5.64956	0.168959
	H	-1645.64	1257.06	-384.309	58.4103	-4.41007	0.132356
	He	-945.901	747.921	-237.984	37.6808	-2.96613	0.0928852
	C	-711.244	558.48	-177.983	28.2547	-2.23145	0.0701374
$N_C = 200$	Electrons	-2234.37	1597.71	-459.647	66.332	-4.79841	0.139019
	H	-1473.64	1109.01	-334.292	50.1417	-3.74133	0.111164
	He	-963.188	765.639	-245.054	39.0745	-3.10123	0.0980047
	C	-738.791	584.928	-187.884	30.0819	-2.39748	0.0760639

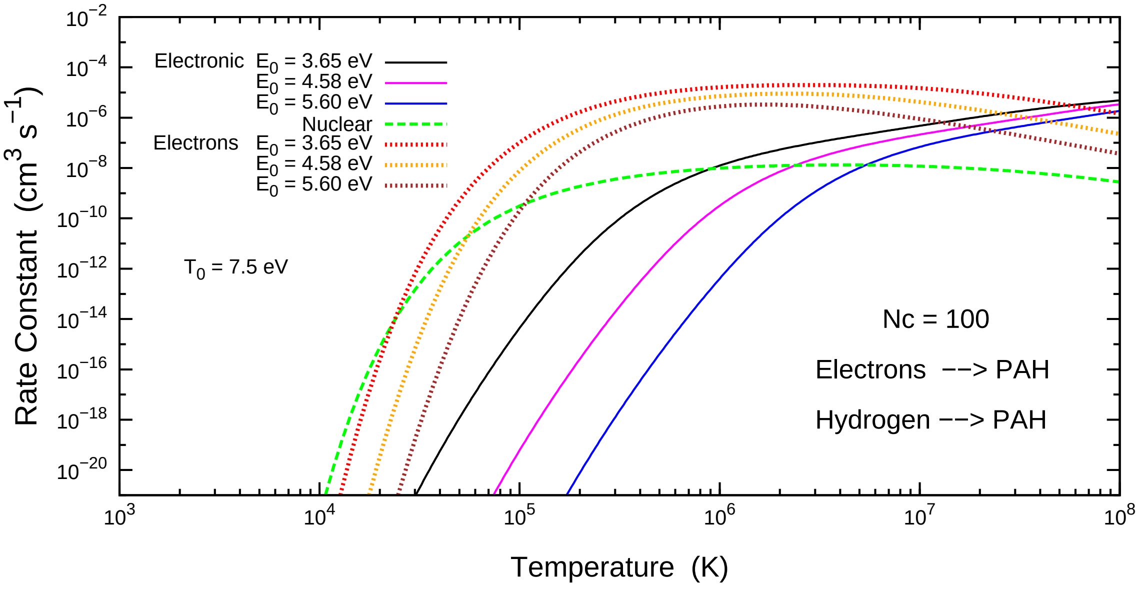

Figure 4.9 — Comparison between carbon atom loss rate constants calculated assuming three values for the electronic dissociation energy, E_0: 3.65, 4.58 and 5.6 eV. The curves refer to electrons and hydrogen impacting against a 100 C-atom PAH. The nuclear rate constant is calculated assuming T_0 = 7.5 eV.

The quantity τ_0 is the time constant appropriate for electron, nuclear and electronic interaction, given by

$$\tau_0 = \frac{N_C}{(2)\,R_T} = \frac{N_C}{J\,n_{H/e}} \tag{4.27}$$

where R_T and J are the thermal collision rate and the rate constant for electrons, nuclear and electronic interactions respectively, and $n_{H/e}$ is the hydrogen/electron density. For electrons and electronic excitation, the rate must be multipliyed by a factor of 2, because each interaction leads to the removal of two carbon atoms from the PAH. The nuclear rate scales linearly with N_C, hence the corresponding fractional carbon atom loss F_L is independent of PAH size.

For any given incoming ion and fixed PAH size N_C, F_L is univocally determined by the hydrogen/electron density $n_{H/e}$ and the gas temperature T. We assume that a PAH is destroyed after the ejection of 2/3 of the carbon atoms initially present in the molecule. This occurs after the time τ_0 (Eq. 4.27) which we adopt as the PAH lifetime against electron and ion bombardment in a gas with given density and temperature.

Table 4.3 summarizes relevant data for four objects characterized by warm-to-hot gas, X-ray emission, and (bright) IR emission features. Clearly, PAHs or related larger species can survive in these environments. Fig. 4.10 shows the fractional C-atom loss, due to electron and ion (H + He + C) collisions, for two widely different objects: the Orion Nebula (M42) and the M82 galaxy (cf. Table 4.3). The famous Orion Nebula is an HII region with high density ($n_H = 10^4$ cm^{-3}) and low temperature ($T = 7000$ K) gas, while M82 is a starburst galaxy, which shows outside the galactic plane, a spectacular bipolar outflow of hot and tenous gas ($n_H = 0.013$ cm^{-3}, $T = 5.8\times10^6$ K).

In M82, PAHs are completely destroyed by electrons, even for the larger PAH, before electronic and nuclear contributions start to be relevant. The electron and electronic fractional losses decrease with PAH size, thus bigger molecules can survive longer, while the nuclear loss is independent of N_C. The destruction timescale is very short: after one thousand years the PAHs should have completely disappeared.

In Orion the situation is reversed. At the temperature considered for this object, electrons and electronic excitation do not contribute to PAH erosion (cf. Fig. 4.5). The damage is caused by nuclear interaction due to He collisions, with a marginal contribution from carbon because of low abundance, and the timescale is much larger: only after 10 million years the PAH destruction becomes relevant. Of course, we have not evaluated the destruction of PAHs by H-ionizing photons in the Orion HII region, which is expected to be very important.

The young ($\simeq$ 2500 yr) supernova remnant, N132D, in the Large Magellanic Clouds has been studied in detail at IR, optical, UV, and X-ray wavelengths (Morse et al. 1995; Tappe et al. 2006). A Spitzer/IRS spectrum of the Southern rim shows evidence for the 15-20 μm plateau – often attributed to large PAHs or PAH clusters (Van Kerckhoven et al. 2000; Peeters et al. 2004) – and, tentatively, weak PAH emission features near 6.2, 7.7, and 11.2 μm (Tappe et al. 2006). Tappe et al. (2006) attribute these features to emission from large ($\sim$ 4000 C-atom) PAHs either just swept up by the blast wave and not yet completely destroyed by the shock or in the radiative precursor of the shock. We calculate a lifetime of small ($50 - 200$ C-atom) PAHs in the relatively dense, hot gas of this young supernova remnant of $\sim$ 4 months (Table 4.3). In contrast, we estimate a lifetime of 150 yr for 4000 C-atom species (cf. Eq. 4.27 and Fig. 4.8). It is clear that the PAH–grain size distribution will be strongly affected in this environment. Given advection of fresh material into the shocked hot gas, the observations are in reasonable agreement with our model expectations. We note that the observed shift to

Table 4.3 — Physical properties and PAH lifetime, τ_0, against erosion due to electron and ion collisions, in objects showing PAH emission characteristics. The lifetime has been calculated for PAHs with N_C = 200. τ_0(ref) has been evaluated adopting our reference values for the interaction parameters, E_0 = 4.6 eV and T_0 = 7.5 eV, τ_0(min) corresponds to the minimum values E_0 = 3.65 eV and T_0 = 4.6 eV, and τ_0(max) to the maximum values E_0 = 5.6 eV and T_0 = 15 eV. $\tau_{\rm object}$ is the lifetime of the object.

Object	$n_{\rm H}$ (cm^{-3})	T K	τ_0(ref) (yr)	τ_0(min) (yr)	τ(max) (yr)	$\tau_{\rm object}$ (yr)	Destruction agent
M82[a]	0.013	5.8×10^6	162	43	1302	$\sim2\times10^7$	electrons
M17[b]	0.3	7×10^6	8.2	2	71	$\sim1\times10^6$	electrons
N132D[c]	10	8×10^6	0.3	0.07	2.5	$\sim3\times10^3$	electrons
Orion[d]	10^4	7×10^3	1.3×10^7	1.4×10^5	7.5×10^{11}	$\sim1\times10^6$	ions

(*a*): Ranalli et al. (2008), (*b*): Townsley et al. (2003)
(*c*): Hwang et al. (1993), (*d*): Tielens (2005)

larger PAH sizes – so evident in the observations – implies that the emitting species are not associated with the precursor but are actualy tracing the postshock gas and are therefore likely heated through collisions with the hot electrons.

This discussion clearly shows that in a low density - high temperature gas, small PAHs are rapidly and completely destroyed. Survival of small PAHs in such environnement (and so the possibility to be detected) requires a protective environment and/or an efficient reformation mechanism.

4.6 Discussion

4.6.1 X-ray absorption

As our calculations show, PAHs are rapidly destroyed in the hot gas associated with stellar winds and supernova explosions. Any PAHs observed near such regions have to be isolated from this hot gas and are presumably in cold gas entrained in these stellar and galactic winds. However, such PAHs would still be exposed to energetic X-ray photons and these can be very destructive as well (Voit 1992; Boechat-Roberty et al. 2008).

The photon absorption cross section of PAHs shows strong peaks at about 6 and 17.5 eV associated with transitions involving the π and σ electronic manifolds and then another broad peak around 286 eV due to carbon K-shell transitions (Keller et al. 1992; de Souza et al. 2002; Regier et al. 2007). Each of these peaks can show various subpeaks due to electronic and vibrational structure. Here, we focus on the high energy peak. Because, we are only concerned with the Planck-averaged cross section all the fine detail will be washed out and we have elected to evaluate the X-ray absorption rate adopting the measured absolute cross section of graphitic carbon taken from the NIST data base (Chantler 1995, 2000). Fig. 4.11 shows the (photon) averaged cross sections as a function of the black body temperature. As this figure illustrates, even the strong absorption edge due to the carbon K-shell is washed out by this averaging process,

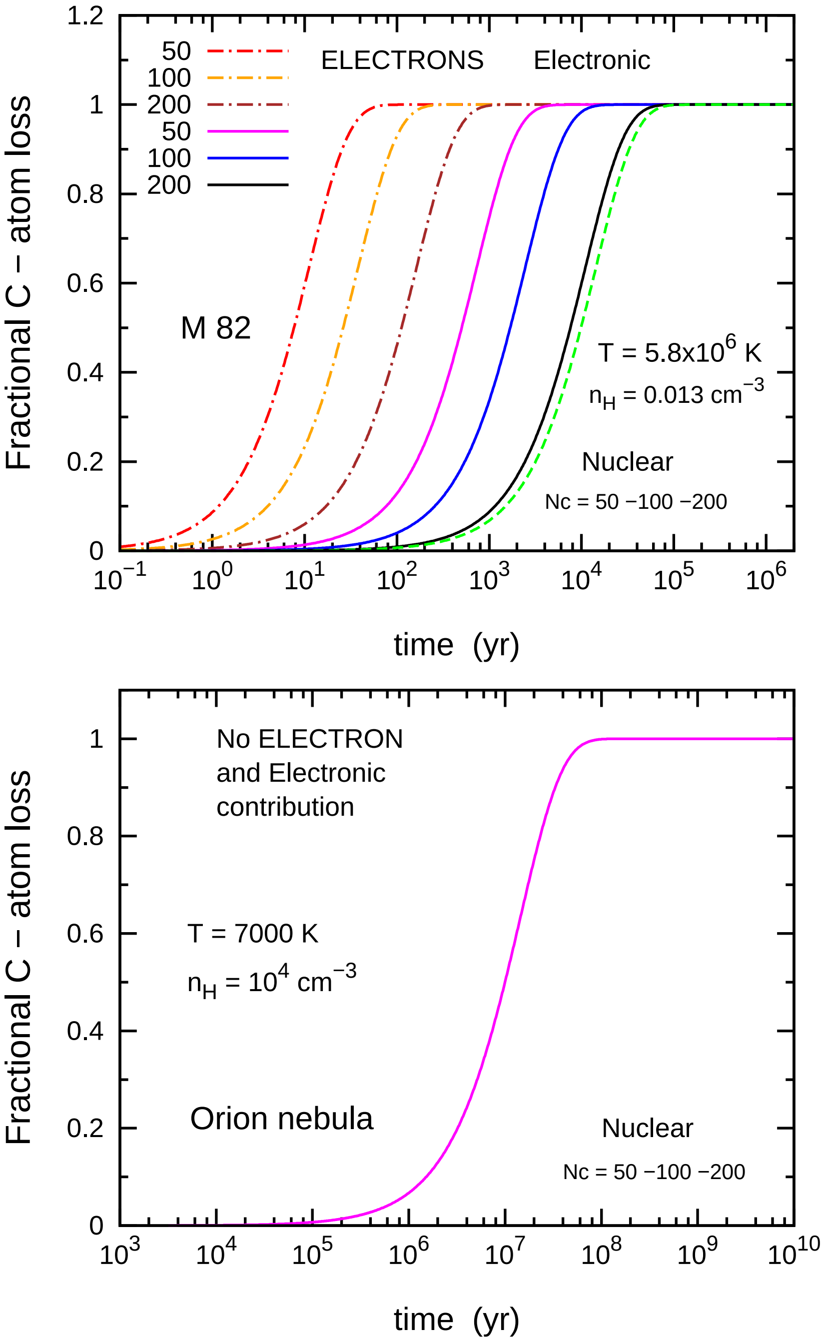

Figure 4.10 — Nuclear and electronic fractional C-atom loss as a function of time in the M82 galaxy (top) and in the Orion Nebula (bottom), calculated for three PAH sizes N_C = 50, 100, 200 C-atoms. The fractional carbon loss is defined as the number of carbon atoms ejected from the PAH after a given time divided by N_C, and represents a direct indicator of the level of destruction of the PAH. Each curve shows the total contribution from collisions with H, He and C. In the nuclear case the fractional loss is independent from N_C, so the three curves coincide, whereas for electrons and electronic interaction the fractional loss varies with the PAH size. In M82 the PAH destruction is dominated by electron collisions and occurs on a very short timescale ($\sim$ thousand years). In Orion instead, because of the low gas temperature no electron and electronic contribution are possible (the rate constant is close to zero, see Fig. 4.5), and hence only nuclear interaction is responsible for the PAH erosion, which however takes place on a long timescale (some 10^7 years).

justifying our neglect of the fine detail in the absorption cross sections of individual PAHs. Our averaged cross section is also in good agreement with the recent study of Boechat-Roberty et al. (2008) for benzene.

The photon absorption rate, R_X, of a PAH exposed to an X-ray photon flux, N_X is then given by,

$$R_X = \sigma_X(T_X)\,N_X \tag{4.28}$$

with $\sigma_X(T_X)$ the Planck average absorption cross section at temperature, T_X. Consider now PAHs embedded in cold gas entrained in the stellar wind of the ionizing stars of the HII region M17. The observed X-ray luminosity is 4×10^{33} erg s^{-1} and the X-ray temperature is 7×10^6 K (Townsley et al. 2003). With a projected emitting area of 42 pc^2 this then implies an average X-ray photon intensity of $\simeq 2.6 \times 10^3$ photons cm^{-2} s^{-1}. With an average cross section of $\sigma_X \simeq 9 \times 10^{-20}$ cm^2/C-atom, we calculate a photon absorption rate of 7.2×10^{-3} photons/C-atom/Myr. After X-ray photon absorption, a PAH will typically lose a few C-atoms and, hence, the estimated lifetime of PAHs entrained in the stellar winds from M17 is $\sim$ 50 Myr. This is in excess of the stellar lifetime and the overall life time of the region. PAHs embedded in cold gas entrained in the galactic superwind of M82 are exposed to somewhat harsher conditions. For M82, at a distance of 3.6 Mpc, the observed soft (0.5-2.0 keV) X-ray flux is 10^{-11} erg cm^{-2} s^{-1} and the temperature is 7×10^6 K. Evaluating the X-ray flux at a distance of 3 kpc from the nuclear starburst region, we calculate a photon absorption rate of 1.8×10^{-2} photons/C-atom/Myr. Hence, in this environment, PAHs would be destroyed on a timescale of $\sim$ 20 Myr, comparable to or larger than the starburst lifetime. It is clear that PAHs in the hot gas are predominantly destroyed by collisions with the hot gas and that X-ray photon absorption plays little role.

Finally, we note that here we have assumed that every X-ray photon absorption will lead to photodissociation. Actually, H-shell electron ejection will be rapidly followed by the Auger effect filling the K-shell again and simultaneously ejecting a second electron. This process may leave the PAH internally excited with typically 15-35 eV[4]. This energy is well above the measured appearance energy of PAH fragmentation for small PAHs under radiative cooling conditions (cf., § 4.4.1) but larger PAHs may survive. Indeed, for an Arrhenius energy of 4.6 eV, a 50 C-atom PAH requires about 24 eV of internal energy to dissociate with a probability of 1/2 (cf., § 4.4.1). Hence, not every X-ray photon absorption will lead to fragmentation, particularly for large PAHs. Further experiments on larger PAHs are required to settle this issue.

4.6.2 PAHs as tracers of cold entrained gas

The results in the previous subsection illustrate that PAHs can survive in the surface regions of cold gas clouds embedded in a hot gas for tens to hundreds of million years. The expansion of a stellar or galactic wind in an inhomogeneous environment will in a natural way lead to the entrainment of cold gas clumps (Chevalier & Clegg 1985; Suchkov et al. 1994; Strickland & Stevens 2000; Marcolini et al. 2005). The material

---

[4] The resulting PAH dication will quickly recombine with electrons and Coulomb explosion is of no consequence for such large PAHs.

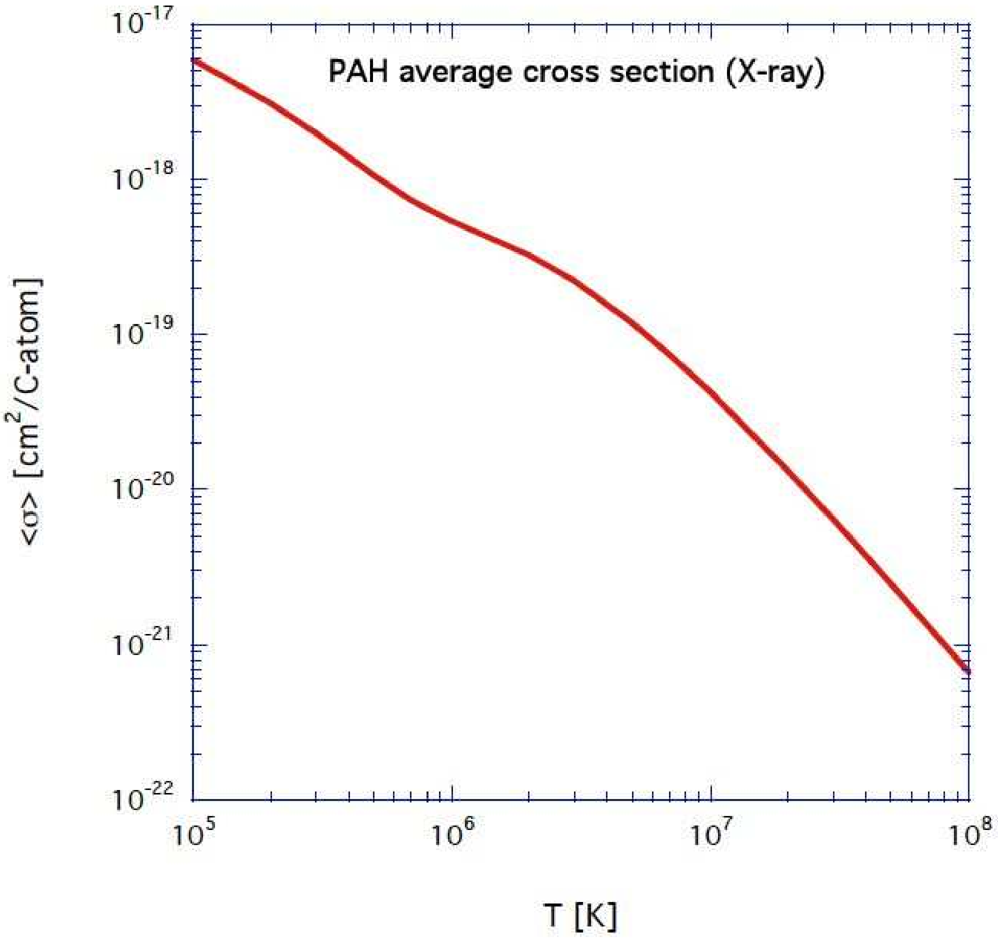

Figure 4.11 — Planck averaged cross section of PAHs as a function of temperature. The cross section is on a per C-atom basis. The strong carbon K shell band edge at $\simeq$ 286 eV (2×10^6 K) has been largely washed out by the averaging process.

in these clumps will only be mildly shocked – and PAH destruction by shocks is not expected as long as the shock velocity is less than about 100 km s^{-1} (Chapter 3) – and can be transported with the wind while losing its identity only slowly, mainly through evaporation into the hot gas driven by thermal conduction. Multiwavelength observations of such winds support this global view and much of the soft X-ray and OVI absorbing and emitting gas is now thought to originate from the interaction interfaces between the tenuous hot gas and the cold dense clumps (Chevalier & Clegg 1985; Heckman et al. 2002).

A typical 0.5 keV X-ray photon will penetrate a column of about 10^{22} H-atoms/cm^2 and hence the 'PAH-bright' surfaces of such PDRs – which are typically only a column of 5×10^{21} H-atoms/cm^2 thick – will be slowly depleted of PAHs on the timescale calculated in section 4.6.1. However, at the same time, entrained clumps will slowly evaporate due to thermal conduction. Considering classical thermal conduction, the mass loss of a cloud due to evaporation into the hot gas is given by

$$\dot{M} \simeq 1.3 \times 10^{-3} \left(\frac{R}{10\ \mathrm{pc}}\right) \left(\frac{T}{6 \times 10^{6}\ \mathrm{K}}\right)^{5/2} \quad \mathrm{M}_{\odot}\ \mathrm{yr}^{-1} \tag{4.29}$$

with T the temperature of the hot gas and R the radius of the clump (cf. Tielens 2005). Consider the galactic wind of M82 and a typical structure with a size of 10 pc. Assuming thermal pressure equilibrium between the clump and the hot gas (eg., ignoring ram pressure confinement which may actually be a factor of 10 larger), we estimate a density of $\simeq 800\ \mathrm{cm}^{-3}$ for a typical PDR temperature of 100 K for the galactic wind region of M82. The lifetime of such a clump is then,

$$\tau_{\mathrm{clump}} \simeq 40 \left(\frac{n_{\mathrm{PDR}}}{10^{3}\,\mathrm{cm}^{-3}}\right) \left(\frac{R}{10\ \mathrm{pc}}\right)^{2} \left(\frac{6 \times 10^{6}\ \mathrm{K}}{T}\right)^{5/2} \quad \mathrm{Myr}. \tag{4.30}$$

Hence, 'fresh' material will continuously be advected to the clump surface where ambient FUV photons can excite it. Thus, we conclude that such clumps can survive for a long time and that, proviso illumination by FUV photons, PAHs will form an excellent 'dye' for tracing the presence of cold entrained material; or more specifically, for the exposed surfaces of photodissociation regions.

4.6.3 Comparison with previous studies

Dwek et al. (1996) determines a sputtering rate for dust in a hot dust gas ($T \geq 10^{6}$ K) that can be used to derive the lifetime, τ of a grain of a give radius in a hot gas of a given density, i.e.

$$\tau \approx \frac{10^{3}}{n_{\mathrm{H}}} \left(\frac{a}{1\text{Å}}\right) \mathrm{yr}, \tag{4.31}$$

where a is the grain size and n_{H} is the gas density. Clearly in this situation it is the smallest grains that suffer the fastest destruction. Hence, a treatment of the small grains, including PAHs, really needs to take into account the detailed physics of the interactions. For illustrative purposes, we can use Eq. 4.31 to show that grains with sizes typical of PAHs ($a \approx 5$Å) should have lifetimes, in a tenuous hot gas ($n_{\mathrm{H}} = 1$ cm^{-3}), of the order of at least a few thousand years. We can see that this timescale is much longer than the typical PAH lifetimes that we derive here, i.e. few years for a 50 carbon atom PAH in a gas with $n_{\mathrm{H}} = 1\ \mathrm{cm}^{-3}$. The timescale determination arrived at using Eq. 4.31 assumes that a PAH just behaves as a small grain. However, in the case of a grain, the sputtering yield is usually much less that unity because atoms displaced by knock-on collisions in the solid can remain in the solid. The very much shorter lifetimes for the PAHs that we find can be ascribed to the fact that the transferred energy in incident electron and ion interactions always leads to the loss of carbon atoms from the PAH when that energy exceeds the relevant binding energy. In fact the equivalent PAH 'sputtering yield' can be greater than unity because multiple atom ejection is possible. Indeed we assume here that the ejected species in the case of electronic interactions are C_2 units.

The evolution of the dust and PAH thermal emission arising from a hot gas is affected by the changing dust size distribution. As pointed out by Dwek et al. (1996), it is the short wavelength emission, coming from the smallest grains, that is most affected by dust destruction. Our work now indicates that the destruction timescale is much shorter than that predicted by Dwek et al. because the erosion of the smallest grains and PAHs is enhanced by as much as three orders of magnitude compared to the earlier work. Thus, the gas cooling rates derived by Dwek (1987) will need to be reduced if a significant fraction of the dust mass is in the form of small grains and PAHs.

4.6.4 C_2 groups loss

The primary channel for PAH erosion in a hot gas is the progressive loss of C_2H_n (n = 0, 1, 2) units following incident electron and ion excitation of the molecule. We note that this can only really occur from the periphery of the PAH (see the lower part of Fig. 3.11 in Chapter 3 for an illustration of this type of erosion). In this case we can see that a coherent aromatic structure will tend to be preserved, which is probably not the case where the inertial sputtering of C atoms is dominant. Thus, we conclude that PAH erosion in a hot gas will tend to preserve the aromatic structure throughout the destruction process.

As emphasized in Chapter 3, PAH destruction may start with complete H-loss followed by isomerization to much more stable pure carbon clusters such as fullerenes (cf. Tielens 2008). While we have not assessed this point, we expect that such species will be more stable than PAHs in a hot gas.

4.7 Conclusions

We have extensively studied the stability of PAHs against electron and ion collisions (H, He and C) in a hot gas, such as the gas behind fast non-radiative shocks and in galactic outflows. Collisions can lead to carbon atom loss, with a consequent disruption and destruction of the molecule. We consider the case of a thermal gas with temperature T in the range $10^3 - 10^8$ K.

An ionic collision consists of two simultaneous processes which can be treated separately: a binary collision between the projectile ion and a single atom in the target (nuclear interaction) and energy loss to the electron cloud of the molecule (electronic interaction).

For the nuclear interaction, as described in MJT, we have modified the existing theory in order to treat collisions able to transfer energy *above* a specific threshold T_0. We adopt T_0 = 7.5 eV as a reasonable value, but experimental determinations of this quantity are necessary.

The electronic energy transfer has been described in term of the stopping power of an electron gas with appropriate electron density (jellium approximation). For electron collisions, we derived an analytical expression for the measured electron stopping power in graphite and applied this to the case of PAHs.

The dissociation probability for a PAH excited by electronic interactions and electron collisions, has been derived using the theory of unimolecular reactions. The parameter E_0, which governs the dissociation probability, is not well constrained. We adopt a value of 4.6 eV consistent with extrapolations to interstellar conditions but better determinations, relevant to the astrophysical situation, are needed.

The PAH destruction process is dominated by electron collisions for gas temperatures above $\sim 3\times10^4$ K, and by nuclear interaction with helium below this value. Small PAHs are more easily destroyed than larger ones below $\sim 10^6$ K, while the difference reduces significantly for a hotter gas. For a 1000 C-atom PAH, nuclear interactions are the dominant destruction process.

In a hot and tenuous gas (e.g. M82 galactic outflows), PAHs with sizes between 50 and 200 C-atom are destroyed by electron collisions in few thousand years. In denser and colder regions (e.g. Orion), PAHs can survive for some 10^7 yr before being destroyed by nuclear interaction processes.

X-ray photon absorption plays little role in PAH destruction in the hot gas associated with stellar winds and supernova explosions, with respect to electron collisions. The PAH destruction process in a hot gas is therefore dominated by electron collisions. Any PAHs observed near such regions have to be isolated from this hot gas and are presumably in a cooler PDR-type gas entrained in the stellar and galactic winds. In this sense, PAHs represent a good tracer for the presence of entrained denser material.

Our calculated PAH lifetime in a hot tenuous gas ($T \sim 10^6$ K, $n_{\rm H} = 1$ cm^{-3}), is much shorter than the lifetime of an equivalent dust grain of roughly the same size ($a \approx 5$Å). Thus, might then imply that the destructive effects of ion and electron collisions with very small grains have previously been underestimated. The enhanced erosion of the smallest grain and PAHs implies that the gas cooling rates for a hot gas ($T > 10^6$ K) – which depend on the grain/PAH size distribution – may need to be reduced if a significant fraction of the dust mass is locked in small grains and PAHs.

PAH erosion in a hot gas occurs mainly through the ejection of C_2 groups following electron collisions and electronic excitation. The C_2 loss occurs at the periphery of the molecule, thus the aromatic structure will tend to be preserved throughout the destruction process.

Acknowledgements

We are grateful to L. Allamandola and L. Verstraete for useful discussions. E.R.M. thanks G. Lavaux for support and technical assistance and acknowledges financial support by the EARA Training Network (EU grant MEST-CT-2004-504604).

Chapter 5

PAH processing by Cosmic Rays

Abstract. Cosmic rays are present in almost all phases of the ISM. PAHs and cosmic rays represent an abundant and ubiquitous component of the interstellar medium. However, the interaction between them has never before been fully investigated. The aim of this work is to study the effects of cosmic ray ion (H, He, CNO and Fe-Co-Ni) and electron bombardment of PAHs in galactic and extragalactic environments. We calculate the nuclear and electronic interactions for collisions between PAHs and cosmic ray ions and electrons with energies between 5 MeV/nucleon and 10 GeV, above the threshold for carbon atom loss, in normal galaxies, starburst galaxies and cooling flow galaxy clusters. The timescale for PAH destruction by cosmic ray ions depends on the electronic excitation energy E_0, the minimum cosmic ray energy $E_{\rm min}$ and the amount of energy available for dissociation. Small PAHs are destroyed faster with He and the CNO group being the more effective projectiles. The shortest survival time that we find is $\sim 10^8$ yr, which is comparable with the lifetime against destruction in interstellar shocks. For electron collisions, the lifetime is independent of the PAH size and varies with $E_{\rm min}$ and the threshold energy T_0, the minimum lifetime in this case is 1.2×10^{13} yr. They process the PAHs in diffuse clouds, where the destruction due to interstellar shocks is less efficient. In the hot gas filling galactic halos, outflows of starburst galaxies and intra-cluster medium, PAH destruction is, however, dominated by collisions with thermal ions and electrons. The observation of PAH emission in such regions is therefore only possible if the molecules are protected in dense clumps transported within the galactic winds. In this sense PAHs must be an excellent tracer for the presence of entrained denser material and their lifetime is set by cosmic ray processing.

E. R. Micelotta, A. P. Jones, A. G. G. M. Tielens
to be submitted to Astronomy & Astrophysics

5.1 Introduction

The mid-infrared spectrum of the general diffuse Interstellar Medium (ISM) as well as that of many objects is dominated by broad emission features at 3.3, 6.2, 7.7 and 11.2 μm. At present, these feature are (almost) universally attributed to the IR fluorescence of far-ultraviolet (FUV)-pumped Polycyclic Aromatic Hydrocarbon (PAH) molecules containing 50 – 100 carbon atoms (Tielens 2008). PAHs are an abundant (3×10^{-7} by number relative to hydrogen) and important component of the ISM; for example, they control the heating of the neutral atomic gas (via the photoelectric effect) and the degree of ionization in the ISM. PAHs can also be important agents in cooling a hot gas, at temperatures above $\sim 10^6$ K (e.g. Dwek 1987), and they play a central role in the chemical evolution of the ISM.

A remarkable characteristic of PAHs is their ubiquity and their IR emission features which are associated with dust and gas illuminated by UV photons, ranging from HII regions to ultraluminous infrared galaxies (see Tielens 2008, for a recent review). PAHs have recently been detected in association with shocked hot gas, but it is difficult to establish a clear connection between the two. Tappe et al. (2006) detected spectral features in the emission of the supernova remnant N132D in the Large Magellanic Cloud, which they attribute to emission by large PAHs. Reach et al. (2006) have identified four supernova remnant with IR colors maybe indicating PAH emission, and Andersen et al. (2007) investigated the presence of PAHs in a subset of galactic supernova remnants in the GLIMPSE survey. PAHs have also been observed interwoven with the X-ray emission arising from the bipolar outflow of the starburst galaxy M82 (Armus et al. 2007) and in the high-latitude coronal gas of the edge-on galaxies NGC 5907, NGC 5529 and NGC 891 (Irwin & Madden 2006; Irwin et al. 2007; Whaley et al. 2009).

Unfortunately the lack of theoretical studies on PAH processing in shocked regions combined with the difficulty in disentangling the PAH features intrinsic to the shocked region with those arising from the surrounding material makes the interpretation of such observations rather complicated. In Chapter 3 and Chapter 4 (papers Micelotta et al. 2009a,b, hereafter MJT09a and MJT09b) we studied the survival of aromatic molecules in interstellar shocks with velocities between 50 and 200 km s^{-1} and in a hot post-shock gas, such as the Herbig- Haro jets in the Orion and Vela star forming regions (Podio et al. 2006), in the local interstellar cloud (Slavin 2008) and in the outflow of the starburst galaxy M82 (Engelbracht et al. 2006). We found that interstellar PAHs ($N_{\rm C} = 50$) do not survive in shocks with velocities greater than 100 km s^{-1} and larger PAHs ($N_{\rm C} = 200$) are destroyed for shocks with velocities $\geq$ 125 km s^{-1}. Even where destruction is not complete, the PAH structure is likely to be severely denatured by the loss of an important fraction ($20 - 40\%$) of the carbon atoms. The typical PAH lifetimes are of the order of a few $\times10^8$ yr for the Galaxy. In a tenuous hot gas ($n_{\rm H} \approx 0.01$ cm^{-3}, $T \approx 10^7$ K), typical of the coronal gas in galactic outflows, PAHs are principally destroyed by electron collisions, with lifetimes measured in thousands of years, i.e. orders of magnitude shorter than the typical lifetime of such objects.

To place everything into perspective, the main destruction agent for small PAHs will be FUV photons in the interstellar radiation field, which will weed the interstellar PAH family to the sturdier species present. The rate at which this happens depends on size and molecular structure, however, the precise limits above which UV photons become ineffective is not well known, but it is probably around 50 C-atoms (Tielens 2008). Shocks with velocities of 100 km/s are also very effective, for any size PAH - (Chapter 3) but such shocks are limited to the warm intercloud medium and diffuse clouds have a very low probability to being processed by them (Jones et al. 1994). PAHs exposed to a very hot gas, e.g. inside compact supernova remnants such as Cas A, are also rapidly destroyed by electron and ion impacts (Chapter 4). However, such regions are generally not long lived as they cool by adiabatic expansion and on a galactic scale are less important than interstellar shocks. PAHs embedded or entrained in a hot gas are well-protected from these processes. However, in such environments, high energy cosmic ray ions and electrons can penetrate denser structures and destroy interstellar PAHs. This is potentially as effective a destruction agent as the evaporation of these denser structures into the warm or hot gas. In this paper, we will address the destruction of PAHs by cosmic rays.

Cosmic rays (CRs) are an important component of the ISM, contributing considerably to its energy density ($\simeq 2$ eV cm^{-3} Tielens 2005). CRs consist mainly of relativistic protons, α-particles ($\sim 10\%$), and heavier ions and electrons ($\sim 1\%$). The spectrum (intensity as a function of the energy) of the ionic CR component measured near the Earth spans from ~ 100 MeV to $\sim 10^{20}$ eV, and decreases steeply with energy. The spectrum of the electronic component is even steeper and ranges from ~ 600 MeV to 10^3 GeV (Ip & Axford 1985; Gaisser & Stanev 2006).

The lowest-energy cosmic rays in the ISM, with energy between 5 MeV and few GeV, are excluded from the heliosphere or severely slowed down by the solar wind. Hence, they cannot be directly observed from inside the heliosphere and their spectra have to be evaluated theoretically (see e.g. Shapiro 1991; Indriolo et al. 2009, and references therein).

Cosmic rays with energy up the few 10^{15} eV (the “knee” observed in the spectrum: O’C. Drury 1994) are thought to be produced in the Galaxy, mainly by supernova shocks in the disk. Because of their charge, CRs are tied to the galactic magnetic field and are confined to a spheroidal volume with radius of ~ 20 kpc and half-thickness of ~ 1 – 15 kpc (Ginzburg 1988; Shibata et al. 2007), with a small but finite escape probability. The magnetic field randomizes the trajectories of CRs as they propagate through the Galaxy, so their distribution is almost isotropic except close to the sources.

From the point of view of PAH destruction, CRs have then two interesting characteristics: first, for energies up to 10 GeV they can efficiently transfer energy to the PAH, with possible consequent destruction (see § 5.2 and § 5.3); second, they permeate almost homogeneously the ISM and can penetrate into regions such as dense clouds which are, for instance, affected by high temperature ions and electrons (Chapter 4).

The aim of this work is then to quantify the destructive potential of cosmic rays and to compare it with other mechanisms (interstellar shocks, collisions within a hot gas, X-ray and FUV absorption), in galactic and extragalactic environment.

The chapter is organized as follows: § 5.2 and § 5.3 describe the treatment of high energy ion and electron interactions with PAHs, § 5.4 presents the cosmic ray spectra adopted for our study and § 5.5 illustrates the calculation of the collision rate between PAHs and cosmic rays. We present our results on PAH lifetime in § 5.6 and discuss the astrophysical implications in § 5.7, summarizing our conclusions in § 5.8.

5.2 High energy ion interactions with solids

5.2.1 Collisions with high energy ions

To describe the effects of high-energy ion collisions with PAH molecules we adopt a similar approach to that used in Chapter 3 and Chapter 4, based on the theory of ion interaction in solids. Ions colliding with a PAH will excite the molecule. This excitation can lead to fragmentation or, alternatively, the excess energy can be radiated away. Calculation of the fragmentation process consists thus of two steps: 1) the calculation of the excitation energy after collision, 2) the probability of dissociation of an excited PAH. The former is discussed here. The latter is described in section § 5.2.2.

The energy loss of ions passing through matter can be described in terms of two simultaneous processes which can be treated separately (Lindhard et al. 1963): the *nuclear stopping* or *elastic energy loss*, where the energy is directly transferred from the projectile ion to a target nucleus via a binary elastic collision, and the *electronic stopping* or *inelastic energy loss*, consisting of the energy loss to the electron plasma of the medium. Above ~ 1 MeV/nucleon (energies characteristic of cosmic rays) electronic stopping, which is well described by the Bethe–Bloch equation (see e.g. Ziegler 1999, and references therein), is far more important than nuclear stopping and dominates the energy loss process.

The Bethe–Bloch equation has been derived considering the electromagnetic interaction of an energetic particle with the electron plasma of a solid. A PAH molecule is not a solid but its large number of delocalized electrons can be treated as an electron gas (see Chapter 4 and references therein). It is therefore appropriate to consider the energy loss to such an electron plasma in terms of the Bethe–Bloch electronic stopping power, S (energy loss per unit length). When S is known, a specific procedure has to be applied to calculate the effective amount of energy transferred into a single molecule, taking into account the finite geometry of the PAH (see § 5.3).

The stopping of high velocity ions in matter has been a subject of interest for more than a century, starting with the work of Marie Curie in 1898-1899 (Curie 1900). For a theoretical review on the topic, we refer the reader to Ziegler (1999) and references therein. In the following, we summarize the basic methods and equations for evaluating the stopping power of high energy ions and we illustrate the modifications introduced into the theory in order to treat the interaction with PAH molecules.

For high energy light ions (H, He and Li above 1 MeV/nucleon), the fundamental relation describing the stopping power, S, in solids is the relativistic Bethe-Bloch equation, commonly expressed as

$$S = \frac{\kappa Z_2}{\beta^2} Z_1^2 L(\beta) \tag{5.1}$$

$$= \frac{\kappa Z_2}{\beta^2} Z_1^2 \left[L_0(\beta) + Z_1 L_1(\beta) + Z_1^2 L_2(\beta)...\right] \tag{5.2}$$

where

$$\kappa \equiv 4\pi r_0^2 m_e c^2, \quad r_0 \equiv e^2/m_e c^2 \ \text{(Bohr electron radius)} \tag{5.3}$$

m_e is the electron mass, Z_1 and Z_2 are the projectile and target atomic numbers respectively and $\beta = v/c$ is the relative projectile velocity. The term $L(\beta)$ is defined as the stopping number, and its expansion in Eq. 5.2 contains all the corrections to the basic ion-electron energy loss process.

The first term L_0 includes the fundamental Bethe-Bloch relation (Bethe 1930, 1932; Bloch 1933a,b) for the stopping of high-energy ions, together with the two corrective terms C/Z_2 and $\delta/2$ introduced by Fano (1963)

$$L_0 = f(\beta) - \frac{C}{Z_2} - \ln\langle I \rangle - \frac{\delta}{2} \tag{5.4}$$

where

$$f(\beta) \equiv \ln\left[\frac{2\, m_e c^2\, \beta^2}{1 - \beta^2}\right] - \beta^2 \tag{5.5}$$

C/Z_2 is the *shell correction* and takes into account the fact that as soon as the projectile loses energy into the target, its velocity decreases from relativistic values, thus the Bethe - Bloch theory requirement of having particles with velocity far greater than the velocity of the bound electron is no longer satisfied. In this case, a detailed accounting of the projectile's interaction with each electronic orbital is required. The shell correction is important for protons in the energy range of 1 – 100 MeV, with a maximum contribution of about 10%.

$\ln\langle I \rangle$, which is part of the original Bethe-Bloch relativistic stopping formula, represents the *mean ionization*, and corrects for the fact that the energy levels of the target electrons are quantized and not continuous.

$\delta/2$ represents the *density effect* and provides the correction to the reduction of the stopping power due to polarization effects in the target. The dielectric polarization of the target material reduces the particle electromagnetic field from its free-space values, resulting in a variation of the energy loss. The density effect becomes important only for particles with kinetic energies exceeding their rest mass (938 MeV for proton).

The term $Z_1\, L_1$ takes into account the Barkas effect. This is due to the target electrons, which respond to the approaching particles slightly changing their orbits before the energy loss interaction can occur.

The term $Z_1^2 L_2$ is the Bloch correction and provides the transition between the two approaches used to evaluate the energy loss of high-energy particles to target electrons: the classical Bohr impact–parameter approach (Bohr 1913, 1915), and the quantum-mechanical Bethe momentum transfer approach (Bethe 1930, 1932).

Both the Barkas and Bloch corrections are usually quite small and contribute less than few percent to the stopping at energies from 1 MeV/nucleon to 10^4 MeV.

The term L_0 can be evaluated as a function of the energy of the incoming ion using the following definition:

$$\beta^2 \equiv \left(\frac{v}{c}\right)^2 = 1 - \frac{1}{\left[1 + E(\mathrm{GeV})\,/\,0.931494\; M_1(\mathrm{amu})\right]^2} \tag{5.6}$$

Using Eq. 5.4, we can rewrite the expression for the stopping power (Eq. 5.2) in the following way

$$S = \frac{\kappa Z_2}{\beta^2} Z_1^2 \left\{ \left[f(\beta) - \frac{C}{Z_2} - \ln\langle I \rangle - \frac{\delta}{2} \right] + Z_1 L_1(\text{Barkas}) + Z_1^2 \mathrm{L}_2(\text{Bloch}) \right\} \quad (5.7)$$

For the stopping power in units of eV/(10^{15} atoms/cm^2) the prefactor constant has the value $\kappa = 5.099 \times 10^{-4}$, while for the stopping units of eV/Åthe above prefactor has to be multiplied by $N/10^{23}$, where N is the atomic density of the target (atoms/cm^3). In our calculation we adopt the values for amorphous carbon ($Z_2 = 6$, $M_2 = 12$, $N = 1.1296 \times 10^{23}$ atoms/cm^3), which yields $\kappa = 5.7508 \times 10^{-4}$.

An empirical expression for the Barkas correction term is available (Ziegler 1999), whereas the Bloch correction can be evaluated using the Bichsel parametrisation (Bichsel 1990). Bonderup estimates that $\langle I \rangle = 11.4\, Z_2$ (eV), but this is not always in agreement with experimental data and unfortunately there are no simple algorithms for the shell correction and density effect. As a consequence, no simple analytical expressions for the stopping power are available.

The SRIM program (Ziegler et al. 1985) calculates accurate stopping powers from Eq. 5.7 using different methods to evaluate the corrective terms. The shell correction C/Z_2 is the average of the values obtained from the Local Density Approximation theory (LDA) and Hydrogenic Wave Function (HWF) approach (Ziegler 1999). The first is an *ab initio* calculation based on realistic solid state charge distributions, while the second uses parameterized functions based on experimental stopping data. For the density correction $\delta/2$, the values tabulated in ICRU (1984) are used, while the term $\ln\langle I \rangle$ is derived by adjusting the theoretical value obtained from the LDA theory (e.g. Lindhard & Scharff 1952) in order to fit the sum $\ln\langle I \rangle + C/Z_2$ evaluated empirically from experimental stopping data.

As already mentioned, Eq. 5.7 is valid for light ions, H, He and Li. The stopping power for ions with $Z_1 > 3$ is usually calculated using the heavy-ion scaling rule, as reported for example by Katz et al. (1972)

$$S(Z_1, \beta) = S(p, \beta)[Z_1^*/Z_p^*]^2 \quad (5.8)$$

where $S(p, \beta)$ is the stopping power of a proton at the same speed as the ion of atomic number Z_1 (Eq. 5.7), Z_1^* and Z_p^* are the effective charge numbers of ion Z_1 and of a proton respectively, with the expression given by Barkas (see e.g. Henriksen et al. 1970).

$$Z_1^* = Z_1 \left[1 - \exp\left(-125\, \beta\, Z_1^{-2/3} \right) \right] \quad (5.9)$$

To verify the effective importance of the corrective terms to the Bethe-Bloch equation in our specific case of interest (H, He, C and Fe impacting on carbon), we compared the output from SRIM with the stopping power calculated from the following approximate equation

$$S = \frac{\kappa Z_2}{\beta^2} Z_1^2 \left[f(\beta) - \ln\langle I \rangle \right] \quad (5.10)$$

where we adopt the carbon mean ionization energy calculated by SRIM[1] using the method described above, $\langle I \rangle$ = 79.1 eV. For the heavier ions C and Fe we use the proton stopping power from Eq. 5.10 into Eq. 5.8.

We find a maximum discrepancy of ~10% between the two curves, indicating that our approximate equation is adequate to describe the energy loss. In this specific case, not only the Barkas and Bloch corrections, but also the shell correction and the density effect play a marginal role. Fig. 5.1 shows the comparison between the 'accurate' SRIM curve and the approximate one for H and Fe, our lighest and heaviest projectiles respectively.

Using Eq. 5.8 and 5.10 we can then calculate the electronic stopping power $\mathrm{d}E/\mathrm{d}x$ of energetic ions and from this the energy loss to the PAH molecule (§ 5.3). Since the stopping power is a decreasing function of the ion energy and increases quadratically with Z_1, the major contribution to the energy loss will come from the less energetic particles for a given ion, and from the heavier species for a given velocity (Fig. 5.1).

5.2.2 Ion energy loss and dissociation probability

To calculate the energy transferred to a PAH during collisions with high energy ions we adopt the configuration shown in Fig. 5.2 (see also Chapter 4).

The molecule is modeled as a thick disk with radius R given by the usual expression for the radius of a PAH: $a_{\rm PAH} = R = 0.9\sqrt{(N_{\rm C})}$ Å, where $N_{\rm C}$ is the number of carbon atoms in the molecule (Omont 1986). For a 50 C-atom PAH, $R = 6.36$ Å. The thickness of the disk, $d \sim 4.31$ Å, is the thickness of the electron density assumed for the PAH (see Chapter 4).

The path l, through the PAH, along which the incoming ion loses its energy is defined by the impact angle ϑ and by the dimensions of the molecule. Inspection of Fig. 5.2 shows that, if $|\tan(\vartheta)| < \tan(\alpha)$, $l(\vartheta) = d/|\cos\vartheta|$, otherwise $l(\vartheta) = 2R/|\sin\vartheta|$. The rigorous method to calculate the energy loss along $l(\vartheta)$ takes into account the progressive slowing down of the projectile in traversing the target. This is explained in §3 of Chapter 4. Nevertheless, in the present case we consider high energy particles for which the energy loss along the path l is small compared to the initial energy (cf. Fig. 5.1). In other words, the energy of the incoming ion remains almost constant during the interaction, thus the amount of energy lost after travelling the distance $l(\vartheta)$ can be simplified to

$$T(\vartheta) = \frac{\mathrm{d}E}{\mathrm{d}x} \times l(\vartheta) \tag{5.11}$$

where $\mathrm{d}E/\mathrm{d}x = S(\vartheta)$ is the stopping power (energy lost per unit length) from Eq. 5.10 and/or 5.8, and $\mathrm{d}E$ is the amount of energy lost after travelling the distance $\mathrm{d}x$. The difference between the results from the two methods is of the order of few percent, which fully justifies the use of approximation in Eq. 5.11.

The ion collision will leave the molecule electronically excited. Internal conversion and/or intersystem crossing will transfer this excitation (largely) to the vibrational manifold. De-excitation can occur through two competing decay channels: emission

---

[1] http://www.srim.org/SRIM/SRIMPICS/IONIZ.htm

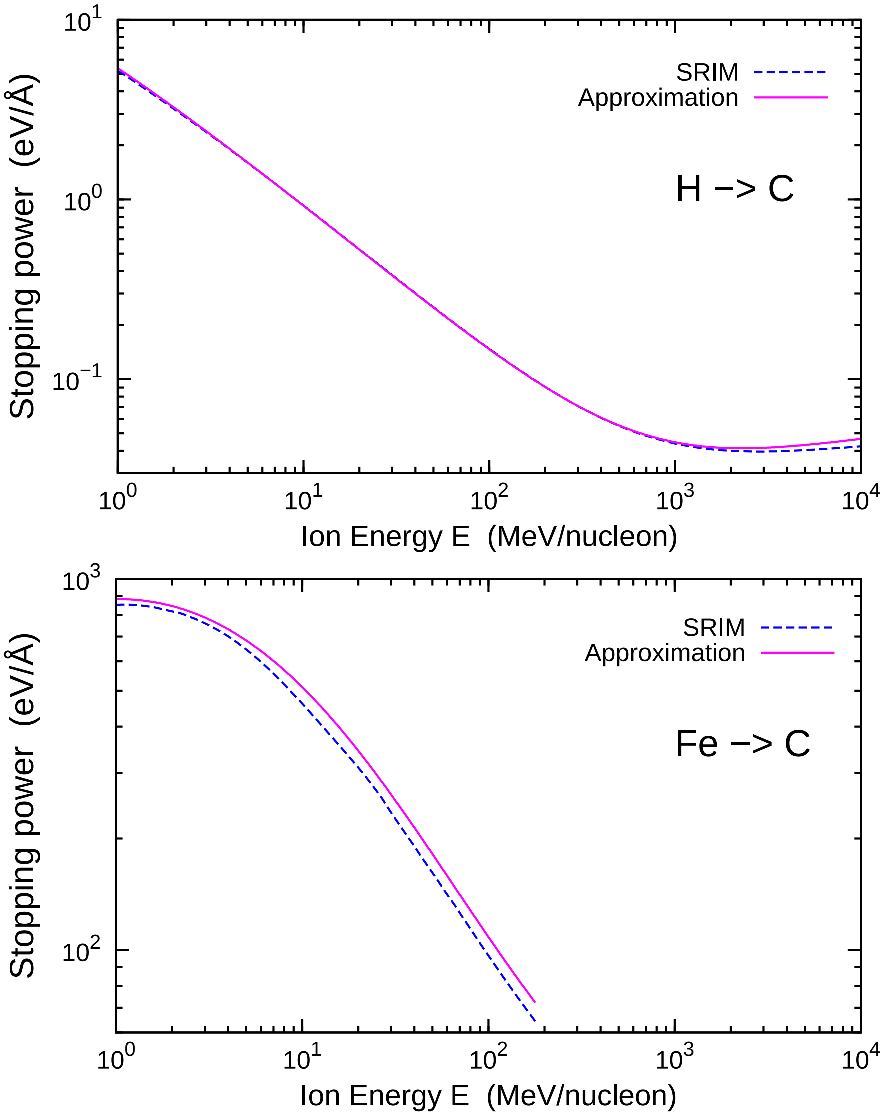

Figure 5.1 — Stopping power of hydrogen and iron impacting on carbon, as a function of the energy per nucleon of the ion. The lower validity limit of the Bethe-Bloch equation is 1 MeV/nucleon. We compare the output from the SRIM code, with computes all corrections and our approximate equation wich includes only the mean ionization correction.

of infrared photons and dissociation and loss of a C_2 fragment. The latter is the process that we are interested in because it leads to PAH fragmentation. The emission of a C_2 fragment is suggested by experiments on fullerene C_{60} which have shown that the ejection of C_2 groups is one of the preferred fragmentation channel. Moreover, the loss of acetylene groups C_2H_2 has been observed in small PAHs. In fact, in a PAH molecule, a side group C_2H_n (with n = 0,1,2) is easier to remove because only two single bonds have to be broken, while the ejection of a single external C-atoms requires one single and one double bond to be broken, and for an inner C-atom from the skeleton three bonds needs to be broken.

To quantify the PAH destruction due to ion collisions we need to determine the

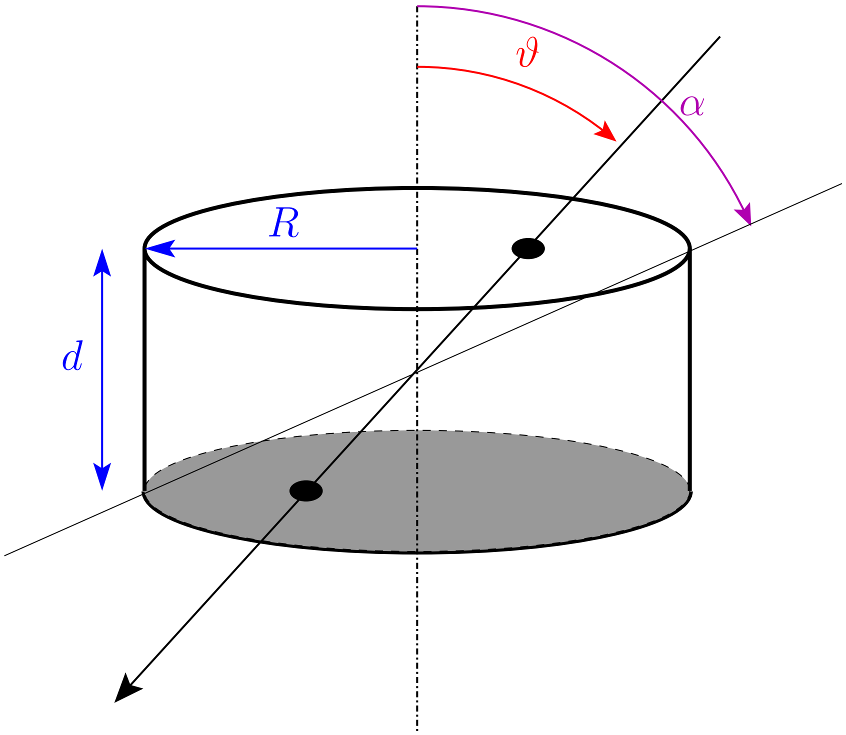

Figure 5.2 — The coordinate system adopted to calculate the energy transferred to a PAH via electronic excitation by ion collisions. The molecule is modeled as a disk with radius R and thickness d. The trajectory of the incoming particle is identified by the angle ϑ, while the angle α corresponds to the diagonal of the disk.

probability of dissociation, P, rather than IR emission. For the detailed calculation and a discussion of the dissociation probability, we refer the reader to §4.1 in Chapter 4. For the sake of clarity, the basic equations are reproduced here. The total dissociation probability is calculated by combining the rates for fragmentation ($k_0 \exp[-E_0/kT_{\rm av}]$) and IR decay ($k_{\rm IR}/(n_{\rm max}+1)$ into the following expression

$$P = \frac{k_0 \exp\left[-E_0/kT_{\rm av}\right]}{\left[k_{\rm IR}/(n_{\rm max}+1)\right] + k_0 \exp\left[-E_0/kT_{\rm av}\right]} \tag{5.12}$$

where k_0 and E_0 are the Arrhenius pre-exponential factor and energy describing the fragmentation process respectively, $k_{\rm IR}$ and $n_{\rm max}$ are the IR photon emission rate and number of IR photons (Chapter 4), and k is the Boltzmann constant. The temperature $T_{\rm av}$ is chosen as the geometrical mean between two specific effective temperatures of the PAH

$$T_{\rm av} = \sqrt{T_0 \times T_{n_{\rm max}}} \tag{5.13}$$

In the microcanonical description of a PAH, the temperature, T, describing the excitation (for fragmentation purposes) is related to the internal energy, E', by

$$T \simeq 2000 \left(\frac{E'(\mathrm{eV})}{N_{\rm C}}\right)^{0.4} \left(1 - 0.2\,\frac{E_0(\mathrm{eV})}{E'(\mathrm{eV})}\right) \tag{5.14}$$

where E_0 is the binding energy of the fragment (Tielens 2005). The temperatures T_0 and $T_{n_{\rm max}}$ in Eq. 5.13 are the temperatures when the internal energy equals the initial transferred energy ($E' = E$) and when the internal energy equals the energy after emission of $n_{\rm max}$ photons ($E' = E - n_{\rm max} \times \Delta\varepsilon$) with $\Delta\varepsilon$ being the average energy of the emitted IR photon. For the number of photons, $n_{\rm max}$, required to be emitted to have the probability per step drop by an order of magnitude, we adopt 10, the average photon energy we set equal to 0.16 eV corresponding to a typical CC mode, and the pre–exponential is set equal to $1.4\times\ 10^{-16}$ $\rm s^{-1}$ (Chapter 4). For the photon emission rate we adopt the typical value $k_{\rm IR}$ = 100 photons $\rm s^{-1}$ (Jochims et al. 1994b).

From the above equations one can see that P depends on the binding energy of the fragment, E_0, on the PAH size, $N_{\rm C}$, and on the energy transferred, T, which in turns depends on the initial energy of the projectile. For a fixed value of the transferred energy, the dissociation probability decreases for increasing E_0 and $N_{\rm C}$ because either more energy is required in the bond that has to be broken or because the energy is spread over more vibrational modes and hence the internal excitation temperature is lower. On the other hand, the more energy that is deposited in the PAH, the higher is the dissociation probability.

The fragment binding energy E_0, which is a crucial parameter in the evaluation of the dissociation probability is, unfortunately, presently not well constrained. As in our previous work (Chapter 4) we investigated the impact on the PAH destruction process for E_0 = 3.65, 5.6 and 4.58 eV, the latter value is consistent with extrapolations to interstellar conditions and is our reference value.

As mentioned at the end of § 5.2.1, the stopping power increases with the atomic number of the projectile and decreases with its energy. Thus, for a given pathlength, the energy transferred, and therefore the dissociation probability, will be higher for low energy heavy particles.

5.3 Collisions with high energy electrons

To model the interaction of high–energy electrons with PAH molecules, we refer to the formalism used to describe the irradiation effects in solid materials, in particular carbon nanostructures (Banhart 1999). In the collisions of high-energy (relativistic) electrons with nuclei, the screening effect of the surrounding electrons is negligible. The electron–nucleus interaction can thus be treated in terms of a binary collision using a simple Coulomb potential, applying the appropriate relativistic corrections (e.g. Reimer & Braun 1989; Banhart 1999).

If the energy transferred to the nucleus exceeds the *displacement energy* $T_{\rm d}$, i.e. the minimum energy required to produce a vacancy– interstitial pair which does not spontaneously recombine, the atom will be knocked out. If its energy is above the threshold value for further displacements, it can remove other atoms in its environment generating a collision cascade.

In this description the "bulk" nature of the target enters only after the first interaction, when projectile and displaced atom propagate into the solid. Therefore, if we limit ourselves to the first interaction only, this approach can be applied to electron–PAH collisions and allows us to take into account the "molecular" nature of our target.

In fact, this is the same binary collision approach used to describe the *nuclear interaction* (elastic energy loss) in collisions between PAHs and relatively low energy ions in interstellar shocks (Chapter 4).

A PAH is a planar molecule with tens to hundreds of carbon atom. In this case the target nucleus is a single carbon in the PAH. If the energy transferred exceeds a threshold value the target nucleus will be ejected from the molecule. The displacement energy then has to be replaced by the threshold energy T_0, which represents the minimum energy to be transferred in order to knock-out a carbon atom from a PAH. The interaction between a high energy cosmic ray electron and a PAH occurs between the impinging electron and one single target carbon atom in the molecule. The energy is transferred from the projectile electron to a target carbon atom through a binary collision. Thus, each electron collision implies the loss of one single carbon atom, in contrast to ion collisions where each interaction causes the ejection of a C_2 fragment from the PAH molecule.

The scattering geometry is shown in Fig. 5.3. After the collision, the target nucleus is knocked out and recoils at an angle Θ with respect of the initial direction of motion of the projectile electron. The energy T transferred to the nucleus depends on the scattering angle

$$T(\Theta) = T_{\max} \cos^2 \Theta \tag{5.15}$$

The term $T_{\max}$ is the maximum transferable energy, corresponding to a head–on collision ($\Theta = 0$), and is given by the following equation (Simmons 1965b)

$$T_{\max} = \frac{2\,E\,\left(E + 2\,m_e c^2\right)}{M_2\,c^2} \tag{5.16}$$

where E is the electron kinetic energy, m_e is the electron mass and M_2 is the target atomic mass.

The total displacement/removal cross section, σ, i.e. the cross section for collisions able to transfer more than the threshold energy T_0, is defined as the integral over the solid angle of the differential cross section $\mathrm{d}\sigma/\mathrm{d}\Omega$, which provides the probability for atomic recoil into the solid angle $\mathrm{d}\Omega$

$$\sigma = \int_0^{\Theta_{\max}} \frac{\mathrm{d}\sigma}{\mathrm{d}\Omega} 2\pi \, \sin\Theta \, \mathrm{d}\Theta \tag{5.17}$$

where $\Theta = 0$ corresponds to the transfer of $T_{\max}$ and $\Theta = \Theta_{\max}$ is the recoil angle corresponding to the transfer of the minimun energy T_0. The calculation of the total cross section σ for atom displacement/removal would require the analytical treatment of the Mott scattering of a relativistic electron by a nucleus (Mott 1929, 1932). The corresponding equations have to be solved numerically, but McKinley & Feshbach (1948) found an analytical approximation which provides reliable values of σ for light target elements such as carbon (under the assumption of an isotropic displacement/threshold energy).

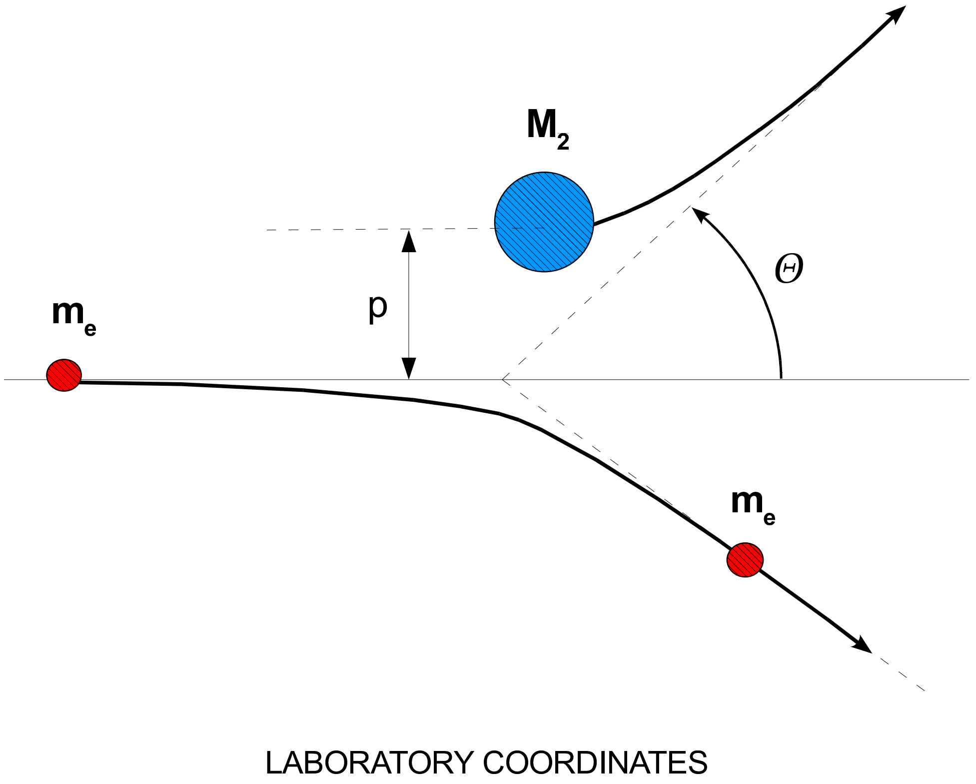

Figure 5.3 — Scattering geometry for the elastic collision of an electron (mass m_e, impact parameter p, initial velocity v) on a massive particle (mass M_2, initial velocity zero). After the impact, the target particle is knocked out and recoils at an angle Θ with respect of the initial direction of motion of the projectile electron.

We adopt the formulation of the analytical expression reported by Banhart (1999)

$$\sigma = \frac{4\,Z_2^2\,E_R^2}{m_e^2\,c^4}\left(\frac{T_{\max}}{T_0}\right)\pi\,a_0^2\left(\frac{1-\beta^2}{\beta^4}\right)\left\{1+2\pi\,\alpha\,\beta\left(\frac{T_0}{T_{\max}}\right)^{1/2} - \frac{T_0}{T_{\max}}\left[1+2\pi\,\alpha\,\beta+\left(\beta^2+\pi\,\alpha\,\beta\right)\ln\left(\frac{T_{\max}}{T_0}\right)\right]\right\} \quad (5.18)$$

where Z_2 is the atomic number of the displaced atom (in our case, carbon), E_R is the Rydberg energy (13.6 eV), $m_e c^2$ is the electron rest mass (0.511 MeV), a_0 is the Bohr radius of the hydrogen atom (5.3×10^{-11} m), $\beta = v/c$, v being the velocity of the incident electron, and $\alpha = Z_2/137$, where $1/137$ is the fine structure constant.

The term T_0 is the minimum energy which has to be transferred into the PAH in order to remove a carbon atom and represents the analog of the displacement energy T_d in a solid. For an extended discussion about the determination of the threshold energy T_0 we refer the reader to Chapter 4 (§ 4.2.2.1). We recall here that the value of T_0 is, unfortunately, not well established, because there are no experimental determinations on PAHs and the theoretical evaluation is uncertain. We decided to explore possible values: 4.5 and 7.5 eV, close to the energy of the single and double C-bond respectively and 15 eV, compatible with the expected threshold for a single walled nanotube. We adopt 7.5 eV as our reference value, consistent with all the experimental data.

To calculate β as a function of the kinetic energy of the incident electron, it is important to remember that we are considering relativistic particles, thus the appropriate expression for the kinetic energy is the following.

$$E_{\mathrm{kin}}^{\mathrm{rel}} = m_{\mathrm{e}}c^2 \left(\frac{1}{\sqrt{1-\beta^2}} - 1 \right) \tag{5.19}$$

From Eq. 5.19 we then derive β

$$\beta = \sqrt{1 - \left(\frac{m_{\mathrm{e}}\, c^2}{E_{\mathrm{kin}}^{\mathrm{rel}} + m_{\mathrm{e}}\, c^2} \right)^2} \tag{5.20}$$

The displacement cross section σ calculated from Eqs. 5.18 and 5.20, is shown in Fig. 5.4 as a function of the electron kinetic energy, for three different values of T_0. Above threshold the cross section increases with electron energy and decreases again at higher energies because of relativistic effects, reaching the constant value given by the following asymptotic expression

$$\sigma \sim \frac{8\, Z_2^2\, E_{\mathrm{R}}^2\, \pi\, a_0^2}{M_2\, c^2} \frac{1}{T_0} \tag{5.21}$$

As expected σ decreases for increasing values of the threshold energy. Around the peak the change of T_0 from 4.5 to 15 eV introduces a variation in the cross section of a factor of about 9, which reduces to 3.4 - the ratio 15/4.5, cf. Eq. 5.21 - for electron energies above ~2 MeV.

5.4 Cosmic ray spectrum

The stopping power of ions with energy above ~1 MeV/nucleon decreases with increasing energy (cf. § 5.2.1). This implies that the cosmic rays responsible for the major energy transfer to a PAH, and subsequent damage, are the lower-energy ones (below 1 GeV/nucleon). Unfortunately this part of the CR spectrum is not accessible from inside the heliosphere because of the phenomenon called *solar modulation* (Shapiro 1991). Cosmic rays entering the heliosphere see their intensity reduced by the effect of the solar wind, especially at low energies and when the solar cycle is at its maximum. The solar magnetic field is frozen within the plasma of the solar wind and drawn out with it into a spiral structure. Cosmic rays encountering the solar wind are then convected outward. Moreover when such charged particles interact with the expanding magnetic field, they are adiabatically decelerated. Hence, the CRs observed at a given energy were originally much more energetic.

Because of the solar modulation, the interstellar CR spectrum at low energies needs to be evaluated theoretically by estimating the solar modulation effect and solving the transport equation for particles in the ISM, assuming an appropriate CR spectrum at the sources and taking into account all possible mechanisms able to modify the intensity of the CRs during their propagation (energy losses, fragmentation etc. Shapiro 1991). The *Pioneer* and *Voyager* spacecraft have probed the heliosphere out to beyond

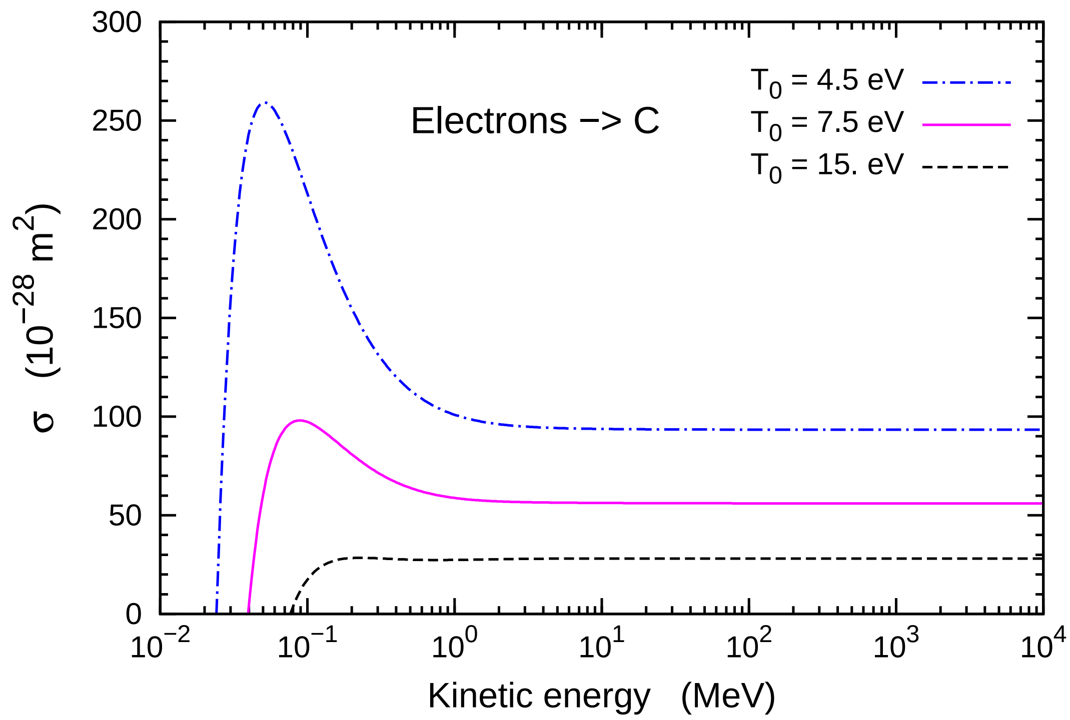

Figure 5.4 — High energy electron cross section for carbon atom removal, calculated for three values of the threshold energy T_0.

60 AU, greatly improving the understanding of the spectra of protons and heavier nuclei with energies above $\sim$ 100 MeV and the effects of solar modulation, although limited information is available on cosmic-ray nuclei below $\sim$ 100 MeV (Webber 1998). To describe the propagation and escape of Galactic CRs (at energies below a few$\times 10^{15}$ eV), a widely used approach is the leaky-box model, which assumes that the particles are confined to the Galaxy, with frequent visits to the disk boundaries where they have a small probability of leaking out (Ip & Axford 1985; Simpson & Garcia-Munoz 1988; Indriolo et al. 2009).

Following Webber & Yushak (1983) and Bringa et al. (2007) the CR intensity $I(E)$ as a function of the total energy per ion, E, is then given by

$$I(E) = C\,E^{0.3} \,/\, (E + E_0^*)^3 \quad \left(\mathrm{cm}^2\ \mathrm{s}\ \mathrm{sr}\ \mathrm{GeV}\right)^{-1} \tag{5.22}$$

The constant C can be determined by matching Eq. 5.22 with the high-energy cosmic ray spectrum measured on the Earth (see below). The scaling factor E_0^* sets the level of low-energy cosmic rays (Webber & Yushak 1983), which is mainly determined by ionization loss and Coulomb collisions (Ip & Axford 1985). At higher energies (above $\sim$ 1 GeV/nucleon) diffusive losses dominate.

The interstellar cosmic ray spectrum can be constrained by molecular observations. Cosmic ray protons ionize atomic and molecular hydrogen and this ionization drives interstellar chemistry through ion-molecule reactions. Analysis of molecular observations in diffuse clouds result in a primary ionization rate of 2×10^{-16} s^{-1} (H-nuclei)$^{-1}$ (Tielens 2005). The cosmic ray ionization rate follows from a convolution of the cosmic

Table 5.1 — Cosmic ray ion spectra parameters.

Ion	$M_1^{(a)}$	$E_0^{*\,(b)}$	$C^{(c)}$	$I_0^{(d)}$	γ
H	1.0	0.12	1.45	11.5×10^{-9}	2.77
He	4.0	0.48	0.90	7.19×10^{-9}	2.64
CNO	14.	1.68	0.36	2.86×10^{-9}	2.67
Fe-Co-Ni	58.	6.95	0.24	1.89×10^{-9}	2.60

(*a*): M_1 in amu.
(*b*): E_0^* (GeV) = E_0^*(H)× M_1 (ion).
(*c*): In units of (cm^2 s sr GeV$^{-1.7}$)$^{-1}$.
(*d*): In units of (cm^2 s sr GeV)$^{-1}$.

ray spectrum, Eq. 5.22, with the hydrogen ionization cross section (Bringa et al. 2007). The scaling factor E_0^* can be calculated then from

$$\zeta = 5.85 \times 10^{-16} \left(E_0^*/0.1\,\mathrm{GeV}\right)^{-2.56} \quad \mathrm{s}^{-1}\ (\mathrm{H\,nuclei})^{-1} \tag{5.23}$$

Again, because of the steep decrease of the ionization cross section with energy, the cosmic ray ionization rate is most sensitive to the low energy cosmic ray flux. For hydrogen this results in $E_0^* \sim 0.12$ GeV. For heavier particles we adopt the same scaling rule as Bringa et al. (2007): E_0^*(ion) = E_0^*(H)× M_1 GeV particle^{-1}, where M_1 is the mass of the particle in amu.

To calculate the constant C, we matched Eq. 5.22 with the high-energy spectrum detected on Earth. For the high energy data, which are not influenced by the solar modulation, we adopt the expression from Wiebel-Sooth et al. (1998)

$$I(E) = I_0 \left[E\,(\mathrm{GeV})/(1000\,\mathrm{GeV})\right]^{-\gamma} \quad \left(\mathrm{cm}^2\ \mathrm{s\ sr\ GeV}\right)^{-1} \tag{5.24}$$

where I_0 and γ depend on the CR ion.

In this study we consider the most abundant CR components: H, He, the group C, N, O and the group Fe, Co, Ni. The latter are in fact often detected as a group because of the experimental difficulty in distinguishing between particles with similar mass. The spectra were calculated using the method described above, with the high-energy parameters I_0 and γ from Wiebel-Sooth et al. (1998). The matching between the low and high energy regimes is at E = 1 TeV. A list of the parameters required for the calculation is reported in Table 5.1, and the resulting cosmic ray spectra are shown in Fig. 5.5. For the lowest energy in the interstellar cosmic ray spectrum, we adopt the value of 5 MeV/nucleon, coherent with the limit of validity of the leaky-box model (∼ 1 MeV/nucleon) and which corresponds to the lower limit of the energy range where ionization loss rapidly diminishes the propagation of cosmic rays in the ISM (Ip & Axford 1985).

The same approach as that used for heavy particles (ions) can be applied to cosmic ray electrons. In this case solar modulation also alters the spectrum of the electrons entering the solar cavity. The interstellar spectrum at low energies has to be calculated solving the transport equation for electrons in the ISM, taking into account the energy loss processes relevant for electrons, i.e. bremsstrahlung, synchrotron and inverse Compton. The low energy spectrum then has to be connected to the measured high-energy spectrum, which is not affected by the modulation. We adopt the expression from Cummings (1973), calculated in the framework of the leaky-box model (see also Ip & Axford 1985; Moskalenko & Strong 1998)

$$I(E) = A\ \left[E(\mathrm{GeV}) \times 10^3\right]^{-\gamma} \quad \left(\mathrm{cm}^2\ \mathrm{s}\ \mathrm{sr}\ \mathrm{GeV}\right)^{-1} \tag{5.25}$$

where E is in GeV and $\begin{cases} A = 0.0254 \times 10^5,\ \gamma = 1.8 & \text{for } 5 \times 10^{-3} \leq E \leq 2, \\ A = 5.19 \times 10^5, \quad \gamma = 2.5 & \text{for } 2 < E \leq 10^3 \end{cases}$

The calculated spectrum is shown in Fig. 5.5. For the lowest energy, we again adopt a value of 5 MeV, coherent with the limit of validity of the leaky-box model and with the range of influence of bremsstrahlung, the dominant energy loss mechanism for electrons with energies less than a few hundreds of MeV.

5.5 Collision rate and C-atom ejection rate

To calculate the collision rate between PAHs and cosmic ray ions and electrons, with energy fluxes described by Eq. 5.22 and 5.25 respectively, we follow the procedure illustrated below.

For ion collisions, where the energy is transferred to the whole PAH via electronic excitation, we first need to calculate the term $\Sigma(E)$, which takes into account all possible ion trajectories through the PAH, with their corresponding transferred energies and dissociation probabilities. Adopting the configuration shown in Fig. 5.2 we have

$$\begin{aligned} \Sigma(E) &= \frac{1}{2\pi} \int \mathrm{d}\Omega\, \sigma_{\mathrm{g}}(\vartheta)\, P(E, \vartheta) & (5.26) \\ &= \int_{\vartheta=0}^{\pi/2} \sigma_{\mathrm{g}}(\vartheta)\, P(E, \vartheta)\, \sin\vartheta\, \mathrm{d}\vartheta & (5.27) \end{aligned}$$

with $\Omega = \sin\vartheta \mathrm{d}\vartheta \mathrm{d}\varphi$, with φ running from 0 to 2π and ϑ from 0 to $\pi/2$. The geometrical cross section seen by an incident particle with direction defined by the angle ϑ is given by

$$\sigma_g(\vartheta) = \pi\, R^2\, \cos\vartheta\, +\, 2\, R\, d\, \sin\vartheta \tag{5.28}$$

which reduces to $\sigma_g = \pi R^2$ for $\vartheta = 0$ (face-on impact) and to $\sigma_g = 2Rd$ for $\vartheta = \pi/2$ (edge-on impact). The term $P(E, \vartheta)$ represents the total probability for dissociation upon ion collision, for a particle with energy E and incoming direction ϑ. The ion collision rate is calculated by convolution of the term $\Sigma(E)$ over the cosmic ray spectrum $I_{\mathrm{i}}(E)$

$$R^{\mathrm{coll}}_{\mathrm{i,CR}} = 4\pi \int_{E_{\mathrm{min}}}^{E_{\mathrm{max}}} F_{\mathrm{C}}\, I_{\mathrm{i}}(E)\, \Sigma(E)\, \mathrm{d}E \tag{5.29}$$

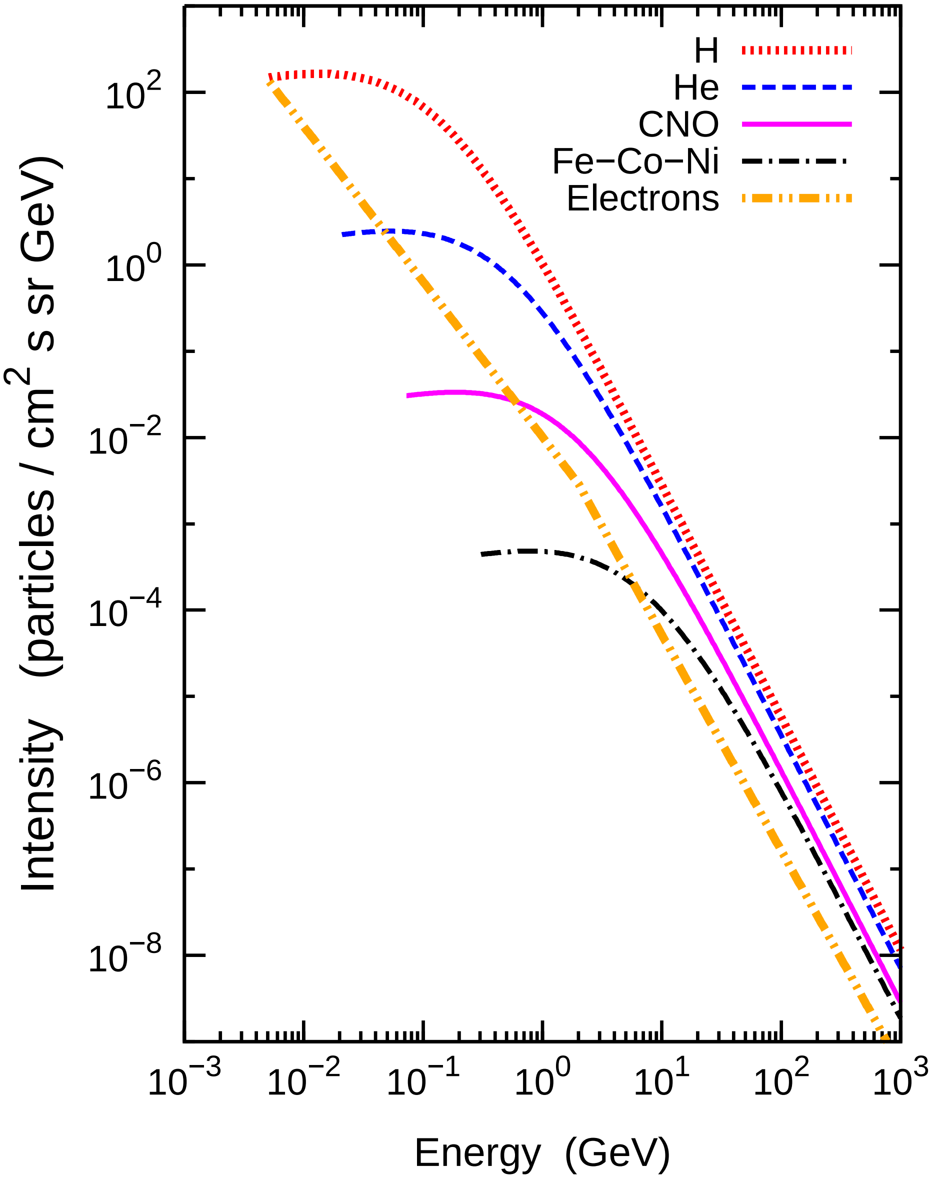

Figure 5.5 — Interstellar cosmic ray spectrum of H, He, CNO, Fe-Co-Ni and electrons as a function of the particle energy.

Because each (electronic) ion interaction leads to the removal of two carbon atoms from the PAH, to obtain the C-atom ejection rate the collision rate has to be multiplied by a factor of 2:

$$R_{\mathrm{i,CR}} = 2 \times R^{\mathrm{coll}}_{\mathrm{i,CR}} = 8\pi \int_{E_{\mathrm{min}}}^{E_{\mathrm{max}}} F_{\mathrm{C}}\, I_{\mathrm{i}}(E)\, \Sigma(E)\, \mathrm{d}E \tag{5.30}$$

The factor, F_{C}, takes Coulombic effects into account (see below). For E_{max} we adopt a value of 10 GeV, corresponding to the highest energy for which experimental stopping determinations exist and thus for which Eq. 5.7 is valid. Moreover the CR intensity and stopping power decrease rapidly, so ions with energy above 10 GeV do not contribute significantly to the integral in Eq. 5.29. Concerning the lower integration limit, we consider E_{min} as a free parameter and perform the calculation for 5 MeV/nucleon and 50 MeV/nucleon. The first is the lower limit assumed for the CR spectra, while the second is in reasonable agreement with the ionization rate derived from observations (Nath & Biermann 1994; Bringa et al. 2007).

For interactions with CR electrons, each binary collision results in the ejection of one single C-atom. Thus the ejection rate coincides with the collision rate, and are both given by the following relation

$$R_{\mathrm{e,\,CR}} = R^{\mathrm{coll}}_{\mathrm{e,\,CR}} = 0.5\, N_{\mathrm{C}}\, 4\pi \int_{E_{\mathrm{min}}}^{E_{\mathrm{max}}} F_{\mathrm{C}}\, I_{\mathrm{e}}(E)\, \sigma(E)\, \mathrm{d}E \tag{5.31}$$

where the ejection cross section *per target atom* σ has to be multiplied by the number of C-atom in the molecule, N_{C}. The factor 0.5 takes the angle averaged orientation into account (Chapter 3). As for the cosmic ray ions we assume integration limit values E_{min} = 5 and 50 MeV and E_{max} = 10 GeV. For the electrons, the upper limit is not constrained by the stopping theory (the expression for the ejection cross section holds for even higher energies) and is only related to the steepness of the spectrum which results in a negligible contribution from electrons with energy above 10 GeV (cf. Fig. 5.5).

The Coulombian correction factor F_{C} (Chapter 4) takes into account the fact that both target and projectiles are charged, and that the collision cross section could be enhanced or diminished depending on the charge of the PAH. Because we are considering high energy ions and electrons, which are unaffected by the Coulombian field, F_{C} is always unity.

5.6 Results

5.6.1 PAH lifetime

Collisions with CR ions and electrons will cause a progressive decrease in the number of carbon atoms in a PAH molecule. For interactions with ions, after a time t this number is reduced to

$$N_{\mathrm{C}}(t) = N_{\mathrm{C}}(0) \, - \, R_{\mathrm{i,\,CR}}\, t \tag{5.32}$$

and the fraction of carbon atoms ejected from this PAH is

$$F_{\mathrm{L}}(t) = \frac{R_{\mathrm{i,\,CR}}\, t}{N_{\mathrm{C}}(0)} \tag{5.33}$$

where $R_{\mathrm{i,\,CR}}$ is the C-atom ejection rate from Eq. 5.30. We assume that the PAH is destroyed after the ejection of 1/3 of the carbon atoms initially present in the molecule. This occurs after a time τ_0 which we adopt as the PAH lifetime against CR ions bombardment, and is given by

$$\tau_0 = \frac{N_{\mathrm{C}}}{3\, R_{\mathrm{i,\,CR}}} \tag{5.34}$$

For electron collisions, the number of carbon atoms in the PAH after a time t is

$$N_{\rm C}(t) = N_{\rm C}(0)\exp\left[-t\,/\,\tau'\right] \tag{5.35}$$

and the fraction of carbon atoms ejected from this PAH is

$$F_{\rm L}(t) = \left(1 - \exp\left[-t\,/\,\tau'\right]\right) \tag{5.36}$$

with the time constant $\tau' = N_{\rm C}/R_{\rm e,\,CR}$, where $R_{\rm e,\,CR}$ is the ejection rate from Eq. 5.31. The ejection of 1/3 of carbon atoms originally present in the PAH molecule, after which the PAH is considered destroyed, takes the time τ_0 given by

$$\tau_0 = \ln\left(\frac{3}{2}\right)\tau' = \ln\left(\frac{3}{2}\right)\frac{N_{\rm C}}{R_{\rm e,\,CR}} \tag{5.37}$$

As for ion collisions, we adopt τ_0 as the PAH survival time against CR electrons. The ejection rate $R_{\rm e,\,CR}$ scales linearly with $N_{\rm C}$, hence the corresponding lifetime τ_0 is independent of PAH size.

For collisions with ions, we calculated the lifetime of PAHs of four sizes $N_{\rm C}$ = 50, 100, 200 and 1000 ($n_{\rm max}$ = 10, 20, 40 and 200 respectively) bombarded by cosmic ray H, He, CNO and Fe-Co-Ni ions, assuming three different values for the electronic binding energy, E_0 = 3.65, 4.58 and 5.6 eV (cf. § 4.4.1 in Chapter 4). The maximum CR energy is $E_{\rm max}$ = 10 GeV per ion, while we consider two values for the lower CR energy, $E_{\rm min}$ = 5 and 50 MeV/nucleon. In principle, not all the energy transferred to the PAH will be internally converted into vibrational modes, with consequent relaxation through dissociation (or IR emission). Other processes can occur, for instance the production of Auger electrons which will carry away from the molecule a part of the transferred energy. We do not know exactly how to quantify this energy partitioning and so we introduce a factor f, which represents the fraction of the transferred energy T that goes into vibrational excitation.

The survival time as a function of the factor f is shown in Fig. 5.6, for $E_{\rm min}$ = 5 MeV/nucleon (left panel) and $E_{\rm min}$ = 50 MeV/nucleon (right panel). The PAH lifetime becomes shorter as more energy goes into vibrational excitation (increasing f) and for lower values of E_0, because this implies a higher temperature, $T_{\rm av}$, and a lower energy to eject a fragment, resulting in a larger dissociation probability (Eq. 5.12).

The dissociation probability is more sensitive to E_0 when the energy available for dissociation is lower i.e. light projectile and small f, and when the same amount of energy has to be spread over more bonds (increasing size). This explains why the separation between the time constant curves corresponding to the different values of E_0 decreases with increasing available energy and mass of the projectile (from H to Fe-Co-Ni), while it gets bigger for larger PAHs. Big PAHs are more resistent to cosmic ray bombardment because for any given transferred energy their dissociation probability is lower.

The lifetime against Fe-Co-Ni bombardment is essentially constant - except for very low available energy and very large molecules ($N_{\rm C}$ = 1000). Its large value, $\tau_0 \sim$ few 10^9 yr, results from the fact that, despite the huge amount of energy transferred into the molecule (cf. Fig. 5.1), the Fe-Co-Ni abundance in cosmic rays is small. This leads

Table 5.2 — Time constant τ_0 for carbon atom ejection following PAH collisions with CR electrons.

	T_0 (eV)			
	4.5	7.5	15.	$E_{\rm min}$ (MeV)
τ_0	1.2×10^{13}	2.0×10^{13}	4.2×10^{13}	5
(yr)	8.0×10^{13}	1.4×10^{14}	2.7×10^{14}	50

to a low collision rate and long lifetime. For hydrogen, the high abundance is not enough to compensate for the small stopping power, which rapidly decreases above 1 MeV/nucleon. As a result the lifetimes are long. Since the energy transferred to the molecule is small, the collision rate and the survival times, are sensitive to the adopted parameters: the fraction of the energy transferred available for dissociation f, the fragment binding energy E_0 and the PAH size. This variability is shown in Fig. 5.6. The situation for helium and CNO lies somewhere between the cases for H and Fe-Co-Ni.

As expected, when $E_{\rm min}$ = 50 MeV/nucleon τ_0 is higher for all sizes, ions and E_0, due to the fact that we include in the calculation only the cosmic rays with higher energies, which have lower intensity and transfer less energy (both the CR spectrum and the stopping power are decreasing functions of the kinetic energy).

The CR electron time constant is independent of the PAH size, and has been calculated for three values of the threshold energy for carbon atom ejection, T_0 = 4.5, 7.5 and 15 eV, and two lower limits for the electron energy, $E_{\rm min}$ = 5 and 50 MeV. The results are shown in Fig. 5.7 and summarized in Table 5.2. The PAH lifetime is longer both for increasing values of T_0 and $E_{\rm min}$, in the first case because of the diminution in the cross section σ, in the second case because we include only the high-energy, low-intensity part of the spectrum. Given that σ is almost constant for energies above $\sim$ 2 Mev, for a fixed T_0 this part of the spectrum does not contribute to the variation. Because of the small ejection cross section and the steep CR electron spectrum, all the calculated time constants are long ($>10^{13}$ yr).

5.6.2 Discussion of the uncertainties

The first source of uncertainty affecting the study of PAH interaction with high energy particles is the accuracy of the stopping theory used to calculate the energy loss of ions in matter. This is a difficult issue because the current theory, based on the Bethe-Bloch equation and described in § 5.2.1, is in fact a combination of different theoretical approaches with corrections coming from fits to the experimental data. A better way to pose the problem is by instead asking: "How accurately can stopping powers be calculated?" The comparison between theory and experiments, together with the evaluation of possible variation sources such as structural variations in the targets, provides an accuracy ranging from 5 to 10 % (Ziegler 1999).

In our calculation we do not use the complete Bethe-Bloch equation (implemented in the SRIM code with all corrective terms) but the analytical approximation given by Eq. 5.10. The discrepancy between the stopping power curves from these two formula-

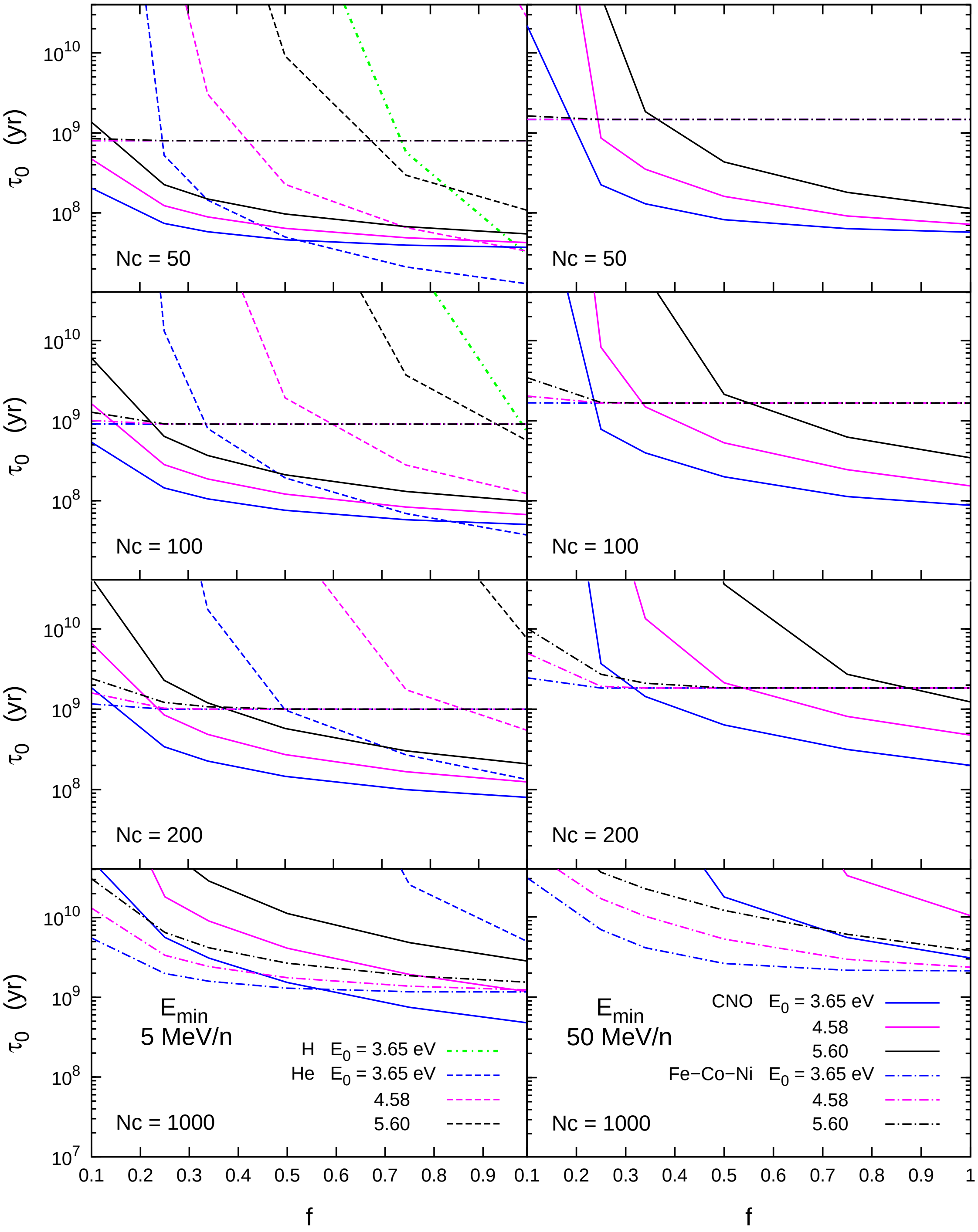

Figure 5.6 — PAH survival time against collisions with cosmic ray ions, as a function of the factor f. The lifetime has been calculated for PAHs of different sizes (N_C), assuming two values for the lower CR energy, E_{min} = 5 MeV/nucleon (*left panel*) and 50 MeV/nucleon (*right panel*). The upper energy E_{max} is 10 GeV for all ions.

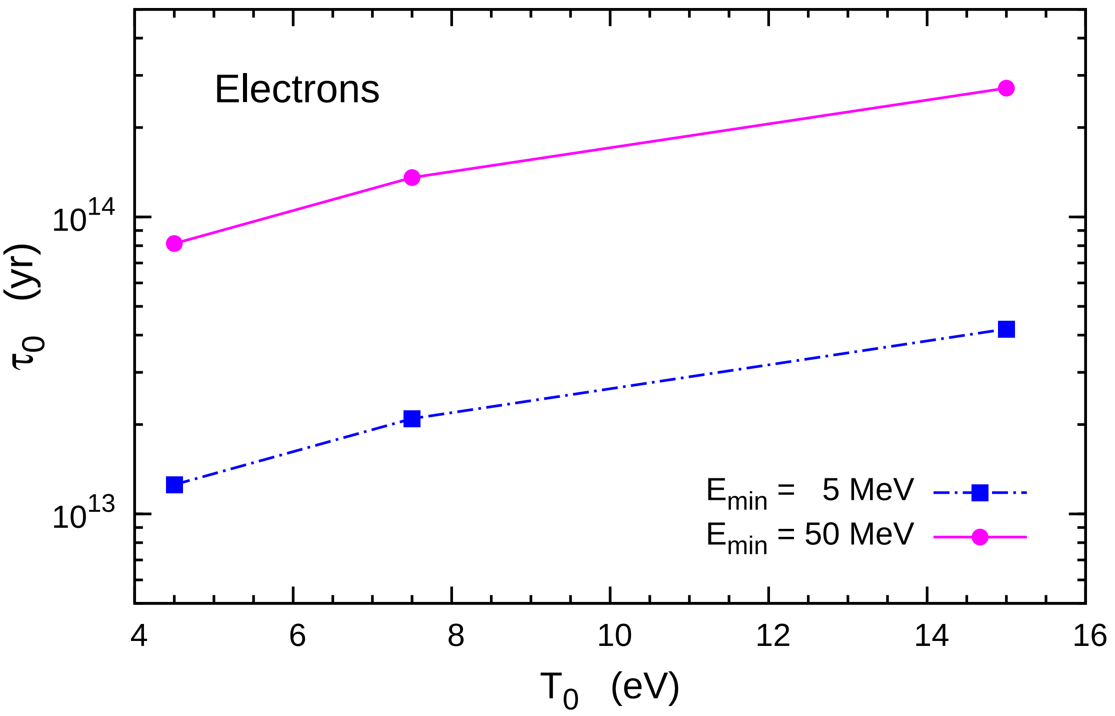

Figure 5.7 — Time constant τ_0 for carbon atoms removal due to collisions with cosmic ray electrons, as a function of the threshold energy T_0, calculated assuming two values for the minimum electron energy E_{min}.

tions is very small, and introduces an uncertainty of at most 10 % in our calculation. An additional source of uncertainty comes from the calculation of the energy transferred to the PAH using the approximation in Eq. 5.11, which assumes a constant stopping power along the distance travelled through the molecule. In this case the difference with the exact calculation is also limited to less than 10 %.

Concerning the collisions with high energy ions, the dominant source of uncertainty in the determination of the PAH lifetime is the fragment binding energy E_0 (cf. Chapter 4, § 4.4.1), which is strongly modulated by other parameters: type of ion, PAH size, fraction of energy available for dissociation and CR low energy limit, as clearly shown in Fig. 5.6. To give an example, when E_0 goes from 3.65 to 5.6 eV and E_{min} = 5 MeV/nucleon, the time constant for a 50 carbon atoms PAH colliding with helium varies by a factor of $\sim 2\times10^7$ for $f = 0.25$ and by a factor of 8 for $f = 1$. For CNO impacting on a 200 C-atom molecule the change is a factor of 7 and 3 for $f = 0.25$ and $f = 1$ respectively, which become 3×10^6 and 6 when E_{min} = 50 MeV/nucleon. These numbers give an idea of the huge and complex variability induced by the uncertainty in the parameter E_0.

In the treatment of PAH collisions with high energy electrons, three sources of uncertainty have to be considered: the analytical approximation to the numerical solution for the ejection cross section (Eq. 5.18), the choice of the threshold energy T_0 and of the lower electron energy E_{min}. While the discrepancy between the analytical expression and the numerical soluton for σ is only a few percent (McKinley & Feshbach 1948), the variation of T_0 from 4.5 to 15 eV implies a variation in the cross section of about a factor of 9 around the peak (electron energy $\sim$ 0.1 MeV), and a factor of 3 above 2 MeV, where the cross section becomes almost constant. This results in a change of the electron time constant of a factor of $\sim$ 3.4 for both values of $E_{\rm min}$, consistent with the cross section variation. When the lower electron energy varies from 5 to 50 Mev, the time constant increases of a factor of $\sim$ 7 for all T_0. Since in the energy range we are considering the cross section is constant for any given T_0, the variation of τ_0 reflects the "cut" made on the CR spectrum, excluding the low-energy high-intensity region which heavily contributes to the collision rate. To summarize, in our study we explored a wide range in values for T_0, E_0 and $E_{\rm min}$, and the resulting variation is in some sense the maximum possible.

A final remark concerns the CR spectrum at low energies. As previously mentioned, the major contribution to PAH destruction comes from low-energy cosmic rays, both because the energy transfer is more efficient for low energy projectiles (ions) and the CR intensity decreases with increasing energy (for both ions and electrons). Unfortunately, because of the solar modulation this part of the spectrum is not accessible to measurements from Earth and needs to be evaluated theoretically. The spectra we adopt, which of course have to match the measured high energy spectra, have been calculated using a rigorous physics and taking into account all possible constraints from available measurements. Nevertheless the lack of data in such a crucial CR energy region introduces a source of uncertainty that is difficult to quantify.

5.7 Discussion

5.7.1 Lifetime of PAHs against cosmic ray processing

In § 5.6.1, we estimated the PAH lifetime against CR bombardment in the neighborhood of the Sun, i.e. considering an interstellar spectrum based on galactic cosmic ray measurement near the Earth but corrected for the influence of the Heliosphere (cf., § 5.4). Fig. 5.8 shows the PAH lifetime against CR bombardment (ions + electrons) as a function of the size of the molecule, $N_{\rm C}$, for $E_{\rm min}$ = 5 and 50 MeV/nucleon, assuming f = 0.5 and our reference values of 7.5 and 4.6 eV for the parameters T_0 and E_0 respectively. These lifetimes should be compared to the lifetime against shock destruction of PAHs of approximately 150 Myr (Chapter 3). For small PAHs (<150 C-atoms) and a low energy cut off for the cosmic ray spectrum (5 MeV/nucleon), cosmic rays are calculated to be the dominant destruction agent in the warm ISM. For larger PAHs and/or a higher minimum cosmic ray energy, shocks take over. In this assessment, it should be kept in mind that shock processing occurs predominantly in warm intercloud medium of the ISM: shocks faster than 100 km s^{-1} are very rare for diffuse clouds since supernova remnants predominantly expand in the warm or hot intercloud medium and the shock speed in clouds is then down by the square root of the density ratio between these different phases in the ISM (Jones et al. 1994). Shock processing of PAHs in diffuse clouds will then predominantly occur when cloud material exchanges with the warm intercloud medium (where shock timescales are short). The timescale for this exchange is included in the lifetime estimate for shock processing. Cosmic rays on the

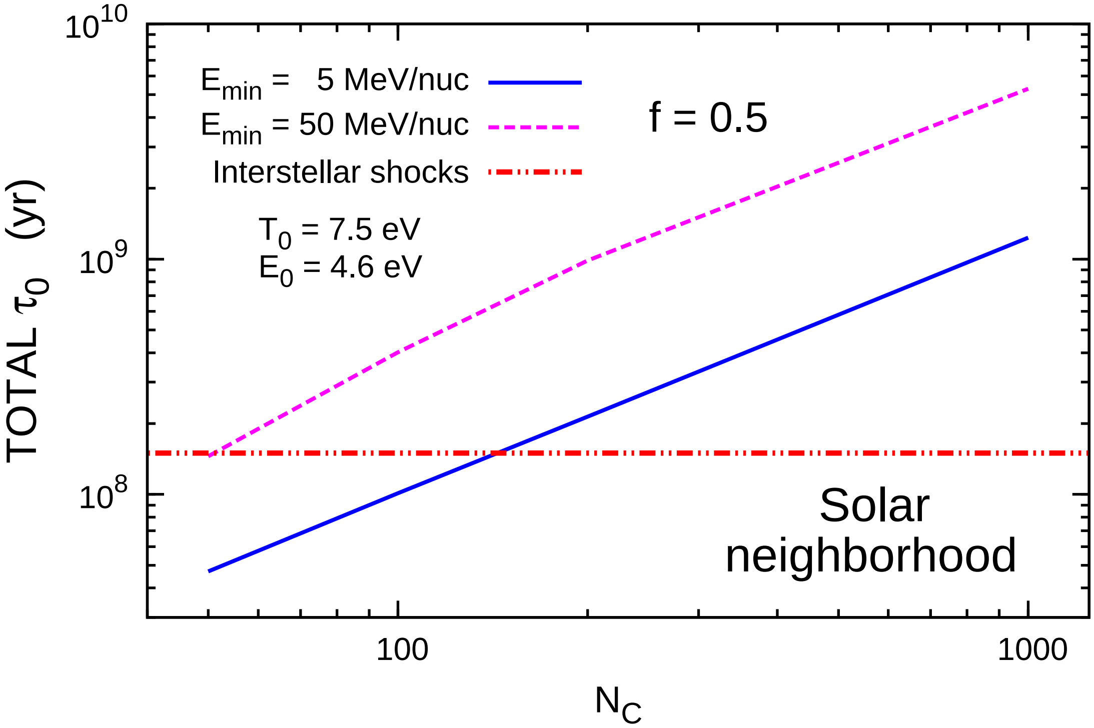

Figure 5.8 — PAH survival time against CR bombardment (ions + electrons) as a function of the molecule size (N_C). The total lifetime shown in the figure has been calculated for E_{min} = 5 and 50 MeV/nucleon, with f = 0.5 and adopting our reference values T_0 = 7.5 eV and E_0 = 4.6 eV, but we remind the reader of the variation in the calculated survival time against CRs, due to the uncertainty on the parameters E_0 and T_0 (cf. Fig. 5.6 and Fig. 5.7). The PAH lifetime against shock destruction in the ISM is shown for comparison.

other hand penetrate all phases of the ISM, except perhaps the densest molecular cloud cores, and can process all material that they interact with.

Finally, we note that cosmic ray electron collisions are not important for the processing of interstellar PAHs. We point out the fact that this study does not include the secondary electrons with an energy of about 30 eV produced by primary CR electrons by the initial ionization of H or H_2 in diffuse clouds. Such electrons are energetic enough to induce some PAH fragmentation but, although initially abundant, they decay easily. Moreover, the estimation of PAH destruction at these energies is a delicate matter because the stopping power (cf. Fig. 4.2) increases sharply with the energy of the impacting electron. A small variation of the energy of the projectile electron will imply a large variation of the stopping power, and then of the amount of energy transferred. The proper estimation of the PAH destruction induced by such secondary electrons would require a more precise knowledge of their energy distribution and abundance. We focused here on the role of primary (CR) electrons, leaving for a future study the detailed evaluation of the effects of the secondary electrons on the PAH population in diffuse clouds.

5.7.2 PAHs in galactic halos

ISO and Spitzer observations revealed that PAHs are abundant in the halos of normal spiral galaxies (Irwin & Madden 2006; Irwin et al. 2007; Whaley et al. 2009). Here, we will discuss the potential role of cosmic rays in the destruction of these PAHs.

After having estimated the PAH lifetime against CR bombardment in the vicinity of the Sun, the question that needs to be addressed is whether the cosmic ray spectrum changes across the galaxy and how this may affect the PAH lifetime.

5.7.2.1 *The cosmic ray spectrum in galactic halos*

A powerful tool to probe the presence of cosmic rays in regions distant from the Solar System has been provided by gamma and radio astronomy. Cosmic ray protons interact hadronically with the nuclei of the interstellar medium (mainly protons and α particles) producing both charged and neutral pions (Fermi 1950; Stecker 1973). Charged pions decay into secondary leptons, while neutral pions decay into two γ photons:

$$
\begin{aligned}
p + N &\rightarrow 2N + \pi^{\pm/0} && (5.38)\\
\pi^{\pm} &\rightarrow \mu^{\pm} + \nu_{\mu}/\bar{\nu}_{\mu} \rightarrow e^{\pm} + \nu_e/\bar{\nu}_e + \nu_{\mu} + \bar{\nu}_{\mu} && (5.39)\\
\pi^0 &\rightarrow 2\gamma && (5.40)
\end{aligned}
$$

Electrons loose energy via synchroton and inverse Compton, producing detectable radio emission, while γ-rays are directly measurable by gamma-ray telescopes. The quantity of cosmic-ray protons can then be calculated from their decay products, moreover, because photons are not affected by magnetic fields, they can provide a direct indication about the location of their sources (e.g. Ramana Murthy & Wolfendale 1993; Hunter et al. 1997).

Different studies (see Shibata et al. 2007, and references therein) have shown that the slope of the energy spectrum is almost independent of the observational site in the Galaxy, but this is not true for the amplitude of the spectrum. In the galactic plane the cosmic ray intensity shows a longitudinal gradient (Shibata et al. 2007), with an exponential decrease from the Galactic center toward the periphery with a scale length of 20 kpc. Assuming the galactic parameters from Shibata et al. (2007) we obtain an enhancement at the Galactic center of about a factor 1.5 with respect to the Solar System.

Radio and gamma observations, together with the study of unstable CR nuclei such as ^{10}Be (Hayakawa et al. 1958; Simpson & Garcia-Munoz 1988) have demonstrated that cosmic rays are not confined to the thin disk which contains their sources, as assumed by the leaky-box model (Simpson & Garcia-Munoz 1988), but are able to travel long distances outside the galactic plane. Various models for CR propagation (e.g. Ginzburg et al. 1980; Ginzburg 1988; Berezinskii et al. 1990; Strong & Moskalenko 1998) assume a thin disk (half-thickness $h_{\rm d} \sim 100 - 200$ pc) located on the galactic plane, where the sources reside, surrounded by a large diffusive halo with half-thickness $h_{\rm h} \sim 1 - 15$ kpc , where cosmic rays spend part of their life.

Using the formalism developed by Shibata & Ito (2007) the latitudinal gradient of the cosmic ray intensity for a given ion i can be written as

$$\frac{I_i(r,z,E)}{I_i(r,0,E)} \simeq \exp\left(-|z|/z_{\rm D}\right) \tag{5.41}$$

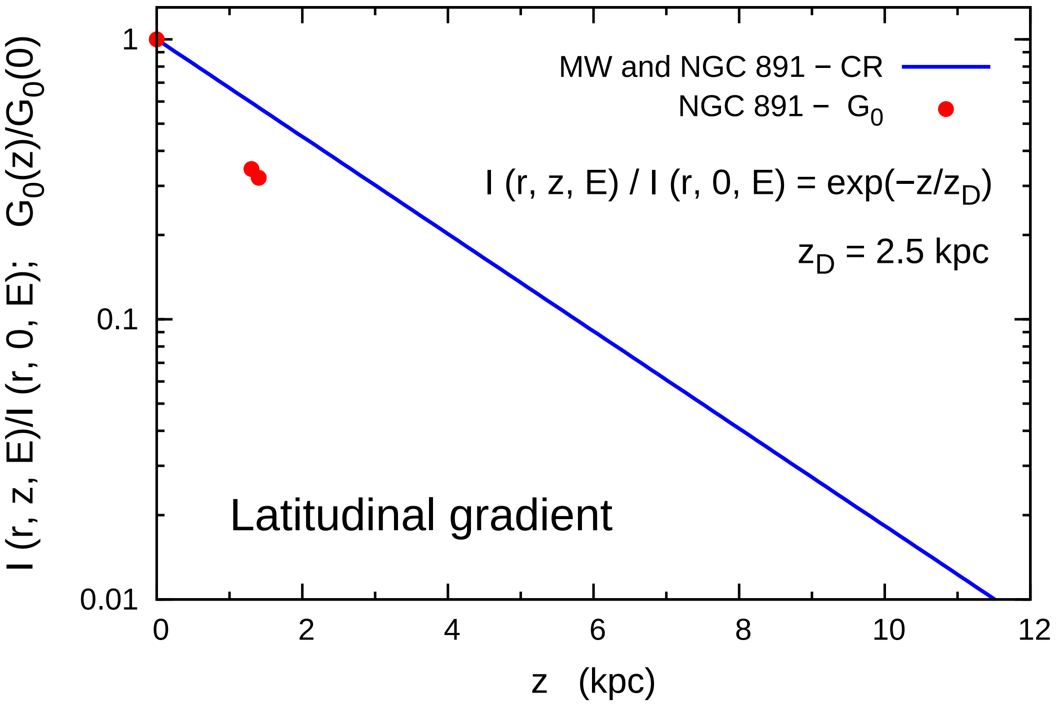

Figure 5.9 — The latitudinal cosmic ray gradient in both Milky Way (MW) and NGC 891, as a function of the vertical distance z from the galactic plane together with the vertical variation of the interstellar radiation field G_0 in NGC 891 (*courtesy F. Galliano*). The cosmic ray intensity I decreases with the scale height z_D of the diffusion coefficient.

where r is the radial distance from the center of the galaxy projected on the galactic plane and z is the latitudinal distance from the Galactic plane. Eq. 5.41 shows that the CR intensity attenuates with the scale height z_D of the diffusion coefficient. The latitudinal gradient is calculated assuming the value z_D = 2.5 kpc proposed by e.g. Shibata et al. (2007) and is shown in Fig. 5.9.

Ultimately, cosmic rays are thought to be accelerated by supernova remnants, tapping some 10% of the SN energy. For other galaxies, we will scale the overall cosmic ray density with the star formation rate of the galaxy and we will adapt scale lengths and scale heights appropriate for the Milky Way. Since the CR intensity decreases exponentially outside the galactic plane, we expect the PAH lifetime at higher latitudes to be enhanced by the same factor.

5.7.2.2 *The origin and evolution of PAHs in galactic halos*

PAH emission has been observed at high latitudes in several normal galaxies with scale heights of 2-3 kpc (Irwin & Madden 2006; Irwin et al. 2007; Whaley et al. 2009). The study of NGC 891, the edge-on twin of the Milky Way, is particularly instructive. While the vertical distribution of the 8 μm PAHs emission is noticably narrower than that of the cold dust radiating at 450 μm, modeling reveals that this likely reflects the variation of the stellar population from the disk to the halo; eg., the dominant (FUV) heating sources of the PAHs are located in the disk while the old stellar population, which contributes substantially to the heating of the dust, extends some 3kpc above the disk (Whaley et al. 2009).

Some of the PAH molecules, as well as the dust, present at high galactic latitudes may originate from mass losing AGB stars in the halo. For the Milky Way, recent optical and infrared surveys (2MASS and DENIS) have revealed the presence of C-rich AGB stars enshrouded in dusty ejecta at distances of 2-6 kpc above the plane (Groenewegen et al. 1997; Mauron 2008). Some 100 such C-stars are known in the halo up to distances of 150 kpc and many of these belong to the tidal stream of the Sgr dwarf galaxy (Mauron & Kendall 2005). There is no complete census of such objects and a mass balance of PAHs and dust in the halo cannot be assessed, yet.

More likely, though, most of the PAHs and dust represent signpost of the large scale circulation of matter between the disk and halo. Indeed, the vertical distribution of PAHs is similar to that of the dust once the differences in heating are accounted for and to other tracers of this circulation pattern such as the diffuse ionized gas. If PAHs are indeed transported to high latitudes through the action of the galactic fountain, then the acceleration associated with this process must have been very gentle since PAHS are quickly destroyed in shocks faster than 100 km s $^{-1}$ (Chapter 3). Likely, PAHs are entrained as diffuse cloud(let)s sheared off the chimney walls in the hot gas of the venting supernovae and lifted that way high above the plane. As shown in Chapter 4, PAHs are rapidly destroyed in hot gas. Hence, after evaporation of these cloudlets driven by thermal conduction from the hot gas, PAHs will be gone and clouds subsequently condensing through thermal instabilities in the halo will not show up in the PAH emission bands.

Hence, PAHs in the halo may represent a 'molecular dye' with which this entrainment aspect of the disk-halo circulation flow can be separated from the evaporation/condensation pattern and followed in detail. The effectiveness of this PAH-dye is modified on the one hand by the diffusion of the FUV photons needed for their excitation from the disk and on the other hand by destruction of PAHs in the harsh environment of the halo. Here, we are concerned with the latter aspect, the lifetime of PAHs at high latitudes above the plane. First, the residence time is of interest. With a total mass of Warm Intercloud material of $\sim 10^9$ $M_\odot$ in the lower ($\sim$ 0.5 kpc) halo and a circulation rate of 5 $M_\odot$/yr between the plane and the halo for the Milky Way, the residence time of PAHs at these latitudes is some 2×10^8 yrs. The residence time at the higher latitudes ($\sim$2 kpc) we are interested in here will be commensurately larger. At the latitudes where PAHs are observed ($\sim$2 kpc), we expect that supernova shock waves, an important destruction agent in the disk of the galaxy, are of little concern. UV photolysis is generally considered to be a main agent for the destruction of small ($<$50 C-atoms) PAHs, weeding out the less stable (eg., smallest and/or non-compact) PAHs on a rapid timescale (Tielens 2008). Indeed, the minimum size in the PAH-size-distribution is thought to reflect this process. However, because this process is very sensitive to size, compact PAHs only slightly larger than this minimum size are essential 'indestructible'. Thus, we expect that PAHs transported upwards from the plane by the galactic fountain have already been weeded down to the most stable forms and because of the decreased UV flux with latitude (Fig. 5.9), further UV photolysis will be of little concern. Using the results of this chapter, we can estimate that destruction of

PAHs by cosmic rays.

Taking the cosmic ray distribution in the halo from § 5.7.2.1 we calculate the cosmic ray destruction timescale. Because of its similarity with the Milky Way, we adopt for NGC 891 the same diffusion scale height z_D = 2.5 kpc. This implies that the latitudinal gradient from Eq. 5.41 will be the same for both galaxies. The CR intensity variation in NGC 891 with respect to the solar neighborhood is given by the following expression

$$\frac{I_{i,\mathrm{NGC891}}(0,|z|,E)}{I_{i,\mathrm{MW}}(r_\odot,0,E)} = (1.5 \times \frac{3.8}{3}) \exp\left(-|z|/z_\mathrm{D}\right) \tag{5.42}$$

where 1.5 is the CR enhancement factor in the galactic center with respect to the solar neighborhood and the factor 3.8/3 takes into account the increased cosmic-ray intensity in NGC 891 due to its higher star formation rate (3.8 $M_\odot$ yr^{-1}, Popescu et al. 2004) with respect to the Milky Way ($\sim$3 $M_\odot$ yr^{-1}, Scalo 1986; Prantzos & Silk 1998). At the typical PAH detection scale height $|z|$ = 3 kpc we obtain a decrease of the CR intensity of a factor of 0.6. The destruction lifetime will be then enhanced by a factor of (1/0.6).

The total PAH survival time in the halo of NGC 891 compared with the circulation timescale is shown in Fig. 5.10. The PAH survival time is comparable to or longer than the circulation timescale. PAHs could be good tracers of material entrained in the plane and carried to high latitudes by the galactic fountain as long as this material never loses its 'identity' through evaporation into the hot gas followed by recondensation into cloudlets. Of course, as emphasized by Whaley et al. (2009), such a study has to properly evaluate the flux of pumping of UV photons in order to be of quantitative value. In that case, mid-IR studies can potentially trace this entrainment process and the exchange between cool and hot phases on a arcsecond scale size. Nevertheless other factors have to be taken into account, such as the possibility of local PAH production in the halo and the chemical PAH destruction which could work on shortest timescales.

5.7.3 PAHs in galactic winds

Starburst galaxies are characterised by very intense star formation, usually concentrated in the nuclear region of the galaxy, which can occur as a single instantaneous burst or as a high star formation activity sustained over a period of time. Since galactic supernovae are considered the most probable acceleration source for cosmic rays with energy below the "knee" (few 10^{15} eV - see e.g. O'C. Drury 1994), we expect that an enhancement of the SFR will result in a corresponding increase of the cosmic ray intensity.

In Chapter 4 we discussed the observation of PAH molecules in the bipolar outflow of the starburst galaxy M82 (Armus et al. 2007; Galliano et al. 2008b). PAHs have been detected far outside the galactic plane at least up to 6 kpc from the disk (Engelbracht et al. 2006), in a region which is spatially correlated with an extended X-ray emission originating from tenuous hot gas (electron density n_e = 0.013 cm^{-3}, temperature T = 5.8×10^6 K). Our study has demonstrated that, under these conditions, PAHs are destroyed by collisions with thermal electrons on a timescale of few thousand years. Our conclusion was that the PAH survival is possible only if the molecules are isolated from this hot gas, probably in a cooler PDR-type gas entrained in the galactic wind.

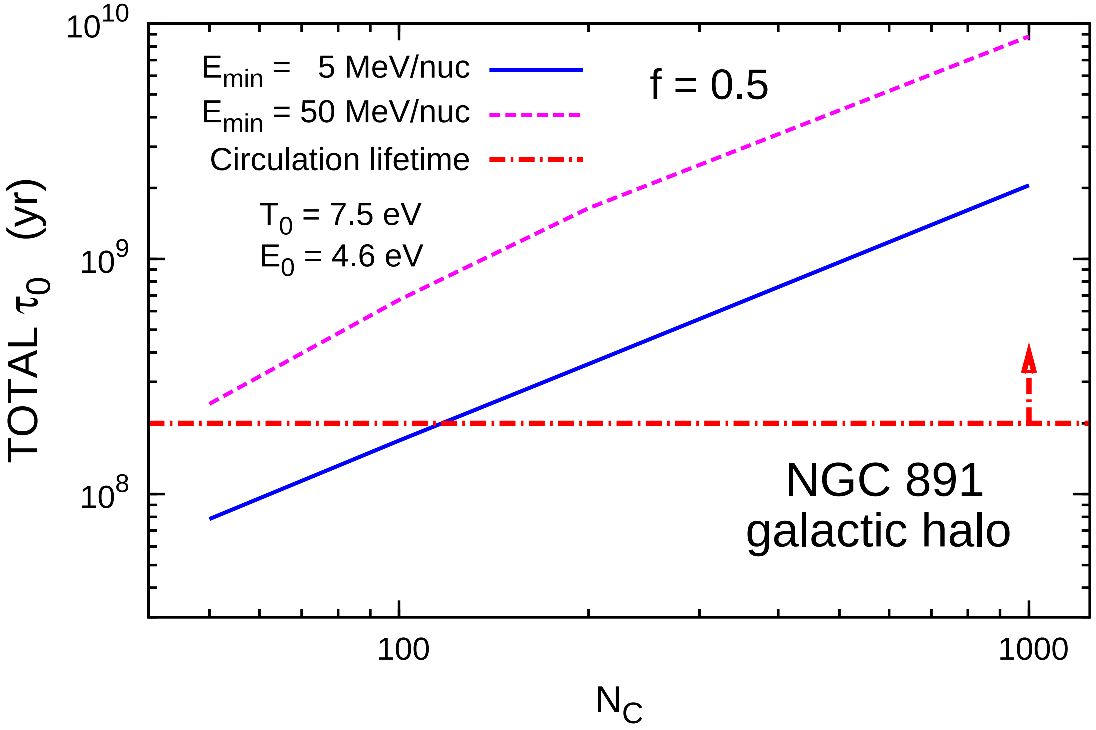

Figure 5.10 — Total PAH lifetime against CR bombardment in the halo of NGC 891, evaluated at an altitude of 3 kpc from the galactic plane, compared with the circulation timescale between the disk and the halo. The value of the circulation lifetime represents a lower limit, as indicated by the arrow. Otherwise as Fig. 5.8. We remind the reader of the variation in the calculated lifetime against CRs, due to the uncertainty on the parameters E_0 and T_0 (cf. Fig. 5.6 and Fig. 5.7).

In fact supernova-driven galactic-scale winds, often called “superwinds”, are commonly observed in starburst galaxies, including M82 (see e.g. Strickland & Heckman 2009, and references therein). In addition theoretical studies (Ipavich 1975; Breitschwerdt et al. 1991, 1993; Zirakashvili et al. 1996; Ptuskin et al. 1997), together with radio (Heesen et al. 2009) and X-ray observations (Everett et al. 2008) suggest the possibility of a CR-driven galactic wind, i.e. the possibility of “bulk” transport of cosmic rays afterwards into the halo, in addition to the diffusive transport predicted by cosmic ray propagation models (cf. § 5.7.1).

Assuming that also the M82 superwind could be partially CR-driven, we can try to evaluate the CR intensity at the high latitudes where PAHs are detected, to assess PAH lifetimes against cosmic ray bombardment and compare them with the survival time in hot gas of the outflow. Unfortunately the properties of superwinds at high galactic latitudes are not well constrained. Theoretical studies mainly concern small regions around the nucleus of the galaxy (radii of few hundred pc from the center), where the transport of matter is dominated by advection (Völk 2003; Strickland & Heckman 2009), while in the outer regions diffusion is expected to be dominant (e.g. Zirakashvili & Völk 2006, for the starburst galaxy NGC 253). This is not the case in the Milky Way, where the CR transport is diffusive on a kpc scale and becomes convective only at larger distances (Ptuskin et al. 1997).

On the other hand, the CR propagation in M82 is not yet totally understood. Star formation, and thus SNRs which re-presents the main CR sources, are concentrated in the small nuclear region from which the galactic superwind originates, we could then expect CRs being advectically transported by the wind out of the galactic plane up to a certain height ($\sim$ few hundred pc), and diffusing after in the volume occupied by the superwind, which is roughly a cylinder flaring at high z with height of $\sim$ 12 kpc on the North side and 7.5 kpc on the South side (Lehnert et al. 1999; Stevens et al. 2003). It would also be possible that CRs occupy a spheroidal halo as in the Milky Way, maybe diffusing back to the disk after leaving the wind region.

Because of this lack of information, especially on the confinement volume for the cosmic rays, what we present here is a toy-model based on some simplifying assumptions, but which could be useful to interpret PAH observations in the outflow of M82. To calculate the CR spectrum in M82 we adopt the same spectral index as in the Milky Way (γ = 2.7) and we assume that in the starburst nucleus the CR intensity scales with the supernova rate $\nu_{\rm SN}$ (SN yr^{-1}) which is directly related to the star formation rate in the galaxy. Taking the values $\nu_{\rm SN}$(M82) = 0.11 SN yr^{-1} (Huang et al. 1994) and $\nu_{\rm SN}$(MW) = 0.02 SN yr^{-1} (Diehl et al. 2006) we obtain $I_{\rm M82}(E)/I_{\rm MW}(E) = \nu_{\rm SN}(\rm M82)/\nu_{\rm SN}(\rm MW)$ = 0.11/0.02 = 5.5.

Since PAHs are detected at vertical distances which are large compared with the typical height of the convective zone, we neglect this latter and assume pure diffusive CR transport above the galactic plane. We adopt the exponentially-decreasing CR latitudinal gradient from Eq. 5.41 (Shibata et al. 2007) with $z_{\rm D} = h_{\rm h}/3$, where $h_{\rm h}$ is the maximum distance that cosmic rays can reach above the plane through diffusion. Since the exact confinement region in M82 is not known, we just take $h_{\rm h}$ equal to the vertical height of the galactic superwind (12 kpc in the North side, 7.5 in the South side), i.e. we assume that CRs can occupy at least as the same volume as the gas from the outflow.

The PAH lifetime against CR bombardment at the vertical distance $|z|$ above the starburst nucleus of M82 is then given by the following expression

$$\tau_{0,\rm M82}(0,|z|) = \frac{1}{5.5 \times 1.5} \frac{\tau_{0,\rm MW}(r_{\odot},0)}{\exp\left(-|z|/z_{\rm D}\right)} \tag{5.43}$$

where 5.5 and 1.5 are the two enhancement factors of the CR intensity in M82 with respect to the Milky Way (5.5) and in the galactic center with respect to the solar neighborhood (1.5), which will imply a decrease of the same factor for the PAH lifetime with respect to the survival time $\tau_{0,\rm MW}(r_{\odot},0)$ in the vicinity of the Solar System (Fig. 5.8). On the other hand the latitudinal gradient will result in a corresponding increase of $\tau_{0,\rm M82}$ for increasing $|z|$, with scale height $z_{\rm D}$(North) = 4 kpc and $z_{\rm D}$(South) = 2.5 kpc.

Let us calculate the PAH lifetime at the maximum distance $|z|$ = 6 kpc where the molecules have been detected. This is done by scaling the time constants $\tau_{0,\rm MW}(r_{\odot},0)$ in Fig. 5.8 by the factor A $\sim$1.3 (averaged over the two hemispheres) and the result is shown in Fig. 5.11.

The PAH lifetime against CRs is comparable to or longer than the circulation lifetime ($\sim$ 200 Myr) and the starburst timescale (tens of Myr). In Chapter 4 we showed that in the outflow of M82 PAH destruction due to X-ray absorption would take place on a timescale of at least $\sim$ 20 Myr (assuming that each X-ray photon absorption will

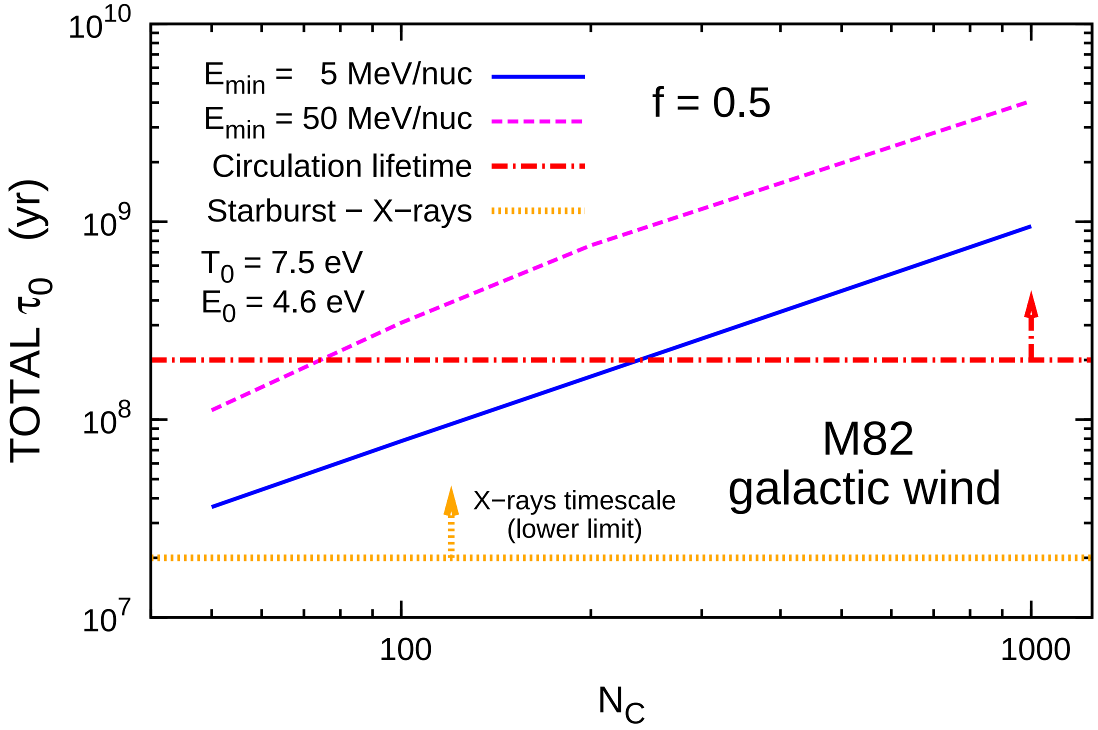

Figure 5.11 — Total PAH lifetime against CR bombardment in the outflow of the starburst galaxy M82, evaluated at an altitude of 6 kpc from the galactic plane. The PAH survival time is compared with the circulation, starburst and X-rays timescales. The values of the circulation and X-rays timescales represent lower limits, as indicated by the arrows. Otherwise as Fig. 5.8. We remind the reader of the variation in the calculated lifetime against CRs, due to the uncertainty on the parameters E_0 and T_0 (cf. Fig. 5.6 and Fig. 5.7).

lead to fragmentation). This is comparable to or larger than the starburst lifetime. PAHs dispersed in the hot gas will be rapidly destroyed by collisions with electrons. To survive they need to be isolated from this hot gas, presumably in a cooler and denser gas entrained in the superwind. On the other hand CRs and X-rays can penetrate in those clumps, thus the PAH lifetime there will be determined by the cosmic radiation and/or X-rays, depending on the PAH size and on the effective value of the survival time against X-rays (cf. § 4.6.1).

5.7.4 PAHs in galaxy clusters

We consider now the PAH processing by cosmic rays in an extragalactic environment, focusing on the specific case of cooling flow galaxy clusters. The measurements of high-energy gamma and neutrino radiation produced by the interaction of cosmic rays (mainly protons) with the intra-cluster medium (ICM) have demonstrated that galaxy clusters are able to confine CRs for cosmological times (Berezinsky et al. 1997). Our choice is thus motivated by the reasonable expectation to find a non-negligible population of CR in such environment, although its spectral index and amplitude are not well constrained by observations.

Many clusters of galaxies with cooling flows host a central galaxy which often shows nuclear activity. Many papers support the presence of cosmic ray protons in the relativistic plasma bubbles produced by Active Galactic Nuclei (AGN), where the energetics are sufficient to inject a significant amount of cosmic rays into the IMC (see Pfrommer & Enßlin 2004, and references therein). The slope of the injected spectrum depends on the fraction of particles released from the plasma. If all the CR content is ejected by the radio plasma, we expect to find a moderately flat spectrum ($\alpha_{\mathrm{inj}} \approx 2.5$) consistent with the flat spectra of cosmic ray electrons indicated by the radio emission from radio galaxies. On the other hand, if only a small fraction of the cosmic ray population is able to leave the plasma via diffusion, we expect to find an even flatter spectrum ($\alpha_{\mathrm{inj}} \approx 2.2$) because the escape probability increases with momentum (Enßlin 2003).

Another possible source of cosmic rays in galaxy clusters is represented by the galactic winds from the central galaxy transporting CRs accelerated within the galaxy itself. Because Supernova Remnants (SNRs) are believed to be the main sources of Galactic cosmic rays (e.g. Ginzburg 1993; O'C. Drury 1994), the expected injection spectral index is $\alpha_{\mathrm{inj}} \approx 2.4$, if no further re-acceleration occurs. Apart from protons, the principal constituents of Galactic cosmic rays are helium, carbon and iron ions.

The CR population in galaxy clusters will then result from the combination of the above-mentioned sources, with a spectral index α_{inj} which reflects its composite origin. After injection from the source, CRs start diffusing away from the central AGN. For the treatment of the transport of cosmic ray *protons* through the thermal ICM, we refer to the model elaborated by Pfrommer & Enßlin (2004). The CR proton distribution function is described by a power-law in energy (or momentum) where the injection spectral index is modified by the diffusion through the intra-cluster gas

$$g(r, E) = \frac{\tilde{n}_{\mathrm{CR},0}}{\mathrm{GeV}} \left(\frac{r}{h_{70}^{-1}\,\mathrm{kpc}} \right)^{-1} \left(\frac{E}{\mathrm{GeV}} \right)^{-\alpha_{\mathrm{p}}} \tag{5.44}$$

with $\alpha_{\mathrm{p}} = \alpha_{\mathrm{inj}} + \alpha_{\mathrm{diff}}$. The coeffiecient α_{diff} results from the fact that diffusion is momentum-dependent, and equals $\approx 1/3$ for active diffusive transport of CR protons in a Kolmogorov-like spectrum of hydro-magnetic turbulence (Kolmogorov 1941). The model assumes the standard ΛCDM cosmology with $H_0 = 70\,h_{70}$ km s^{-1} Mpc^{-1}, where h_{70} indicates the scaling with H_0. The normalization factor $\tilde{n}_{\mathrm{CR},0}$ is the crucial parameter required to determine the CR spectrum.

Pfrommer & Enßlin (2004) constrained $\tilde{n}_{\mathrm{CR},0}$ for a sample of nearby cooling flow galaxy clusters with the aid of γ-ray observations, using the fact that cosmic ray protons interact hadronically with the thermal intra-cluster gas producing both charged and neutral pions (see § 5.7.2.1). Charged pions decay into secondary electrons / positrons + neutrinos/antineutrinos, while neutral pions decay into two γ's ($\pi^0 \rightarrow 2\gamma$). The amount of cosmic protons can then be calculated from their decay products, which are detectable in the γ-ray and radio bands.

It is important to remember here that the threshold energy for pion production is E_{th} = 0.78 GeV, implying that only the proton population with energy exceeding the threshold is able to produce pions hadronically, and can then be constrained by γ-ray and radio observations. At lower energies the dominant energy loss mechanism for cosmic ray protons is Coulombian diffusion on the electrons in the plasma (electronic excitation), which results in the depopulation of the cosmic ray energy distribution with consequent modification of the power-law spectrum (Mannheim & Schlickeiser 1994).

Unfortunately, it is not possible to observationally constrain the low-energy cosmic ray population in galaxy clusters, thus following the argument from Nath & Biermann (1994) we decided to extrapolate Eq. 5.44 down to a minimum energy $E_{\rm min}$ representing the characteristic energy scale at which the spectrum deviates from a power-low. A similar approach is used by Pfrommer & Enßlin (2004) as well. For the cut-off energy we adopt the value $E_{\rm min}$ = 50 MeV, consistent with the range $\sim$ 50 - 75 MeV found by Nath et al. (2006) in their study the production of ^{6}Li by cosmic ray protons in galaxy clusters. $E_{\rm min}$ represents the lower energy that an energetic proton has to reach before suffering large Coulombian losses, and can be equivalently expressed in terms of the quantity of matter to be traversed in order to experience the same Coulombian losses. In our Galaxy, a similar range $E_{\rm min} \sim$ 30-100 MeV has been derived using the ionization rates inferred from observations of diffuse clouds (cf. § 5.5).

As previously mentioned, we assume the presence in the cluster cosmic ray population of the main components of the Galactic cosmic rays other than hydrogen: helium, carbon and iron. The distribution function (5.44) for the heavier elements is obtained by simply scaling the proton distribution function $g(r, E)$ with the abundance with respect to the hydrogen χ_i of the corresponding ion i = H, He, C, Fe

$$g_i(r, E) = \chi_i \, g\,(r, E) \tag{5.45}$$

where E is the *total* kinetic energy of the CR ion. For the cosmic ray abundances we assume the standard values of the galactic cosmic rays: $\chi_{\rm H} : \chi_{\rm He} : \chi_{\rm C} : \chi_{\rm Fe} = 1 : 0.1 : 10^{-2} : 10^{-3}$ (Maurin & Taillet 2003). The low-energy cut-off for the heavier ions has been derived in the same way as for Galactic cosmic rays, i.e. scaling the proton value $E^{\rm p}_{\rm min}$ = 50 MeV by the ion atomic mass, $E^{i}_{\rm min} = M_{1,i}\, E^{\rm p}_{\rm min}$, but different parametrizations are also possible (Nath & Biermann 1994).

The cosmic ray intensity $I(E)$ (to which we usually refer as "spectrum") is related to the distribution function by the following expression

$$I_i(E) = \frac{v}{4\pi} \, g_i(r_{\rm c}, E) \tag{5.46}$$

where $v = \beta/c$ is the velocity of the ion. The distribution function g_i is calculated for a given distance $r_{\rm c}$ from the center of the cluster. We adopt the value corresponding to the cooling radius of the cluster, which defines the region where the majority of the hadronically-generated γ-ray luminosity originate.

When the CR intensity is known, we can estimate the total lifetime against cosmic ray bombardment, τ_0. As an example, we calculate τ_0 in two nearby cooling flow clusters from the Pfrommer & Enßlin (2004) sample, A85 and Virgo, which main properties are listed in Table 5.3. A85 is one of the farthest cluster in the sample, with low electron density $n_{\rm e}$, large core radius $r_{\rm c}$ and high central temperature T_0. Virgo is the closest cluster to us, with quite high electron density, very small core radius and high central temperature.

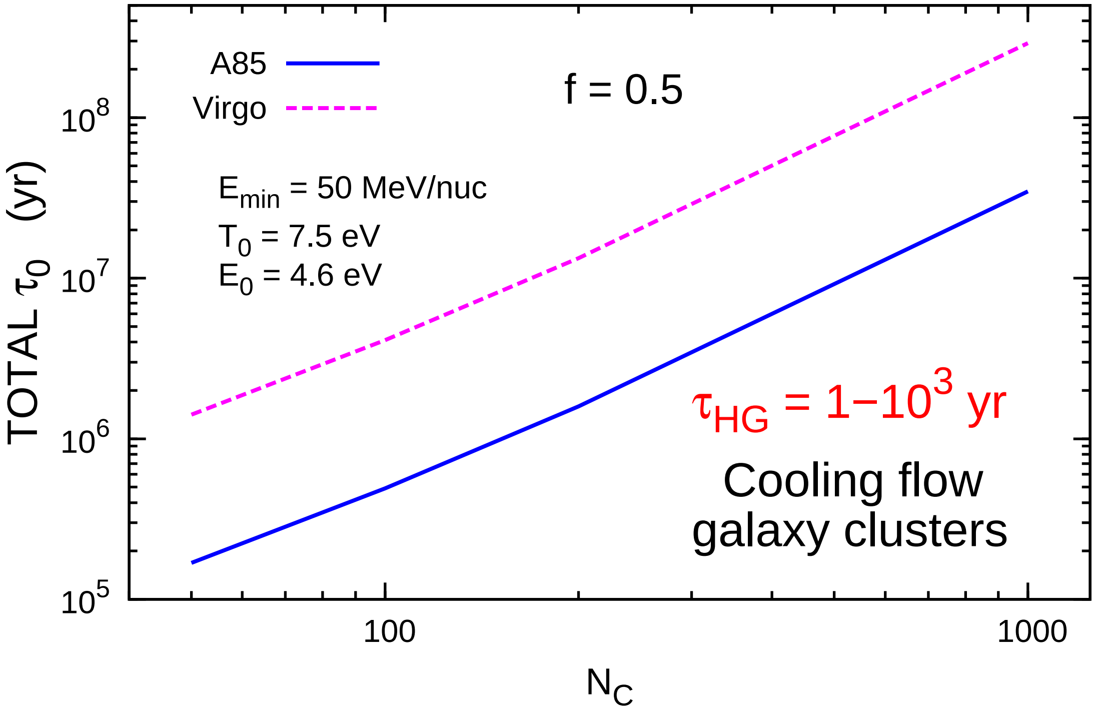

Figure 5.12 — Total PAH lifetime against CR bombardment in the cooling flow galaxy clusters A85 and Virgo, compared with the survival time, $\tau_{\rm HG}$, in a hot gas. Otherwise as Fig. 5.8. We remind the reader of the variation in the calculated lifetime against CRs, due to the uncertainty on the parameters E_0 and T_0 (cf. Fig. 5.6 and Fig. 5.7).

Pfrommer & Enßlin (2004) calculated $\tilde{n}_{\rm CR,0}$ for different values of the proton spectral index $\alpha_{\rm p}$. We adopt the value corresponding to $\alpha_{\rm p} = \alpha_{\rm inj} + \alpha_{\rm diff} = 2.7$, with $\alpha_{\rm diff} \approx 1/3$, because is consistent with the spectrum of the CR sources (AGN + SNRs) and allows a direct comparison with Galactic cosmic rays.

The results of our calculation are shown in Fig.5.12. In the galactic clusters under examination the cosmic-ray density is enhanced with respect to the solar neighborhood, resulting in lifetimes which are shorter by about 2-3 orders of magnitude (cf. Fig. 5.8). The longer time constants obtained for Virgo are the consequence of its lower CR density with respect to A85.

In Chapter 4 we showed that collisions with thermal electrons and protons represent an efficient destruction mechanism for PAHs immersed in an ionized gas of $\sim 10^6$ K. Since the ICM is a moderately tenuous hot plasma, it would be not surprising to find a quite short lifetime $\tau_{\rm HG}$ for the PAHs dispersed in the medium, due to such collisions. In both clusters, PAHs embedded in the hot gas are rapidly destroyed on timescales of $1 - 10^3$ yr. In cold embedded gas, the lifetime of PAHs is set by cosmic rays to be $\sim 10^6 - 2 \times 10^8$ yr (Virgo) and $\sim 10^5 - 3 \times 10^7$ yr (A85).

The existence of PAHs in the intra-cluster medium is not yet well constrained observationally. In fact to the best of our knowledge this detection has not been reported, but hopefully future observations will be able to provide more insights. Many of the

Table 5.3 — Relevant parameters and CR normalization factor $\tilde{n}_{\mathrm{CR},0}$ for the two cooling flow clusters A85 and Virgo from the Pfrommer & Enßlin (2004) sample.

Cluster	z	r_{c} h_{70}^{-1} kpc	n_{e} $h_{70}^{1/2}\,\mathrm{cm}^{-3}$	T 10^7 K	$\tilde{n}^{a}_{\mathrm{CR},0}$ $h_{70}^{1/2}\,\mathrm{cm}^{-3}$
A85^b	0.0551	45	3.08×10^{-2}	6.4	9.9×10^{-5}
Virgo^c	0.0036	1.6	1.5×10^{-1}	1.4	4.2×10^{-7}

(*a*): From Pfrommer & Enßlin (2004), with $\alpha_{\mathrm{p}} = 2.7$.
(*b*): Parameters from Mohr et al. (1999) and Oegerle & Hill (2001)
(*c*): Parameters from Matsushita et al. (2002) and Ebeling et al. (1998).

quantities involved in our calculation are not well constrained, in particular the exact amplitude, shape and composition of the cosmic rays spectrum in the cluster and the value of the parameters E_0 and T_0. Because the PAH lifetime in galaxy clusters set by cosmic rays is still short, a replenishing mechanism would be required to explain their observation in such environments. We face here another example of the well-known conundrum about the discrepancy between the PAH/dust lifetime and the injection time scale into the interstellar medium (2.5×10^9 yr).

5.8 Conclusions

We have extensively investigated the stability of PAHs against cosmic ray ion (H, He, C and Fe) and electron bombardment in both galactic and extragalactic environments. We consider CR particles with energies between 5 MeV/nucleon and 10 GeV. Collisions can lead to carbon atom ejection, with a consequent disruption and destruction of the molecule. The effects of cosmic rays have then been compared with the other destruction mechanisms discussed in our previous works: PAH processing by shocks with velocities between 50 and 200 km s^{-1} (Chapter 3) and collisions with thermal ions and electrons in a hot gas ($T = 10^3 - 10^8$ K, Chapter 4).

An ionic collision consists of two simultaneous processes which can be treated separately: a binary collision between the projectile ion and a single atom in the target (nuclear interaction) and energy loss to the electron cloud of the molecule (electronic interaction). In the high-energy regime considered here the nuclear stopping is totally negligible, and the energy loss process is dominated by the electronic interaction, well described by the Bethe-Bloch equation. The interaction of PAHs with high-energy electrons can be treated in term of a binary collision between the incident electron and a single nucleus in the target.

The cosmic ray spectra we adopt in the solar neighborhood are based on measurement near the Earth but corrected for the influence of the Heliosphere (solar modulation). To estimate the CR variation across the disk and in the galactic halo we adopt specific models based on γ-ray measurements. In external galaxies we scale the overall cosmic ray density with the star formation rate of the galaxy, adapting scale lengths and scale heights appropriate for the Milky Way.

Our calculation shows that the CR processing lifetime is comparable to or longer than the calculated lifetime in the diffuse ISM against shock processing. The latter occur predominantly in the warm intercloud medium of the ISM, while CRs have access to all phases (except perhaps the densest molecular cloud cores) and can process all material.

PAHs have been detected both in the halo of normal galaxies like NGC 891 and in the outflows of starburst galaxies like M82. Our work shows that in both these environments the lifetime against CR bombarding of large PAHs ($N_C > 100$) is comparable to or longer than the circulation timescale between disk and halo and the starburst lifetime. PAHs dispersed in the hot gas filling the galactic halo and the starbust outflow are rapidly destroyed by collisions with thermal ions and electrons, but this mechanism is inefficient if the molecules are isolated from this gas in denser cloudlets. CRs can access the denser clouds and together with X-rays will set the lifetime of those protected PAHs, which can be used as a 'dye' for tracing the presence of cold entrained material.

In cooling flow galaxy clusters like A85 and Virgo the cosmic ray intensity is remarkably enhanced with respect to the solar neighborhood, as a consequence the PAH lifetime is much shorter. The survival time against CR bombardment is at least two orders of magnitude longer than the PAH lifetime in a hot gas, implying that the molecules will be rapidly destroyed in the gas phase of the ICM. Nevertheless they could survive if protected in some cold entrained material and in this case the PAH lifetime will be set by cosmic rays. Future observations would hopefully provide more insights about the validity of our predictions.

The major source of uncertainty in the determination of the time scale for PAH processing by cosmic rays resides in the choice of the nuclear threshold energy T_0 (for electron collisions), the fragment binding energy E_0 (for ion collisions) and the minimum cosmic ray energy $E_{\rm min}$. Our conclusions are robust despite the large variability in the PAH lifetime induced by the uncertitude on the above parameters. Nevertheless this variation enphasizes again the importance of a better determination of these quantities.

We find that thermal ions/electrons in a hot gas are much more effective in destroying PAHs than cosmic rays. This is due to the fact that the stopping power of the thermal ions/electrons under consideration ($T \sim 10^7$ K, $n_e \sim 0.1$ cm^{-3}) is high, close to its maximum value, and allows the transfer into the molecule of enough energy to have the dissociation probability close to one (the dissociation probability increases with the transferred energy). Almost any ion/electron is able to destroy a PAH, and the resulting destruction efficiency is very high (cf. Chapters 3 and 4).

On the other hand, in the energy range we consider here for CR ions (5 MeV/nucleon - 10 GeV), the stopping power, and then the energy transferred into the PAH and the dissociation probability for PAHs, decrease rapidly for increasing energy of the incoming ion. For CR electrons (5 MeV - 10 GeV) the cross section for carbon atom removal is almost constant but very small ($\sim 6\times10^{-}23$ cm^2). For both ions and electrons the CR spectra are decreasing functions of the energy. The combination of these two factors implies that only few CRs are able to destroy PAHs, resulting in a destruction efficiency very low compared to thermal ions/electrons in a hot gas.

Acknowledgements

We are grateful to F. Galliano for providing us with the values of G_0 in NGC 891. E.R.M. thanks G. Lavaux for support and technical assistance and acknowledges financial support by the EARA Training Network (EU grant MEST-CT-2004-504604).

Chapter 6

Conclusions and Perspectives

6.1 Key questions

As already mentioned in §1.6, the research described in this thesis aims to establish *how* the different conditions in the ISM affect PAHs, focusing on the *collisional* processing due to high velocity ions and electrons. These high velocities arise from the thermal and relative (inertial) motion induced in the gas by moderate velocity shocks, from the energy injected into the gas by very fast shocks (thermal motion), and from cosmic ray acceleration. In fact, a detailed study of the physics of the interaction between PAHs and high energy particles (ions and electrons) was lacking, although PAHs are a key component of the ISM and these processes play a crucial role in the evolution of PAHs. The first key question we addressed in this thesis is:

What happens to PAH molecules when bombarded by high energy ions and electrons? Will they be able to survive, maintaining their character, or will they be severely damaged or even completely destroyed?

From this it follows the second key question:

What are the astrophysical implications of PAH processing?
i.e.
What is the connection between the microscopic processes (ion/electron – PAH interaction) and the macroscopic effects on the interstellar PAH population?

6.2 Results

In **Chapter 2** we present a multiwavelength study of the complex environment of the supernova remnant N157B in the Large Magellanic Clouds. This chapter provides an analysis of a SNR and the different environments a PAH can find itself. The coexistence of various components, which besides the SNR include a molecular cloud, dust filaments, bubbles of hot shocked gas, an OB association and a HII region, makes this region a very good laboratory to study a variety of conditions PAHs can experience. From Spitzer photometric mapping and spectroscopy we find that there is no evidence of an infrared counterpart to the supernova remnant in the IRAC and MIPS images. The infrared emission is dominated by a cloud of dust/PAH and molecular gas adjacent to the remnant, containing the compact 2MASS source J05375027-6911071. This object has a diameter of about 3 pc, an electron-density of 100-250 cm^{-3}, and is photo-ionized by an O8–O9 star. It is probably an open HII blister structure, seen from the back. In spite of the projected overlap between the SNR X-ray emission and the infrared cloud, we find only weak emission from the shock-indicator [FeII], and both the excitation and the heating of the extended cloud are dominated by photo-ionization by the early O stars of LH 99. The absence of clear evidence of shocks implies that at present the molecular/dust cloud is not significantly impacted by the remnant. This suggests that the supernova progenitor was a moderately massive star of mass $M \approx 25$ $M_{\odot}$.

Chapter 3 and **Chapter 4** present the models we have developed and that allow for the first time a quantitative description of the collisional processing of PAH molecules by ions (H, He and C) and electrons with energies between 10 eV and 10 keV. Specific models were needed because PAHs are molecules and not small solid fragments, thus the classical approach from solid state physics cannot be applied. In a solid, the incoming energetic particle will transfer energy to a target atom. If more energy is transferred than the binding energy at the lattice site, a primary recoil atom is created. The primary recoil atom will collide with other target atoms distributing the energy via a collision cascade. In the PAH, the target atom is a single C atom, and if the energy transferred exceeds a threshold value, there will be no collision cascade but rather the atom will be ejected from the molecule. When treating a molecule then, there will be only "first" interactions, which can be conveniently described applying appropriated modifications to the binary collision approximation used for solids. The energy loss to the atomic electrons will not be distributed around the impact region, as in a solid, but spread out over the entire molecule because of the finite size of the PAH. The results in terms of PAH destruction cannot be extrapolated from the behaviour of dust grains and strongly depend on the kind of projectile and on the energies involved.

We have developed a model for the interaction of energetic ions and electrons with PAHs, taking the molecular aspects of this interaction fully into account. A schematic outline of the PAH destruction analysis is shown in Table 6.1. The interaction between PAHs and ions is described in terms of nuclear (elastic) and electronic (inelastic) energy loss, which can lead to carbon atom loss with consequent disruption and destruction of the molecules. The nuclear energy loss results from a binary collisions between the projectile and one single atom in the target. If the energy transferred exceeds a specific threshold, T_0, a carbon atom is ejected. This is the case we are interested in, which has not been treated in previous studies. For the nuclear threshold energy we adopt T_0 = 7.5 eV as a reasonable value, but experimental determinations are necessary. The energy loss to the atomic electrons (electronic interaction) has been described in term of the stopping power of an electron gas with appropriate electron density (jellium approximation), adopting a geometry adequate to the shape and finite size of the PAH. For collisions with electrons having energies between 10 eV and 10 keV, we derived an analytical expression for the measured electron stopping power in graphite and applied this to the case of PAHs. The dissociation probability for a PAH excited by electronic interactions and electron collisions, has been derived using the theory of unimolecular reactions. The parameter E_0, which governs the dissociation probability, is not well constrained. We adopt a value of 4.6 eV consistent with extrapolations to interstellar conditions but better determinations, relevant to the astrophysical situation, are needed.

Table 6.1 — Summary table for PAH collisions with ions and electrons.

			Projectiles			
			Ions		Electrons	
Environment	Energy distrib.	Energy range (eV)	Elastic (Nuclear) interaction	Inelastic (Elec.) interaction	Elastic (Nuclear) interaction	Inelastic (Elec.) interaction
Interst. Shocks[a] **Chapter 3**	Inertial	$10 - 10^4$	✓ § **3.2** § **3.3.1**	✓ § **3.3.2**		
	Thermal	$5 - 50$	✓ § **3.2** § **3.3.1**	✓ § **3.3.2**		✓✓[c] § **3.3.3**
Hot Gas[b] **Chapter 4**	Thermal	$10 - 10^4$	✓ § **4.2.2**	✓ § **4.2.1**		✓✓[c] § **4.3**
Cosmic Rays **Chapter 5**	CR energy distribution	5 MeV – 10 GeV		✓✓[c] § **5.2**	✓ § **5.3**	

(*a*): Shock velocity, $v_S = 50 - 200$ km s^{-1}.
(*b*): Gas temperature, $T = 10^5 - 10^8$ K.
(*c*): For each environment the double check mark ✓✓ indicates the main agent for destruction of PAHs with $N_C = 50$.

In **Chapter 3** we use our models to estimate the lifetime of PAHs against collisions with ions and electrons having high velocities arising from the thermal and relative motions induced in the gas by moderate velocity interstellar shocks (v_s between 50 and 200 km s^{-1} – cf. Table 6.1). We find that interstellar PAHs ($N_C \sim 50$) do not survive in shocks with velocities greater than 100 km s^{-1} and larger PAHs ($N_C \sim 200$) are destroyed for shocks with velocities ≥ 125 km s^{-1}. For shocks in the $\approx 75 - 100$ km s^{-1} range destruction is not complete and PAHs can survive, although their structure is likely to be severely denatured by the loss of an important fraction ($20 - 40\%$) of the carbon atoms. The calculation of PAH lifetime against destruction t_{SNR} is $\sim 1.6 \times 10^8$ yr and $\sim 1.4 \times 10^8$ yr for N_C = 50 and 200 respectively. Small PAHs are preferentially destroyed by electrons, big PAHs by ions. These results are robust and independent of the uncertainties in the key parameters T_0 and E_0 that have yet to be well-determined experimentally. The calculated lifetimes are smaller than the values found for carbonaceous grains (6×10^8 yr) but close to that for hydrogenated amorphous carbon (2×10^8 yr), and far from the stardust injection timescale of 2.5×10^9 yr. The presence of PAHs in shocked regions therefore requires an efficient reformation mechanism and/or a protective environment.

In **Chapter 4** we adopt our models to evaluate the PAH survival time in a hot X-ray emitting gas with temperatures between 10^3 and 10^8 K (Table 6.1). In this case the high velocities of ions and electrons are due to the energy injected into the gas by very fast shocks (thermal motion). We find that the PAH destruction process is dominated by electron collisions for gas temperatures above $\sim 3 \times 10^4$ K, and by nuclear interaction with helium below this value. Small PAHs are more easily destroyed than larger ones below $\sim 10^6$ K, while the difference reduces significantly for a hotter gas. For a 1000 C-atom PAH, nuclear interactions are the dominant destruction process. In a hot and tenuous gas (e.g. M82 galactic outflows), PAHs with sizes between 50 and 200 C-atom are destroyed by electron collisions in few thousand years. In denser and colder regions (e.g. Orion), PAHs can survive for some 10^7 yr before being destroyed by nuclear interaction processes. X-ray photon absorption plays little role in PAH destruction in the hot gas associated with stellar winds and supernova explosions, with respect to electron collisions. Any PAHs observed near such regions have to be isolated from this hot gas and are presumably in a cooler PDR-type gas entrained in the stellar and galactic winds. In this sense, PAHs represent a good tracer for the presence of entrained denser material. The erosion of PAHs occurs via C_2 loss from the periphery of the molecule, thus preserving the aromatic structure. The PAH lifetime in a tenuous hot gas ($n_H \approx 0.01$ cm^{-3}, $T \approx 10^7$ K), typical of the coronal gas in galactic outflows, is found to be about thousand years, orders of magnitude shorter than the typical lifetime of such objects, and also much shorter than the lifetime of an equivalent dust grain of roughly the same size ($a \approx 5$Å). Thus, this might then imply that the destructive effects of ion and electron collisions with very small grains have previously been underestimated.

In **Chapter 5** we consider much more energetic projectiles, i.e. cosmic ray ions (H, He, CNO, Fe-Co-Ni) and electrons with energies between 5 MeV and 10 GeV (see Table 6.1). The energy loss of such high-energy particles required a specific treatment based on a different formalism with respect to the low-energy cases considered before.

Concerning the ions, the nuclear stopping is totally negligible, and the energy loss process is dominated by the electronic interaction, well described by the Bethe-Bloch equation (instead of the Lindhard & Scharff equation). The interaction of PAHs with high-energy electrons can be treated in terms of binary collisions between the incident electron and a single nucleus in the target, which is not the case at low energies. We evaluated the destructive effects of cosmic ray collisions on PAHs and estimate for how long the molecules can survive this ubiquitous cosmic ray bombardment in various environments (galactic disks, galactic halos, starburst galaxy outflows and cooling flow galaxy clusters). The cosmic ray spectra we adopt in the solar neighborhood are based on measurement near the Earth but corrected for the influence of the Heliosphere (solar modulation). To estimate the CR variation across the disk and in the galactic halo we adopt specific models based on γ-ray measurements. In external galaxies we scale the overall cosmic ray density with the star formation rate of the galaxy, and for galaxy clusters we adopt CR estimates based on γ-ray measurements.

We find that the timescale for PAH destruction by cosmic ray ions depends on the electronic excitation energy E_0, the minimum cosmic ray energy $E_{\rm min}$ and the amount of energy available for dissociation. Small PAHs are destroyed faster with He and the CNO group being the more effective projectiles. The shortest survival time that we find is $\sim 10^8$ yr, which is comparable with the lifetime against destruction in interstellar shocks. Nevertheless, CRs are able to process PAHs in diffuse clouds, where the destruction due to interstellar shocks is less efficient. For electron collisions, the lifetime is independent of the PAH size and varies with $E_{\rm min}$ and the threshold energy T_0, the minimum lifetime in this case is 1.2×10^{13} yr. Such a long timescale excludes cosmic ray electrons as an important agent for PAH destruction. In the halo of normal galaxies like NGC 891 and in the outflows of starburst galaxies like M82 the PAH lifetime against CR bombarding ($\gtrsim 10^8$ yr) is comparable to or longer than the circulation timescale between disk and halo and the starburst lifetime ($\sim$200 Myr and $\sim$ 20 Myr respectively). In cooling flow galaxy clusters like A85 and Virgo the cosmic ray intensity is remarkably enhanced with respect to the solar neighborhoods, as a consequence the PAH lifetime is much shorter. Nevertheless, the survival time against CR bombardment is at least two orders of magnitude longer than the PAH lifetime in a hot gas ($1 - 10^3$ yr), implying that the molecules will be rapidly destroyed in the gas phase of the intracluster medium. In conclusion, PAHs dispersed in a hot gas filling galactic halos, starbust outflows and intracluster media are rapidly destroyed by collisions with thermal ions and electrons, but this mechanism is inefficient if the molecules are isolated from this gas in denser cloudlets. CRs can access the denser clouds and will set the lifetime of those protected PAHs, which can be used as an excellent ‘dye’ for tracing the presence of cold entrained material.

As a summary of this work we have evaluated the lifetime of PAHs in the interstellar medium of the Milky Way. We have adopted a 2 phase model for the ISM where matter is rapidly cycled between the Warm Intercloud and cold cloud phases. PAHs (and dust) are destroyed by supernova shocks in the intercloud phase. The timescale for supernova shock processing has been evaluated following McKee (1989) (cf. Chapter 3). Fig. 6.1 shows the timescale for cosmic rays and supernova shock waves to destroy PAHs, calculated assuming our reference values, T_0 = 7.5 eV and E_0 = 4.6 eV.

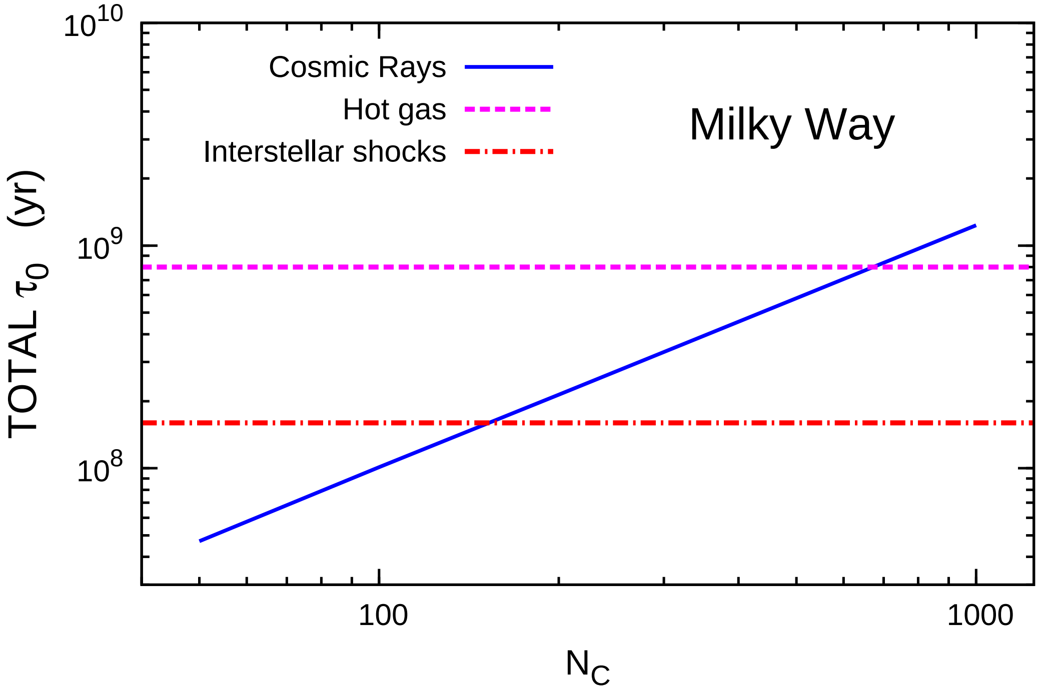

Figure 6.1 — Timescale for PAH destruction in the Milky Way by Cosmic Rays, interstellar radiative shocks ($50 \leq v_S \leq 200$ km s^{-1}) and hot gas heated by adiabatic shocks with $v_S > 200$ km s^{-1}, calculated assuming our reference values, T_0 = 7.5 eV and E_0 = 4.6 eV.

The curve labelled cosmic rays refers to CR ion and electron in the Milky Way. The curve labelled interstellar shocks refers to low velocity shocks (< 200 km s^{-1}) which cool radiatively, while the curve labelled hot gas refers to high velocity shocks (> 200 km s^{-1}) when the supernova remnant cools through adiabatic expansion.

6.3 Answers to key questions

We are now able to answer the key questions listed in §6.1. Concerning the first question, we can say that the fate of PAHs when bombarded by high energy ions and electrons strongly depends on the energy range and energy distribution of the projectiles, and on the size of the target PAH molecule. PAHs with 50 carbon atoms, and more, can survive in shocks with velocities below 100 km s^{-1}, although their structure is likely to be denatured by the loss of carbon atoms due to inertial processing. Above 100 km s^{-1} they are totally destroyed by thermal collisions (**Chapter 3**), and the same happens in a million-degree gas (**Chapter 4**). In both shocks and hot gas, electrons are the main agent for destruction. When processed by high-energy (5 MeV – 10 GeV) particles from cosmic rays, destruction is due to inelastic collisions with ions (**Chapter 5**). In all considered cases big PAHs are more resistant than small PAHs.

Concerning the second key question, we first showed that, even in a region of spatially limited extent, interstellar PAHs can undergo a variety of conditions able to alter their characteristics (**Chapter 2**). Shock processing occurs predominantly in the warm intercloud phase of the ISM, while it is less efficient in diffuse clouds. On the other hand, cosmic rays have access to all phases (except perhaps the densest molecular cloud cores) and can process all material. PAHs dispersed in a hot gas such as in galactic halos, starburst outflows and intracluster medium are rapidly destroyed by collision with electrons. This mechanism is inefficient if the molecules are isolated from this gas in denser cloudlets. However, cosmic rays can access these denser clouds and will set the lifetime of those protected PAHs, which can be used as a dye for tracing the presence of cold entrained material. This conclusion arises from combining the results from **Chapter 3**, **Chapter 4** and **Chapter 5** and highlights the connection between microscopic processing and macroscopic affects on the interstellar PAH population.

6.4 Future perspectives

The major source of uncertainty in our study resides in the choice of the two key parameters governing ion/electron collisions with PAHs: the nuclear threshold energy for PAHs T_0 which governs the elastic (nuclear) part of the ion/electron interaction with PAHs, and the fragment binding energy E_0 which governs the inelastic (electronic) part of the interaction. We explored a range of possible values and adopted $T_0 = 7.5$ eV and $E_0 = 4.6$ eV as reference. The value for T_0 is coherent with experimental determinations made on fullerene and carbon nanotubes which may be a reasonable analog for PAH molecules, but no measurement on PAHs are available. The value for E_0 is consistent with extrapolations to interstellar conditions, unfortunately the extrapolation technique is very model-dependent and the only laboratory data available refers to very small catacondensed PAHs with a very open carbon skeleton (e.g., naphthalene, anthracene, and phenanthrene), The data on astrophysically more relevant large pericondensed PAHs are missing, partly due to the difficulty in reproducing interstellar conditions on experimental timescales. The big picture resulting from our models is robust despite the large variability in the PAH lifetime induced by the uncertainties in the above parameters. Nevertheless, this variation emphasizes the importance of a better experimental determination of these quantities for PAHs under interstellar conditions.

Our models have been developed to treat ion and electron collisions with molecular targets, specifically PAH molecules with sizes between 50 and 1000 carbon atoms. Dust destruction models by Jones et al. (1994, 1996), which treat spherical dust grains using the approach for bulk particles, collect the smallest fragments (radius < 5 Å) in the smallest size bin and do not process them. We start from planar PAH molecules with a similar size (50 carbon atoms – disk radius ~ 6.4 Å), increasing progressively the number of carbon in the molecule and using an approach adequate for *molecular* target. It would be instructive to extend the PAH size up to the typical sizes for dust grains, to verify how far in size we can go with our molecular approach before getting discrepant results and to check whether and how the transition between the molecular and solid state domains takes place. In this way, the interrelationship of PAHs and small dust grains can be better understood (see § 1.2).

In this thesis we study the destructive effects on PAHs due to J-type (J for Jump) shocks, i.e. shocks where the physical conditions (density, temperature and velocity) change abruptly between the pre-shock and post-shock regions (cf. § 1.1.1). In this case, the gas is suddenly stopped and heated to a high temperature and insignificant radiative and non-radiative relaxation can take place. A natural extension of this work would be the treatment of the other type of shock of interest in the interstellar medium, the C-type shocks, where C stands for continuous because the physical parameters vary smoothly across the shock front. Such shocks occur in a magnetized medium with a low degree of ionization (see § 1.1.1). In the diffuse ISM, the density may be 10^2 cm^{-3} with an ionization fraction of 5×10^{-4}. In molecular clouds, the density is higher, 10^4 cm^{-3}, and the ionization fraction is lower, 10^{-7}. In J-shocks the role of magnetic fields is reduced, whereas in C-shocks they can deeply modify the structure of the shock, leading to the existence of multi-fluid shocks where the neutral and charged fluids are decoupled and have to be described in term of magnetohydrodynamics. Guillet et al. (2007) studied the evolution of dust grains in C-shocks in molecular clouds, which requires a very different treatment with respect to the dust processing in J-shocks. The authors show that such shocks strongly modify the grain size distribution through erosion and vaporization processes that are modulated by the magnetic field and grain charge charge effects. An analogous study would be desirable for PAH in C-shocks, where they are one of the most important negative carriers, developing of course a physical model which fully takes into account the molecular nature of PAHs.

Our results indicate that PAHs do not survive the passage of shocks with velocities above 100 - 150 km s^{-1} (depending on their size), while they can resist destruction in lower velocity shocks. Jones et al. (1996) proposed that PAHs can be produced in the post-shock region, by grain fragmentation in grain-grain collisions at shocked column densities of the order of 10^{17} - 10^{18} cm^{-2}. If the daughter PAHs are injected at velocities around 100 km s^{-1}, then they will be destroyed equally as well as the 'primitive' PAHs pre-existing the shock arrival. Only in low velocity shocks, or turbulent regions of the ISM, where grain-grain collisions happen at relatively low velocities (of the order of few km s^{-1}) and where there are no associated destructive processes are in operation, PAHs can form via fragmentation of big grains. Since the PAH lifetime in shocks - $\approx$ (2 - 4) $\times10^8$ yr - is much shorter than the injection timescale (2.5×10^9 yr), for PAHs we find the same conundrum as for dust grains, i.e. an inability to explain the observed high dust/PAH abundance because of their short lifetimes. Observations of PAHs in regions of the diffuse ISM affected by shocks faster than 100 – 150 km s^{-1} would require an efficient (re-)formation route. However, because PAHs are a product of high temperature chemistry involving abundant carbon bearing precursors such as C_2H_2 and C_2H_4, this is difficult to imagine in the low temperature diffuse ISM, which is an O-rich environment where the PAH precursors are not expected to be abundant. Further studies are required to clarify these points. Another interesting field of investigation is the *chemical* evolution of PAH after shock processing, both in terms of chemical reactions with impacting species, such as H, He, C and N, and in terms of the structural re-arrangement of the relic carbon skeleton into different species.

Our study of PAH survival in galactic halos has been stimulated by the observation of PAHs at high galactic latitudes in several normal galaxies with scale heights of 2–3 kpc (Irwin & Madden 2006; Irwin et al. 2007; Whaley et al. 2009). Considering the specific case of NGC 891, the edge-on twin of the Milky Way, we assumed that UV photolysis is negligible in term of PAH destruction because of the decreased UV flux

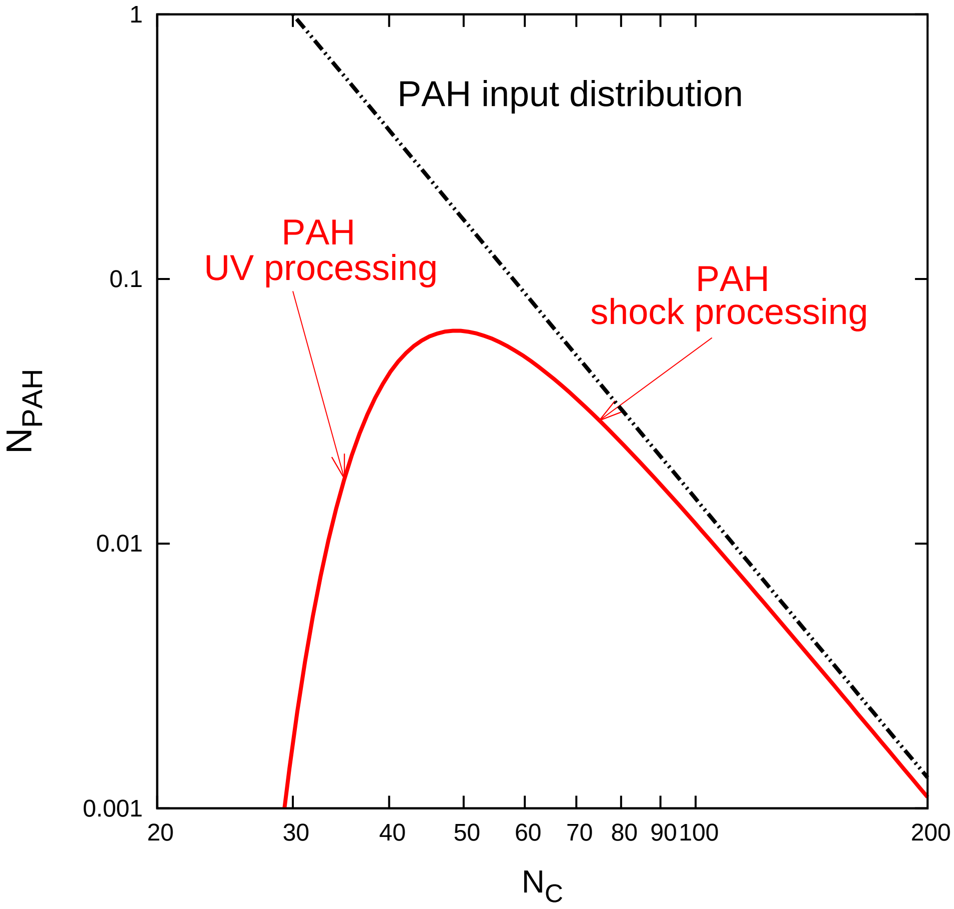

Figure 6.2 — Schematic representation of the PAH size distribution after processing (full line). The PAH input distribution (dot-dot-dashed line) and the major processes responsible for determining the size distribution are indicated.

with latitude. UV photolysis is generally considered to be the main agent for the destruction of small ($<$ 50 C-atoms) PAHs (cf. Fig. 6.2), weeding out the less stable (eg., smallest and/or non-compact). Indeed, the minimum size in the PAH-size-distribution is thought to reflect this process. However, this process is very sensitive to size, and the minimum PAH size is not completely well established. It would be an interesting follow-up to make a more detailed study of PAH photoprocessing in the halo based on a precise modelling of the variation of the FUV field with latitude. Taking into account the possibility of local PAH production in the halo and the chemical destruction of PAHs, this study would provide a quantitative estimation of the role of PAHs as tracers of the entrainment process and the exchange between the cool and hot ISM phases on arcsecond size scales.

In this thesis we present examples of the application of our PAH processing models to specific observations, but our aim is of course to extend this application to a larger variety of objects showing the signatures of shock activity, typically supernova remnants, young stellar objects with supersonic jets, galactic outflows and regions characterized by large scale shocks and turbulence such as colliding galaxies. A very interesting example of a large scale shocked region is the Stephan's Quintet (Moles et al. 1997), a compact group of galaxies where a galaxy collision produces a giant X-ray emitting shock that heats the gas to more than five million degrees (Appleton et al. 2006; Guillard et al. 2009).

Galliano et al. (2008a) and Dwek et al. (2009) considered the distinct formation and evolutionary trends for PAHs and dust in galaxies. They found that abundance of PAHs is observed to follow that of the carbon dust from AGB stars while the silicate dust follows the evolutionary trend for SN-condensed dust. The delayed injection of PAHs, from AGB stars, into the ISM provides a natural explanation for the paucity of these large molecules in low metallicity systems. The subsequent rise in the PAH-to-gas mass ratio with metallicity is then a natural consequence of the increasing contribution of AGB stars to the chemical enrichment of the gas in the ISM as they evolve off the main sequence. The success of their chemical evolution model, in reproducing the trend of PAH abundances with metallicity, strongly suggests the importance of stellar evolutionary effects in determining the abundances and composition of dust in galaxies. In particular such models can explain the presence of large amounts of dust in young dusty hyperluminous infrared galaxies in which supernovae are the only viable source of newly-condensed dust. The study of the temporal evolution of the formation and destruction processes of dust and PAHs traced back to the early universe, is also within the perspective of the new data that will be provided by the Herschel and JWST telescopes, and appears as a very promising research field for the future.

Bibliography

Alexander, T., Sturm, E., Lutz, D., et al. 1999, ApJ, 512, 204

Allain, T., Leach, S., & Sedlmayr, E. 1996, A&A, 305, 616

Allamandola, L. J., Hudgins, D. M., & Sandford, S. A. 1999, ApJ, 511, L115

Allamandola, L. J., Tielens, A. G. G. M., & Barker, J. R. 1989, ApJ, 71, 733

Andersen, M., Rho, J., Hewitt, J., & Reach, W. 2007, in Bulletin of the American Astronomical Society, Vol. 38, Bulletin of the American Astronomical Society, 932–+

Appleton, P. N., Xu, K. C., Reach, W., et al. 2006, ApJ, 639, L51

Armus, L., Draine, B., Engelbracht, C., et al. 2007, in Bulletin of the American Astronomical Society, Vol. 38, Bulletin of the American Astronomical Society, 789–+

Banhart, F. 1997, Journal of Applied Physics, 81, 3440

Banhart, F. 1999, Reports on Progress in Physics, 62, 1181

Barlow, M. J. 1978, MNRAS, 183, 367

Beirão, P., Brandl, B. R., Appleton, P. N., et al. 2008, ApJ, 676, 304

Berezinskii, V. S., Bulanov, S. V., Dogiel, V. A., & Ptuskin, V. S. 1990, Astrophysics of cosmic rays, ed. V. S. Berezinskii, S. V. Bulanov, V. A. Dogiel, & V. S. Ptuskin

Berezinsky, V. S., Blasi, P., & Ptuskin, V. S. 1997, ApJ, 487, 529

Bernard-Salas, J. 2008, in preparation

Berné, O., Joblin, C., Deville, Y., et al. 2007, A&A, 469, 575

Bernstein, M. P., Sandford, S. A., Allamandola, L. J., et al. 1999, Science, 283, 1135

Bethe, H. 1930, Ann. Physik, 5, 325

Bethe, H. 1932, Zeitschrift fur Physik, 76, 293

Bichsel, H. 1990, Phys. Rev. A, 41, 3642

Bloch, F. 1933a, Zeitschrift fur Physik, 81, 363

Bloch, F. 1933b, Annalen der Physik, 408, 285

Boechat-Roberty, H. M., Neves, R., Pilling, S., Lago, A. F., & de Souza, G. G. B. 2008, ArXiv e-prints

Bohr, N. 1913, Philos. Mag., 25, 10

Bohr, N. 1915, Philos. Mag., 30, 581

Borkowski, K. J. & Dwek, E. 1995a, ApJ, 454, 254

Borkowski, K. J. & Dwek, E. 1995b, ApJ, 454, 254

Bouwman, J., Paardekooper, D. M., Cuppen, H. M., Linnartz, H., & Allamandola, L. J. 2009, ApJ, 700, 56

Brandl, B. R. 2008, in preparation

Bréchignac, P. & Pino, T. 1999, A&A, 343, L49

Bregman, J. D., Allamandola, L. J., Witteborn, F. C., Tielens, A. G. G. M., & Geballe, T. R. 1989, ApJ, 344, 791

Bregman, J. N. 1980, ApJ, 236, 577

Breitschwerdt, D., McKenzie, J. F., & Voelk, H. J. 1991, A&A, 245, 79

Breitschwerdt, D., McKenzie, J. F., & Voelk, H. J. 1993, A&A, 269, 54

Bringa, E. M., Kucheyev, S. O., Loeffler, M. J., et al. 2007, ApJ, 662, 372

Cardelli, J. A., Meyer, D. M., Jura, M., & Savage, B. D. 1996, ApJ, 467, 334

Chantler, C. T. 1995, J. Phys. Chem. Ref. Data, 24, 71

Chantler, C. T. 2000, J. Phys. Chem. Ref. Data, 29(4), 597

Chen, Y., Wang, Q. D., Gotthelf, E. V., et al. 2006, ApJ, 651, 237

Cherchneff, I., Barker, J. R., & Tielens, A. G. G. M. 1992, ApJ, 401, 269

Chevalier, R. A. & Clegg, A. W. 1985, Nature, 317, 44

Chokshi, A., Tielens, A. G. G. M., & Hollenbach, D. 1993, ApJ, 407, 806

Chu, Y.-H., Kennicutt, Jr., R. C., Schommer, R. A., & Laff, J. 1992, AJ, 103, 1545

Cosslett, V. E. 1978, J. Microsc.

Cowie, L. L. 1978, ApJ, 225, 887

Cummings, A. C. 1973, PhD thesis, CALIFORNIA INSTITUTE OF TECHNOLOGY.

Curie, M. 1900, Comptes Rendus, 130, 76

Curl, R. F. & Smalley, R. E. 1988, Science, 242, 1017

Czyzewski, Z., O'Neill MacCallum, D., Romig, A., & Joy, D. C. 1990, Journal of Applied Physics, 68, 3066

Danziger, I. J., Goss, W. M., Murdin, P., Clark, D. H., & Boksenberg, A. 1981, MNRAS, 195, 33P

de Souza, G. G. B., Boechat-Roberty, H. M., Rocco, M. L. M., & Lucas, C. A. 2002, J. Electron Spec. Rel. Phen., 123, 315

Decin, L., Morris, P. W., Appleton, P. N., et al. 2004, ApJ, 154, 408

Desert, F.-X., Boulanger, F., & Puget, J. L. 1990, A&A, 237, 215

Dickel, J. R., Milne, D. K., Kennicutt, R. C., Chu, Y.-H., & Schommer, R. A. 1994, AJ, 107, 1067

Diehl, R., Halloin, H., Kretschmer, K., et al. 2006, Nature, 439, 45

D'Odorico, S., Dopita, M. A., & Benvenuti, P. 1980, A&AS, 40, 67

Draine, B. T. 2003, ARA&A, 41, 241

Draine, B. T. 2009, ArXiv e-prints

Draine, B. T. & Lazarian, A. 1998, ApJ, 508, 157

Draine, B. T. & Li, A. 2001, ApJ, 551, 807

Draine, B. T. & Salpeter, E. E. 1979a, ApJ, 231, 438

Draine, B. T. & Salpeter, E. E. 1979b, ApJ, 231, 438

Draine, B. T. & Salpeter, E. E. 1979c, ApJ, 231, 77

Dwek, E. 1987, ApJ, 322, 812

Dwek, E. 1998, ApJ, 501, 643

Dwek, E., Arendt, R. G., Bouchet, P., et al. 2008, ApJ, 676, 1029

Dwek, E., Foster, S. M., & Vancura, O. 1996, ApJ, 457, 244

Dwek, E., Galliano, F., & Jones, A. 2009, ArXiv e-prints

Dwek, E. & Scalo, J. M. 1980, ApJ, 239, 193

Ebeling, H., Edge, A. C., Bohringer, H., et al. 1998, MNRAS, 301, 881

Engelbracht, C. W., Kundurthy, P., Gordon, K. D., et al. 2006, ApJ, 642, L127

Enßlin, T. A. 2003, A&A, 399, 409

Everett, J. E., Zweibel, E. G., Benjamin, R. A., et al. 2008, ApJ, 674, 258

Fano, U. 1963, Annual Review of Nuclear and Particle Science, 13, 1

Fazio, G. G., Hora, J. L., Allen, L. E., et al. 2004, ApJ, 154, 10

Fermi, E. 1950, Progress of Theoretical Physics, 5, 570

Ferrara, A. & Dettmar, R.-J. 1994, ApJ, 427, 155

Ferrell, T. 1979, Solid State Communications, 32, 419

Fesen, R. A., Blair, W. P., & Kirshner, R. P. 1985, ApJ, 292, 29

Field, D., May, P. W., Pineau des Forets, G., & Flower, D. R. 1997, MNRAS, 285, 839

Frenklach, M. & Feigelson, E. D. 1989a, ApJ, 341, 372

Frenklach, M. & Feigelson, E. D. 1989b, ApJ, 341, 372

Füller, T. & Banhart, F. 1996, Chem. Phys. Lett.

Gaisser, T. K. & Stanev, T. 2006, Nuclear Physics A, 777, 98

Galliano, F., Dwek, E., & Chanial, P. 2008a, ApJ, 672, 214

Galliano, F., Madden, S. C., Tielens, A. G. G. M., Peeters, E., & Jones, A. P. 2008b, ApJ, 679, 310

Geballe, T. R., Tielens, A. G. G. M., Allamandola, L. J., Moorhouse, A., & Brand, P. W. J. L. 1989, ApJ, 341, 278

Genzel, R., Lutz, D., Sturm, E., et al. 1998, ApJ, 498, 579

Ginzburg, V. L. 1988, Soviet Physics Uspekhi, 31, 491

Ginzburg, V. L. 1993, Physics Uspekhi, 36, 587

Ginzburg, V. L., Khazan, I. M., & Ptuskin, V. S. 1980, Ap&SS, 68, 295

Giveon, U., Sternberg, A., Lutz, D., Feuchtgruber, H., & Pauldrach, A. W. A. 2002, ApJ, 566, 880

Griffiths, R. E., Ptak, A., Feigelson, E. D., et al. 2000, Science, 290, 1325

Groenewegen, M. A. T., Oudmaijer, R. D., & Ludwig, H.-G. 1997, MNRAS, 292, 686

Guillard, P., Boulanger, F., Pineau des Forets, G., & Appleton, P. N. 2009, ArXiv e-prints

Guillet, V., Jones, A., & Pineau Des Forets, G. 2008, in COSPAR, Plenary Meeting, Vol. 37, 37th COSPAR Scientific Assembly, 1110–+

Guillet, V., Pineau Des Forêts, G., & Jones, A. P. 2007, A&A, 476, 263

Habing, H. J. & Israel, F. P. 1979, ARA&A, 17, 345

Hadjar, O., Hoekstra, R., Morgenstern, R., & Schlathölter, T. 2001, Phys. ReV. A, 63, 033201

Hayakawa, S., Ito, K., & Terashima, Y. 1958, Progress of Theoretical Physics Supplement, 6, 1

Heckman, T. M., Norman, C. A., Strickland, D. K., & Sembach, K. R. 2002, ApJ, 577, 691

Heesen, V., Beck, R., Krause, M., & Dettmar, R.-J. 2009, A&A, 494, 563

Heger, A., Fryer, C. L., Woosley, S. E., Langer, N., & Hartmann, D. H. 2003, ApJ, 591, 288

Henize, K. G. 1956, ApJ, 2, 315

Henriksen, T., Horan, P. K., & Snipes, W. 1970, Radiation Res., 43, 1

Higdon, S. J. U., Devost, D., Higdon, J. L., et al. 2004, PASP, 116, 975

Hollenbach, D. J. & Tielens, A. G. G. M. 1999, Reviews of Modern Physics, 71, 173

Houck, J. R., Roellig, T. L., van Cleve, J., et al. 2004, ApJ, 154, 18

Hovington, P., Drouin, D., & Gauvin, R. 1997, Scanning, 19, 1

Huang, Z. P., Thuan, T. X., Chevalier, R. A., Condon, J. J., & Yin, Q. F. 1994, ApJ, 424, 114

Hunter, S. D., Bertsch, D. L., Catelli, J. R., et al. 1997, ApJ, 481, 205

Hwang, U., Hughes, J. P., Canizares, C. R., & Markert, T. H. 1993, ApJ, 414, 219

ICRU. 1984, H. O. Wyckoff (ICRU Scientific Counsellor), ICRU Report No. 37, Intl. Comm. on Rad. Units, Bethesda, MD

Indriolo, N., Fields, B. D., & McCall, B. J. 2009, ApJ, 694, 257

Ip, W.-H. & Axford, W. I. 1985, A&A, 149, 7

Ipavich, F. M. 1975, ApJ, 196, 107

Irwin, J. A., Kennedy, H., Parkin, T., & Madden, S. 2007, A&A, 474, 461

Irwin, J. A. & Madden, S. C. 2006, A&A, 445, 123

Israel, F. P. 1978, A&A, 70, 769

Jochims, H. W., Ruhl, E., Baumgartel, H., Tobita, S., & Leach, S. 1994a, ApJ, 420, 307

Jochims, H. W., Ruhl, E., Baumgartel, H., Tobita, S., & Leach, S. 1994b, ApJ, 420, 307

Johansson, L. E. B., Greve, A., Booth, R. S., et al. 1998, A&A, 331, 857

Jones, A. P. 2004, in Astronomical Society of the Pacific Conference Series, Vol. 309, Astrophysics of Dust, ed. A. N. Witt, G. C. Clayton, & B. T. Draine, 347–+

Jones, A. P., Tielens, A. G. G. M., & Hollenbach, D. J. 1996, ApJ, 469, 740

Jones, A. P., Tielens, A. G. G. M., Hollenbach, D. J., & McKee, C. F. 1994, ApJ, 433, 797

Joy, D. C. 1995, Scanning, 17, 270

Joy, D. C. & Luo, S. 1989, Scanning, 11, 176

Karttunen, H. 1995, Fundamental Astronomy (Springer)

Katz, R., Sharma, S. C., & Homayoonfar, M. 1972, Nuclear Instruments and Methods, 100, 13

Keller, J. W., Coplan, M. A., & Goruganthu, R. 1992, ApJ, 391, 872

Kokkin, D. L., Troy, T. P., Nakajima, M., et al. 2008, ApJ, 681, L49

Kolmogorov, A. 1941, Akademiia Nauk SSSR Doklady, 30, 301

Latter, W. B. 1991, ApJ, 377, 187

Lazendic, J. S., Dickel, J. R., Haynes, R. F., Jones, P. A., & White, G. L. 2000, ApJ, 540, 808

Le Marne, A. E. 1968, MNRAS, 139, 461

Le Page, V., Snow, T. P., & Bierbaum, V. M. 2001, ApJ, 132, 233

Le Page, V., Snow, T. P., & Bierbaum, V. M. 2003, ApJ, 584, 316

Leach, S. 1987, in NATO ASIC Proc. 191: Polycyclic Aromatic Hydrocarbons and Astrophysics, ed. A. Leger, L. D'Hendecourt, & N. Boccara, 99–127

Leger, A. & Puget, J. L. 1984, A&A, 137, L5

Lehnert, M. D., Heckman, T. M., & Weaver, K. A. 1999, ApJ, 523, 575

Lindhard, J., Nielsen, V., & Scharff, M. 1968, Mat. Fys. Medd. Dan. Vid. Selsk., 36, No. 10

Lindhard, J. & Scharff, M. 1952, Mat. Fys. Medd. Dan. Vid. Selsk., 27, No. 15

Lindhard, J., Scharff, M., & Schiott, H. E. 1963, Mat. Fys. Medd. Dan. Vid. Selsk., 33, No. 14

Ling, Y. & Lifshitz, C. 1996, Chemical Physics Letters, 257, 587

Ling, Y. & Lifshitz, C. 1998, JPC A, 102, 708

Long, K. S., Blair, W. P., Kirshner, R. P., & Winkler, P. F. 1990, ApJ, 72, 61

Long, K. S. & Helfand, D. J. 1979, ApJ, 234, L77

Lucke, P. B. & Hodge, P. W. 1970, AJ, 75, 171

Madden, S. C., Galliano, F., Jones, A. P., & Sauvage, M. 2006, A&A, 446, 877

Mannheim, K. & Schlickeiser, R. 1994, A&A, 286, 983

Marcolini, A., Strickland, D. K., D'Ercole, A., Heckman, T. M., & Hoopes, C. G. 2005, MNRAS, 362, 626

Marshall, F. E., Gotthelf, E. V., Zhang, W., Middleditch, J., & Wang, Q. D. 1998, ApJ, 499, L179+

Martín-Hernández, N. L., Vermeij, R., Tielens, A. G. G. M., van der Hulst, J. M., & Peeters, E. 2002, A&A, 389, 286

Martins, F., Schaerer, D., & Hillier, D. J. 2002, A&A, 382, 999

Mathis, J. S., Rumpl, W., & Nordsieck, K. H. 1977, ApJ, 217, 425

Matsushita, K., Belsole, E., Finoguenov, A., & Böhringer, H. 2002, A&A, 386, 77

Maurin, D. & Taillet, R. 2003, in Physique et Astrophysique du Rayonnement Cosmique, ed. E. Parizot, A. Marcowitch, V. Tatischeff, G. Pelletier, & P. Salati

Mauron, N. 2008, A&A, 482, 151

Mauron, N. & Kendall, T. 2005, in ESA Special Publication, Vol. 576, The Three-Dimensional Universe with Gaia, ed. C. Turon, K. S. O'Flaherty, & M. A. C. Perryman, 699–+

McCray, R. & Snow, Jr., T. P. 1979a, ARA&A, 17, 213

McCray, R. & Snow, Jr., T. P. 1979b, ARA&A, 17, 213

McGee, R. X., Brooks, J. W., & Batchelor, R. A. 1972, Australian Journal of Physics, 25, 581

McKee, C. 1989, in IAU Symposium, Vol. 135, Interstellar Dust, ed. L. J. Allamandola & A. G. G. M. Tielens, 431–+

McKee, C. F., Hollenbach, D. J., Seab, G. C., & Tielens, A. G. G. M. 1987, ApJ, 318, 674

McKee, C. F. & Ostriker, J. P. 1977, ApJ, 218, 148

McKinley, W. A. & Feshbach, H. 1948, Physical Review, 74, 1759

Micelotta, E. R., Jones, A. P., & Tielens, A. G. G. M. 2009a, (MJT09a), accepted for publication in A&A

Micelotta, E. R., Jones, A. P., & Tielens, A. G. G. M. 2009b, (MJT09b), accepted for publication in A&A

Mills, B. Y., Turtle, A. J., & Watkinson, A. 1978, MNRAS, 185, 263

Mohr, J. J., Mathiesen, B., & Evrard, A. E. 1999, ApJ, 517, 627

Moles, M., Sulentic, J. W., & Marquez, I. 1997, ApJ, 485, L69+

Montet, G. L. 1967, Carbon

Montet, G. L. & Myers, G. E. 1971, Carbon

Morse, J. A., Winkler, P. F., & Kirshner, R. P. 1995, AJ, 109, 2104

Moskalenko, I. V. & Strong, A. W. 1998, ApJ, 493, 694

Mott, N. F. 1929, Royal Society of London Proceedings Series A, 124, 422

Mott, N. F. 1932, Royal Society of London Proceedings Series A, 135, 429

Mott, N. F. & Massey, H. S. W. 1949, The theory of atomic collisions (The theory of atomic collisions, by Mott, N. F.; Massey, Harrie Stewart Wilson. Oxford, Clarendon Press, 1949.)

Nakai, K., Kinoshita, C., & Matsunaga, A. 1991, Ultramicroscopy

Nath, B. B. & Biermann, P. L. 1994, MNRAS, 267, 447

Nath, B. B., Madau, P., & Silk, J. 2006, MNRAS, 366, L35

O'C. Drury, L. 1994, Contemporary Physics, 35, 231

O'Connor, D. J. & Biersack, J. P. 1986, Nuclear Instruments and Methods in Physics Research B, 15, 14

Oegerle, W. R. & Hill, J. M. 2001, AJ, 122, 2858

O'Halloran, B., Madden, S. C., & Abel, N. P. 2008, ApJ, 681, 1205

O'Halloran, B., Satyapal, S., & Dudik, R. P. 2006, ApJ, 641, 795

Oliva, E., Moorwood, A. F. M., Drapatz, S., Lutz, D., & Sturm, E. 1999, A&A, 343, 943

Omont, A. 1986, A&A, 164, 159

Ostriker, J. P. & McKee, C. F. 1988, Reviews of Modern Physics, 60, 1

Pauldrach, A. W. A., Hoffmann, T. L., & Lennon, M. 2001, A&A, 375, 161

Peeters, E., Hony, S., Van Kerckhoven, C., et al. 2002a, A&A, 390, 1089

Peeters, E., Martín-Hernández, N. L., Damour, F., et al. 2002b, A&A, 381, 571

Peeters, E., Spoon, H. W. W., & Tielens, A. G. G. M. 2004, ApJ, 613, 986

Pfrommer, C. & Enßlin, T. A. 2004, A&A, 413, 17

Pino, T., Dartois, E., Cao, A.-T., et al. 2008, A&A, 490, 665

Podio, L., Bacciotti, F., Nisini, B., et al. 2006, A&A, 456, 189

Popescu, C. C., Tuffs, R. J., Kylafis, N. D., & Madore, B. F. 2004, A&A, 414, 45

Poppe, T. & Blum, J. 1997, Advances in Space Research, 20, 1595

Povich, M. S., Stone, J. M., Churchwell, E., et al. 2007, ApJ, 660, 346

Prantzos, N. & Silk, J. 1998, ApJ, 507, 229

Ptuskin, V. S., Voelk, H. J., Zirakashvili, V. N., & Breitschwerdt, D. 1997, A&A, 321, 434

Puska, M. J. & Nieminen, R. M. 1983, Phys. Rev. B, 27, 6121

Puska, M. J. & Nieminen, R. M. 1993, Phys. Rev. A, 47, 1181

Ramana Murthy, P. V. & Wolfendale, A. W. 1993, Gamma-ray Astronomy, ed. P. V. Ramana Murthy & A. W. Wolfendale

Ranalli, P., Comastri, A., Origlia, L., & Maiolino, R. 2008, MNRAS, 386, 1464

Rapacioli, M., Joblin, C., & Boissel, P. 2005, A&A, 429, 193

Reach, W. T. & Rho, J. 2000, ApJ, 544, 843

Reach, W. T., Rho, J., Tappe, A., et al. 2006, AJ, 131, 1479

Regier, T. Z., Shi, J., Tersingi, A., et al. 2007, Canadian Light Source, 51

Reimer, L. & Braun, C. 1989, Appl. Opt., 28, 4718

Rieke, G. H., Young, E. T., Engelbracht, C. W., et al. 2004, ApJ, 154, 25

Romanini, D., Biennier, L., Salama, F., et al. 1999, Chem. Phys. Letters

Ruiterkamp, R., Halasinski, T., Salama, F., et al. 2002, A&A, 390, 1153

Salama, F., Bakes, E. L. O., Allamandola, L. J., & Tielens, A. G. G. M. 1996, ApJ, 458, 621

Salama, F., Galazutdinov, G. A., Krełowski, J., Allamandola, L. J., & Musaev, F. A. 1999, ApJ, 526, 265

Sasaki, M., Haberl, F., & Pietsch, W. 2000, A&AS, 143, 391

Scalo, J. M. 1986, Fundamentals of Cosmic Physics, 11, 1

Schaerer, D. & de Koter, A. 1997, A&A, 322, 598

Schild, H. & Testor, G. 1992, A&AS, 92, 729

Schlathölter, T., Hadjar, O., Hoekstra, R., & Morgenstern, R. 1999, Physical Review Letters, 82, 73

Schwering, P. B. W. 1989, A&AS, 79, 105

Sedov, L. 1959, Similarity and Dimensional Methods in Mechanics (New York: Academic)

Serra Díaz-Cano, L. & Jones, A. P. 2008, A&A, 492, 127

Shapiro, M. M. 1991, NATO ASIC Proc. 337: Cosmic Rays, Supernovae and the Interstellar Medium, ed. M. M. Shapiro, R. Silberberg, & J. P. Wefel, pages 1 – 27

Shibata, T., Honda, N., & Watanabe, J. 2007, Astroparticle Physics, 27, 411

Shibata, T. & Ito, T. 2007, ApJ, 655, 892

Sigmund, P. 1981, Sputtering by Particle Bombardment Vol.1, ed. R. Behrisch, in Topics in Applied Physics, Vol. 47 (Springer - Verlag)

Simmons, J. H. W. 1965a, Radiation Damage in Graphite (Pergamon Press)

Simmons, J. H. W. 1965b, Radiation Damage in Graphite (Pergamon Press)

Simpson, J. A. & Garcia-Munoz, M. 1988, Space Science Reviews, 46, 205

Slavin, J. D. 2008, Space Science Reviews, 50

Smith, J. D. T., Draine, B. T., Dale, D. A., et al. 2007, ApJ, 656, 770

Smith, J. D. T., Rudnick, L., Delaney, T., et al. 2008, ArXiv e-prints

Smith, R. C. & MCELS Team. 1998, Publications of the Astronomical Society of Australia, 15, 163

Sofia, U. J. 2009, in Cosmic Dust - Near and Far, ed. T. Henning, E. Grun, & J. Steinacker

Stecker, F. W. 1973, ApJ, 185, 499

Stevens, I. R., Read, A. M., & Bravo-Guerrero, J. 2003, MNRAS, 343, L47

Strickland, D. K. & Heckman, T. M. 2007, ApJ, 658, 258

Strickland, D. K. & Heckman, T. M. 2009, ArXiv e-prints

Strickland, D. K. & Stevens, I. R. 2000, MNRAS, 314, 511

Strong, A. W. & Moskalenko, I. V. 1998, ApJ, 509, 212

Suchkov, A. A., Balsara, D. S., Heckman, T. M., & Leitherer, C. 1994, ApJ, 430, 511

Tappe, A., Rho, J., & Reach, W. T. 2006, ApJ, 653, 267

Thielemann, F.-K., Nomoto, K., & Hashimoto, M.-A. 1996, ApJ, 460, 408

Tielens, A. G. G. M. 1997, Astrophys. Space Sci, 251, 1

Tielens, A. G. G. M. 1998, ApJ, 499, 267

Tielens, A. G. G. M. 2005, The Physics and Chemistry of the Interstellar Medium (University of Cambridge Press)

Tielens, A. G. G. M. 2008, ARA&A, 46, 289

Tielens, A. G. G. M., McKee, C. F., Seab, C. G., & Hollenbach, D. J. 1994, ApJ, 431, 321

Tomita, S., Andersen, J. U., Gottrup, C., Hvelplund, P., & Pedersen, U. V. 2001, Physical Review Letters, 87, 073401

Townsley, L. K., Broos, P. S., Feigelson, E. D., et al. 2006, AJ, 131, 2140

Townsley, L. K., Feigelson, E. D., Montmerle, T., et al. 2003, ApJ, 593, 874

Tran, Q. D., Lutz, D., Genzel, R., et al. 2001, ApJ, 552, 527

Vacca, W. D., Garmany, C. D., & Shull, J. M. 1996, ApJ, 460, 914

van den Ancker, M. E., Tielens, A. G. G. M., & Wesselius, P. R. 2000, A&A, 358, 1035

Van Kerckhoven, C., Hony, S., Peeters, E., et al. 2000, A&A, 357, 1013

Vermeij, R., Damour, F., van der Hulst, J. M., & Baluteau, J.-. P. 2002, A&A, 390, 649

Vermeij, R. & van der Hulst, J. M. 2002, A&A, 391, 1081

Voit, G. M. 1992, MNRAS, 258, 841

Völk, H. J. 2003, ArXiv Astrophysics e-prints

Wang, Q. D. & Gotthelf, E. V. 1998, ApJ, 494, 623

Waters, L. B. F. M. 2004, in Astronomical Society of the Pacific Conference Series, Vol. 309, Astrophysics of Dust, ed. A. N. Witt, G. C. Clayton, & B. T. Draine, 229–+

Webber, W. R. 1998, ApJ, 506, 329

Webber, W. R. & Yushak, S. M. 1983, ApJ, 275, 391

Welty, D. E., Jenkins, E. B., Raymond, J. C., Mallouris, C., & York, D. G. 2002, ApJ, 579, 304

Werner, M. W., Roellig, T. L., Low, F. J., et al. 2004, ApJ, 154, 1

Westerlund, B. E. 1997, The Magellanic Clouds (University of Cambridge Press)

Whaley, C. H., Irwin, J. A., Madden, S. C., Galliano, F., & Bendo, G. J. 2009, MNRAS, 395, 97

Wiebel-Sooth, B., Biermann, P. L., & Meyer, H. 1998, A&A, 330, 389

Winterbon, K. B., Sigmund, P., & Sanders, J. B. 1970, Mat. Fys. Medd. Dan. Vid. Selsk., 37, No. 14

Woosley, S. E. & Weaver, T. A. 1995, ApJ, 101, 181

Zel'dovitch, Y. B. & Raizer, Y. P. 1966, Physics of Shock Waves and High Temperature Hydrodynamic Phenomena, Vol. 1 and 2 (New York: Academic Press)

Ziegler, J. F. 1999, Journal of Applied Physics, 85, 1249

Ziegler, J. F., Biersack, J. P., & Littmark, U. 1985, The Stopping and Ranges of Ions in Matter, ed. J. F. Ziegler, Vol. 1 (Pergamon Press)

Zirakashvili, V. N., Breitschwerdt, D., Ptuskin, V. S., & Voelk, H. J. 1996, A&A, 311, 113

Zirakashvili, V. N. & Völk, H. J. 2006, ApJ, 636, 140

Nederlandse samenvatting

Dit proefschrift beschrijft onderzoek naar de fysische processen die polycyclische aromatische koolwaterstoffen (of Polycyclic Aromatic Hydrocarbons, PAHs) ondergaan tijdens hun reis door de ruimte.

PAH-verbindingen zijn in grote mate aanwezig op aarde. Ze komen van nature voor in ruwe olie en kolen als product van de chemische omzetting van natuurlijke grondstoffen, en worden tevens gevormd bij de onvolledige verbranding van koolstofhoudende brandstoffen zoals hout, kolen, diesel, vet, tabak en wierook. Zodoende zijn PAHs aanwezig in uitlaatgassen van auto's, sigarettenrook en (te ver) gebakken vlees. Dit alles maakt de groep van PAHs een van de meest verspreide organische vervuilende stoffen die vaak de aandacht van de media trekt, omdat ontdekt is dat sommige soorten PAHs carcinogene, mutagene en teratogene eigenschappen hebben. Vooral de PAH-verbinding benzo[a]pyreen (Fig. 1) is bekend omdat het de eerst ontdekte chemische kankerverwekkende stof (carcinogeen) is, en één van de vele carcinogenen die voorkomen in sigarettenrook.

Onderzoek heeft aangetoond dat PAHs veel voorkomen in de ruimte en dat ze een belangrijk deel uitmaken van het Interstellaire Medium (ISM). Ze zijn nauw verwant aan stof en worden gevormd in de gasuitstroom van geëvolueerde en stervende sterren. PAHs dragen substantieel bij aan de opwarming van het ISM en spelen een cruciale rol in de interstellaire chemie en in de kosmische levenscyclus. Bovendien kunnen ze gebruikt worden voor de bepaling van omgevingscondities in astrofysische objecten.

Het Interstellaire Medium en de kosmische levenscyclus

Met de term Insterstellair Medium (ISM) wordt, zoals de naam al suggereert, de materie bedoeld die de ruimte tussen de sterren in een sterrenstelsel vult. Het ISM bestaat voornamelijk uit ijl waterstof- en heliumgas, en een klein aandeel zwaardere elementen die als gas (atomair of moleculair) of als vaste stof aanwezig kunnen zijn. Het ISM is onderverdeeld in een aantal fasen die elk specifieke eigenschappen hebben. De verschillende **fasen** en **componenten** van het ISM zijn niet statisch en geïsoleerd van elkaar, maar zijn voortdurend in interactie door de kosmische levenscyclus, zoals hieronder beschreven en samengevat in Fig. 2. Het verhaal van een nieuwe ster begint in de donkere, koude kernen van compacte **moleculaire wolken**. Zolang de druk het effect van de zwaartekracht kan compenseren is een wolk stabiel. Maar zodra de massa van de kern boven een kritische waarde komt, zal de gravitatie de magnetische/turbulente druk overwinnen, en zal de kern ineenstorten. Als de temperatuur en de dichtheid hoog genoeg zijn om de omzetting van waterstof in helium (ook wel kernfusie of verbranding genoemd) te initiëren, is er een nieuwe ster ontstaan. Hebben we te maken met een ster van lage of gemiddelde massa, dan zal de energie die vrijkomt bij de kernfusie voorkomen dat de ster verder ineenstort tijdens de lange ($10^7 - 10^{10}$ jaar), stabiele 'hoofdreeks'-levensfase. Kernreacties in deze sterren kunnen nieuwe elementen vormen tot aan koolstof, zuurstof en stikstof. Na het verlaten van de hoofdreeks zal de ster uiteindelijk op de asymptotische reuzentak (Asymptotic Giant Branch, AGB) komen. In deze fase zijn de buitenste lagen slechts losjes gebonden aan de stellaire kern, en thermische instabiliteiten zorgen ervoor dat het kern-

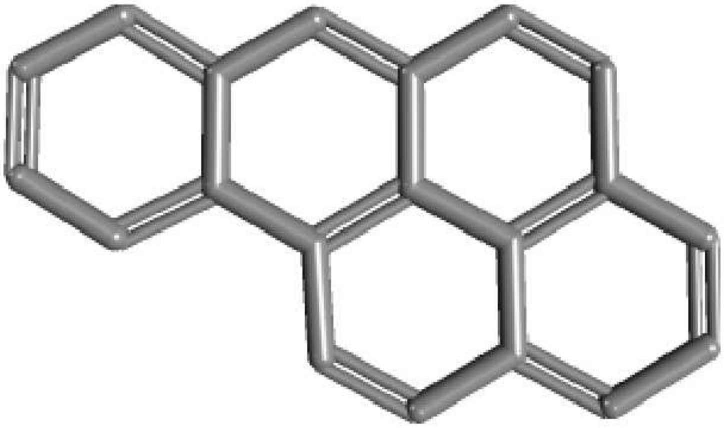

Figuur 1 — Het PAH-molecuul benzo[a]pyreen, het eerst ontdekte chemische carcinogeen, en één van de vele carcinogenen die gevonden zijn in sigarettenrook.

materiaal (koolstof en zuurstof) zich vermengt en naar de oppervlakte komt. Uiteindelijk zal de buitenste laag (envelop) in zijn geheel afgestoten worden, zodat de uitgestrekte nevel rond de ster wordt blootgesteld aan de straling van de hete ioniserende kern. Het resultaat is een planetaire nevel. Zonder verdere verbranding zal de kern uiteindelijk afkoelen en eindigen als een witte dwerg.

De evolutie van een zware ster ($M_* > 8\ M_\odot$) verloopt heel anders. Zware sterren verbruiken hun brandstof veel sneller dan lichte sterren. Bovendien zijn ze in staat koostof en zuurstof om te zetten in zwaardere elementen, tot aan ijzer. Verdere verbranding is niet mogelijk omdat de reactie dan endotherm zou zijn, en uiteindelijk stort de kern ineen terwijl de buitenste lagen exploderen: de ster is dan een type II Supernova. De explosie kan de ster totaal verwoesten, of een neutronenster of pulsar achterlaten. Explosieve nucleosynthese kan plaatsvinden tijdens de laatste fases van de ster, zodat elementen zwaarder dan ijzer gevormd worden die vervolgens in het ISM geïnjecteerd worden.

Gedurende hun leven beïnvloeden sterren hun omgeving in sterke mate, en hun levenscyclus is nauw verbonden met de fysische en chemische evolutie van de materie van het ISM. Ioniserende fotonen van O- en B-sterren (zware, hete, heldere sterren) creëren HII-gebieden (**warm geïoniseerd gas**) en kunnen **interstellaire moleculen** vernietigen. De meerderheid van de zwaardere elementen die gemaakt zijn door sterren, wordt in het ISM geïnjecteerd in de vorm van kleine vaste **stofkorrels**, die voornamelijk gevormd zijn in de expanderende koelende gasuitstroom van geëvolueerde of stervende sterren (AGB en RGB), mogelijk in de uitstoot van supernovae (maar de hoeveelheid stof gevormd in SN is niet goed bekend), en in mindere mate in superreuzen, Wolf-Rayet sterren en novae. Naast stofdeeltjes bevat de uitstoot van geëvolueerde sterren en supernovae ook verschillende moleculen, van de meest simpele zoals CO tot veel complexere zoals afgeleiden van acetyleenketens (bijvoorbeeld HC_7) en **Polycyclische Aromatische Koolwaterstoffen (PAHs)**.

Na de injectie in het ISM door sterrewinden of explosies kan het nieuwgevormde sterrenstof en moleculen vele malen de cyclus doorlopen, met afwisselende fasen tussen de wolken in (**warm neutraal gas**) en in de wolk zelf (**koud neutraal gas**). Door UV-straling in het diffuse ISM, bombardering door **kosmische stralen** en reacties met ionen worden moleculaire verbindingen voortdurend vernietigd en opnieuw gevormd, zodat alleen de meest stabiele stoffen kunnen overleven. In het warme geïoniseerde medium (**Warm Ionized Medium (WIM)**) wordt

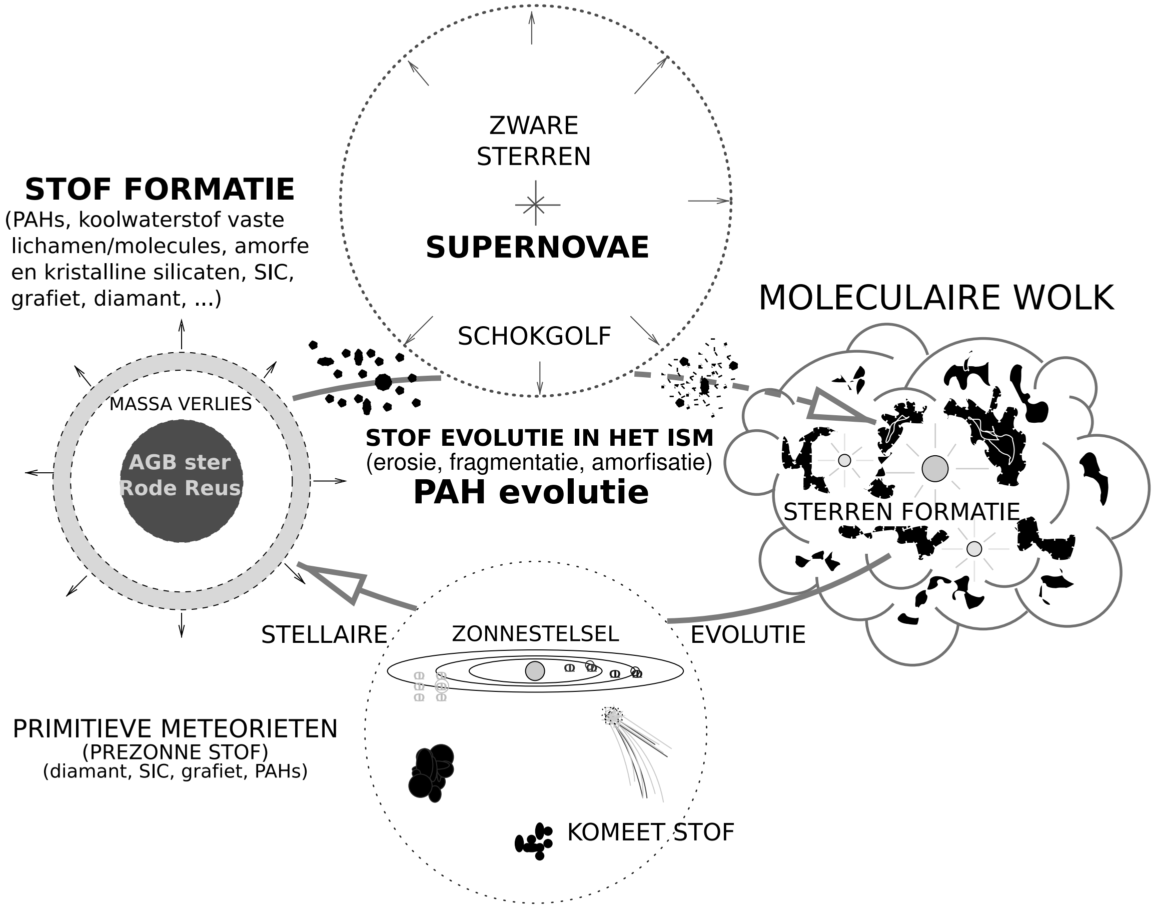

Figuur 2 — Een schematisch overzicht van de kosmische levenscyclus. *Figuur aangepast van Jones (2004).*

stof voornamelijk bewerkt door sterke **schokgolven** veroorzaakt door **supernova-explosies**. Door botsingen met energetische ionen in het hete geschokte gas kunnen atomen van de stofkorrels afspatten, terwijl botsingen tussen stofdeeltjes met hoge snelheden kunnen leiden tot verdamping, smelten, fase-overgangen en vernietiging van de botsende partners. De energie die aan het gas wordt meegegeven door supernova-explosies veroorzaakt een aparte fase van het ISM, het hete geïoniseerde medium tussen de wolken (**Hot Ionized/Intercloud Medium (HIM)**), gekenmerkt door lage dichtheid en hoge temperatuur. In de dichtere gebieden - diffuse compacte wolken - zijn de fysische condities zodanig, dat stoffen in de gasfase op stofkorrels kunnen neerslaan en zo een mantel vormen.

De moleculaire wolken waarin stof en moleculen bestaan, kunnen gravitationeel onstabiel worden en instorten, zodat een nieuwe generatie sterren geboren wordt van welke de chemische samenstelling bepaald wordt door de vorige sterpopulatie. Protoplanetaire schijven worden mogelijk gevormd rond sterren van lage massa, en waarschijnlijk verdampen alle interstellaire stofkorrels volledig, om daarna opnieuw gecondenseerd te worden als condensaten in een zonnestelsel. De cirkel is gesloten en de cyclus begint opnieuw.

Polycyclisch Aromatisch Koolwaterstoffen (PAHs)

Zoals eerder vermeld, heeft het interstellaire medium naast stofdeeltjes ook een populatie grote moleculen die algemeen aangeduid worden als Polycyclische Aromatische Koolwaterstoffen

(Polycyclic Aromatic Hydrocarbons, PAHs). Deze classificatie is vastgesteld door het analyseren van de infrarood (IR)-emissie van verschillende soorten objecten. Het IR-spectrum van de meeste objecten, van individuele HII-gebieden en reflectienevels tot galactische kernen en hele sterrenstelsels, wordt gedomineerd door brede infrarode emissie-karakteristieken die sterke overeenkomsten vertonen met de eigenschappen van emissiekarakteristieken van PAHs. Deze emissiebanden komen voort uit het vibrationele relaxatieproces van PAH-soorten die bestaan uit zo'n 50 –100 koolstofatomen, en geëxciteerd zijn door FUV-fotonen. Met een zeer hoge abundantie van $\sim 10^{-7}$ ten opzichte van waterstof bevatten PAHs 10% van het elementaire koolstof en vertegenwoordigen ze een belangrijke component van het ISM.

Interstellaire PAHs worden vaak geassocieerd met stofkorrels, aan de ene kant omdat ze gevormd worden als bijproduct van formatie van koolstofhoudend stof, aan de andere kant omdat het er inderdaad op lijkt dat ze een aansluiting vormen van op de grootte-verdeling van interstellaire stofkorrels richting het moleculaire domein. Sommige eigenschappen van stofkorrels, zoals de elektrische lading, kunnen redelijkerwijs geëxtrapoleerd worden naar PAHs als een paar details worden meegenomen die gerelateerd zijn aan hun geringe grootte. Toch is het belangrijk te onthouden dat PAHs moleculen zijn, en dat de benadering vanuit de vaste stof fysica zoals toegepast op stofkorrels (zoals bijvoorbeeld botsingsprocessen in schokgolven) niet gebruikt kan worden voor moleculen omdat hun fysica en chemie op vele manieren verschillen van die van stof.

Definitie

PAHs behoren tot de familie van koolwaterstoffen, en worden gekenmerkt door de schikking van koolstofatomen in een ééndimensionale honingraatstructuur van samengevoegde zesvoudige aromatische ringen met H-atomen rondom.

PAHs zijn onderverdeeld in twee hoofdgroepen zoals Fig. 3 laat zien. Peri-gecon-denseerde PAHs (links) hebben een compacte structuur waarin C-atomen deel uitmaken van drie of twee aparte ringen (in het laatste geval alleen aan de buitenkant). Binnen deze klasse vinden we de centraal gecondenseerde, quasi-circulaire PAHs zoals coroneen en circum-coroneen, waarbij de centrale ring omgeven is door een aantal ringen. Dit proefschrift spitst zich toe op deze compacte, centraal gecondenseerde PAHs die het meest stabiel zijn. Een typische compacte interstellaire PAH met 50 koolstofatomen (N_C = 50) heeft een straal van $\sim$ 6.4 Å, terwijl stofkorrels typisch opgebouwd zijn uit vele honderden of duizenden atomen, zoals afgeleid is uit extinctie-metingen. Typische PAH-groottes in het ISM zijn dus zeker kleiner dan die van 'klassieke' stofkorrels. Ortho-gecondenseerde PAHs (rechts) daarentegen worden gekenmerkt door open structuren waarin geen enkel C-atoom tot meer dan twee ringen behoort. De aromatische ringen zijn gerangschikt in rechte ketens (naftaleen, anthraceen, tetraceen) of gebogen rijen (fenanthreen, tetrafeen).

Formatie en evolutie

Men denkt dat interstellaire PAHs ontstaan in de enveloppen van koolstofrijke AGB-sterren, als bijproduct van de processen die leiden tot de formatie van koolstofhoudende stofkorrels (roet). Vanwege hun structuur en hoge stabiliteit zijn PAHs inderdaad de bouwstenen van koolstof-roet. Omdat PAHs nauw verwant zijn aan stofkorrels zullen ze waarschijnlijk een soortgelijk evolutiepatroon volgen. Na te zijn vrijgekomen in het ISM zullen PAHs dramatische veranderingen ondergaan. Ze kunnen groeien en materie aantrekken, worden mogelijk zelf onderdeel van een stofkorrel en kunnen zwaardere hetero-atomen aan zich binden, zoals stikstof. In koude en dichte moleculaire wolken bevriezen PAHs in de ijsmantels die het op-

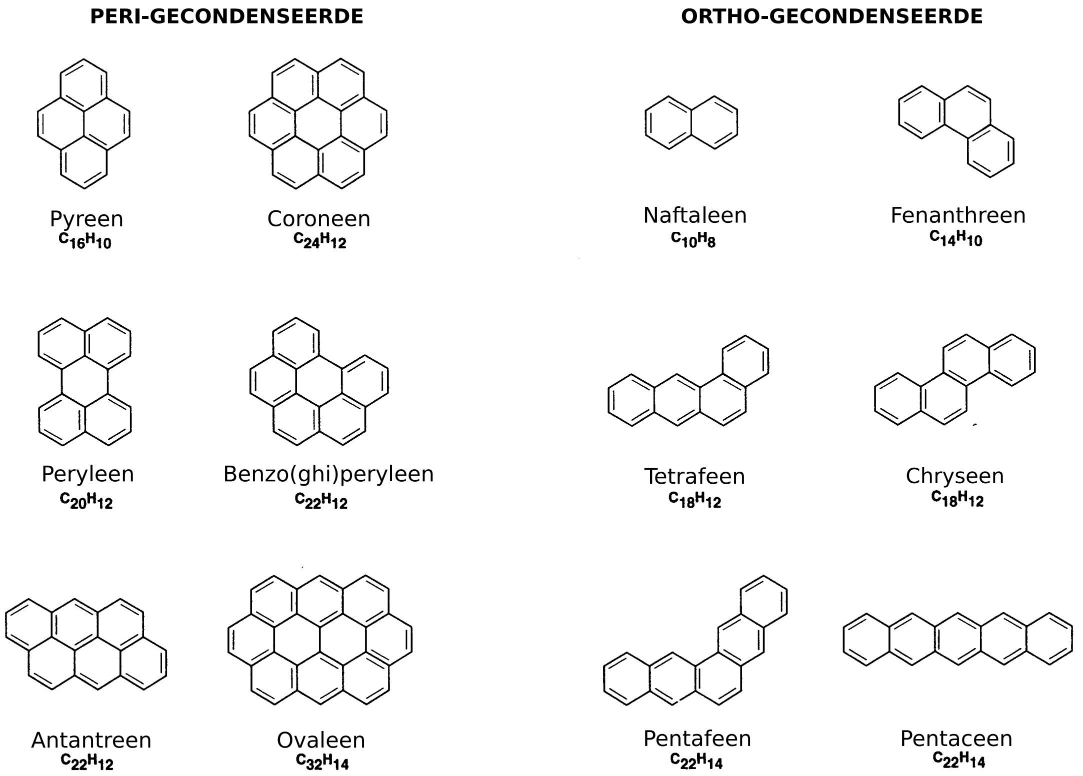

Figuur 3 — De moleculaire structuur van enkele representatieve PAHs. *Figuur aangepast van Salama et al. (1996).*

pervlak van stofkorrels omgeven. UV-straling en bombardering met kosmische stralen veroorzaken vele scheikundige processen aan het oppervlak waardoor complexere soorten kunnen ontstaan. Net als stofkorrels worden ook PAHs blootgesteld aan destructieve processen. Ze kunnen deels of geheel vernietigd worden door fotonen met hoge energie, kosmische stralen en sterke schokgolven in het diffuse ISM, hoewel alleen de kleine PAHs door fotodestructie aangetast lijken te kunnen worden.

Excitatie-mechanismen en IR-spectroscopie

We beschouwen nu een klein, neutraal PAH-molecuul in de singlet electronische grondtoestand. De absorptie van UV-fotonen met energieën die overeenkomen met de discrete electronische energieniveaus zal de PAH in een geëxciteerde staat brengen, gevolgd door een variëteit aan mogelijke de-excitatieprocessen. In een botsingsvrije omgeving zoals in de ruimte zal infrarode emissie het dominerende relaxatie-proces zijn. Het geëxciteerde molecuul zal naar een lagere electronische staat terugvallen, waarbij het grootste deel van de oorspronkelijke excitatie-energie in de vorm van vibrationele energie vrijkomt. Vervolgens zal het sterk vibrationeel geëxciteerde molecuul afkoelen, voornamelijk door IR-emissie in specifieke banden.

Eerder was al genoemd dat het IR-spectrum van bijna elk object en gebied waar gas en stof aan UV-straling worden blootgesteld, gedominieerd wordt door relatief brede emissiekarakteristieken bij 3.3, 6.2, 7.7, 8.6, 11.3 en 12.7 μm (Fig. 4), plus verscheidene zwakkere karakteristieken. Tot bijna tien jaar geleden bleven de dragers een mysterie, zodat ze alge-

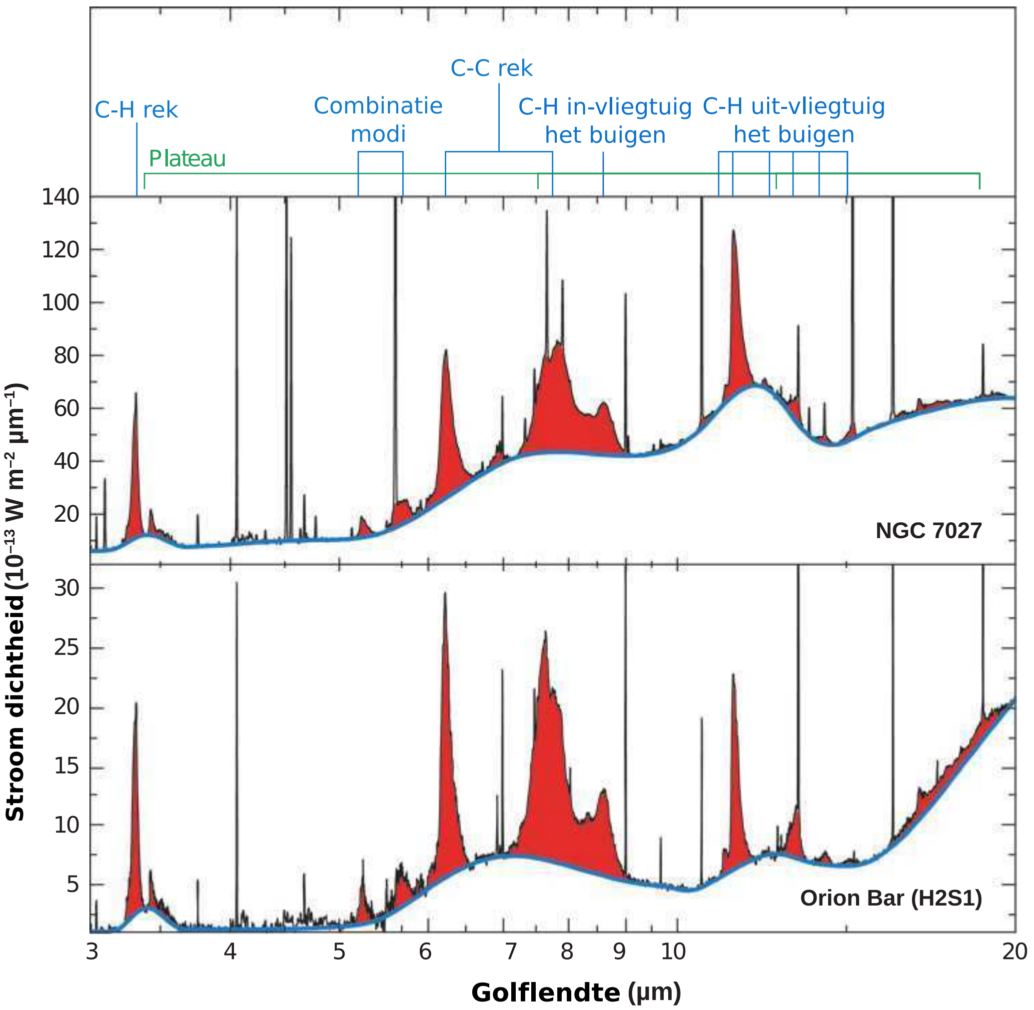

Figuur 4 — Het mid-infrarode spectrum van de het fotodissociatie-gebied in de Orion-bar en in de planetaire nevel NGC 7027. De spectra worden gedomineerd door een serie emissie-karakteristieken, die (bijna) allemaal toegeschreven kunnen worden aan de vibrationele toestanden van polycyclische aromatische koolwaterstoffen (boven). De smalle karakteristieken zijn atomaire of ionische lijnen die uit het HII-gebied of het foto-dissociatie-gebied afkomstig zijn. *Figuur overgenomen van Tielens (2008), een aangepaste versie van Peeters et al. (2002a).*

meen bekend werden als ongeïdentificeerde infrarode banden (Unidentified InfraRed, UIR). Later werd het mogelijk, door het vergelijken van astronomische spectra met laboratoriumspectroscopie en quantum-chemische berekeningen van de overgangen van bekende stoffen, de PAHs te identificeren als de veroorzakers van de UIR-banden. De waargenomen karakteristieken zijn kenmerkend voor de strekkende en buigende vibrationele toestanden van aromatische koolwaterstoffen.

Echter, hoewel de aromatische aard van de dragers van de UIR-band onbetwist vaststaat, is over de identificatie van de exacte soort lange tijd gedebatteerd. Koolstofhoudende vaste stoffen met een substantiële aromatische component – zoals kolen en amorfe roetdeeltjes – vertonen ook infrarode emissie die algemene gelijkenis vertoont met de waargenomen interstellaire spectra, maar dit zijn ongeordende structuren en hun emissie-karakteristieken zijn vaak veel breder dan die van de observaties. Bovendien zijn voor emissie bij de waargenomen golflengtes veroorzakers nodig met een grootte van 50 – 100 C-atomen. Deze grootte-eis en de aromatische natuur van de veroorzaker samen vormen een sterke aanwijzing voor de keuze voor PAHs als veroorzaker, in de vorm van moleculen en/of kleine clusters, hoewel er nog geen specifieke moleculen geïdentificeerd zijn. Een moeilijkheid is dat de PAHs die in het laboratorium bestudeerd werden, veel kleiner zijn ($<$ 50 C-atomen) dan de veronderstelde interstellaire PAH. Het lijkt waarschijnlijker dat het gaat om een familie van PAHs, in plaats van één enkel PAH-molecuul.

Het belang van interstellaire PAHs

De meest opvallende eigenschap van interstellaire PAHs is dat ze overal aanwezig zijn. De UIR-banden, waarvoor de PAHs de meest logische veroorzakers zijn, zijn aangetroffen in bijna elke astrofysische omgeving waar stof en gas door UV-fotonen bestraald worden, wat natuurlijk niet uitsluit dat ze ook aanwezig zijn op plaatsen waar ze niet de kans hebben geëxciteerd te worden. PAH-karakteristieken (alleen de ‘waarneembare’ in acht genomen), zijn geobserveerd in fotodissociatie-gebieden (PhotoDissociation Regions, PDRs), reflectienevels, jonge stellaire objecten, planetaire nevels, post-AGB objecten, galactische kernen, starburststelsels (hevig stervormende sterrenstelsels), Ultraluminous Infrared Galaxies (ULIRGs, stelsels met extreem hoge lichtkracht het infrarood), maar ook in infrarode cirrus bij hoge galactische latitudes op de oppervlaktes van donkere wolken, en in het algemeen in het interstellaire medium van sterrenstelsels.

Gezien deze wijdverspreidheid is het niet vreemd dat PAHs een cruciale rol wordt toegedacht in veel astrofysische processen. Vanwege de hoge stabiliteit van PAHs, de neiging van aromatische brandstoffen om te roeten, en de structurele gelijkenis tussen de koolstofbasis van PAHs en die van roet, worden PAHs geacht de bouwstenen te zijn van het koolstofcondensatieproces. Door middel van het foto-electrisch effect, infrarode emissie en afkoeling door gas-stofkorrelbotsingen domineren PAHs (en stofkorrels) de opwarming en afkoeling van het ISM, wat uiteindelijk de fysische condities en de fasestructuur van het ISM bepaalt en daardoor ook de evolutie van het ISM in sterrenstelsels. PAHs beïnvloeden de ladingsbalans, die de evenwichtstoestand van chemische reacties en gas-fase abundanties in moleculaire wolken weerspiegelt. Aan het oppervlak faciliteren ze een groot gebied voor chemische reacties aan het oppervlak, en zo spelen ze een significante rol in de interstellaire chemie. Er is voorgesteld dat PAHs de mogelijke veroorzakers zijn van de Diffuse Interstellaire Banden (DIB’s), en mogelijk ook betrokken zijn bij de 2175 Åkarakteristiek die de interstellaire UV-extinctiecurve domineert.

PAHs hebben vanwege hun eigenschappen ook een veelbelovende rol als tracer voor verscheidene astrofysische fenomenen. De wijdverspreidheid van hun emissiekarakteristieken en hun overwicht in het mid-IR spectrum van massieve stervormingsgebieden maken PAHs tot een potentieel krachtig werktuig voor de studie van stervorming door het hele heelal. In wezen gedragen de PAHs zich als een kleurstof voor de aanwezigheid van pompende FUV-fotonen en markeren ze daardoor de aanwezigheid van massieve sterren. De aanwezigheid van PAH-karakteristieken is ook gebruikt om onderscheid te maken tussen geschokt gas en PDRs. PAHs zijn, in combinatie met de emissielijnen, gebruikt in extragalactische studies om de fysische processen die ten grondslag liggen aan de lichtkracht van galactische kernen vast te leggen. Deze studies laten zien dat ULIRGs hun lichtkracht meer halen uit stervorming dan uit actieve galactische kernactiviteit (Active Galactic Nucleus- of AGN-activiteit). Hierdoor kunnen de sterktes van PAH-banden ook gebruikt worden om evolutionaire effecten te onderzoeken en om de evolutie van elementen in sterrenstelsels te volgen. PAH-karakteristieken zijn ook gedetecteerd in gebieden die ruimtelijk gecorreleerd zijn met de röntgenstraling (X-ray) van het hete gas in het stervormingsgebied M17 en in de gasuitstroom van het starburststelsel M82. Deze emissie vindt waarschijnlijk zijn oorsprong in gas dat is opgeslokt uit moleculaire wolken en getransporteerd door superwinden en galactische fonteinen. PAHs zouden dan gebruikt kunnen worden als markering voor meegevoerd materiaal om deze transportatiemechanismen aan te duiden.

Waarom we het botsingen van PAHs in het ISM bestuderen

De fotofysica en fotochemie van PAHs in de ruimte zijn uitgebreid onderzocht. PAH-fotoexcitatie met daarop volgend IR-emissie en fotodestructie zijn zowel theoretisch als experimenteel goed bestudeerd, en de observationele weerslag daarvan is bevestigd. Laboratoriumstudies van moleculen in omstandigheden zoals verwacht in het insterstellaire medium, hebben de kennis van de aard van de interstellaire stoffen en de betrokken processen verbeterd. De satellieten ISO en Spitzer hebben de alomtegenwoordigheid van de UIR-banden bevestigd, en de enorme rijkdom van het UIR-spectrum en de wijdverspreide variaties in de relatieve sterktes en profielen van deze karakteristieken aangetoond, van object tot object en binnen objecten.

Ook de bewerking van stofkorrels door processen in het ISM is uitgebreid bestudeerd, niet alleen op gebied van interactie met fotonen (zoals verstrooiing, extinctie of foto-electrische verhitting), maar ook de invloed van botsingen, voornamelijk door supernova-schokgolven. Berekeningen voorspellen de complete vernietiging van grote stofkorrels in snelle schokgolven die zich door de warme fase van het interstellair medium (WIM) bewegen. schokgolven met snelheden groter dan 50 km s^{-1} zijn ook in staat de grootste korrels (1000 Å$\leq a \leq$ 2500 Å) te verbrijzelen in fragmenten met een straal kleiner dan $\approx$ 500 Å. Tussen de fragmenten zouden ook PAHs kunnen zitten, waarvan verwacht wordt dat deze vervolgens ook door de schok bewerkt zullen worden. Helaas wordt in deze modellen geen rekening gehouden met de vernietiging van PAHs door het wegkaatsen van atomen in het gas achter de schokgolf, wat wel degelijk relevant zou kunnen zijn voor de evolutie van de interstellaire PAH-populatie.

Als men dit alles bekijkt, valt op dat een belangrijke schakel in de keten mist: de behandeling van de invloed van botsingen op PAHs in het ISM. PAHs en stofkorrels zijn nauw verbonden en men kan redelijkerwijs aannemen dat ze dezelfde soort botsingsprocessen doormaken gedurende hun levenscyclus. Waar voor stofkorrels de fysica van deze processen onderzocht is en de astrofysische implicaties in kaart zijn gebracht, is dit niet het geval voor PAHs. Theoretische modellen die botsingsprocessen meenemen (met name de processen die leiden tot beschadiging en vernietiging van PAHs) zijn er niet, en dit gebrek aan informatie maakt de interpretatie van PAH-observaties moeilijk in gebieden waar deze processen plaatsvinden. Vanuit observationeel oogpunt is er momenteel weinig bewijs voor het bestaan van PAHs in gebieden die supernova-schokgolven ondergaan. Dit laat zien hoe moeilijk het is om de emissie van supernovaresten te onderscheiden van de achtergrond van materie van het sterrenstelsel. Aan de andere kant heeft een studie van de supernovarest (SuperNova Remnant, SNR) N132D in de Grote Magellaanse Wolk de aanwezigheid aangetoond van karakteristieken die worden toegeschreven aan PAH-soorten met relatief veel koolstof ($N_C \sim$ 4000 C-atomen). PAH-emissie is gedetecteerd in verband met het door schokgolven verhitte, röntgen-stralende gas in het stervormingsgebied M17, en de superwind die aangedreven wordt door de nucleaire starburst in M82.

Het doel van ons onderzoek is deze lacune in ons begrip van de fysica achter botsingsprocessen van PAHs op te vullen, en duidelijk te maken hoe dit de PAH-evolutie in astrofysische context beïnvloedt. Deze kennis zou kunnen helpen de effectieve rol van PAHs in de kosmische levenscyclus beter te begrijpen, met name hun relatie met stofkorrels. Deze resultaten zouden ook nieuwe inzichten kunnen geven om de detectie – of non-detectie van PAHs in specifieke gebieden te interpreteren en zouden uiteindelijk meer argumenten kunnen leveren voor PAHs als moleculaire kleurstof, bijvoorbeeld om gebieden met compacter ingevangen materiaal te volgen.

Sleutelvragen

Het onderzoek dat in dit proefschrift wordt beschreven, heeft als doel vast te stellen *hoe* de verschillende omstandigheden in het ISM de PAHs beïnvloeden, waarbij de nadruk gelegd wordt op de *botsingsprocessen* door electronen en ionen met hoge snelheden. Deze hoge snelheden ontstaan door de thermische en relatieve (inerte) beweging, die wordt veroorzaakt door de energie die door zeer snelle schokgolven (thermische beweging) in het gas geïnjecteerd wordt en door kosmische straling. Hoewel PAHs een hoofdbestanddeel van het ISM zijn en deze processen een cruciale rol spelen in de ontwikkeling van de PAHs, ontbrak het tot nog toe aan een gedetailleerde studie naar de fysica achter de interactie tussen PAHs en hoog-energetische deeltjes (ionen en electronen). De eerste sleutelvraag die we in dit proefschrift behandelen is:

Wat gebeurt er met PAH-moleculen wanneer ze gebombardeerd worden door hoog-energetische ionen en electronen? Zijn ze in staat om (ongeschonden) te overleven, of worden ze zwaar beschadigd of zelfs volledig vernietigd?

Hieruit volgt de volgende belangrijke vraag:

Wat zijn de astrofysische implicaties van de processen die PAHs beïnvloeden?
i.e.
Wat is het verband tussen microscopische processen (ion/electron - PAH interactie) en de macroscopische effecten op de interstellaire PAH-populatie?

Resultaten van dit proefschrift

In **Hoofdstuk 2** presenteren we een studie van de complexe omgeving van de SNR N157B, in de Grote Magellaanse Wolk. We gebruiken hiervoor waarnemingen over meerdere golflengtes. Het hoofdstuk bevat een analyse van een SNR en de verschillende habitatten van PAHs. In deze SNR bevinden zich uiteenlopende omgevingen zij aan zij, zoals een moleculaire wolk, stroken van stof, hete bellen van geschokt gas, een OB-associatie en een HII-gebied, waardoor het gebied een zeer goed laboratorium is voor de studie naar PAHs en de omstandigheden waaraan zij blootgesteld worden. Uit IRAC- en MIPS-afbeeldingen genomen door Spitzer, concluderen we dat er geen bewijs is voor een infrarode tegenhanger van de SNR. De infrarode straling die we waarnemen wordt gedomineerd door een wolk van stof/PAH en moleculair gas, die aan de SNR grenst. De wolk bevat de compacte 2MASS-bron J05375027-6911071. Dit object heeft een diameter van ongeveer 3 parsec, een electronen-dichtheid van 100-250 cm^{-3}, en is gefoto-ioniseerd door een O8-O9 ster. Van de achterkant gezien is het waarschijnlijk een zogenaamde "open HII blaarstructuur" [1]. Ondanks het feit dat de SNR röntgenstraling en de

---

[1] Een dergelijke structuur ontstaat wanneer een massieve ster gevormd wordt aan de rand van een HII-gebied. Wanneer de ioniserende straling van de ster de rand van de HII-wolk bereikt, stroomt het geïoniseerde HII materiaal tussen de wolken door. Dit veroorzaakt, afhankelijk van de gezichtshoek een typische configuratie, ofwel blaarstructuur.

infrarode wolk elkaar (in projectie) overlappen, vinden we slechts zwakke emissie die duidt op schokgolven ([FeII]). Zowel het exciteren als het verwarmen van de uitgebreide wolk, worden gedomineerd door foto-ionisatie door de jonge hete O-sterren van LH 99. Het gebrek aan duidelijk bewijs voor schokgolven geeft aan dat de moleculaire stofwolk op het moment niet significant wordt beïnvloed door de SNR. Dit doet vermoeden dat de voorloper van de SN een ster was van gemiddelde massa $M \approx 25\ \mathrm{M}_\odot$.

In **Hoofdstuk 3** en **Hoofdstuk 4** presenteren we de door ons ontwikkelde modellen, die ons voor het eerst in staat stellen de effecten van botsingen tussen PAHs en ionen (H, He en C) en tussen PAHs en electronen (met een energie tussen de 10 eV en 10 keV) kwantitatief te beschrijven. Er is behoefte aan specifieke modellen, aangezien PAHs moleculen zijn, wat betekent dat de klassieke benadering met behulp van de vaste stof fysica niet kan worden toegepast. In een vaste stof draagt het invallende energetische deeltje energie over aan het atoom. Als de overgedragen energie hoger is dan de bindingsenergie op het inslagpunt, dan wordt er een primair atoom weggeslagen. Dit atoom zal botsen met andere atomen, waarbij de energie wordt verdeeld via een reeks botsingen. In een PAH zal een enkel C-atoom met name op deze manier geraakt worden. Wanneer de overgedragen energie dan een bepaalde grenswaarde overschrijdt, vindt er geen botsingsreeks plaats, maar zal het atoom uit het molecuul worden geschoten. In een molecuul spelen zich dus uitsluitend enkele transacties af, die kunnen worden beschreven met behulp van een aangepaste versie van de tweevoudige botsingsmodellen die voor vaste stoffen worden gebruikt. Het energieverlies ten opzichte van de atomaire electronen zal niet worden verdeeld rondom het gebied van de botsing, zoals in een vaste stof, maar zal verspreid worden over de beperkte straal van de PAH. Het resultaat in termen van de vernietiging van PAHs kan niet worden geëxtrapoleerd uit het gedrag van stofdeeltjes en hangt sterk af van het soort projectiel en de hoeveelheid energie die er mee gepaard gaat.

We hebben een model ontwikkeld voor de interactie tussen energetische ionen en electronen en PAHs, waarbij we rekening houden met de moleculaire aspecten van deze interactie. Een schematische weergave van de analyse van PAH-vernietiging is te zien in Tabel 1. De interactie tussen PAHs en ionen wordt beschreven in termen van nucleair (elastisch) en electronisch (inelastisch) energieverlies, wat kan leiden tot het verlies van koolstofatomen en daaropvolgend ontwrichting en vernietiging van de moleculen. Het energieverlies in de kern ontstaat door botsingen tussen het projectiel en een enkel atoom in het doelwit. Als de energie die wordt overgedragen hoger is dan een bepaalde grenswaarde T_0, dan wordt het koolstofatoom weggeschoten. Dit is de situatie waarin wij zijn geïnterresseerd, aangezien het nog niet in eerdere studies behandeld is. We hanteren een grenswaarde T_0=7.5 eV, wat een redelijke waarde is, maar het is ook nodig om deze waarde experimenteel te bepalen. Het energieverlies ten opzichte van de atomaire electronen (electron-interactie) wordt beschreven in termen van de remkracht van een electronengas met een geschikte electronendichtheid (jellium benadering"), waarbij een geometrie toegepast wordt die past bij de vorm en eindige afmetingen van de PAH. Voor botsingen met electronen met een energie tussen de 10 eV en 10k eV, hebben we een analytische uitdrukking afgeleid voor de gemeten remkracht in grafiet en deze hebben we toegepast op de PAHs. De kans dat een door electron-interacties en -botsingen aangeslagen PAH uiteenvalt, is afgeleid met behulp van ontledingsreacties, waarbij een enkel reactant (de PAH) ontleed wordt in verschillende reactieprodukten. De waarde van de parameter E_0, die deze kans bepaalt, kan nogal variëren. Wij kiezen een waarde van 4.6 eV, wat overeenkomt met een extrapolatie van interstellaire condities, maar een betere bepaling is vereist.

In **Hoofdstuk 3** gebruiken we onze modellen om de levensduur te bepalen van PAHs die onderhevig zijn aan botsingen met ionen en electronen. Deze hebben hoge snelheden, die ont-

Tabel 1 — Overzichtstabel voor PAH botsingen met ionen en electronen.

			Projectielen			
			Ionen		Electronen	
Omgeving	Energie verdeling	Energie bereik (eV)	Elast. (Nucleair) interactie	Inelast. (Elec.) interactie	Elast. (Nucl.) interactie	Inelast. (Elec.) interactie
Interst. Schokgolven[a] **Hoofdstuk 3**	Inert	$10 - 10^4$	✓ § **3.2** § **3.3.1**	✓ § **3.3.2**		
	Thermisch	$5 - 50$	✓ § **3.2** § **3.3.1**	✓ § **3.3.2**		✓✓[c] § **3.3.3**
Heet Gas[b] **Hoofdstuk 4**	Thermisch	$10 - 10^4$	✓ § **4.2.2**	✓ § **4.2.1**		✓✓[c] § **4.3**
Kosmische straling **Hoofdstuk 5**	CR energie verdeling	5 MeV – 10 GeV		✓✓[c] § **5.2**	✓ § **5.3**	

(*a*): Schoksnelheid, $v_\mathrm{S} = 50 - 200\ \mathrm{km\ s^{-1}}$.
(*b*): Gas temperatuur, $T = 10^5 - 10^8$ K.
(*c*): Voor elke omgevingssoort geeft het dubbele teken (✓✓) de belangrijkste oorzaak voor PAH vernietiging weer (met $N_\mathrm{C} = 50$).

staan zijn door de thermische en relatieve bewegingen van interstellaire schokgolven, die met een matige snelheid door het gas bewegen (v_s tussen de 50 en 200 km s^{-1} – zie Tabel 1). We vinden dat interstellaire PAHs ($N_C \sim 50$) niet overleven in schokgolven met snelheden groter dan 100 km s^{-1} en dat grotere PAHs. ($N_C \sim 200$) worden vernietigd wanneer deze snelheid ≥ 125 km s^{-1} is. Voor schokgolven met een snelheid tussen de $\approx 75 - 100$ km s^{-1} heeft de PAH een kans te overleven, hetzij in een nieuwe vorm aangezien het waarschijnlijk is dat de PAH een behoorlijke fractie ($20 - 40\%$) van zijn koolstofatomen zal verliezen. De levensduur van een PAH tot aan vernietiging is $t_{\rm SNR} \sim 1.6 \times 10^8$ yr en $\sim 1.4 \times 10^8$ yr voor N_C is respectievelijk 50 en 200. Kleine PAHs worden voornamelijk vernietigd door electronen, grote door ionen. Deze resultaten zijn robuust en onafhankelijk van de onzekerheden in de parameters T_0 en E_0, die beiden nog niet nauwkeurig genoeg bepaald zijn in experimenten. De berekende levensduur is kleiner dan de waarden die zijn gevonden voor koolstofhoudende korrels (6×10^8 yr), maar ligt dichtbij de levensduur van gehydrateerde, amorfe koolstof (2×10^8) en ver van de tijdschaal waarop sterrestof wordt geïnjecteerd (2.5×10^9 yr). De waargenomen aanwezigheid van PAHs in geschokte gebieden vereist daarom een efficiënt hervormingsmechanisme en/of een beschermende omgeving.

In **Hoofdstuk 4** brengen we onze modellen in stelling om te bepalen hoe lang een PAH overleeft in een heet gas dat röntgenstraling uitzendt (temperatuur tussen de 10^3 en 10^8 K, zie Tabel 1). In dit geval worden de snelheden van de ionen en electronen veroorzaakt door de energie die in het gas wordt geïnjecteerd door zeer snelle schokgolven (thermische beweging). We vinden dat het PAH vernietigingsproces gedomineerd wordt door electronbotsingen wanneer de temperatuur boven de $\sim 3 \times 10^4$ K komt, en door nucleaire interactie met helium bij lagere temperaturen. Kleine PAHs worden makkelijker vernietigd dan grote als de temperatuur lager is dan $\sim 10^6$ K, maar dit verschil wordt kleiner in een heter gas. Voor een PAH van 1000 C-atomen zijn nucleaire interacties de belangrijkste oorzaak van vernietiging. In een heet en ijl gas (bv. de gasuitstroom van M82) worden PAHs met afmetingen tussen de 50 en 200 C-atomen binnen een paar duizend jaar vernietigd door middel van electronbotsingen. In koudere en meer compacte gebieden (bv. Orion) kunnen PAHs wel enkele 10^7 jaar overleven voordat ze worden vernietigd door nucleaire interactie-processen. De absorptie van röntgenfotonen, speelt in verhouding tot electronbotsingen een kleine rol bij de vernietiging van PAHs in het hete gas dat verbonden is met sterrewinden en supernova-explosies. De PAHs die in de buurt van zulke gebieden waargenomen worden, moeten geïsoleerd zijn van dit hete gas en bevinden zich waarschijnlijk in een kouder PDR-achtig gas dat meegevoerd wordt door sterrewinden en galactische winden. Zo beschouwd vormen PAHs dus een goede aanwijzing voor de aanwezigheid van meegevoerd compacter materiaal. De erosie van PAHs gebeurt via C_2-verlies aan het oppervlak van het molecuul, waarbij de aromatische structuur dus behouden blijft. De levensduur van een PAH in een ijl, heet gas ($n_H \approx 0.01$ cm^{-3}, $T \approx 10^7$ K, kenmerkend voor het gas in de gasuitstromen van een sterrenstelsel), is ongeveer duizend jaar, een orde van grootte korter dan de gemiddelde levensduur van dit soort objecten en ook veel korter dan de levensduur van een stofdeeltje van ongeveer dezelfde grootte ($a \approx 5$Å). Dit kan betekenen dat de vernietigende kracht van ion- en electronbotsingen met zeer kleine korrels tot nu toe onderschat is.

In **Hoofdstuk 5** beschouwen we projectielen met veel meer energie, zoals bijvoorbeeld ionen van kosmische straling (H, He, CNO, Fe-Co-Ni) en electronen met energieën tussen de 5 MeV en 10 GeV (zie Tabel 1). Het energieverlies van een dergelijk hoog-energetisch deeltje vereist een speciale behandeling die gebaseerd is op een formalisme dat afwijkt gevallen met lagere energie die zojuist behandeld zijn. Wat de ionen betreft, is het afstoppen door de kern volkomen verwaarloosbaar en wordt het energieverlies gedomineerd door electronische interactie, die goed beschreven wordt door de Bethe-Bloch-vergelijking (in plaats van de Lindhard & Scharff vergelijking). De interactie van PAHs met hoogenergetische electronen kan worden gezien als botsingen tussen het inkomende electron en de enkele kern in de PAH. Dit is niet het geval voor lagere energieën. We bepalen de vernietigende kracht van invallende kosmische straling op PAHs en de tijd die de PAHs dit alomtegenwoordige bombardement kunnen overleven onder verschillende omstandigheden (in schijven van sterrenstelsels, halos, de gasuitstroom van starbursts en de koelende gasstromen in clusters van sterrenstelsels). De spectra van kosmische straling die we gebruiken voor de zon en omstreken zijn afkomstig van metingen die dichtbij de aarde zijn genomen, maar gecorrigeerd zijn voor de invloed van de Heliosfeer (ofwel zonsmodulatie). Om er achter te komen hoe de kosmische straling varieert over de schijf van de melkweg en de halo, gebruiken we specifieke modellen, die gebaseerd zijn op metingen van γ-straling. Voor overige sterrenstelsels schalen we de dichtheid van kosmische straling met de stervormingssnelheid van het sterrenstel, voor een bepaling van de kosmische straling in clusters gebruiken we γ-straling waarnemingen.

We vinden dat de tijd die het kost om PAHs door de ionen in kosmische straling te vernietigen afhangt van de electron excitatie-energie E_0, de minimale energie van de kosmische straling E_{min} en de hoeveelheid energie die beschikbaar is voor dissociatie. Kleine PAHs worden sneller vernietigd, met name door He en CNO. De kortste levensduur die we vinden is $\sim 10^8$ yr, wat vergelijkbaar is met de levensduur in interstellaire schokgolven. Kosmische straling is beter in staat om de PAH in verstrooide wolken aan te tasten, waar de invloed van interstellaire schokgolven minder groot is. Voor electronbotsingen is de levensduur onafhankelijk van de grootte van de PAH, maar varieert hij met E_{min} en de grenswaarde voor de energie T_0. De minimale levensduur is in dit geval 1.2×10^{13} yr. Een dergelijk lange levensverwachting sluit kosmische straling uit als belangrijke PAH-vernietiger. In de halo van normale sterrenstelsels zoals NGC 891 en in de gasstromen van starbursts zoals M82 is de levensverwachting van PAHs, ten opzichte van vernietiging door kosmische straling, $\gtrsim 100$ Myr, wat vergelijkbaar is met (of zelfs iets langer is dan) de circulatie tijdschaal tussen de schijf en halo en duur van de starburst (respectievelijk ~ 200 Myr en ~ 20 Myr). In de clusters met koelende stromen, zoals A85 en Virgo, is de intensiteit van kosmische straling vergeleken met de zonsomgeving opmerkelijk sterker. Hierdoor is de PAH levensverwachting veel korter. Desalniettemin is die verwachting met betrekking tot de vernietiging door kosmische straling tenminste 100 keer zo hoog dan de verwachting in een heet gas ($1 - 10^3$yr). Dit betekent dat de moleculen zeer snel worden vernietigd in de gasfase van het inter-cluster medium. Tenslotte worden de PAHs die verspreid zijn in het hete gas dat te vinden is in de halos van sterrenstelsels, de uitstromen van hevig stervormende sterrenstelsels en het inter-cluster media, snel vernietigd door botsingen met thermische ionen en electronen. Dit mechanisme is echter inefficiënt wanneer de moleculen geïsoleerd zijn van het gas, in kleine, meer compacte wolken. Kosmische straling is wel in staat die compacte wolken te bereiken en zal de levensduur bepalen van deze beschermde PAHs. Dit kan gebruikt worden als aanwijzing voor de aanwezigheid van koud, meegevoerd materiaal.

Om dit werk samen te vatten, hebben we de levensduur van PAHs bepaald in het interstellaire medium van de Melkweg. We hebben een model gebruikt voor het ISM, dat uit 2 fasen bestaat. In dit model verplaatst de materie zich snel van de warme gebieden tussen de wolken naar de koude wolken. PAHs (alsmede stof), worden vernietigd door SN schokgolven wanneer ze zich tussen de wolken bevinden. De tijd die het kost om SN schokgolven te ontwikkelen is afgeleid volgens McKee (1989) (zie Hoofdstuk 3). Fig. 5 laat de tijd zien die kosmische straling en supernova schokgolven nodig hebben om PAHs te vernietigen. Deze waarden zijn bepaald onder aanname van T_0=7.5 eV en E_0=4.6 eV. De kromme met de naam "cosmic rays" (kosmi-

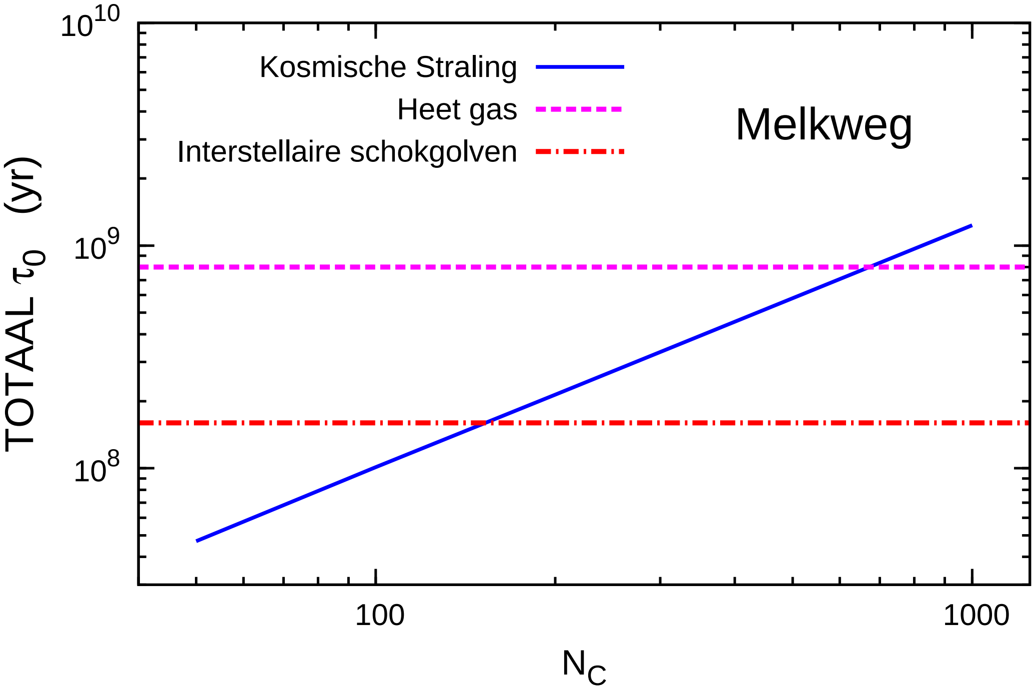

Figuur 5 — De levensverwachting van PAHs in de Melkweg ten opzichte van kosmische straling, interstellaire schokgolven ($50 \leq v_S \leq 200$ km s^{-1}) en heet gas dat door adiabatische schokgolven is verhit ($v_S > 200$ km s^{-1}).

sche straling) refereert aan kosmische straling ion- en electroninteractie in de Melkweg. De lijn waarbij "interstellar shocks" (interstellaire schokgolven) staat, refereert aan schokgolven met lage snelheden ($<$ 200 km s^{-1}), deze schokgolven koelen door middel van straling af, terwijl de lijn genaamd "hot gas" (heet gas) refereert aan schokgolven met hoge snelheden ($>$ 200 km s^{-1}), waarbij de SNRs afkoelen door middel van adiabatische expansie.

Antwoorden op de sleutelvragen

We zijn nu in staat om de sleutelvragen die we opgesteld hebben in §6.1 te beantwoorden. Wat de eerste vraag betreft, kunnen we stellen dat het lot van PAHs die worden gebombardeerd met hoog energetische ionen en electronen sterk afhangt van zowel het energiebereik en de energieverdeling van de projectielen, als de grootte van het PAH-molecuul. PAHs met minstens 50 koolstofatomen kunnen schokgolven overleven met snelheden tot 100 km s^{-1}, hoewel hun structuur waarschijnlijk verandert door het verlies van koolstofatomen. Bij snelheden groter dan 100 km s^{-1} worden de PAHs volledig vernietigd (**Hoofdstuk 3**). Hetzelfde geschiedt in een gas van een miljoen graden (**Hoofdstuk 4**). Zowel in schokgolven als in een heet gas zijn electronen de voornaamste oorzaken van de vernietiging. Wanneer de vernietiging wordt toegebracht door de hoogenergetische deeltjes van kosmische straling (5 MeV – 10 GeV), dan wordt deze veroorzaakt door inelastische botsingen met ionen (**Hoofdstuk 5**). In alle gevallen zijn grote PAHs weerbaarder dan kleine PAHs.

Betreffende de tweede vraag, hebben we allereerst aangetoond dat, zelfs op kleine schaal, PAHs onderhevig zijn aan een keur van omstandigheden die in staat zijn hun karakteristieke eigenschappen te veranderen (**Hoofdstuk 2**). De invloed van schokgolven is met name merkbaar in het warme deel van de interstellaire materie, tussen de wolken en is minder efficiënt in diffuse wolken. Kosmische straling daarentegen, kan de PAHs overal bereiken (behalve misschien in de meest compacte kernen van moleculaire wolken) en kan elk materiaal aantasten. PAHs die verspreid zijn in een heet gas zoals in de halos van sterrenstelsels, de uitstromen van starbursts en het ICM worden snel vernietigd door botsingen met electronen. Dit mechanisme is inefficiënt als de moleculen zich in compactere, geïsoleerde wolken bevinden. Kosmische straling kan ook deze geïsoleerde wolken bereiken en bepaalt de levensduur van deze beschermde PAHs. Dit kan gebruikt worden om de aanwezigheid van koud, meestromend materiaal aan te duiden. Deze conclusie kan worden getrokken uit de gecombineerde resultaten van **Hoofdstuk 3**, **Hoofdstuk 4**, en **Hoofdstuk 5** en onderstreept het verband tussen microscopische en macroscopische effecten op de interstellaire PAH-populatie.

Curriculum vitae

I was born the 28th of July 1974 in Torino, Italy. After less than a year I started moving with my family to different Italian cities (Milano, Roma) and other countries (Lybia, Canada and Tunisia). I attended primary and secondary school, and the first year of high school (Liceo Scientifico) between Canada, Italy and Tunisia, until we settled back in Milano where I finished high school and started university.

I studied Physics at the University of Milano, with specialization in Astrophysics. For my Master thesis (Tesi di Laurea) I have analyzed the characteristics of cosmic ray protons detected in space during the *Alpha Magnetic Spectrometer* (AMS) experiment, studying the propagation of these particles in the Earth magnetosphere and the processes of production of cosmic rays as a function of the geographical distribution of the sources.

After graduation, I got a research fellowship from CILEA (Interuniversity Consortium for Supercomputing) and I worked on high performance calculations for astroparticle experiments and development of software for data analysis. I subsequently obtained a second research fellowship, this time from INFN (National Institute for Nuclear Physics). I was engaged in a complete simulation of the bombardment of the space station ISS by cosmic rays, with comparison to AMS experimental data and study of the propagation of cosmic rays into the heliosphere. I was also enrolled in the realization and management of a system for data transfer and data handling for the phase-2 of the AMS experiment on the International Space Station. During my research activity I have made several working visits at CERN (Switzerland).

In November 2004, I started my Ph.D. in Astronomy at the Sterrewacht Leiden (Leiden University) under the supervision of Prof. dr. Frank Israel and Prof. dr. Alexander Tielens, as a Marie Curie Fellow in the EARA-EST project. My research has been dedicated to investigate for the first time the *collisional* processing of Polycyclic Aromatic Hydrocarbons (PAHs) in astrophysical environments subjected to shocks and cosmic ray bombardment. As part of the EARA traineeship, I had the opportunity to spend ten months in the Institut d'Astrophysique de Paris (IAP - Paris, France), and I worked one year at the Institut d'Astrophysique Spatiale (IAS - Université Paris-Sud XI, Orsay, France) with Prof. dr. Anthony Jones.

During the Ph.D. I participated in the NOVA fall school (Dwingeloo) and in the Les Houches Physics School on Interstellar Dust in Les Houches (France). I presented my work during conferences, workshops and seminars in Paris (France), Pasadena (USA), Orsay (France) and Arcachon (France). In Leiden I followed a course on Project Management and EU Funding and I had a two day training on Research Management. I also was for one year the organizer of the Starburst group meetings.

I would like to continue my career in Astrophysics.

Acknowledgments

Here we are. The last words of my thesis. A journey through memories, to remember the persons who accompanied me during this adventure. Maybe with some of you we met only few times, or we did not spend to much time together. It does not matter. The persons you meet can really change your life, and only the lack of space prevents me to mention you all.

Thanks Sterrewacht Leiden for being a place where I will always feel at home.

To our secretaries, Kirsten, Jeanne, Anita, Elise and Liesbeth, I appreciated your empathy and your help in any circumstance. Computer guys, David, Tycho, Erik and Aart, I'm grateful for all the problems you solved with such a patience. I would like also acknowledge the financial support that I received during my PhD from the Sterrewacht, from Leiden University and from the Leids Kerkhoven-Bosscha Fonds.

Astrochemisty group (and infiltrators in the 5th floor!) thanks to all of you because, even if I wasn't there so often I feel like you have adopted me. Raymond, I always enjoyed the discussions with you and I thank you so much for translating my stellingen in Dutch. Stijn, Frank, Franco, Michele, Vy, Leonie, Kirsten, Paola, Saskia, Rafael, Annelies, Dominic, Demerese, Pedro, Brent, the other members of the Starburst group and all of you, beautiful people of the Sterrewacht that I had the chance to meet during these years. With some of you we became close friends, with some others maybe we just did not have the time. This is for you. *Bedankt.*

Herma, you are my friend and my example. Your sensibility and authentic participation, your encouragement. I will keep them as a treasure. Isa, thanks for your hospitality and your delicious soup! I had such a good time in your place and I will never forget your generosity when I was sick and you took care of me. Liesbeth, when I was away I missed you so much, and our perfect office and the time we spent together. Maaike, our wonderful conversations about books, cooking, life. Thank you for sharing all of this with me. To you and Liesbeth my gratitude for the great English-Dutch translation of my summary. Carolina, your smiling eyes, your enthusiasm and your support have been so important for me. Anne-Marie, when you proposed to share the hotel room at the NAC I was in Leiden only from few months and I didn't know many people. I was so happy! Your friendship is precious.

A special acknowledgment goes to Nori Poppeliers from the P&O department, thank you so much for your aid with the administration, and to Hylke Bosma, Coordinator of the Graduate School Office, who helped me to deal with the procedure required to get to the PhD defense: if I was finally able to set the date, is because of you.

Maureen, when I was looking for a place to stay in Leiden your help has been invaluable. Dinie & Joop, you are the nicest landlords I have ever met.

I started my PhD as a Marie Curie Fellow in the EARA-EST project (FP6 of the European Union). Not only this paid my salary for three years, but also gave me the possibility to spend ten months at the Institut d'Astrophysique de Paris (France) as a Secondment Stay. I would like to acknowledge the EU for this unique opportunity and all the persons at the IAP who made this visit possible, in particular Chantal Le Vaillant, who took care of many things, from administration to housing. Chantal, you have been my first friend in Paris, I'm looking forward to see you again. I thank Lysiane and Geneviève for being always so kind and helpful. Gwenaël, Beta, Kumiko, Aurélian, Clément, Sara and all my friends at the IAP, you made my stay so special, *merci.*

I had a wonderful time working at the IAS in Orsay and I will never thank enough all the people who made this possible, researchers, support staff and the great group of PhD students and Post-Docs. Ghislaine, your help in the library has been fundamental. Sophie, Pavel, Marie, Manuel, Vincent, Pierre and all who remain unmentioned, *merci* for your warm welcome, continuous support and friendship.

Lou, Eli and Frédéric, I really appreciated our conversations, so useful and pleasant. Sue, thanks for your support.

Caesar & Alicia, Victor & Beatrice, I enjoyed every moment with you. Bruno & Veronica, I will never forget the amazing boat trip you organized for my birthday. It was a great suprise. You are wonderful friends.

Clara, *amiga mia*, we met for the first time at the Dutch class, almost five years ago. How many things happened since then! Thank you for your care and attention, even when we were far away. I'm so happy to share this moment with you.

A would like to send a special thank to Prof. L. Pasinetti, Prof. C. Paizis and Prof. G. Chincarini from Milano University. Dear Laura, Costa and Guido, thanks for what I have learned from you, which is much more than Astrophysics, and for your invaluable support. Without you, this thesis would has never been started.

Grazie alle mie Amiche: Isabella, Elena, Michela, Eleonora, Elena. So che voi ci siete sempre.

Claire, Yves, Liliane, merci d'avoir été ma deuxieme famille.

Grazie a voi Cari Nonni, che mi pensate sempre, augurandomi ogni bene.

Mamma, Papá, Lucia, Evelyn: finalmente ce l'abbiamo fatta. Sono stati anni entusiasmanti, ma anche lunghi e faticosi, e voi mi siete mancati ogni giorno. Grazie per avermi sempre incoraggiato ad inseguire i miei sogni, ovunque mi portassero. Questa tesi e' per voi.

Et à toi, Guilhem, qu'est-ce que je peux dire? Merci parce que tu as toujours cru en moi, merci pour ta patience, merci pour avoir été toujours lá quand j'étais tellement fatiguée et le but semblait si loin.

Here we are. This journey is over. A new one just started. I thank you all.

We dance round in a circle and suppose,
but the secret sits in the middle and knows.

Robert Frost